CWP-121

— Project Review —

Consortium Project on
Seismic Inverse Methods for Complex Structures
May 26-29, 1992

prepared by

Mohammed Alfaraj, Phil Anno, Norman Bleistein,
Tong Chen, Jack K. Cohen, Lydia Deng,
Michel Dietrich, Francesca Fazzari, Tong Fei,
Dave Hale, Ken Larner, Jianchoa Li,
Zhenyue Liu, and Omar Uzcategui

Table of Contents

Table of Contents (continued)

INTRODUCTION

This book is a review of the research program at the Center for Wave Phenomena, Colorado School of Mines, as of April 30, 1992.

The projects described here reflect our dual interests in 1) computer-efficient seismic data processing, and 2) inversion — including amplitude effects(dynamics) as well as phase effects (kinematics) in seismic methods.

Two new sponsors have joined our consortium during this year. We welcome the support and interaction of Elf Acquitaine and Compagnie Générale de Géophysique (CGG).

CWP people

The consortium project has been led by Norm Bleistein, Jack Cohen, Dave Hale and Ken Larner. We currently have two visiting faculty: Michel Dietrich, from CNRS, Grenoble, France; and Jianchao Li from the Department of Geophysics, China University of Geosciences, Beijing. Both men will return to their home countries this summer. Michael Zhdanov, Head of the Troitsk Branch of the Institute of the Physics of the Earth, USSR Academy of Sciences, begins a one-year visit with us in May.

Students who received partial or full support by the project during the past year are Phil Anno, Craig Artley, Tong Chen, Lydia Deng, Francesa Fazzari, Tong Fei, and Andreas Reuger. Other students who worked with the CWP faculty include Mohammed Alfaraj, Tariq Alkhalifah, Zhenyue Liu, and Omar Uzcategui.

Jo Ann Fink manages our administrative matters, and Barbara McLenon is our publications and technical editor. Marge Hoage, in her role as Ken Larner's secretary, also contributes her efforts to CWP. Research associate John Stockwell serves as our systems manager and resident scholar.

Below is a summary of CWP activities during the past project year.

Presentations at the '91 SEG meeting

The following authors presented papers at the International Meeting of the Society of Exploration Geophysicists in Houston:

- Mohammed Alfaraj and Ken Larner, Dip-Moveout for Mode-Converted Waves
- Phil D. Anno, Emergence Planes for Three-Dimensional Ray Tracing
- Craig T. Artley, Dip-Moveout Processing for Depth-Variable Velocity
- Norman Bleistein and Jack K. Cohen, The Cagniard Method in Complex Time Revisited
- Justin P. Hedley, 3-D Migration via McClellan Transformations on Hexagonal Grids

- Ken Larner, Migration Overview
- Zhenyue Liu and Norman Bleistein, Velocity Analysis by Inversion

Status of recent papers

CWP-090: Dong, W., Emanuel, M.J., Bording, P., and Bleistein, N., 1990, A computer implementation of 2.5D common shot inversion: Geophysics, 56, 9, 1384-1394.

CWP-095: Hale, D., 1990, Stable explicit depth extrapolation of seismic wavefields: Geophysics, 56, 11, 1770-1777.

CWP-096: Hale, D., 1990, 3-D depth migration via McClellan transformations: Geophysics, 56, 11, 1780-1785.

CWP-098: Bleistein, N., and Cohen, J.K., 1991, An alternative approach to the Cagniard deHoop method: to appear, Geophysical Prospecting.

CWP-099: Li, Z., 1990, Compensating finite-difference errors in 3-D migration and modeling: Geophysics, 56, 10, 1650-1660.

CWP-100: Mikulich, W., and Hale, D., 1990, Steep-dip v(z) imaging from an ensemble of Stolt-like migrations: Geophysics, 57, 1, 51-59.

CWP-101: Dong, W., and Bleistein, N., 1990, 2.5D Kirchhoff inversion theory applied to VSP and crosshole data: joint paper with MIT, submitted to Geophysical Prospecting.

CWP-103: Bleistein, N., 1991, Mathematica and the method of steepest descents: to appear in two parts, Seismic Exploration Journal.

CWP-105: Alfaraj, M. and K. Larner, 1992, Short Note: Transformation to zero offset for mode-converted waves: Geophysics, 57, no. 3, 474-477.

CWP-106: Aldolaijan, A., 1991, Residual phase estimation by homomorphic transformation: submitted to Geophysics.

CWP-108: Cohen, J., 1992, Packages for logic and set theory: Mathematica Journal, 2, no. 1, 91-93.

CWP-109: Cohen, J. and David R. DeBaun, 1991, Discrete approximation of linear functionals: submitted to Mathematica Journal.

CWP-110: Hedley, J.P., 1991, 3-D migration via McClellan transformations on Hexagonal Grids: to appear in Geophysics August, 1992.

CWP-111: Worley, Shelby C., 1991, The geometry of reflection: submitted to Geophysics.

CWP-112: Hale, D., and C. Artley, 1991, Squeezing dip moveout for depth-variable velocity: submitted to Geophysics.

CWP-113: Dietrich, M., and J.K. Cohen, 1992, 3-D migration to zero offset for a constant velocity gradient: submitted to Geophysical Prospecting.

Excerpts from the following student theses appear in this review. Sponsors will receive the completed reports in the near future:

CWP-114: Deng, H.L., 1992, Seismic wave propagation in thinly-layered media with steep reflectors: M.Sc. thesis, Colorado School of Mines.

CWP-115: Artley, C., 1992, Dip moveout processing for depth variable velocity: M.Sc. thesis, Colorado School of Mines.

CWP-116: Fazzari, F., 1992, A dip-dependence divergence correction: M.Sc. thesis, Colorado School of Mines.

CWP-117: Anno, P., 1992, A Klein-Gordon Theory for Acoustic Modeling and Imaging: Ph.D. thesis, Colorado School of Mines.

Computer program documentation

We now offer our software on unix tar diskettes or tapes. Sponsors with access to Internet can also acquire files by FTP. Call us if you have questions on how to access those files.

U08R: Docherty, P., Documentation for the 2.5-D common shot program CSHOT, 1988. Proprietary: 1/27/91. Revised version distributed to the sponsors, July, 1991.

U13R: Dong, W., CXZCS: A 2.5D common shot inversion program in a c(x,z) medium. Edited by Z. Liu. Proprietary: 2/14/93. Revised version distributed to the sponsors March, 1992.

U15: Hsu, C., CXZCO: A 2.5D common offset inversion program in a c(x,z) medium. Edited by Z. Liu. Proprietary: 10/12/94.

Two additional codes written by Dave Hale are also available to sponsors on request through the FTP directory or by request:

- Migration by extrapolation
- Triangular modeling package

Transformation to Zero Offset for Mode-Converted Waves by Fourier Transform

Mohammed Alfaraj

Center for Wave Phenomena
Colorado School of Mines
Golden, Colorado 80401
(303) 273-3557

Transformation to zero offset for mode-converted waves by Fourier transform

Mohammed Alfaraj

ABSTRACT

Approximate transformation to zero offset (TZO) for mode-converted waves can be done in the frequency-wavenumber (f–k) domain by using an expression for the moveout of reflections from dipping reflectors in a constant-velocity medium. The moveout expression is derived by first writing both time and offset as power series in a slowness parameter ν. Traveltime is then obtained as a power series in offset, by matching like powers of ν in those two power series.

The f–k formulation for TZO, here, is based on the hyperbolic approximation to the derived moveout expression. Unlike that for ordinary p-waves, at this level of approximation the f–k formulation for mode-converted waves has an extra, time-invariant, linear phase shift corresponding to a constant lateral shift in space. For a horizontal reflector, the lateral position of the conversion point for mode-converted waves should actually change as a function of depth and offset. I further modify the phase shift to be time-variant to better resemble this behavior of converted waves. Besides being shifted, the impulse response of this TZO method is an ellipse that is slightly squeezed relative to that of ordinary p-waves. Application of this TZO method to synthetic data shows that even at this level of approximation it is important to tailor TZO to treat mode-converted waves. Conventional TZO fails to correct data as well.

INTRODUCTION

Transformation to zero-offset (TZO) for a constant-velocity medium is well understood and is readily implemented when dealing with either p-waves or s-waves. For instance, TZO can be achieved by first applying normal moveout (NMO) correction and then applying dip moveout (DMO) correction to the prestack seismic data (e.g., Hale, 1984). The TZO process transforms prestack seismic data in such a way that

common-midpoint (CMP) gathers are closer to being common-reflection-point (CRP) gathers after the transformation.

Converted (p–s or s–p) waves are different from normal (p–p or s–s) waves in that the downgoing and upgoing waves travel at different velocities, even in an isotropic, homogeneous medium. This makes the kinematics more complicated than those encountered in the absence of mode conversion.

TZO for mode-converted waves has been investigated by several researchers. Sword (1984) suggested that mode-converted data be transformed, in both offset and midpoint, prior to any conventional processing. His analysis is valid for only small offsets. Harrison (1990) and den Rooijen (1991) have proposed integral solutions for the TZO process for converted waves in constant-velocity media. Implementation of their methods is carried out in such a fashion that the recorded nonzero-offset time t is directly mapped into its corresponding zero-offset time t_0. TZO for mode-converted waves can also be achieved by applying DMO prior to NMO correction (Alfaraj and Larner, 1992) by means of transforming the prestack data into a nonphysical offset-time domain. The DMO correction depends only on the *ratio* of the velocities, not on the individual velocities themselves. Although kinematically correct, this nonphysical-domain TZO approach falls short of properly treating phase and amplitude.

Here, a method is proposed to address the TZO problem for converted waves in the frequency-wavenumber (f–k) domain. The derivation is based on an approximate expression for the moveout of reflections from a dipping reflector in a constant-velocity medium. The derived moveout relation expresses traveltime-squared as a power series in offset; the f–k TZO formulation itself is based on the hyperbolic approximation to the derived moveout relation. This level of approximation avoids having to deal with cubic and higher-order equations. To alleviate the discrepancy arising from truncating the power series, I modify the f–k formulation to yield a TZO operator that honors the lateral shift in conversion point, relative to the midpoint, for horizontal reflectors.

THE KINEMATICS OF CONVERTED WAVES

For ordinary p-waves, and in a constant-velocity medium, traveltime can be expressed as an explicit function of offset, zero-offset time, velocity, and dip (Levin, 1971). This relation, the well-known hyperbolic moveout equation, is used as the basis in deriving TZO by Fourier transform for ordinary p-waves (Hale, 1984). For mode-converted waves, an exact time-distance relation was introduced by Harrison (1990) and by Alfaraj and Larner (1992). Unfortunately, unlike the situation for ordinary p-waves, the traveltime expressions for mode-converted waves are not explicit functions of dip. To formulate an f–k TZO operator, we need a moveout relation in which time explicitly depends on dip. An approximate dip-dependent moveout relation is derived next.

The derivation is based on the model of a single dipping reflector in a constant-velocity medium, as shown in Figure 1. In that figure, the offset distance separating

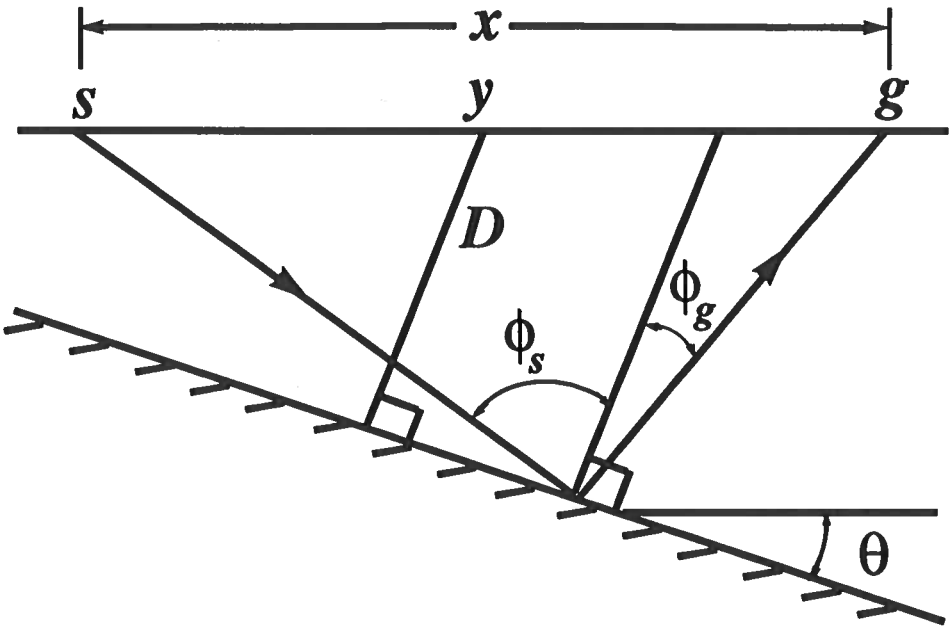

FIG. 1. Depth section depicting a mode-converted, reflection ray path in a homogeneous medium with a dipping reflector.

source s and geophone g is x. The quantity D designates the distance from the midpoint y (between s and g) to the reflector, whose dip angle is θ. The angles between the normal to the reflector and the incident and reflected (mode-converted) rays are, respectively, ϕ_s and ϕ_g. From the geometry of the figure, offset x can be expressed as

$$x = \frac{2D(\tan\phi_s + \tan\phi_g)}{2\cos\theta + \sin\theta(\tan\phi_s - \tan\phi_g)}. \tag{1}$$

With the downgoing and reflected waves traveling at speeds v and γv, respectively, the traveltime for the reflection is then given by

$$t = \frac{1}{v}\left[D\left(\frac{1}{\cos\phi_s} + \frac{1}{\gamma\cos\phi_g}\right) + \frac{x\sin\theta}{2}\left(\frac{1}{\gamma\cos\phi_g} - \frac{1}{\cos\phi_s}\right)\right]. \tag{2}$$

The angles ϕ_s and ϕ_g can be expressed in terms of a slowness parameter ν along the dipping interface using Snell's law:

$$\nu = \frac{\sin\phi_s}{v} = \frac{\sin\phi_g}{\gamma v}. \tag{3}$$

In the presence of dip, and unlike that for ordinary p-waves, traveltime for mode converted waves is no longer an even function of offset within a CMP gather. That

is, considering p–sv conversion for example, interchanging s and g in Figure 1 yields a different ray path and, hence, a different traveltime. The dependence of time t on offset x can thus be expressed in the following series form

$$t^2 = c_0 + c_1 x + c_2 x^2 + c_3 x^3 + \ldots, \tag{4}$$

which includes both odd and even powers of x. In the absence of mode conversion, odd powers of x would drop out from this power series expression.

Equations (1) and (2) can be expressed in terms of the slowness parameter ν by substituting for ϕ_s and ϕ_g their values from equation (3). Consequently, t^2, x, x^2, x^3, ..., are expressed as power series (Taylor expansion) in the slowness parameter ν. After substitution of those into equation (4), the coefficients c_i can then be recursively solved for by matching like powers of ν. The first five coefficients are

$$\begin{aligned}
c_0 &= \left(\frac{2D}{v_a}\right)^2 \equiv t_0^2, \\
c_1 &= \frac{2(1-\gamma)t_0 \sin\theta}{(1+\gamma)v_a}, \\
c_2 &= \frac{4\gamma\cos^2\theta + (1-\gamma)^2\sin^2\theta}{(1+\gamma)^2 v_a^2}, \\
c_3 &= \frac{8\gamma(1-\gamma)\cos^2\theta\sin\theta}{(1+\gamma)^3 t_0 v_a^3}, \\
c_4 &= \frac{4\gamma(1-\gamma)\cos^2\theta\left[(\gamma-1)\cos^2\theta + (2-2\gamma-\gamma^2)\sin^2\theta\right]}{(1+\gamma)^4 t_0^2 v_a^4},
\end{aligned}$$

where v_a is an average velocity (Alfaraj and Larner, 1992), given by

$$\frac{2}{v_a} = \left[\frac{1}{v} + \frac{1}{\gamma v}\right].$$

If the series in equation (4) is truncated beyond the third term, the approximate moveout relation, after some algebra and trigonometric substitution, becomes

$$t^2 = t_0^2 + \frac{2(1-\gamma)t_0 x \sin\theta}{(1+\gamma)v_a} + \frac{4\gamma x^2}{(1+\gamma)^2 v_a^2} + \frac{\left[(1-\gamma)^2 - 4\gamma\right]x^2\sin^2\theta}{(1+\gamma)^2 v_a^2}. \tag{5}$$

This relation is clearly an even function of neither offset nor dip. Note that when $\gamma = 1$ (no mode conversion), equation (5) reduces to the well-known hyperbolic relation for ordinary p-waves. Equation (5) will next be used to facilitate the derivation of TZO in the f–k domain.

$f-k$ TZO FOR CONVERTED WAVES

The third term in equation (5) has no dip dependence, and is referred to here as T^2. Define NMO-corrected time t_n by

$$t_n^2 \equiv t^2 - T^2, \tag{6}$$

with the assumption that the recorded and the NMO-corrected seismograms, p and p_n, respectively, are related by $p_n(t_n, y, h) = p(t, y, h)$. Here, y denotes midpoint and h is half-offset, given by $x/2$. Zero-offset time t_0 is then obtained from (5) and (6) as

$$t_0 = \frac{2(\gamma-1)h\sin\theta + \sqrt{t_n^2(1+\gamma)^2 v_a^2 + 16\gamma h^2 \sin^2\theta}}{(1+\gamma)v_a}, \tag{7}$$

where it is assumed, again, that $p_0(t_0, y, h) = p_n(t_n, y, h)$.

For a given half-offset h, the 2-D Fourier transform of $p_0(t_0, y, h)$ is defined by

$$P_0(\omega, k, h) = \int dt_0\, e^{i\omega t_0} \int dy\, e^{-iky}\, p_0(t_0, y, h). \tag{8}$$

The integration over t_0 in the above transformation can be expressed in terms of t_n using the change of variables given by equation (7). Making use of the relations for the zero-offset slope $(\Delta t_0/\Delta y)$ in the physical and Fourier domains, i.e.,

$$\frac{\Delta t_0}{\Delta y} = \frac{2\sin\theta}{v_a} = \frac{k}{\omega},$$

it follows from (7) that

$$A \equiv \frac{dt_n}{dt_0} = \sqrt{1 + \frac{4\gamma h^2 k^2}{(1+\gamma)^2 t_n^2 \omega^2}},$$

and the transformation in (8) can then be written as

$$P_0(\omega, k, h) = \int dt_n\, A^{-1}\, e^{i\omega A t_n}\, e^{iBk} \int dy\, e^{-iky}\, p_n(t_n, y, h), \tag{9}$$

where $B = h(\gamma-1)/(\gamma+1)$. The fact that B is a constant (for a constant offset $2h$) implies a linear spatial phase shift, i.e. e^{iBk}, in the Fourier domain. This linear phase shift, in turn, corresponds to a constant lateral shift in the space domain. Specifically, this constant shift is the asymptotic approximation (offset very small compared with depth) for the spatial location of the conversion point for a horizontal reflector.

2-D inverse transformation of equation (9) yields the desired TZO data, i.e., $p_0(t_0, y, h)$, as follows

$$p_0(t_0, y, h) = \frac{1}{(2\pi)^2} \int d\omega\, e^{-i\omega t_0} \int dk\, e^{iky}\, P_0(\omega, k, h).$$

The corresponding TZO operator in the t–y domain is obtained by finding the inverse Fourier transform of $P_0(\omega, k, h)$ when $p_n(t_n, y, h)$ is an impulse. This is accomplished by applying the method of stationary phase to equation (9) (see, for example, Bleistein, 1984; and Liner, 1988). The TZO operator in the t–y domain is found to be an ellipse, given by

$$\left(\frac{t_0}{t_n}\right)^2 + \left(\frac{Y_0}{H}\right)^2 = 1. \tag{10}$$

The quantity H is a scaled version of half-offset h, given by

$$H = \frac{2\sqrt{\gamma}}{1+\gamma} h. \tag{11}$$

Equation (11) implies that the TZO impulse response for converted waves is a squeezed version of that for ordinary p-waves. The quantity Y_0 is the location of the output zero-offset trace; it is shifted from the output location for ordinary p-waves, y_0, and is given by

$$Y_0 = y_0 - \frac{1-\gamma}{1+\gamma} h. \tag{12}$$

When $\gamma = 1$ (no mode conversion), equation (10) reduces, again, to the well-known DMO ellipse for ordinary p-waves.

The offset scaling as implied by (11), and the shift in the output zero-offset trace as suggested by (12), are equivalent to the transformation introduced by Sword (1984). Sword suggested that each prestack seismic trace, in the time-space domain, be given a new midpoint location and a new offset, consistent with equations (11) and (12), prior to any processing. The TZO approach introduced here, on the other hand, accounts for the location of the new midpoints, as suggested by Sword, without having to deal with trace interpolation in the time-space domain; each trace is simply shifted to the desired location by introducing a spatial phase shift in the f–k domain, as suggested by the transform in equation (9).

The formulation of this TZO approach was based on a truncated version of the series in equation (4). Considering only the first three terms of the series, as was done in the derivation above, results in a quadratic equation in t_0, as a function of t_n, the solution of which is not difficult to find and is given in equation (7). If higher-order terms of the series are also considered, the resultant equation in t_0 becomes cubic or higher order. Solutions to the cubic and higher-order equations are too lengthy for our purposes and are, therefore, deemed impractical to implement.

One result of the truncation of the power series was that the phase shift obtained in (9) was constant and time-invariant. The actual spatial shift of the conversion point for a horizontal reflector, however, is known to vary with reflection depth, or time (Tessmer and Behle, 1988). It is easy to embed time-variance of the conversion point in the phase shift of the transform in (9), and thus partially alleviate errors arising from truncating the series. Figures 2 and 3 show impulses and TZO impulse responses for TZO constructed in this way.

Figure 2 shows ten impulses on a common-offset ($2h = 5000$ m) section. Assuming a p–sv mode conversion with velocity ratio $\gamma = 1/2$, the response of the TZO operator to those impulses is shown in Figure 3. Each impulse response is an ellipse that

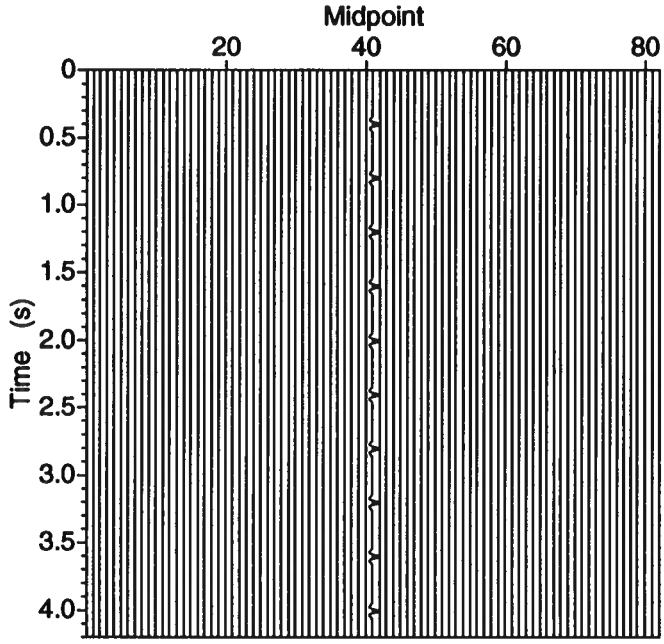

FIG. 2. Ten impulses in a constant-offset section used to test the response of the TZO operator for mode-converted waves. The offset here, 5000 m, is chosen large to emphasize the lateral shifts seen in the impulse responses in Figure 3. The midpoint spacing is 100 m.

has now been squeezed, relative to that for ordinary p-waves, in the sense that its horizontal axis, when extended to the surface, spans a distance that is smaller than offset $2h$. The ellipses in Figure 3 also differ somewhat from the actual asymmetric trajectories expected in the zero-offset mapping for mode-conversion (see, for example, Harrison, 1990). Furthermore, each ellipse has been laterally shifted in such a way that the apex now corresponds to the conversion point for a horizontal reflector.

APPLICATION TO SYNTHETIC DATA

Seismic data were simulated based on the zero-offset model depicted in Figure 4. p–sv mode conversion, with a velocity ratio $\gamma = 1/2$, is assumed. The downgoing velocity is 2000 m/s, corresponding to an average velocity v_a of 1333 m/s. The velocity used to NMO-correct the data is

$$v_{NMO} = v\sqrt{\gamma} = 1414\,m/s,$$

as dictated by the term T introduced in equation (6); this choice matches that typically made in practice—stacking velocity for reflections from nearly horizontal reflectors. An NMO-corrected CMP gather, with no TZO applied, is shown in Figure 5.

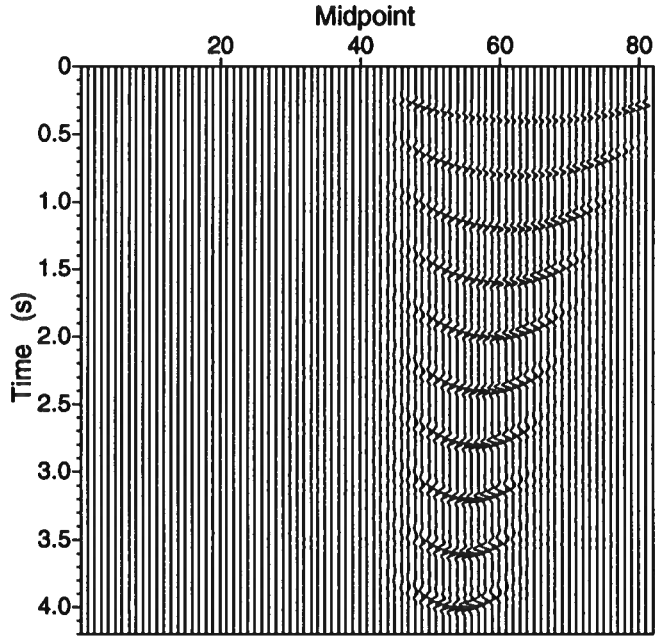

FIG. 3. Response of the TZO operator to the impulses shown in Figure 2. The squeezed ellipses have time-variant lateral shifts. Midpoint spacing is 100 m.

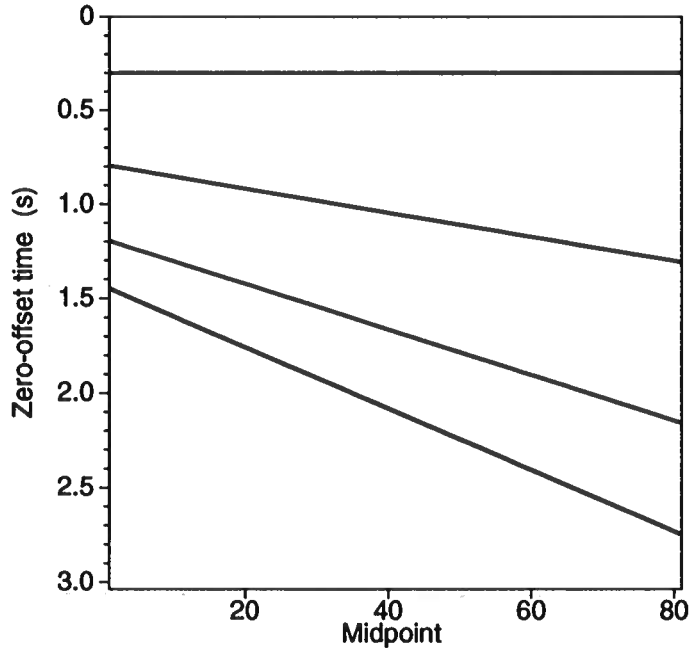

FIG. 4. Constant-velocity, zero-offset model consisting of four reflectors in a homogeneous medium. The dip angles are 0, 20, 40, and 60 degrees, respectively. The midpoint spacing is 12.5 m.

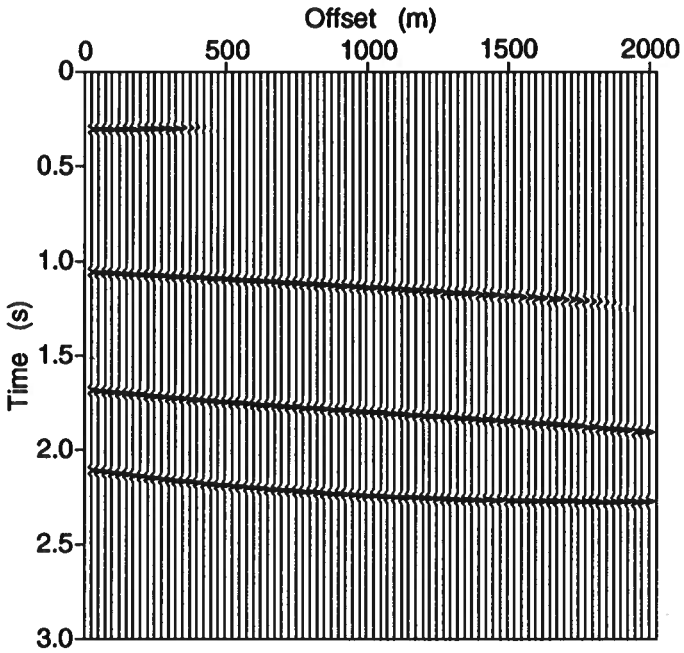

FIG. 5. NMO-corrected CMP gather taken from the middle of Figure 4 (midpoint 41), with trace spacing of 25 m. TZO correction has not been applied. Reflections from the dipping reflectors are poorly aligned.

As seen in the figure, not only are reflections from dipping reflectors poorly aligned, the residual moveout for the mode-converted data does not exhibit the hyperbolic behavior typical of poorly-corrected, ordinary p-wave data. Moreover, these data have the appearance of being under-corrected, whereas NMO-correction of ordinary p-wave data leads to over correction prior to TZO. Clearly, these data will not produce an acceptable stack of the reflections from the dipping reflectors.

After the NMO correction, the data in this test were sorted into common-offset gathers, transformed to zero offset using the f–k approach outlined above, then back-sorted into CMP (or, more precisely, CRP) gathers. The TZO-corrected CRP gather, corresponding to Figure 5, is shown in Figure 6. Alignment of reflections has been considerably improved, although the reflections on the far-offset traces for the deepest reflector, with a dip of 60 degrees, have been over-corrected. Each TZO-corrected CRP gather was then stacked. The stack, shown in Figure 7, exhibits reflection times that are close to those predicted for the zero-offset model in Figure 4. The amplitudes of the reflections from the steepest reflector are reduced somewhat as a result of the imperfect alignment of the TZO-corrected reflections in Figure 6. The relatively-low amplitudes seen in the reflections on the first few midpoints in the stack are attributed to the fact that this TZO method tends to shift seismic energy to the right (to the left if sv–p mode conversion), consistent with the results observed in the impulse responses shown in Figure 3.

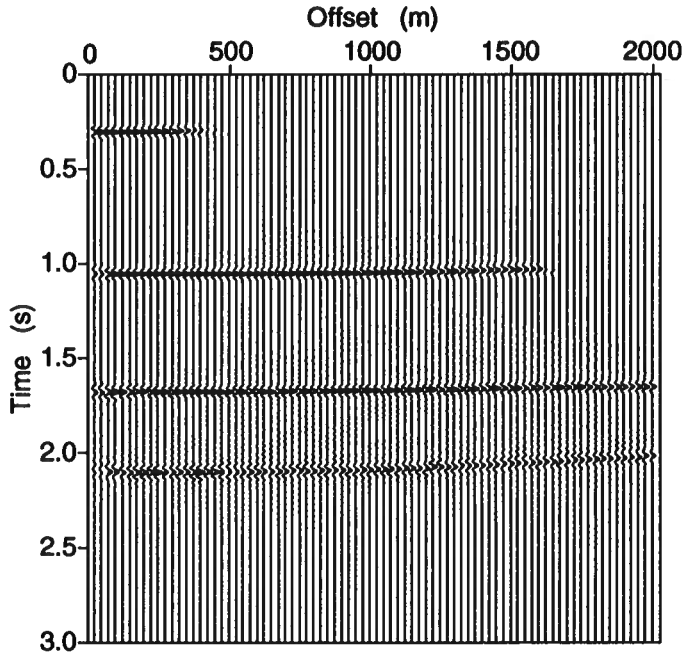

FIG. 6. TZO-corrected CRP gather corresponding to Figure 5. Alignment is improved, although residual moveout exists on the far-offset traces for the deepest (steepest) reflector.

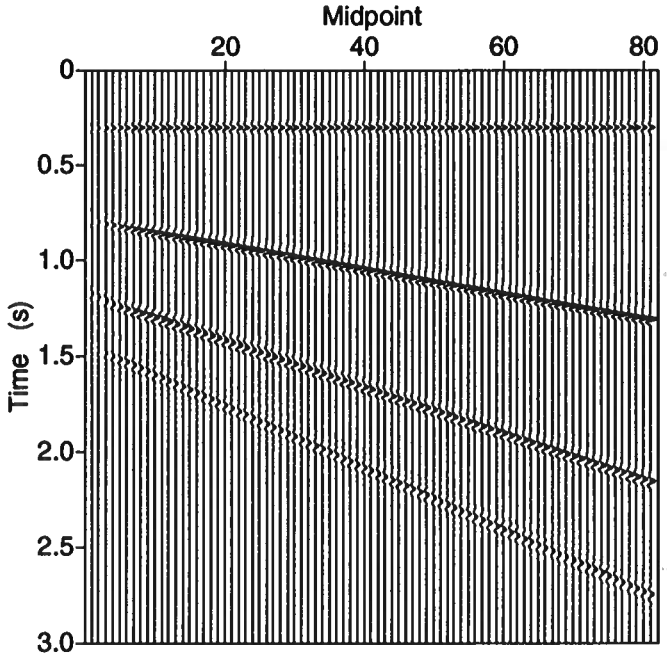

FIG. 7. Stack of the data after applying TZO. Reflection times are close to those expected for the zero-offset model depicted in Figure 4.

For comparison, the NMO-corrected mode-converted data in Figure 5 were also processed by applying the conventional f–k TZO method; i.e., with $\gamma = 1$, thus assuming no mode-conversion. The result, Figure 8, exhibits alignments of reflections

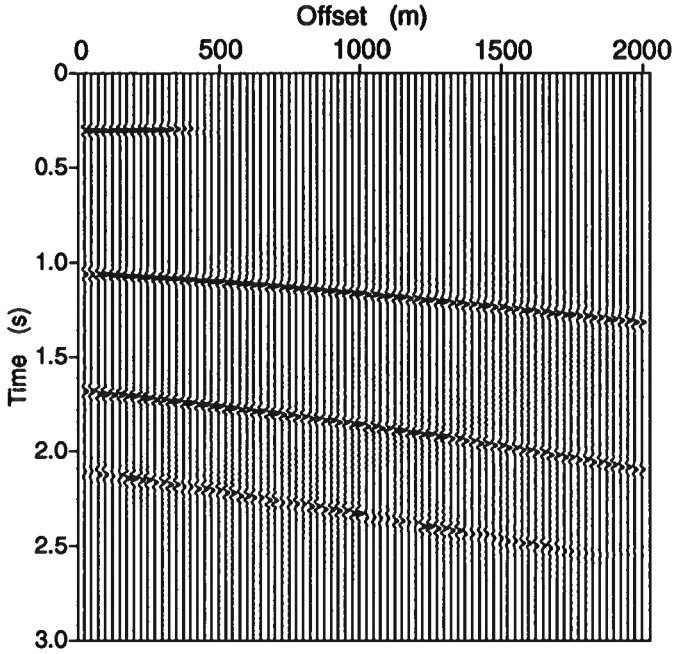

FIG. 8. CRP gather corresponding to Figures 5 and 6 after application of conventional TZO, which erroneously assumes no mode conversion. Alignment is poorer than that in both Figures 5 and 6.

that are not only poorer than that in Figure 6, they are even worse than that in the NMO-corrected gather (Figure 5) with no TZO applied. Mode-converted seismic data, therefore, *should not be TZO-processed* with conventional TZO algorithms that do not account for mode conversion.

As equation (5) implies, reflection times for mode-converted waves depend on both dip and the sign of dip. The f–k TZO method derived here, however, has no preference (bias) as to the sign of dip and, therefore, is expected to handle both positive and negative dips equally well. This assertion is verified by testing the f–k TZO method on synthetic seismic data, generated based on the zero-offset model depicted in Figure 9. The four reflectors, in this model, have dips that are the negative of those in Figure 4, with midpoint 41 having the same zero-offset reflection times in both models. Again, the downgoing velocity is 2000 m/s, and the velocity ratio is 0.5. The NMO-corrected gather corresponding to midpoint 41, prior to TZO, is shown in Figure 10. Reflections from dipping interfaces have now been severely over-corrected; recall that the same reflections were under-corrected when the dips had opposite signs, Figure 5. It is clear, again, that these data will not produce an acceptable stack of reflections from the dipping interfaces.

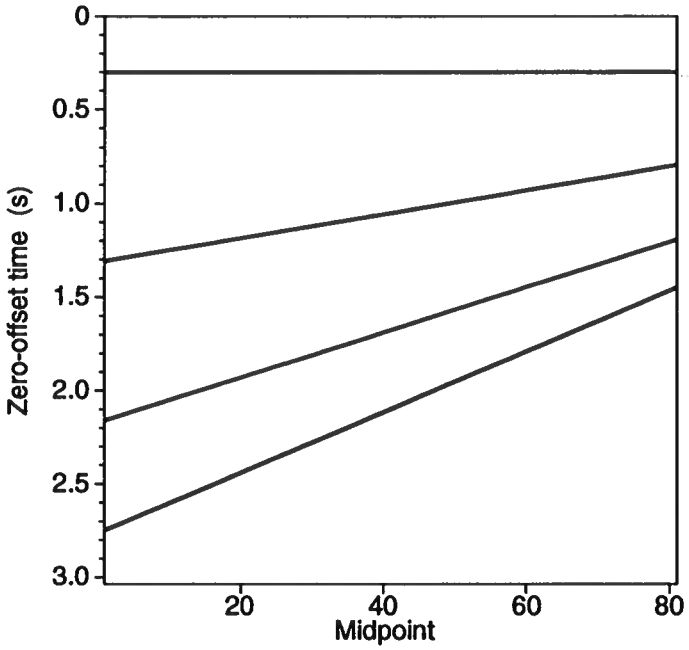

FIG. 9. Constant-velocity zero-offset model consisting of four reflectors in a homogeneous medium. The midpoint spacing is 12.5 m. This model is a mirror image of that depicted in Figure 4.

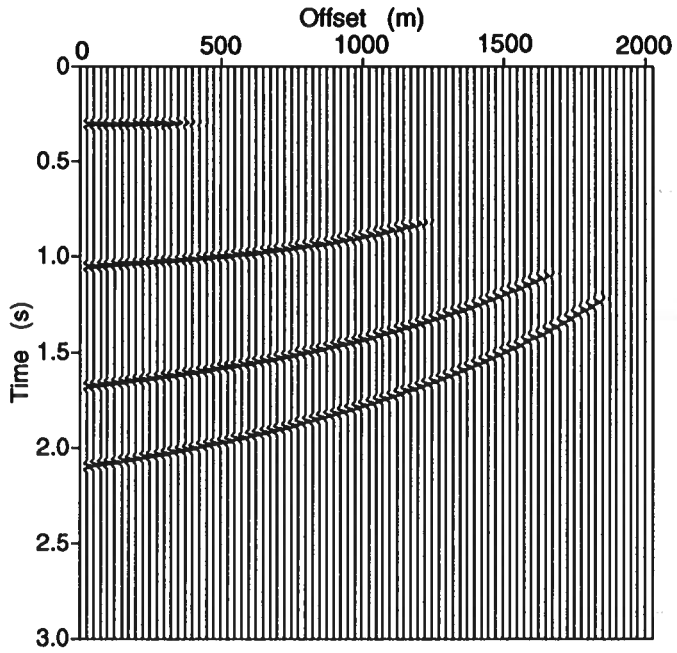

FIG. 10. NMO-corrected CMP gather taken from the middle of Figure 9 (midpoint 41), with trace spacing of 25 m. TZO-correction has not been applied. Reflections from dipping reflectors are severely over-corrected. Compare with those in Figure 5; the only difference is in the sign of dip.

The counterpart of Figure 10, after application of TZO as described above, is shown in Figure 11. Alignment has significantly been improved. Reflections on the

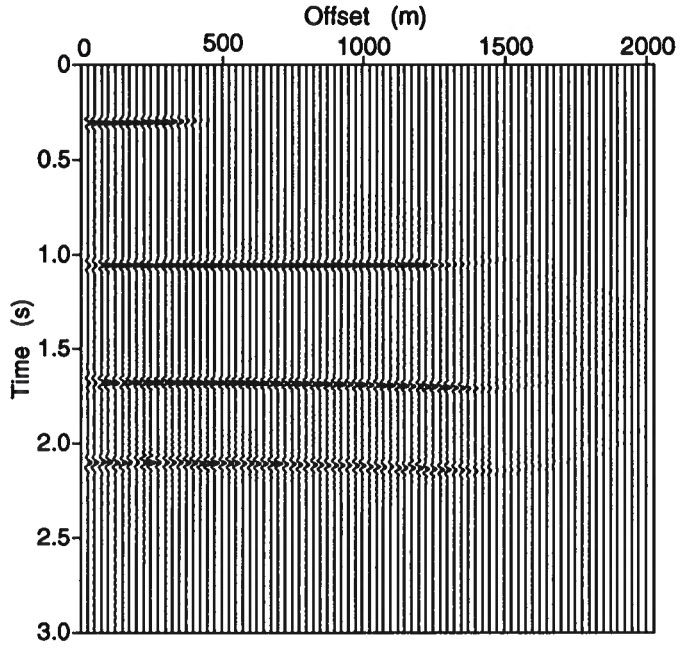

FIG. 11. TZO-corrected CRP gather corresponding to Figure 10. Alignment of reflections have significantly been improved. Reflections on the far-offset traces for the deepest reflector are now slightly under-corrected, as opposed to that being over-corrected for opposite dips (Figure 6); the difference is only in the sign of dip.

far-offset traces for the deepest (steepest) reflector have now been slightly under-corrected, whereas those in Figure 6 (opposite dips) were over-corrected. The stacked section, corresponding to the TZO-corrected data in this test, is shown in Figure 12. Reflection times from all reflectors are, again, consistent with those in the zero-offset model, Figure 9.

Finally, to further emphasize the negative consequences stemming from ignoring mode conversion in TZO when dealing with mode-converted data, the NMO-corrected data of this test were also TZO-processed assuming no mode conversion. The erroneously TZO-corrected CRP gather corresponding to Figures 10 and 11 is shown in Figure 13, in which reflections from dipping reflectors are clearly over-corrected (compare with those under-corrected, Figure 8, when dips were opposite in sign).

CONCLUSION

A method has been introduced for doing transformation to zero offset in the f–k domain for mode-converted waves. The formulation is based on a truncated series for traveltime as a function of offset, assuming a single dipping reflector in a constant-velocity medium. Similar to that of ordinary p-waves, this f–k TZO method works on NMO-corrected data, and yields an impulse response that is an ellipse that is shifted

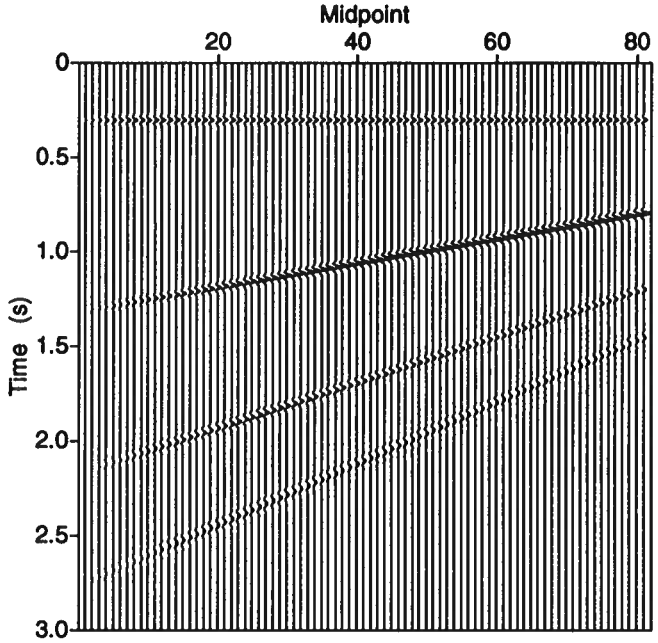

FIG. 12. Stack of the TZO-corrected CRP gathers. Reflection times are practically the same as those predicted for the zero-offset model depicted in Figure 9.

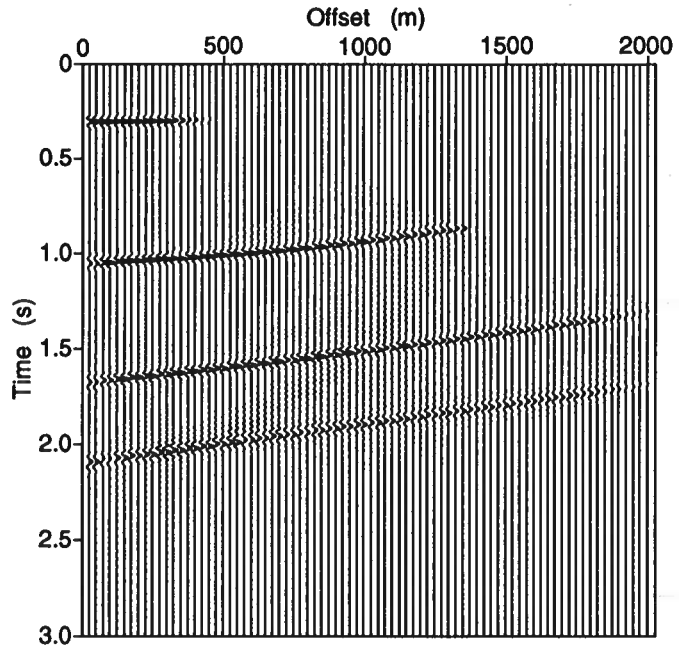

FIG. 13. CRP gather corresponding to Figures 10 and 11. which erroneously assumes no mode conversion. Alignment is clearly poor and, therefore, data processed in this way will not produce an acceptable stack.

and squeezed relative to that for ordinary p-wave data. Results from synthetic data tests indicate that

1. the *f–k* TZO approach here acts to correct misalignment of NMO-corrected data on CMP gathers, regardless of the sign of dip, and
2. mode-converted seismic data *should not be TZO-processed* with conventional TZO algorithms that ignore mode conversion.

ACKNOWLEDGEMENTS

The author thanks Professor Ken Larner for critical reviewing and improving an earlier draft of the paper, and for his technical discussion and valuable suggestions. Thanks are due to the Center for Wave Phenomena, Colorado School of Mines, for their technical support, and also to Saudi ARAMCO, Saudi Arabia, for its financial support.

REFERENCES

Alfaraj, M., and Larner, K., 1992, Transformation to zero offset for mode-converted waves: Geophysics, **57**, 474–477.

Bleistein, N., 1984, Mathematical methods for wave phenomena: Academic Press.

den Rooijen, H. P. G. M., 1991, Stacking of p–sv reflection data using dip moveout: Geophysical Prospecting, **39**, 585–598.

Hale, D., 1984, Dip-moveout by Fourier transform: Geophysics, **49**, 741–757.

Harrison, M., 1990, Converted wave DMO: Presented at the 60th Ann. Internat. Mtg., Soc. Expl. Geophys., Expanded Abstracts, 1370–1373.

Levin, F., 1971, Apparent velocity from dipping interface reflections: Geophysics, **36**, 510–516.

Liner, C., 1988, Mapping reflection seismic data to zero offset: Colorado School of Mines, CWP-073R.

Sword, C., 1984, Approximating the kinematics of converted waves: Stanford Exploration Project Report **41**, 347–368, Stanford University.

Tessmer, G., and Behle, A., 1988, Common reflection point data-stacking technique for converted waves: Geophysical Prospecting, **36**, 671–688.

Transformation to Zero Offset for Mode-Converted Waves in the $k - t_1$ Domain

Mohammed Alfaraj

Center for Wave Phenomena
Colorado School of Mines
Golden, Colorado 80401
(303) 273-3557

Transformation to zero offset for mode-converted waves in the $k-t_1$ domain

Mohammed Alfaraj

ABSTRACT

The principles underlying the Gardner dip moveout (DMO) approach, which was originally developed for ordinary p-waves, are readily extended to mode-converted waves. The process achieves transformation to zero-offset (TZO) of mode-converted seismic waves in two steps. First, DMO correction is applied by simply transforming the prestack data into a nonphysical offset-time domain. Velocity analysis in the nonphysical domain yields a dip-independent average velocity as the velocity that best stacks the data. TZO is then achieved by applying normal-moveout (NMO) correction, using the average velocity, and finally stacking the gathers in the nonphysical domain.

Implementation of this TZO method, however, is deemed unfavorable due to three problems. The problems in increasing order of severity are: amplitude and phase distortion, an amplitude-versus-offset problem, and a large-offset problem. The problem of amplitude and phase distortion seems unsolvable for mode-converted waves when using this TZO method. In addition, neither the AVO nor the large-offset problems can be overcome, even when dealing only with ordinary p-waves.

Despite these problems, useful information can still be obtained from this TZO method. Brute zero-offset sections, with coarse treatment of amplitudes, can be generated. Also average velocities, for converted-wave reflections, can be obtained from conventional velocity analysis performed on gathers in the nonphysical domain. The average velocity is useful in exploration applications, such as migration and conversion from time to depth. Study of synthetic seismic gathers shows that the average velocity obtained is not highly sensitive to the choice of the velocity ratio.

INTRODUCTION

Alfaraj and Larner (1992) have described a method for the transformation to zero offset (TZO) of mode-converted seismic waves that is an extension of the Gardner dip moveout (DMO) method (Forel and Gardner, 1988) originally developed for ordinary

p-waves. Just as with the Gardner method, the derivation of TZO for mode-converted waves is based on the assumption that seismic waves propagate in a homogeneous, isotropic medium.

Practical implementation of this TZO method encounters, in increasing order of severity, three problems: amplitude and phase distortion of data when the prescribed transformation of coordinates is done, a similar distortion in amplitude as a function of source-to-receiver offset, and an additional problem at large offset. I present an alternative approach in light of the foregoing problems.

THE (k, t_1) TZO METHOD

TZO for mode-converted waves can be achieved in two steps. First, the seismic data are corrected for DMO; second, normal moveout (NMO) correction is applied to the data. The first TZO step, i.e., DMO correction, is independent of velocity. DMO correction can be applied automatically to the data by transforming the recorded seismic data from the physical (offset-time) domain into a nonphysical domain, Gardner's (k, t_1) domain.

To transform the data to the nonphysical domain, consider a seismic trace whose half-offset between source and receiver is h and whose recorded time is t. Ignoring the fact that there is no mode conversion at zero-offset, let b denote the position, relative to the midpoint, of an equivalent zero-offset trace, as shown in Figure 1. Alfaraj and Larner (1992) have shown that the physical half-offset h can be transformed into a new half-offset k, and the recorded time t into a new time t_1 according to

$$k^2 = h^2 - b^2, \tag{1}$$

and

$$t_1 = \frac{\sigma k}{\sqrt{2h(\alpha h + \beta b)}} t, \tag{2}$$

where σ, α, and β are constants, depending only on the *ratio*, γ, of the upgoing velocity to the downgoing velocity,

$$\begin{aligned} \sigma &\equiv 1 + 1/\gamma, \\ \alpha &\equiv 1 + 1/\gamma^2, \\ \beta &\equiv 1 - 1/\gamma^2. \end{aligned} \tag{3}$$

After the transformation, seismic reflections in the (k, t_1) domain have hyperbolic moveout given by

$$t_1^2 = t_0^2 + \left(\frac{2k}{v_a}\right)^2, \tag{4}$$

where t_0 is the time experienced along a zero-offset ray travelling down with a velocity v (p-wave velocity, for example) and reflected up with a velocity γv (sv-wave velocity,

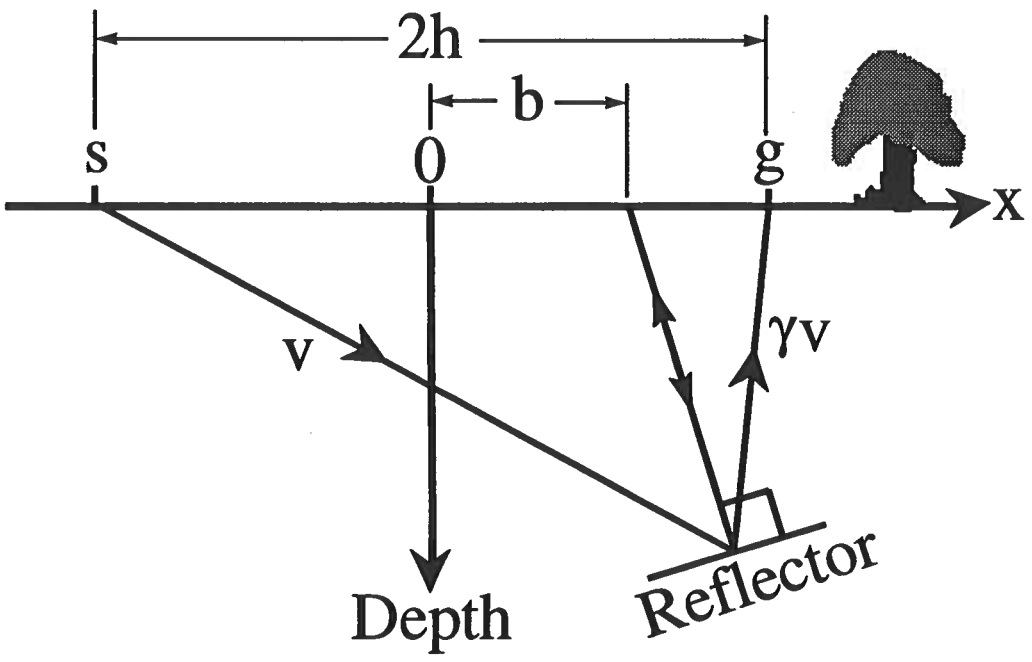

FIG. 1. Depth section depicting mode-converted reflection. Here, $2h$ is the offset distance between source s and receiver g. The midpoint is located at the surface point $x = 0$. The downgoing and the upgoing velocities are, respectively, v and γv. The equivalent zero-offset trace, for this geometry, is located a distance b from the midpoint.

for example). The velocity, v_a, relates two-way time along a zero-offset ray to distance traveled along the same zero-offset ray. Its reciprocal is the arithmetic mean of the downgoing and upgoing slownesses. That is, for a downgoing velocity v, the relationship for the average velocity v_a is given by

$$\frac{1}{v_a} = \frac{1}{2}\left(\frac{1}{v} + \frac{1}{\gamma v}\right). \tag{5}$$

From (3), v_a is also given by

$$v_a = \frac{2v}{\sigma}. \tag{6}$$

Equation (4) is a standard NMO equation; time t_1 is hyperbolic with the new offset k. In this NMO equation, the moveout velocity, v_a, is dip independent, as seen in equation (6), one of the goals in transforming data to zero-offset. Hence, after the transformation, the data are DMO corrected. Note that the transformation (and hence the DMO correction itself) does not depend on the individual p- or sv-wave velocities themselves; rather, it depends only on the velocity *ratio* γ .

Having applied DMO correction, TZO can now be completed by applying NMO correction to the data. Obviously, as equation (4) implies, conventional velocity

analysis in the (k, t_1) domain yields the dip-independent average velocity, v_a, as the velocity that best stacks the data. Consequently, the data can be stacked, after NMO correction, to yield reflections at their true zero-offset times.

Furthermore, as shown in Figure 1, after TZO the zero-offset data and the recorded nonzero-offset data pertain to a *common reflection point.* That is, TZO has removed the problem of reflection-point dispersal (Deregowski, 1986) for mode-converted data. In addition, recall that for ordinary p-wave data, reflection-point dispersal is not an issue when the reflector is horizontal. For mode-converted data, however, it is. TZO, as described here, removes reflection-point dispersal for mode-converted data when the reflector is horizontal, as well as when it has dip.

PROBLEMS WITH THE (k, t_1) TZO METHOD

Amplitude and phase distortion

Although the theory holds from the kinematics point of view, implementation of this (k, t_1) TZO method does not treat amplitude and phase properly. Figure 2b shows an output (k, t_1) gather. The input data consist of 101 synthetic common-

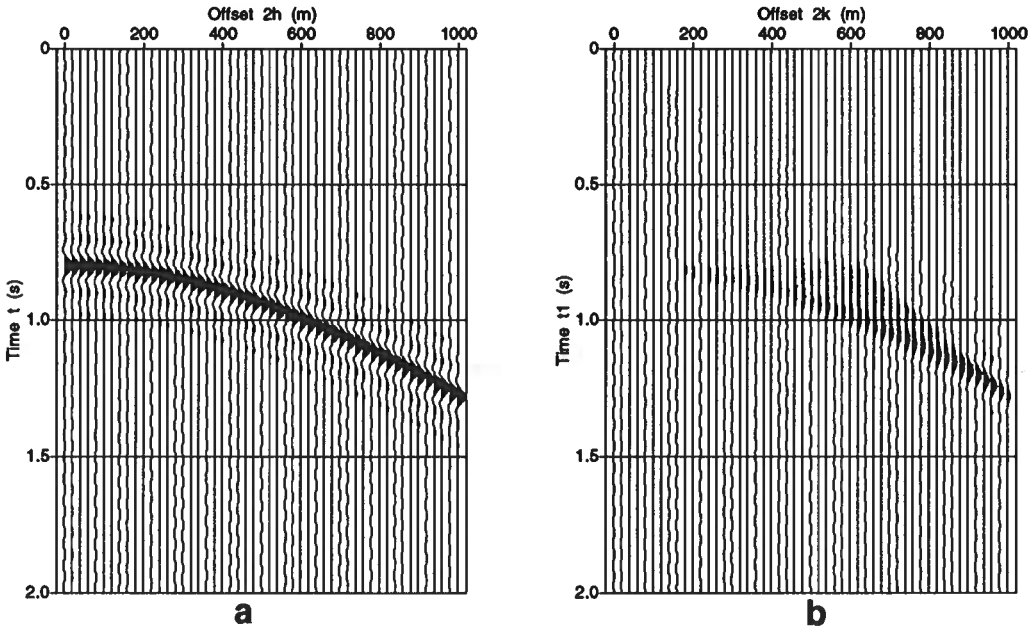

FIG. 2. (a) Representative synthetic CMP gather over a horizontal reflector at 400-m depth. (b) Output (k, t_1) gather, with severely distorted amplitude and phase. The input data are ordinary p-wave ($\gamma = 1$) synthetic CMP gathers, and the medium velocity is 1000 m/s.

midpoint (CMP) gathers over a single horizontal reflector. Only ordinary p-waves

are considered in this example, i.e., $\gamma = 1$. The input wavelet is a sinc function, with unit amplitude and a dominant frequency of 12.5 Hz (a low frequency is assumed here to emphasize the shape of the output wavelet). Each input CMP gather consists of 51 traces (including the zero-offset trace), with an increment in source-receiver separation distance of 20 m. The distance separating two consecutive CMP gathers is 10 m. For this horizontal-reflector model, all input CMP gathers are identical; one such gather is shown in Figure 2a. The location of the output (k, t_1) gather is at CMP location 51, midway along the line. All 101 CMP gathers contribute equally, without any special weighting, to the output (k, t_1) gather shown in Figure 2b.

The (k, t_1) result depicted in Figure 2b clearly shows an increase in amplitude with offset (with the exception of the last few traces). The maximum amplitude (offset $\approx$ 900 m) is about 40 times larger than the input unit amplitude (the zero-offset trace). The variation in amplitude is due to changing Fresnel-zone width as a function of k and t_1. The Fresnel-zone width for this model (Appendix A) is shown in Figure 3 for different values of k. For the range of k values shown in Figure 3a, the

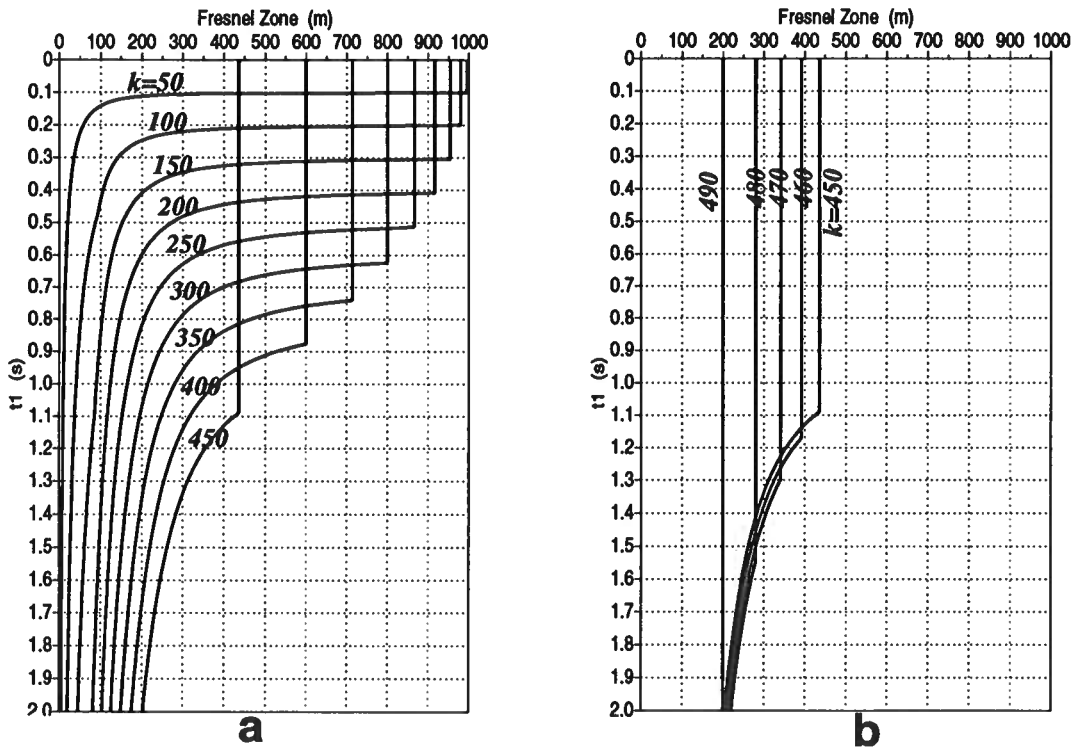

FIG. 3. Fresnel-zone width for the (k, t_1) gather depicted in Figure 2b. The Fresnel zone increases with increasing k in the time window 0.8 – 1.25 s for the range of k shown in (a). In (b), the Fresnel-zone width decreases as k (large) increases for the same time window. Corners seen on the curves are explained in Appendix A.

Fresnel-zone width, and therefore the amplitude, increases as k increases across the time window of interest (0.8—1.25 s). Figure 3b shows the Fresnel zone for another range of k's, this time the large k's. Consistent with the observation that amplitude

starts to decrease with increasing k in this offset range (starting at offset $2k \approx 900$ m in Figure 2b), the Fresnel-zone width also decreases with increasing k.

Compared with the zero-phase input wavelet in Figure 2a, the wavelet in the output (k, t_1) gather has undergone a significant amplitude and phase distortion that varies with time and offset. The distortion is worst at offset $2k \approx 600$ m, where the Wavelet contains a low-frequency precursor. To see how this distortion takes place, first note again, that each output trace gets contributions from many midpoints and many offsets. In fact, any offset-midpoint combination satisfying equation (1) will contribute to this single, constant-offset output trace in the (k, t_1) domain. Furthermore, the number of physical traces, contributing to a single (k, t_1) trace, varies as a function of k and t_1. The final (k, t_1) trace is a result of stacking the contributions from all possible traces in the (h, t) domain. In other words, each output trace is a mixture of traces from different offsets and midpoints. Figure 4 shows the contributions from all possible midpoints, before stack, to the (k, t_1) trace whose offset, in Figure 2b, is 600 m. In this figure, it is clear that the stacked trace will eventu-

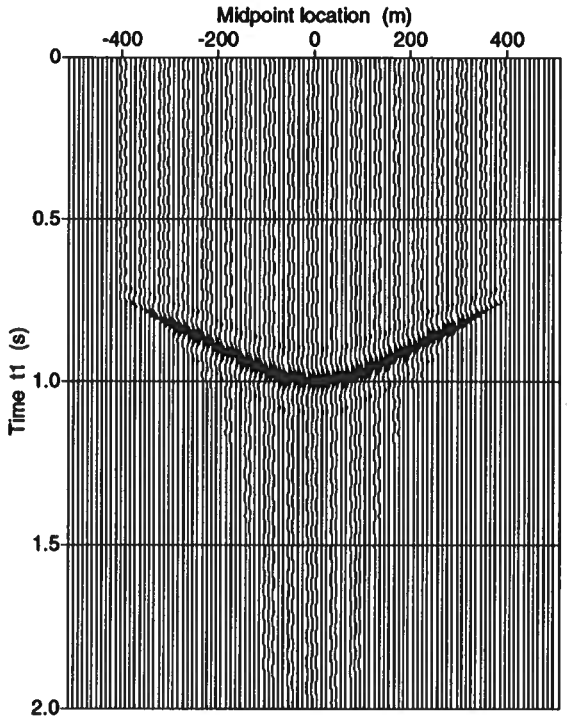

FIG. 4. Contributions from many midpoints to one single output trace in the (k, t_1) domain. In this example, the stack of this gather forms the trace whose offset is 600 m in Figure 2b. The locations of contributing midpoints are relative to the location of the output (k, t_1) gather.

ally have an amplitude that depends on the width of the Fresnel zone for the event. Besides, stacking the curved event (smile) in that figure introduces a rho-filtering (Newman, 1990), which gives rise to the precursor seen in the final stacked trace.

Due to the complexity arising with the kinematics of mode conversion, an analytic description of those smiles is not available when $\gamma \neq 1$ (even for horizontal reflectors) and, therefore, an inverse rho-filter cannot be readily designed. For ordinary p-waves, the analytic expression describing such smiles depends, among other things, on dip. Consequently, when generating a k trace, an expression for the Fresnel-zone width derived assuming some dip, will be correct for only that dip. The Fresnel-zone widths shown in Figure 3 were obtained assuming a horizontal reflector. Widths based on a horizontal reflector (Appendix A) are later used to balance amplitudes in (k, t_1) gathers.

Aside from the amplitude and phase distortion, as the theory predicts, the event in the (k, t_1) gather of Figure 2b is approximately hyperbolic, with a moveout velocity equal to that of the medium. This is shown by applying a constant-velocity (1000 m/s) NMO correction to the synthetic gather of Figure 2b. The result, depicted in Figure 5, shows that the main energy of the (distorted) event is now flattened.

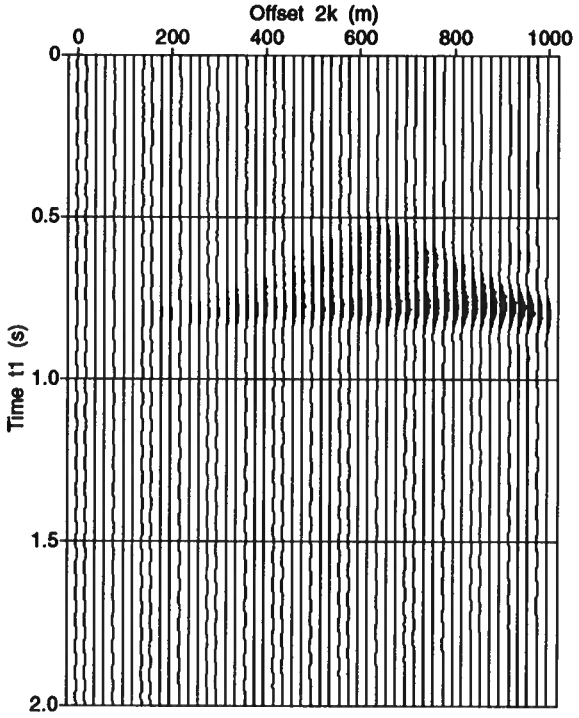

FIG. 5. The (k, t_1) gather of Figure 2b is flattened after applying a constant-velocity NMO correction to the data. The velocity used is the medium velocity, 1000 m/s.

For ordinary p-waves, Forel (1986) avoided this amplitude and phase problem completely by not transforming the data to the (k, t_1) domain. Instead, he selected a different method for implementing DMO—the constant-velocity-migration approach outlined by Ottolini (1982). Forel and Gardner (1988), however, did apply the (k, t_1) TZO implementation to ordinary p-wave, 3-D synthetic data. They observed, just

as I have shown for the 2-D case, that the amplitude and phase had undergone a distortion that varied with time and offset, although the kinematics (timing of events) were correct.

The AVO problem

It is only when b is zero that the new offset k is the same as the physical offset h, as equation (1) implies. This condition (i.e., $b = 0$) is always true only for a horizontal reflector with no mode-converted waves, in which case TZO is not even needed. In general, however, k and h are not the same; for mode-converted waves, they differ even when the reflector is horizontal. Even when k and h are the same, the final (k, t_1) trace is always a mixture of traces from different offsets and different midpoints. This drawback certainly makes AVO analysis in the (k, t_1) domain meaningless.

The large-offset problem

Further investigation of equation (1) reveals yet another problem intrinsic to the (k, t_1) domain—one that arises for large offsets $2k$. Large-k traces cannot be correctly constructed in most cases. The half-offset k is considered large when its value is comparable to the largest physical half-offset, $2h$, in question.

The relationship between the physical and the nonphysical offsets, given in equation (1), is schematically shown in Figure 6. In that figure, each circle, whose radius

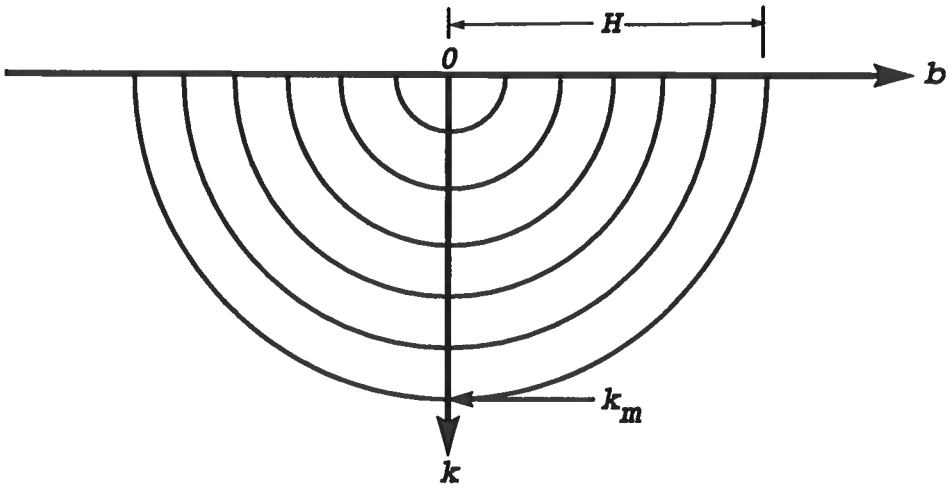

FIG. 6. Schematic diagram showing the relationship between the physical and the nonphysical half-offsets as given in equation (1). Here, circles represent constant, physical half-offsets. The maximum physical and nonphysical offsets are H and k_m, respectively.

is equal to a constant physical half-offset h, shows the relationship between k and b. The largest circle has a radius H, corresponding to the maximum physical half-offset

in question. As k increases, larger circles, and hence larger physical offsets, are involved; this, in turn, limits the values allowed for b to progressively smaller ranges in constructing k traces. In the extreme case, when the nonphysical half-offset is maximum, k_m, and is equal to H, only one value for b ($b = 0$) is allowed.

For horizontal reflectors with no mode conversion (the case when b is really zero), there should be no problem with generating traces with large k's. Figure 2b is an example of this case. For dipping reflectors (with or without mode conversion), however, large-k traces will always be erroneous. That is, the time t_1 will depart from a hyperbolic trajectory. For mode-converted waves, large-k traces will always be also erroneous even for horizontal reflectors. The reason for the error in these two cases is simply that the actual b, in the corresponding physical seismic traces, is never zero, whereas only small values for b are used (allowed) in the process of generating the k trace.

Synthetic (k, t_1) gathers from different models, Figure 7, show the problem encountered with the large-k traces. To minimize the amplitude variations from trace to trace, each trace has had a gain (based on the Fresnel-zone width, as discussed earlier) applied to it as a function of k and t_1. For all these (k, t_1) gathers in Figure 7, the input data consist of 101 CMP gathers synthesized over a reflector whose depth is 400 m; the largest offset ($2h$) is 1000 m. The medium velocity is 1000 m/s, and the input wavelet is zero phase with unit amplitude. The reflector in gather (a) is horizontal, with only ordinary p-waves. Since the actual b is exactly zero for this model, the event is hyperbolic as expected—no kinematics problems arise with the large-k traces. Gather (b) is the same as (a), but now the reflector dips 20° downward from source to receiver; note the nonhyperbolic behavior of the event in the large-offset traces. Gathers (c) and (d) show the case when dealing with mode-converted waves (downgoing velocity = 1000 m/s, $\gamma = 0.5$) for a horizontal and a dipping (20°, downward from source to receiver) reflector, respectively. Events in the large-offset traces, of gathers (c) and (d), weaken and clearly follow a nonhyperbolic path, confirming the existence of the problem with the kinematics for large values of k.

In generating a k trace, contributions from different midpoints (i.e., from a range of b values) are stacked. Figure 4 is an example of the contributing traces before they are stacked. For each k trace, the theoretical b range (Appendix D) may or may not be totally included within the available range calculated based on equation (1). (e.g., large-k traces typically require large-h traces which in turn, especially when b is large, may not have been recorded). When generating a k-trace, reflections from contributing midpoints, before stack, typically form a 'smile' in the (k, t_1) domain. The maximum time t_1 along a smile is attributed to a midpoint that really pertains to the same reflection point as that dictated by b. That is, the appropriate midpoint (the one giving rise to the actual b value in question) yields the maximum t_1 along a smile. The stack of the smile will ultimately have its timing close to that of the maximum t_1 of the smile (Appendix E). As long as the b range, used in generating

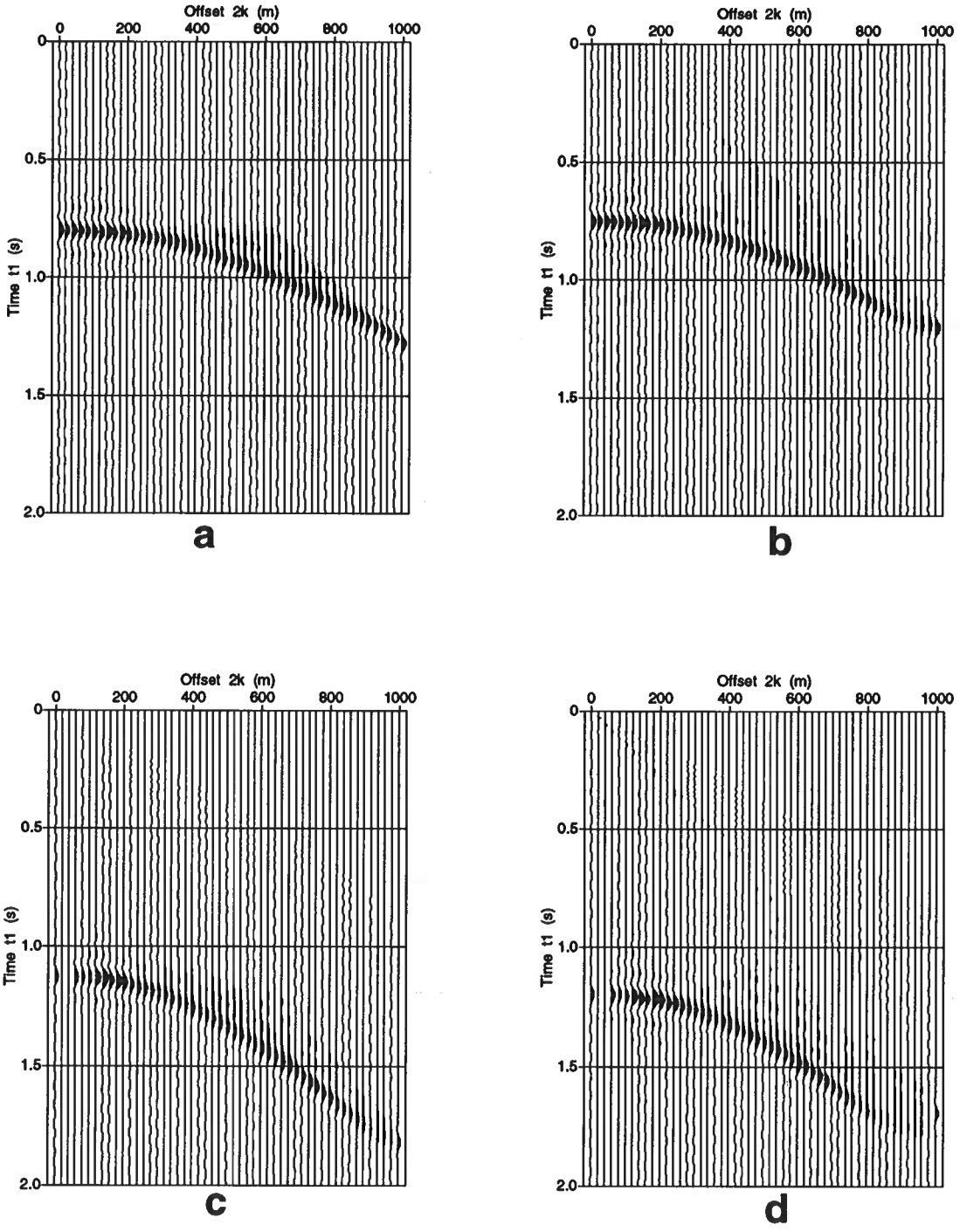

FIG. 7. The problem with large-k traces. The event in (a) is hyperbolic for all k values, because the reflector is horizontal with no mode-converted waves. When the reflector is dipping, or when mode conversion is present, large-k traces become erroneous (i.e., nonhyperbolic), as depicted in (b), (c), and (d). In (b), the reflector dips 20° downward from source to receiver. Events in (c) and (d) show the problem for mode-converted waves; the reflector in (c) is horizontal, whereas that in (d) dips 20° downward from source to receiver.

a k trace, encompasses the actual b associated with this k trace, the moveout of the corresponding k-trace (after stack) will be hyperbolic in accordance with equation (4).

As an example, the smile in Figure 4 peaks when the midpoint location is equal to zero; this corresponds to the actual value for b in that model, for a horizontal reflector with no mode conversion. In general, the extent to which an event in a k trace (after stack) will follow a hyperbolic trajectory in a (k, t_1) gather depends on whether or not the actual value of b for that trace is within the range of b values used in generating the k trace itself; the actual b value for each k trace, however, is a complicated function of dip, depth, and velocity ratio (Appendix E).

ALTERNATIVE SOLUTION

Despite the problems associated with the (k, t_1) TZO method, some useful information may still come out of use of this method. When amplitude is not of concern, for example, one can use the (k, t_1) approach to generate a zero-offset section for mode-converted waves. Off course, the zero-offset section will then have distorted amplitudes. The (k, t_1) method can also be used to deduce velocity information when dealing with mode-converted waves.

As equation (4) implies, velocity analysis in the (k, t_1) domain yields the average velocity, v_a, as the velocity that will best stack the data. With the average velocity determined, TZO by some alternative method (e.g., Harrison, 1990) can then be used. After substituting for k and t_1 their expressions in equations (1) and (2), respectively, equation (4) can be rewritten as follows

$$t_0^2 = (h^2 - b^2)\left[\frac{(\sigma t)^2}{2h(\alpha h + \beta b)} - \left(\frac{2}{v_a}\right)^2\right]. \tag{7}$$

Equation (7) shows that the average velocity can be used to directly transform the prestack seismic data from recorded time t to zero-offset time t_0.

VELOCITY ESTIMATION

Velocity analysis was performed on three models: one with a horizontal reflector and two with reflectors dipping 25° downward and upward (from source to receiver), respectively. The parameters for all these models are such that all have the same zero-offset time (0.95 s) at the location where velocity analysis is performed. The dominant frequency of the input zero-phase wavelet is 12.5 Hz (a low frequency chosen to emphasize the shape of the output wavelet; higher frequencies yield similar results). The downgoing velocity is 2000 m/s, and a $\gamma = 0.5$ is chosen, yielding an average velocity, v_a, of 1333 m/s based on equation (6). For comparison, velocity analysis was performed in both the (h, t) and (k, t_1) domains.

For the reflector dipping 25° downward, the results from the (k, t_1)-domain approach are shown in Figure 8. Figure 8a shows the output (k, t_1) gather, whereas

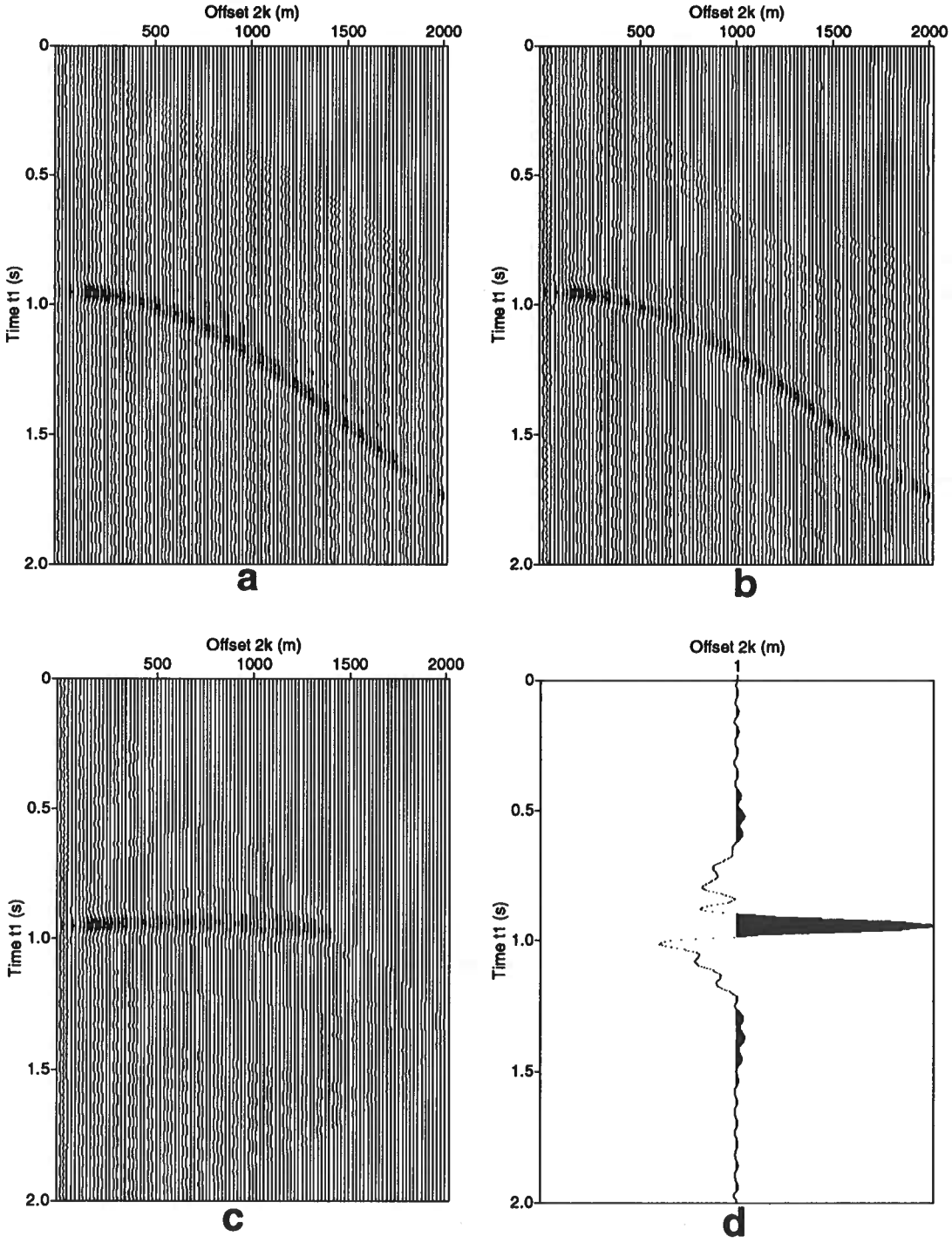

FIG. 8. Analysis in the (k, t_1) domain for a reflector dipping 25°, downward from source to receiver. (a) is the output (k, t_1) gather. (b) is the same gather after filtering. The NMO-corrected gather (v = 1370 m/s) is shown in (c). The stacked gather yields the trace shown in (d).

Figure 8b shows the same gather after applying a low-cut filter with a corner frequency of 3 Hz. The filter was applied to suppress the near-DC component in the output gather in Figure 8a. Because of the problem with the large-k traces, as discussed earlier, the last few traces were muted out before doing the velocity analysis. The stacking velocity for this event is found to be 1370 m/s, which is close to the average velocity (1333 m/s). The NMO-corrected (k, t_1) gather is shown in (c) in that figure, and the stacked (zero-offset) trace is shown in (d). Note that the peak of the stacked trace is at 0.95 s, the correct zero-offset time. A conventional CMP gather, at the same location as that of the above (k, t_1) gather, is shown in Figure 9a. Velocity analysis on this gather yields an erroneous stacking velocity of 1200 m/s, 10 percent *lower* than the average velocity. This low value in stacking velocity clearly cannot be attributed to the familiar $\cos\theta$ *dip-correction factor.* The NMO-corrected gather is shown in (b), and the stacked trace, shown in (c), shows that the event is now 20 ms later than the expected zero-offset time. Note, however, the stacked (k, t_1) wavelet in Figure 8d is not as close to being zero-phase (input wavelet) as that of the (h, t) wavelet in Figure 9c; the quality degradation in the (k, t_1) wavelet is due to improper phase treatment.

For the horizontal reflector, the results of the analysis in the (k, t_1) domain and the (h, t) domain are shown in Figures 10 and 11, respectively. The stacking velocity obtained in the (k, t_1) domain (1350 m/s) is practically the same as the average velocity, whereas that obtained in the (h, t) domain (1480 m/s) is 11 percent higher than the average velocity. The timing of the event did not differ much from the true zero-offset time in either case.

For the reflector that is dipping 25° upward, the results are shown in Figures 12 and 13. The stacking velocity obtained in the (k, t_1) case (1360 m/s) is, again, practically the same as the average velocity. This time, however, the stacking velocity from the (h, t) domain (2450 m/s) is about 85 percent higher than the average velocity, again not accounted for by the θ factor.

From the foregoing examples, I conclude that velocity analysis in the (h, t) domain, for mode-converted waves, yields erroneous results; the velocity depends only not on the dip, but also on the sign of the dip. Those velocities should not be used in time-to-depth conversion or any application other than CMP stacking. On the other hand, the velocity obtained in the (k, t_1) domain does not depend on dip; it is close to the average velocity. This average velocity can be reliably used in seismic applications, such as transformation to zero offset, migration, and even time-to-depth conversion.

CONCLUSION

Investigation of the (k, t_1) TZO method reveals that this method has three problems; namely, improper treatment of amplitude and phase, AVO distortion, and a problem with the large-offset traces. In addition, neither the AVO nor the large-offset problems can be overcome, even when dealing only with ordinary p-waves. I recom-

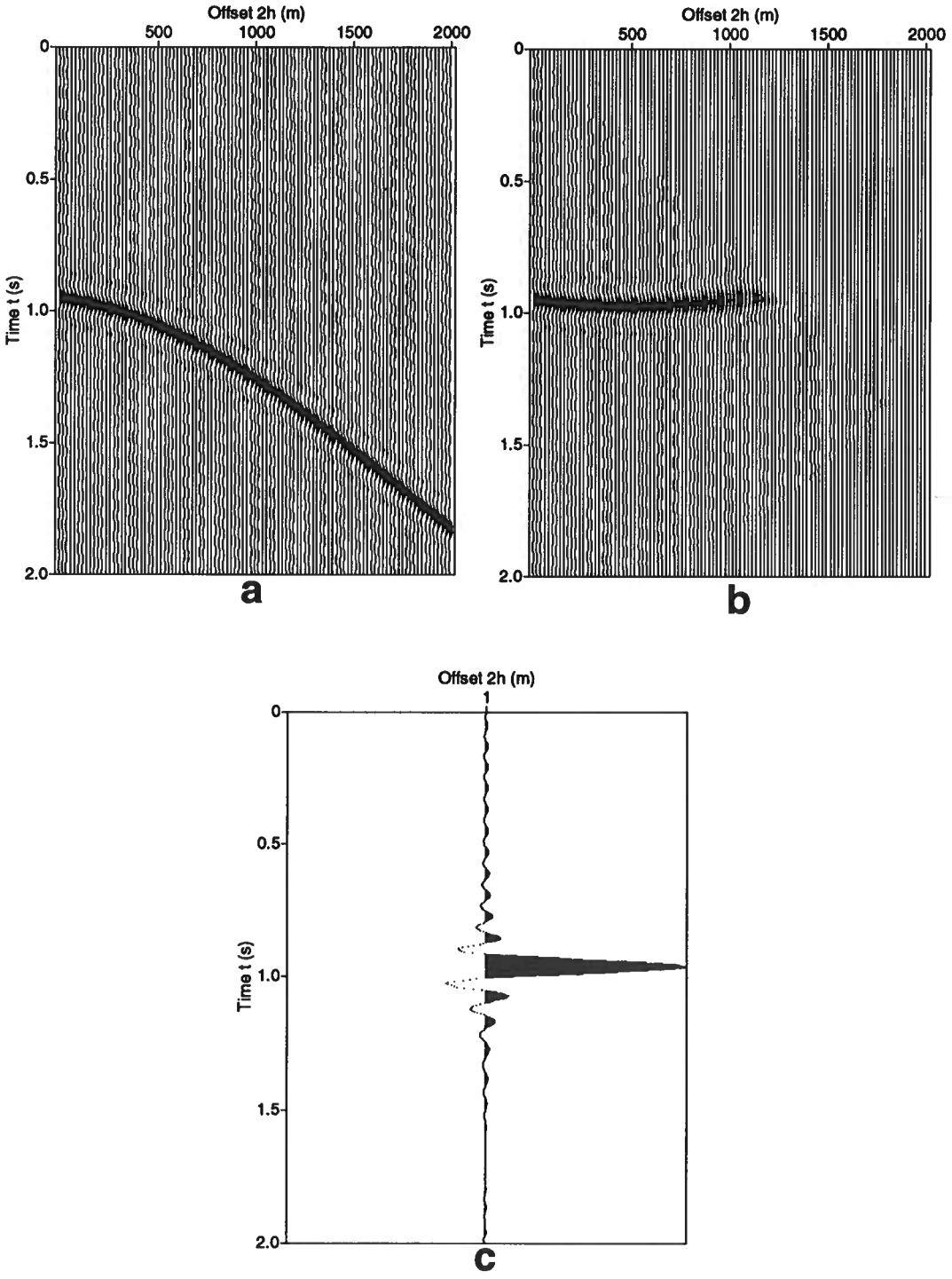

FIG. 9. Analysis in the (h,t) domain for a reflector dipping 25° downward from source to receiver. (a) CMP gather at the location where velocity is analyzed. The NMO-corrected gather ($v = 1200$ m/s) is shown in (b). The stacked gather yields the trace shown in (c).

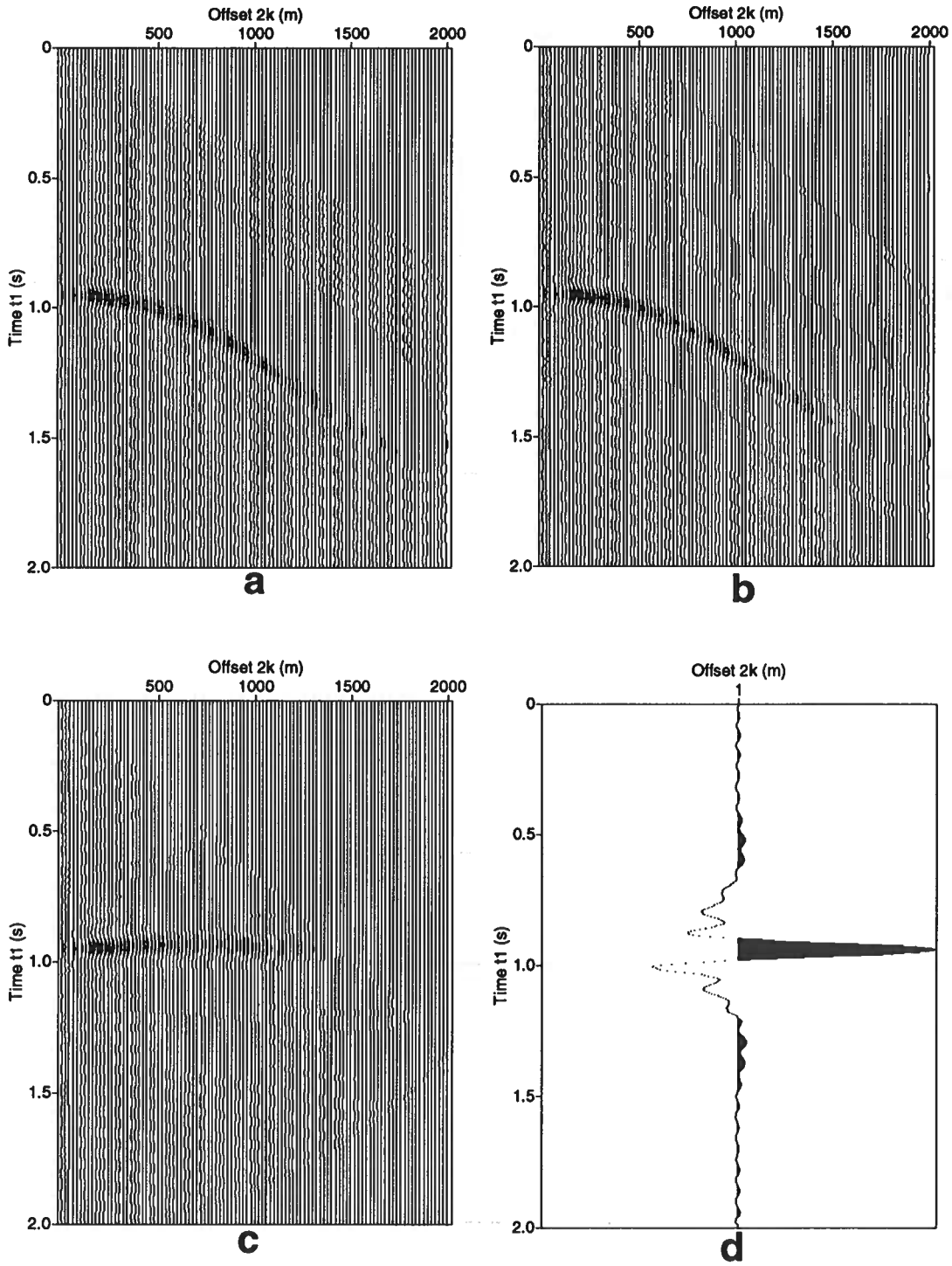

FIG. 10. Analysis in the (k, t_1) domain for a horizontal reflector. (a) Output (k, t_1) gather. (b) Same gather after filtering. The NMO-corrected gather (v = 1350 m/s) is shown in (c). The stacked gather yields the trace shown in (d).

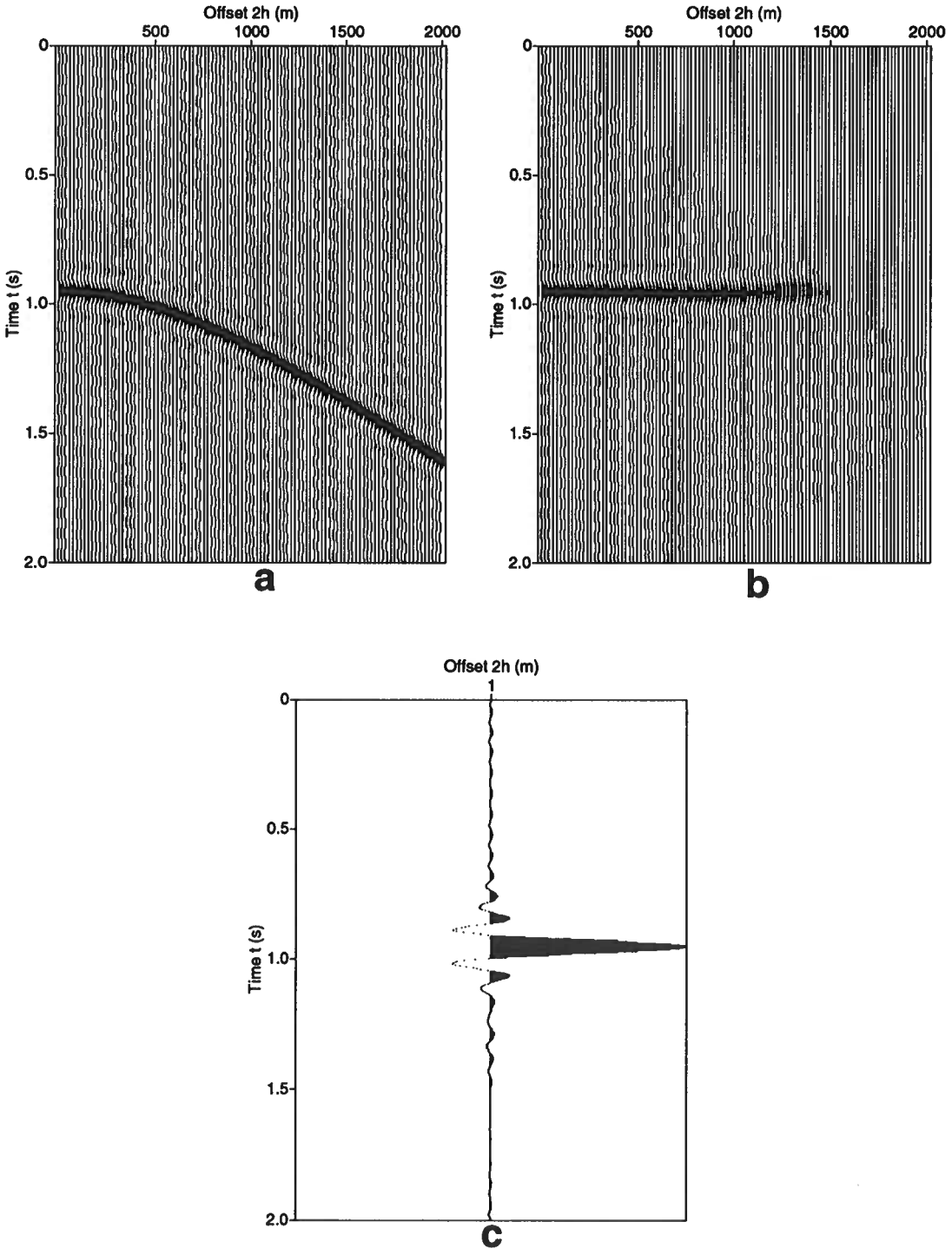

FIG. 11. Analysis in the (h,t) domain for a horizontal reflector. (a) CMP gather at the location of the velocity analysis. The NMO-corrected gather (v = 1480 m/s) is shown in (b). The stacked gather yields the trace shown in (c).

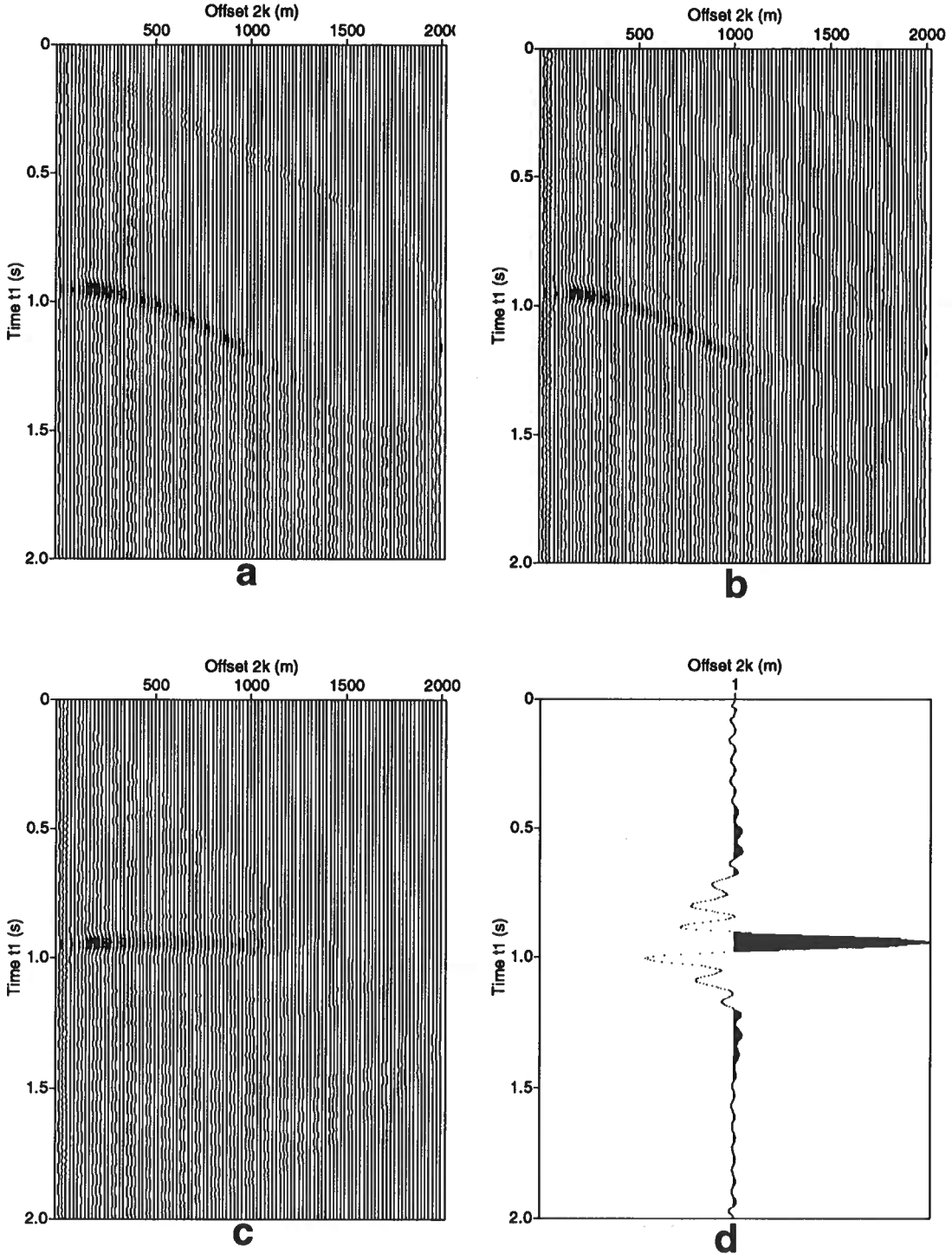

FIG. 12. Analysis in the (k, t_1) domain for a reflector (dip=25° upward from source to receiver). (a) Output (k, t_1) gather. (b) Same gather after filtering. The NMO-corrected gather ($v = 1360$ m/s) is shown in (c). The stacked gather yields the trace shown in (d).

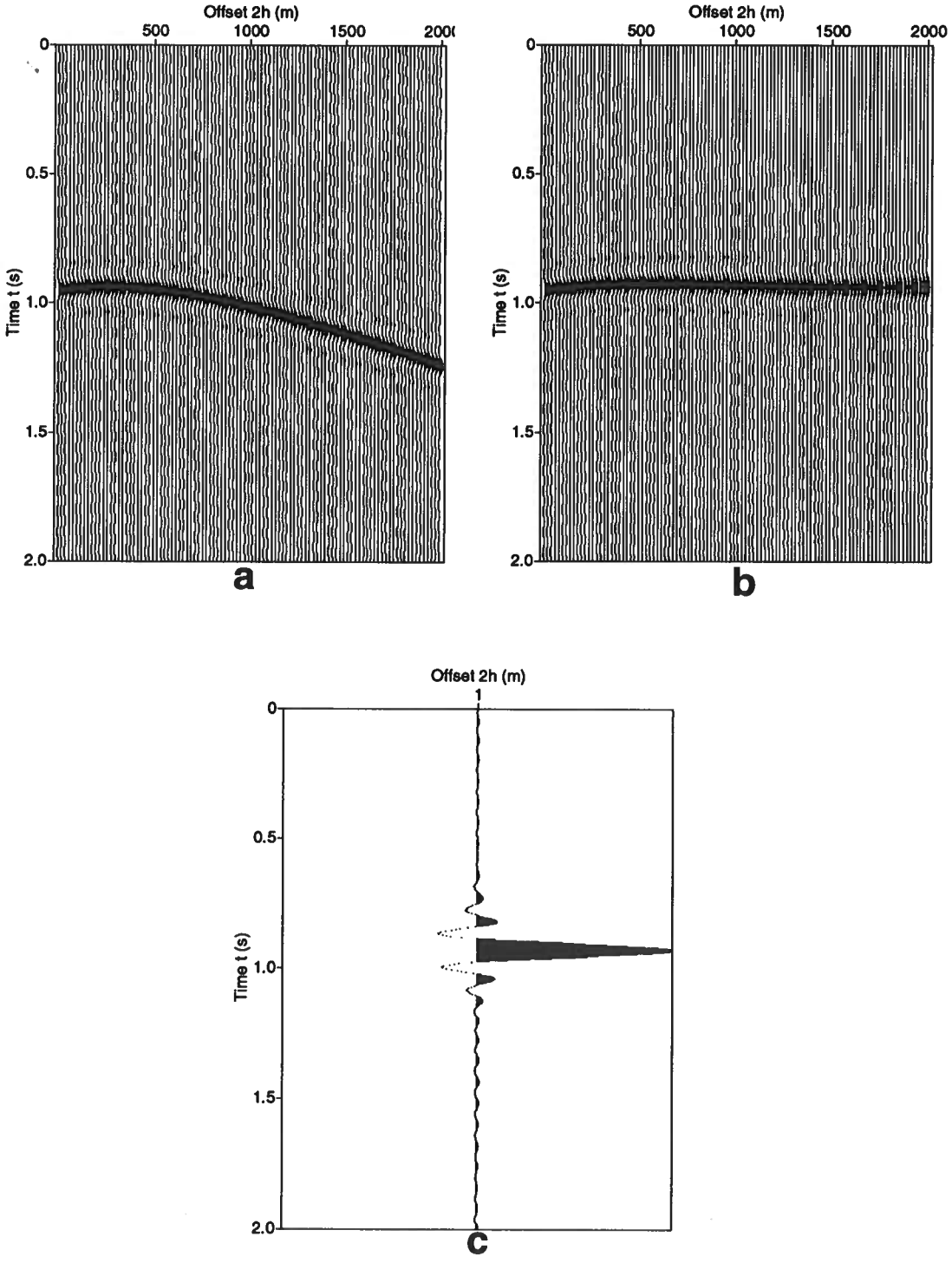

FIG. 13. Analysis in the (h,t) domain for a reflector (dip=25° upward from source to receiver). (a) Input CMP gather. The NMO-corrected gather (v = 2450 m/s) is shown in (b). The stacked gather yields the trace shown in (c).

mend, therefore, that the (k, t_1) TZO approach *not be used* as a primary processing scheme of seismic data. This approach, however, could be useful in deducing velocity information, especially for mode-converted data since this (k, t_1) transformation is not highly sensitive to the choice of velocity ratio.

ACKNOWLEDGEMENT

I thank Professor Ken Larner for critical reviewing and improving an earlier draft of the paper, and for his suggestions. Thanks are due to the Center for Wave Phenomena, Colorado School of Mines, for its technical support, and also to Saudi ARAMCO, Saudi Arabia, for its financial support.

REFERENCES

Alfaraj, M., and Larner, K., 1992, Transformation to zero offset for mode-converted waves: Geophysics, **57**, 474–477.

Deregowski, S.M., 1986, What is DMO: First Break, **4**, 7–24.

Forel, D., and Gardner, G., 1988, A three-dimensional perspective on two-dimensional dip moveout: Geophysics, **53**, 604–610.

Forel, D., 1986, Dip moveout correction in three and two dimensions: M.S. Thesis, University of Houston.

Harrison, M., 1990, Converted wave DMO: Presented at the 60th Ann. Internat. Mtg., Soc. Expl. Geophys., Expanded Abstracts, 1370–1373.

Levin, F., 1971, Apparent velocity from dipping interface reflections: Geophysics, **36**, 510–516.

Newman, P., 1990, Amplitude and phase properties of a digital migration process: First Break, **8**, 397–403.

Ottolini, R., 1982, Migration of reflection seismic data in angle-midpoint coordinates: Ph.D. Thesis, Stanford University.

APPENDIX A: FRESNEL-ZONE WIDTH

Before discussing the Fresnel zone, the general form of the smile, the stack of which generates a (k, t_1) trace, will first be derived. Only ordinary p-waves are considered, i.e., $\gamma = 1$. For $\gamma \neq 1$, the mathematics become rather tedious, as quartic symbolic equations arise.

Consider the surface point a, Figure A-1, at which a (k, t_1) gather is to be generated from input CMP gathers. A constant-velocity, single-reflector medium is assumed. With D being the distance from point a to the reflector, the theoretical

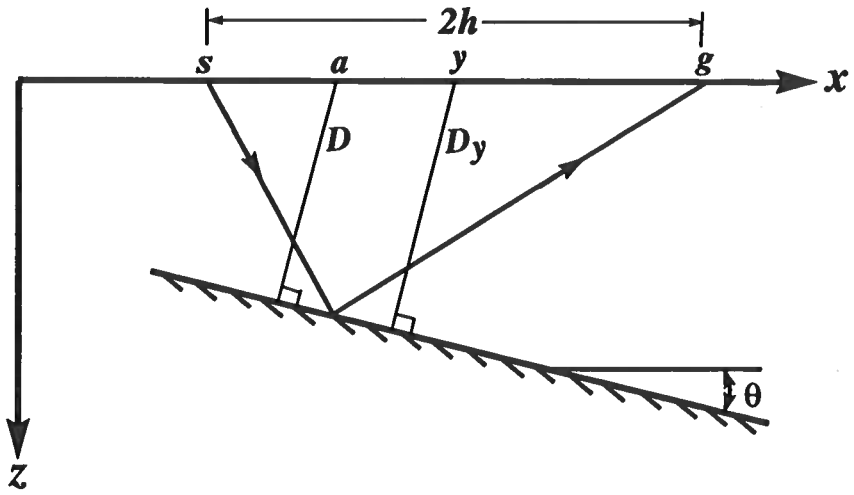

FIG. A-1. Subsurface model consisting of a single dipping reflector in a constant-velocity medium. An output (k, t_1) gather is desired at location a. Any midpoint y with source-receiver $(s$–$g)$ offset $(2h)$ encompassing point a will contribute to the output (k, t_1) gather. The zero-offset time, which the (k, t_1) gather inherits, is experienced along path D.

zero-offset time at point a is given by

$$t_0 = \frac{2D}{v}, \tag{A-1}$$

where v is the medium velocity. Any trace whose source-receiver line encompasses point a will contribute to the output (k, t_1) gather. One such trace is depicted in the figure, with distance $2h$, between source s and receiver g, encompassing point a. Because the reflector is dipping, the distance D_y from midpoint y to the reflector varies with location of midpoint.

The recorded time t from the source down to the reflector and back up to the receiver can be expressed as

$$t^2 = t_{0y}^2 + \left(\frac{2h\cos\theta}{v}\right)^2, \tag{A-2}$$

where t_{0y} is the midpoint zero-offset time given by $t_{0y} = 2D_y/v$. For convenience, let point a be the origin. Then t_{0y} can be expressed as

$$t_{0y} = t_0 + \frac{2y\sin\theta}{v}, \tag{A-3}$$

with positive dip being downward from source to receiver. Substitution of equation (A-3) into equation (A-2) yields

$$t^2 = \left(t_0 + \frac{2y\sin\theta}{v}\right)^2 + \left(\frac{2h\cos\theta}{v}\right)^2. \tag{A-4}$$

For $\gamma = 1$, equation (2) becomes $t_1 = kt/h$, which, from equation (A-4), can be written as

$$t_1^2 = \frac{k^2}{h^2}\left[\left(t_0 + \frac{2y\sin\theta}{v}\right)^2 + \left(\frac{2h\cos\theta}{v}\right)^2\right]. \tag{A-5}$$

Noting that y (Figure A-1) and b (Figure 1) are equal with opposite signs, equation (1) can be used to eliminate h from equation (A-5). The result, after simplification, becomes

$$t_1^2 = \frac{k^2}{k^2+y^2}\left(t_0 + \frac{2y\sin\theta}{v}\right)^2 + \left(\frac{2k\cos\theta}{v}\right)^2. \tag{A-6}$$

For constant k, equation (A-6) gives the general form of the smile in generating a k trace.

The behavior of the smile depends, among other parameters, on dip, which is normally unknown. In deriving the Fresnel-zone width, I shall assume a horizontal reflector ($\theta = 0$). Then equation (A-6) reduces to

$$t_1^2 = \frac{k^2 t_0^2}{k^2+y^2} + \left(\frac{2k}{v}\right)^2, \tag{A-7}$$

which describes a symmetric smile whose maximum time t_{1max} (occurring at $y = 0$) given by

$$t_{1max}^2 = t_0^2 + \left(\frac{2k}{v}\right)^2. \tag{A-8}$$

Let the width of the zone that the smile spans within a time interval Δt_1 be $2\Delta y$. With $\Delta t_1 \equiv t_{1max} - t_1$, then t_{1max}, t_1, and Δt_1 are also related by

$$t_{1max}^2 - t_1^2 = (\Delta t_1)^2 + 2t_1\Delta t_1. \tag{A-9}$$

From equations (A-7) and (A-8), we can write

$$t_{1max}^2 - t_1^2 = t_0^2 - \frac{k^2 t_0^2}{k^2 + (\Delta y)^2}, \tag{A-10}$$

which, after substituting for t_0 its value from equation (A-7) and simplification, can be written as

$$t_{1max}^2 - t_1^2 = \frac{(\Delta y)^2}{k^2}\left[t_1^2 - \left(\frac{2k}{v}\right)^2\right] \tag{A-11}$$

Equating the right-hand sides of equations (A-9) and (A-11) and solving for y yields

$$\Delta y = k\sqrt{\frac{(\Delta t_1)^2 + 2t_1\Delta t_1}{t_1^2 - \left(\frac{2k}{v}\right)^2}}. \tag{A-12}$$

If Δt_1 is chosen to be half a cycle, i.e., $\Delta t_1 = T/2$, where T is the dominant period of the wavelet, then Δy (half the Fresnel-zone width) can be expressed as

$$\Delta y = k \sqrt{\frac{\frac{1}{f}\left(\frac{1}{4f} + t_1\right)}{t_1^2 - \left(\frac{2k}{v}\right)^2}}, \tag{A-13}$$

where f is the dominant frequency of the wavelet.

It should also be noted that the Fresnel-zone width cannot exceed a maximum value determined by the maximum offset present in the data. Take, for example, the case when $k = 300$ m in Figure 3a. The maximum half-offset was 500 m. As equation (1) implies, the maximum Fresnel-zone width should be $2\sqrt{500^2 - 300^2} = 800$ m. In other words, Fresnel-zone widths greater than 800 m, in this example, require larger offsets not present in the data. This explains the corners seen in the curves of Figure 3.

APPENDIX B: GENERAL TRAVEL-TIME EQUATION

From the hyperbolic relation, equation (4), and after substituting for k^2 and t_1 their expressions from equations (1) and (2), the travel time t can be solved for as follows

$$t^2 = \frac{2h(\alpha h + \beta b)}{\sigma^2(h^2 - b^2)}\left(t_0^2 + \frac{4(h^2 - b^2)}{v_a^2}\right). \tag{B-1}$$

From the relationship between D and D_y (Figure A-1), with positive dips being downward from source to receiver, and noting that $b \equiv a - y$, the relation between t_0 and t_{0y} can be expressed as

$$t_0 = t_{0y} + \frac{2b\sin\theta}{v_a}. \tag{B-2}$$

Substitution of equation (B-2) into equation (B-1) yields the following general expression for the travel time t for any velocity ratio γ

$$t^2 = \frac{2h(\alpha h + \beta b)}{\sigma^2(h^2 - b^2)}\left[\left(t_{0y} + \frac{2b\sin\theta}{v_a}\right)^2 + \frac{4(h^2 - b^2)}{v_a^2}\right]. \tag{B-3}$$

APPENDIX C: QUARTIC EQUATION FOR b

For ordinary p-wave reflection, the location of an equivalent zero-offset reflection, i.e., b, can be analytically derived, as a function of offset, depth, and dip. Figure C-1, which shows a depth section with a dipping reflector, is used to find b in the presence of mode-conversion.

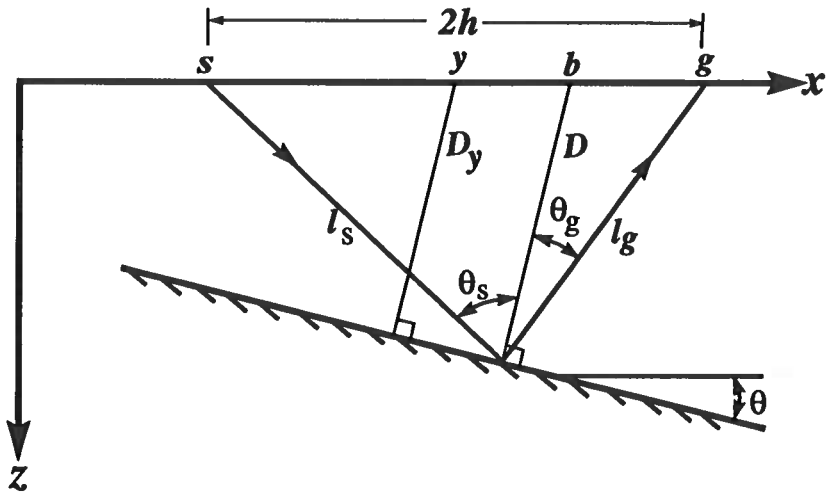

FIG. C-1. Depth section depicting a ray path for p–sv mode conversion. The trace has offset $2h$ between source s and receiver g. The distance from the midpoint y to the dipping (θ) reflector is D_y, and that from b (the location of an equivalent zero-offset trace) to the reflector is D. The distance from s along the ray path to the reflector is l_s, and that from the reflector to g is l_g. The incidence and reflection angles are θ_s and θ_g, respectively.

From Pythagorean theorem, and noting that $D = D_y + b \sin\theta$, the distance along the ray path from the source to the reflector, l_s, and that from the reflector to the receiver, l_g, can be expressed as

$$l_s = \sqrt{(h+b)^2\cos^2\theta + (D_y - h\sin\theta)^2}, \tag{C-1}$$

$$l_g = \sqrt{(h-b)^2\cos^2\theta + (D_y + h\sin\theta)^2}. \tag{C-2}$$

At the reflection point, Snell's law is

$$\frac{\sin\theta_s}{\sin\theta_g} = \frac{1}{\gamma}. \tag{C-3}$$

From the geometry of Figure C-1, and taking positive dips downward from source to receiver, it can be shown that

$$\sin\theta_s = \frac{(h+b)\cos\theta}{l_s}, \tag{C-4}$$

and

$$\sin\theta_g = \frac{(h-b)\cos\theta}{l_g}. \tag{C-5}$$

By substituting equations (C-4) and (C-5) into equation (C-3), we get

$$l_g = \frac{l_s}{\gamma}\frac{h-b}{h+b}. \tag{C-6}$$

For a downgoing velocity v, and recorded time t, we have

$$vt = l_s + l_g/\gamma. \tag{C-7}$$

Substitution of equation (C-6) into equation (C-7) yields

$$vt = l_s\left(1 + \frac{1}{\gamma^2}\frac{h-b}{h+b}\right). \tag{C-8}$$

Equation (C-8), upon substituting expression (C-1) for l_s and squaring both sides, becomes

$$(vt)^2 = \left[(h+b)^2\cos^2\theta + (D_y - h\sin\theta)^2\right]\left[1 + \frac{1}{\gamma^2}\frac{h-b}{h+b}\right]^2, \tag{C-9}$$

but the term $(vt)^2$ can also be solved for, from the kinematics relation for mode-converted waves (Alfaraj and Larner, 1992), as

$$(vt)^2 = 2h(\alpha h + \beta b)\left[1 + \frac{D^2}{h^2 - b^2}\right], \tag{C-10}$$

which can also be expressed in terms of D_y as

$$(vt)^2 = 2h(\alpha h + \beta b)\left[1 + \frac{(D_y + b\sin\theta)^2}{h^2 - b^2}\right]. \tag{C-11}$$

Eliminating $(vt)^2$ from equations (C-9) and (C-11) and simplifying yields the following quartic equation in b

$$\begin{aligned}\left[(h+b)^2 cos^2\theta + (D_y - h\sin\theta)^2\right](\alpha h + \beta b)(h-b) = \\ 2h(h+b)\left[h^2 - b^2 + (D_y + b\sin\theta)^2\right].\end{aligned} \tag{C-12}$$

APPENDIX D: RANGE OF b

When dealing with ordinary p-waves, the DMO impulse response (i.e., the DMO ellipse) has a lateral extent of $2h$. The part of that lateral extent corresponding to non-evanescent seismic data (i.e., the range of b) is, Forel and Gardner (1988), bounded by

$$b = \pm\frac{2h^2}{vt}, \tag{D-1}$$

relative to the midpoint.

Now, consider mode-conversion. Let the range of b be bounded by b_{max} and b_{min} relative to the midpoint. A surface of constant traveltime (pseudo ellipse) is depicted in Figure D-1. The extreme points, x_{max} and x_{min}, are trivially deduced as

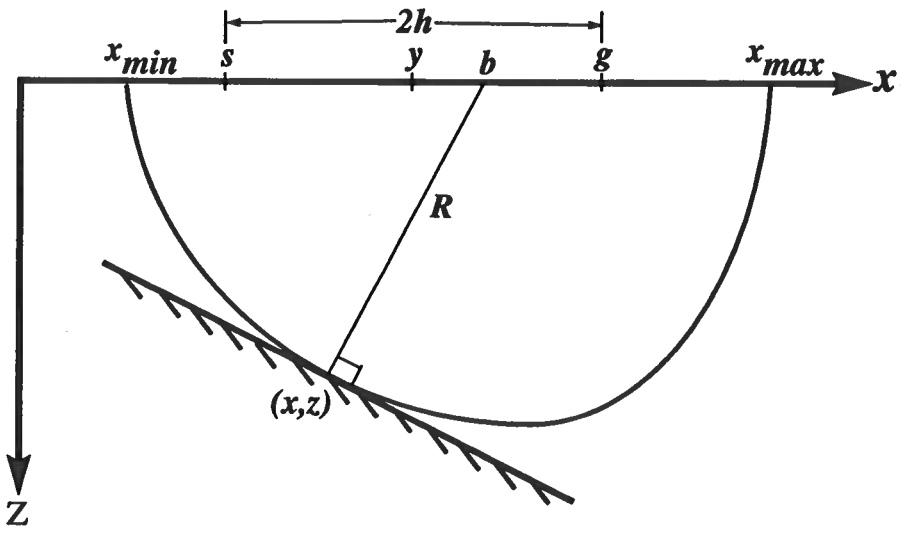

FIG. D-1. Surface of constant travel time (pseudo ellipse) for a mode-converted wave. The range of b corresponding to possibly recorded seismic data is along the line connecting source s and recorder g, but shorter than offset $2h$.

$$x_{max} = \frac{vt - \eta h}{\sigma}, \tag{D-2}$$

and

$$x_{min} = -\frac{vt + \eta h}{\sigma}, \tag{D-3}$$

where σ is given by equation (3), and $\eta = 1 - 1/\gamma$ is another constant that depends only on the velocity ratio. For reflections from a vertical wall (z=0), the distance R, from point b to reflection point (x, z), can be expressed as

$$R = x_{max} - b_{max}, \tag{D-4}$$

or

$$R = x_{min} - b_{min}, \tag{D-5}$$

depending on whether the wall is situated to the right or to the left of the midpoint y, respectively. The expression for R^2 (Alfaraj and Larner, 1992), is given by

$$R^2 = (h^2 - b^2)\left[\frac{(vt)^2}{2h(\alpha h + \beta b)} - 1\right], \tag{D-6}$$

where α and β are defined in equation (3). Substituting for x_{max} and x_{min} their respective values from equations (D-2) and (D-3), squaring of equations (D-4) or (D-5), and inserting the result in equation (D-6) yields quadratic equations for b_{max} and b_{min} respectively. Solutions for b_{max} and b_{min} are, respectively,

$$b_{max} = \frac{h(2\alpha h - \eta vt)}{\sigma(vt - 2\eta h)}, \tag{D-7}$$

and

$$b_{min} = \frac{h(2\alpha h + \eta v t)}{\sigma(-vt - 2\eta h)}. \tag{D-8}$$

For $\gamma = 1$, the range of b as given by equations (D-7) and (D-8) reduces exactly to that in equation (D-1).

APPENDIX E: MAXIMUM t_1 ALONG A SMILE

A 'smile' in the (y, t_1) domain, after stack, typically generates an event on a k trace. The maximum t_1, along a smile, occurs at a midpoint y corresponding to the b value that is the location of an equivalent zero-offset trace. The proof of this assertion, when $\gamma = 1$, follows.

Consider the relation for t_1^2 as given by equation (A-6). Differentiating that equation with respect to y and setting dt_1/dy to zero yields the following quadratic relation in y

$$2y^2 \sin\theta + t_0 v y - 2h^2 \sin\theta = 0. \tag{E-1}$$

Since $y = -b$, equation (B-2) can also be written as

$$t_0 = t_{0y} - \frac{2y \sin\theta}{v}. \tag{E-2}$$

Substituting for t_0 its value from the above equation, and solving equation (E-1) for y yields

$$y = \frac{2h^2 \sin\theta}{v t_{0y}} = \frac{h^2 \sin\theta}{D_y} = -b, \tag{E-3}$$

which is the same as that derived by Levin (1971). This proves the assertion made above.

Although not proven analytically, this same assertion also holds for mode-converted waves ($\gamma \neq 1$); I have shown this numerically.

CWP-117

A Klein-Gordon Theory for Acoustic Modeling and Imaging

Phil Anno, Jack K. Cohen and Norman Bleistein

Excerpt from

— Ph.D. Thesis —

by
Phil Anno

Center for Wave Phenomena
Colorado School of Mines
Golden, Colorado 80401
(303) 273-3557

A Klein–Gordon Theory for Acoustic Modeling and Imaging

Phil D. Anno
Jack K. Cohen
Norman Bleistein

ABSTRACT

We propose the Klein–Gordon differential operator from electromagnetics as a basis for acoustic modeling and imaging of waves in variable–density media. A change of the dependent variable in the acoustic, variable–density wave equation reveals it to be essentially the Klein–Gordon equation in disguise.

Moreover, the Klein–Gordon operator is dispersive and, in the acoustic context, contains a damping coefficient related to the density gradient. This means that density gradients distort the traveltimes of waves through dispersion. Specifically, those gradients enter into phase and group velocity expressions derived from the Klein–Gordon operator. A companion ray–theoretical prediction supplements this wave analysis. Density gradients impact ray traveltimes (appear in a new eikonal equation) when the wavelength of density variation is on the scale of the seismic wavelength.

The new dependent variable q is related to the original pressure p of the variable–density wave equation through $p = \sqrt{\rho}\, q$, where ρ represents density of the medium. It is the quantity q that satisfies the Klein–Gordon equation. We see that p is related to q through an amplitude factor alone, so that variable–density traveltimes are governed completely by the Klein–Gordon dispersion relation. This relation should therefore account correctly for traveltime distortion produced by density variation. Furthermore, one corrects the Klein–Gordon wavefield amplitude to a variable–density amplitude simply by multiplying by $\sqrt{\rho}$.

Importantly, no density gradient calculations are required for Klein–Gordon modeling or imaging, as with the variable–density wave equation. Instead, one conveniently parameterizes Klein–Gordon models by the speed of the medium and a damping coefficient. Loosely speaking, different choices of the damping coefficient correspond to different rates of density variation.

INTRODUCTION

In our experience, geophysicists do not associate traveltime variation with density variation in acoustic or elastic wavefield interpretation. Rather, given a constant index of refraction, density variation within the medium of propagation is associated only with amplitudes. This point of view prevails because density does not occur as a variable in Snell's Law or the eikonal equation.

Nevertheless, in this paper we predict a continuum of density effects on acoustic wavefields—including a traveltime distortion when density variation is rapid. We also derive, exactly and asymptoticly, the dispersion relation which should account properly for that distortion during acoustic modeling or imaging procedures. The dispersion relation can be written in the *Klein–Gordon* form (see e.g., Bleistein, 1984) found in electromagnetic applications.

We express the governing equation for acoustic propagation in a variable–density medium as

$$\rho(\boldsymbol{x})\nabla\cdot\left[\frac{\nabla p}{\rho}\right]-\nabla\cdot\left[\frac{\nabla\rho}{\rho}\right]p-\frac{1}{c^2(\boldsymbol{x})}\frac{\partial^2 p}{\partial t^2}=-f(\boldsymbol{x},t). \tag{1}$$

This result is derived in detail in Appendix A as equation (A-20). The symbols p, ρ, c, and f denote a small pressure fluctuation, density of the acoustic medium, material speed, and an acoustic source, respectively. Oftentimes, the *fractional density* term (where $\nabla\rho/\rho$ is fractional density) in equation (1) is neglected (Claerbout, 1985; Wapenaar and Berkhout, 1989). However, this term can be large (and will affect traveltime) if density varies rapidly over space. DeSanto (1989) gives a derivation which preserves the fractional density term. We will, at each appropriate juncture, point out how its exclusion affects the results. Essentially, none of the new concepts we present hinge on the presence of the fractional density term, though it certainly exerts a quantitative influence.

We first undertake a limited but exact analysis of equation (1). This reveals that waves do not propagate with speed c, as they do in constant density media. Instead, speed of propagation is wavelength dependent. That is to say, a variable density acoustic medium is *dispersive*, though assumed to be perfectly elastic. The damping coefficient responsible for this dispersion is proportional to the gradient and curvature of the density function. Consequently, rapid density variations produce a dispersive traveltime distortion.

Following that exact analysis we perform an asymptotic analysis beginning with equation (1). This approach extends the scope of speed functions c that can be considered analytically, though at the expense of making the usual high frequency wavefield approximation (Cerveny et al., 1977). Initially we selectively scale equation (1) to obtain a ray analog to the wave analysis. Importantly, the scaled equation admits asymptotics not only for slow variation in ρ and c, the usual limitation, but also allows rapid variation in ρ. A hierarchy of asymptotic dispersion relations (and solutions) emerges for the variable–density wave equation. That hierarchy embeds

results for slow variation as a special case, and points again to the Klein–Gordon dispersion relation.

WAVE ANALYSIS

We begin our investigation by analyzing equation (1) for the case of constant c and specifically restricted density functions. Though this is a special case, it can be solved exactly—at least as far as is needed to identify several important propagation characteristics in a variable–density medium. Furthermore, the restrictions of this exact analysis can be met locally in any inhomogeneous medium. Consequently, we expect that wave phenomena predicted for our special case will in some sense manifest themselves in the case of general inhomogeneity.

The main aim of the wave analysis will be to derive a dispersion relation and phase and group velocity expressions for particular constant–c variable–ρ media. These expressions will establish that density gradients act as a damping mechanism in acoustic media, causing dispersive propagation.

The key step of analysis is a change of the dependent variable from pressure p to q where

$$q \stackrel{\text{def}}{=} \frac{p}{\sqrt{\rho}} \ . \tag{2}$$

This change transforms equation (1) to the well–studied Klein–Gordon form, giving the advantage of a much simpler and well–trod path. Fourier transforms reduce, for our constant–c variable–ρ example, the new equation on q to an algebraic expression; the solution for q is expressed in terms of inverse Fourier transforms. One deduces phase and group velocity by evaluating the inverse transform over temporal frequency.

Klein–Gordon form

The Klein–Gordon differential form derives from substitution of the change of variable of equation (2) into equation (1). Accordingly, we shall analyze the problem described by

$$\begin{aligned} &\Delta q - \frac{b^2}{c^2} q - \frac{1}{c^2}\frac{\partial^2 q}{\partial t^2} = 0, \\ &q(\boldsymbol{x}, 0) = r(\boldsymbol{x}), \qquad \frac{\partial}{\partial t} q(\boldsymbol{x}, 0) = s(\boldsymbol{x}), \end{aligned} \tag{3}$$

with

$$b^2 \stackrel{\text{def}}{=} c^2 \frac{\Delta\sqrt{\rho}}{\sqrt{\rho}} \ . \tag{4}$$

The symbol Δ designates the Laplacian operator. The identity

$$\frac{\Delta\sqrt{\rho}}{\sqrt{\rho}} \equiv \frac{\Delta\rho}{2\rho} - \frac{\nabla\rho}{2\rho} \cdot \frac{\nabla\rho}{2\rho} \tag{5}$$

is central to collapsing terms to a single Laplacian on $\sqrt{\rho}$. We have also elected to replace the source term of equation (1) with equivalent initial data r and s.

The Klein–Gordon differential equation also governs electromagnetic waves in the ionosphere and de Broglie waves for free relativistic particles. In the electromagnetic context, symbol b in the Klein–Gordon operator corresponds to a resonant frequency of the plasma and serves to introduce damping . *Relative curvature* $\Delta\sqrt{\rho}/\sqrt{\rho}$ of the square root of the density function, scaled by c^2, introduces damping in the present context. Equation (5) expresses the relative curvature of $\sqrt{\rho}$ as a weighted sum of curvature and fractional density terms in ρ.

We see from equation (2) that Klein–Gordon amplitudes are related to variable–density amplitudes through an amplitude factor alone, albeit a spatially varying factor. This means that variable–density traveltimes are governed totally by the Klein–Gordon dispersion relation (that we shall derive below). Equation (2) does not, however, apply at discontinuities in either the damping or speed coefficients. This is because interface conditions, and not the wave equations (1) and (3), govern amplitudes at boundaries. Interface conditions should be applied to compute amplitudes at boundaries.

Finally, we point out that the Klein–Gordon operator is self–adjoint while the operator of equation (1) is not. Propagation problems for variable–density media may therefore be done in q—rather than p—for the sake of convenience if for no other reason. If one excludes the $\nabla\cdot(\nabla\rho/\rho)p$ term from equation (1), b^2 of equations (3) and (4) becomes

$$c^2\left[\frac{\Delta\sqrt{\rho}}{\sqrt{\rho}} - 2\frac{\nabla\rho}{2\rho}\cdot\frac{\nabla\rho}{2\rho}.\right]$$

The Klein–Gordon form is therefore retained, but with a more complicated damping coefficient than the one in equation (4).

Velocities

Consider now the constant coefficient case of equations (3). This case limits c to a constant (c_o) and ρ to that class of density functions satisfying

$$\Delta\sqrt{\rho} = \frac{b_o^2}{c_o^2}\sqrt{\rho} \tag{6}$$

with b_o^2/c_o^2 constant. Herein lies another analytical reward for the change of variable in equation (2). The Klein–Gordon representation makes it possible to work with a constant coefficient—yet variable density—wave equation.

That is, a single value for b_o/c_o implies a density *function*, from equation (6). Hence, Klein–Gordon modeling and imaging algorithms may "think" in terms of the damping and speed for a layer, rather than speed and a density function. Klein–Gordon algorithms avoid thusly the need to calculate gradients of a density function, a requirement for variable–density algorithms based on equation (1). Indeed, we

assert from equations (3) that the canonical acoustics problem is constant b and constant c—not constant ρ and constant c—as one might presume. Constant density is a special case described jointly by $b_o = 0$ in the q variable, and $p = \sqrt{\rho_o}\, q$. Acoustic modeling and imaging algorithms for variable–coefficient problems may be designed naturally as a repeated implementation, once for each constant–coefficient layer, of the canonical problem.

It is important, in turn, that one understands the solutions to equation (6). One must ensure that the density function implied by a given value of b_o is physical. Suffice it to say now that there are solutions to equation (6) and that they may be used to construct many physically realizable density functions.

To proceed toward velocity expressions we define forward Fourier transforms on q as

$$Q(\boldsymbol{k}, w) = \int_{-\infty}^{\infty} d\boldsymbol{x} \int_{0}^{\infty} dt\, q(\boldsymbol{x}, t) e^{-i(\boldsymbol{k}\cdot\boldsymbol{x} - \omega t)}$$

and apply them to equations (3) to obtain

$$\left[-k^2 + \frac{w^2}{c_o^2} - \frac{b_o^2}{c_o^2}\right] Q = -\frac{S(\boldsymbol{k})}{c_o^2} + i\omega \frac{R(\boldsymbol{k})}{c_o^2}\,.$$

Scalar quantity k represents the magnitude of the $\boldsymbol{k}$ vector and S and R are transforms of the initial data in equation (3). The solution q can now be written as an inverse Fourier transform of Q. That is,

$$q(\boldsymbol{x}, t) = \frac{1}{(2\pi)^4} \int d\boldsymbol{k} \int d\omega \left[\frac{i\omega R(\boldsymbol{k}) - S(\boldsymbol{k})}{\omega^2 - c_o^2 k^2 - b_o^2}\right] e^{i(\boldsymbol{k}\cdot\boldsymbol{x} - \omega t)}\,. \tag{7}$$

Limits and paths of integration are left unspecified, to be chosen according to physical constraints on q.

The dispersion relation emerges as a by–product of evaluating the integral over ω in equation (7). Residue calculus supplies an exact method of evaluation. For the integral at hand, residues come from simple poles in the integrand on both the real and imaginary ω–axis at

$$k^2 = \frac{\omega^2}{c_o^2} - \frac{b_o^2}{c_o^2}\,. \tag{8}$$

Indeed, equation (8) is the Klein–Gordon *dispersion relation.*

Planes of constant phase travel with speed ω/k to give

$$\begin{aligned} v_p &= \frac{\sqrt{c_o^2 k^2 + b_o^2}}{k} \\ &= c_o \sqrt{1 + \frac{1}{k^2}\left(\frac{\Delta\sqrt{\rho}}{\sqrt{\rho}}\right)_o}\,. \end{aligned} \tag{9}$$

Group (energy) velocity v_g, given by $d\omega/dk$, is

$$v_g = c_o \Big/ \sqrt{1 + \frac{1}{k^2}\left(\frac{\Delta\sqrt{\rho}}{\sqrt{\rho}}\right)_o} \tag{10}$$

from equation (8). Clearly, inhomogeneity in density imposes a dispersive traveltime distortion upon propagating acoustic waves. Equations (9) and (10) disclose that the diagnostic propagation speeds depend on the relative curvature of $\sqrt{\rho}$ as well as wavenumber, and $v_p \neq c \neq v_g$.

Density profiles

The above dispersion relation and velocities are contingent upon constant coefficients in equation (3). That is, speed c must be constant and $\sqrt{\rho}$ must satisfy a differential equation, namely equation (6). In this section we present several of the requisite density solutions for three–dimensional and one–dimensional (layered) media. Any linear combination of these density functions is valid because equation (6) is linear and homogeneous in $\sqrt{\rho}$. It will be clear that these functions are not physical over the entire solution domain. For example, density may become much too small (even negative) beyond a certain region in space. One must limit the range of the independent (space) variable in any single layer to restrict these solutions to their physical domain.

Consider a density scatterer having three-dimensional spherical symmetry. Radial distance r defines the distance from the center of the scatterer. For this symmetry, equation (6) assumes the form of a modified Bessel differential equation (Abramowitz and Stegun, 1965) with solutions

$$\sqrt{\rho} = \begin{cases} C_1 \dfrac{\sinh(|\kappa| r)}{|\kappa| r} & , \ \kappa \stackrel{\text{def}}{=} \dfrac{b_o}{c_o} \ ; \\ C_2 \dfrac{\cosh(|\kappa| r)}{|\kappa| r} & , \ C_1, C_2 \text{ arbitrary constants.} \end{cases} \tag{11}$$

These two solutions may be combined linearly to produce density functions that decay or grow with r. The choice one makes for ratio $|b_o|/c_o$ controls the rate of growth or decline away from the center of the scatterer. Equations (11) offer three–dimensional profiles for studying the effect of density scatterers on wavefield dispersion—independent of wave phenomena that originate from variable c.

Let us now turn to density solutions for layered media, taking the depth coordinate to be z. Equation (6) simplifies greatly for $\rho = \rho(z)$. By elementary techniques one finds solutions

$$\sqrt{\rho} = \begin{cases} C_1 e^{\kappa z}, \ C_2 e^{-\kappa z} & , b_o^2 > 0 \ ; \\ C_1 \cos(|\kappa| z), \ C_2 \sin(|\kappa| z) & , b_o^2 < 0 \ . \end{cases} \tag{12}$$

For real b_o the ratio $|b_o|/c_o$ again sets a rate of growth or decay for the density function. For imaginary b_o, $|b_o|/c_o$ determines a wavenumber for sinusoidal density oscillation.

From equation (6), imaginary b_o corresponds physically to a negative relative curvature in $\sqrt{\rho}$. Equations (12) provide suitable density functions for analyzing the effects of layered density gradients on acoustic wave propagation.

It is also interesting to consider those density functions given by a constant fractional density $\nabla\rho/\rho$. Though this condition restricts density more than equation (6), the identity in equation (5) provides a motivation. Equation (5) shows that the relative curvature of $\sqrt{\rho}$, when expanded, contains fractional density terms. In fact, if one chooses

$$\frac{\nabla\rho}{\rho} = 2\kappa\hat{\gamma}_o, \qquad \hat{\gamma}_o \stackrel{\text{def}}{=} \frac{\nabla\rho}{|\nabla\rho|}, \tag{13}$$

then

$$\frac{\Delta\sqrt{\rho}}{\sqrt{\rho}} = \kappa^2$$

as before. That is to say, forcing fractional density to be constant forces the same on the relative curvature of $\sqrt{\rho}$. (The converse statement is not true.) For the case of equations (13)

$$\rho(\boldsymbol{x}) = Ce^{2\kappa\hat{\gamma}_o\cdot\boldsymbol{x}}. \tag{14}$$

Recalling that κ (or b_o) may be real or imaginary, equation (14) reduces to equations (12) for layered media.

As we cautioned above, the density solutions presented here do not take on physical values over the entire range of their independent variable. Those solutions that vary exponentially depart from their physical bounds particularly rapidly. We shall address this difficulty by giving formulas that calculate a physical range δz over which the depth coordinate of equations (12) may vary for one continuous layer.

First we derive a range formula for the real, exponential solutions of equations (12). We write

$$\rho(\delta z) = \rho_{min}e^{2\kappa\delta z},$$

where ρ_{min} is the smallest value we wish to accept for density. One then solves for that δz such that

$$\rho_{min}e^{2\kappa\delta z} = \rho_{max},$$

obtaining

$$\delta z = \frac{1}{2}\frac{c_o}{|b_o|}\ln\left(\frac{\rho_{max}}{\rho_{min}}\right). \tag{15}$$

Equation (15) gives the restriction on δz necessary to keep density values between ρ_{min} and ρ_{max}, based on the ratio of speed and the damping coefficient in a layer.

An example calculation with equation (15) will provide a concrete sense of its physical implications. We choose a medium with sizable intrinsic dispersion, say $|b_o| = (1/2)\omega_o$, where ω_o is defined to be the dominant frequency of the signal. The dispersion relation $k^2 = (\omega_o^2/c_o^2) - (b_o^2/c_o^2)$ quantifies dispersion as "sizable" when $|b_o|$ is not neglible in relation to ω_o. We pick $\omega_o = (2\pi)30$ Hz, $c_o = 3000$ m/s,

$\rho_{min} = 2.2$ g/cm^3 and $\rho_{max} = 2.4$ g/cm^3. Equation (15) yields a layer thickness of about 1.5 m for those parameter selections.

That layer is quite thin, considering that the dominant wavelength computed from the dispersion relation is 115 m, about seventy-five times as long. We thus predict that the propagating signal cannot disperse appreciably through a single layer of this type. The amount of time spent traveling in that 1.5 m layer is negligible with respect to the period of a 30 Hz signal. However, that same density profile, when stacked in a thick repetitive sequence, should significantly disperse the propagating wave.

One can follow similar logic to derive a range formula for the sinusoidal solutions of equations (12). For those solutions we obtain

$$\delta z = \frac{c_o}{|b_o|}\left(\pi - 2\arcsin\sqrt{\frac{\rho_{min}}{\rho_{max}}}\right). \tag{16}$$

The value of ρ_{max} specifies the peak of the sinusoid. Evaluating equation (16) with the same parameters used in equation (15), layer thickness $\delta z = 18.5$ m. Clearly, sinusoidal density variation can be sustained over a much greater depth range than can exponential variation. On the other hand, the dominant wavelength still exceeds the layer thickness considerably. We again estimate that some stacking of density layers of the sinusoidal type will be necessary to induce measurable dispersion.

We conclude our discussion of density, and the acoustic damping created through density variation, by examining what happens when $b \equiv 0$ in equation (3). When $b \equiv 0$ the Klein–Gordon equation reduces to the constant–density form of the wave equation. To our immediate satisfaction, the special restriction on b does *not* also impose constant density. This means that—in the q variable—variable density modelling can be accomplished with the constant–density wave equation. This statement is true for all density functions that satisfy Laplace's equation,

$$\nabla^2\sqrt{\rho} = 0. \tag{17}$$

Of course, many functions satisfy equation (17), particularly when $\sqrt{\rho}$ varies over two spatial dimensions. In two dimensions, the real and imaginary parts of all analytic functions are available as variable density profiles for constant–density modeling. The required density functions are quadratic in z for $\rho = \rho(z)$.

SCALED WAVE EQUATIONS

Now we turn to scaling of the variable–density wave equation. In doing so we seek to proceed consistently from the exact wave methods of the preceding material to a companion asymptotic approach. This properly scaled equation will admit an entire spectrum of asymptotic dispersion relations, each corresponding to a different relative choice for the wavelength of density variation.

Let us expand the gradients on pressure in equation (1) and take a Fourier transform over time t to obtain

$$\Delta p(\boldsymbol{x}) - \left(\frac{\nabla\rho}{\rho(\boldsymbol{x})}\right)\cdot\nabla p - \nabla\cdot\left(\frac{\nabla\rho}{\rho}\right)p + \frac{\omega^2}{c^2(\boldsymbol{x})}p = 0. \tag{18}$$

The source term f may be dropped without loss of generality. The ray method, used in obtaining asymptotic solutions, replaces source excitations with equivalent initial data for ordinary differential equations written along the rays. We prepare equation (18) for asymptotic analysis by explicitly representing all *length* and *time scales* of its independent variables and coefficients. In the present context these scaling constants carry units of length, inverse time, or their product, and characterize spatial and temporal rates of variation.

Imagine that the density and speed functions have dominant wavelengths (length scales) Λ_ρ and Λ_c and introduce scaled coefficients

$$\tilde{\rho}(\tfrac{2\pi}{\Lambda_\rho}\boldsymbol{x}) \stackrel{\text{def}}{=} \rho(\boldsymbol{x})\,, \qquad \tilde{c}(\tfrac{2\pi}{\Lambda_c}\boldsymbol{x}) \stackrel{\text{def}}{=} c(\boldsymbol{x})\,. \tag{19}$$

We define scaling constants L and ω_o of the spatial coordinate $\boldsymbol{x}$ and frequency ω in equation (18) through the relations

$$\omega = \omega_o\tilde{\omega}\,, \qquad \boldsymbol{x} = (L/2\pi)\boldsymbol{x}_1\,. \tag{20}$$

Angular frequency ω_o is interpreted as a reference or dominant frequency. Length scale L carries the length units of the spatial coordinate, implying that $|\boldsymbol{x}_1|$ is dimensionless and $O(1)$. It is also expedient to make the definitions

$$\mu \stackrel{\text{def}}{=} L/\Lambda_\rho\,, \qquad \eta \stackrel{\text{def}}{=} L/\Lambda_c\,, \tag{21}$$

and write

$$\tilde{\rho} = \tilde{\rho}(\mu\boldsymbol{x}_1)\,, \qquad \tilde{c} = \tilde{c}(\eta\boldsymbol{x}_1)\,. \tag{22}$$

One "scales" equation (18) by making the substitutions of equations (19), (20), and (22). We arrive at

$$\Delta_1 p(\tfrac{L}{2\pi}\boldsymbol{x}_1) - \left(\frac{\nabla_1\tilde{\rho}}{\tilde{\rho}(\mu\boldsymbol{x}_1)}\right)\cdot\nabla_1 p - \nabla_1\cdot\left(\frac{\nabla_1\tilde{\rho}}{\tilde{\rho}}\right)p + \lambda^2[\tilde{\omega}\tilde{n}(\eta\boldsymbol{x}_1)]^2 p = 0 \tag{23}$$

given

$$\nabla_1 \stackrel{\text{def}}{=} \frac{L}{2\pi}\nabla$$

and

$$\lambda \stackrel{\text{def}}{=} \frac{\omega_o L}{(2\pi)c_o}\,, \qquad \tilde{n} \stackrel{\text{def}}{=} \frac{c_o}{\tilde{c}}\,. \tag{24}$$

The speed constant c_o symbolizes a reference speed for the medium. Formally, all asymptotic analysis should start from equation (23). This equation is scaled such

that its coefficients are dimensionless and can be weighted in a balance of terms through choice of the time and length scales.

Hence we shall proceed from equation (23) to the specific scaled equation we require. In effect, we select another change of the spatial coordinate that will bias the asymptotic analysis towards speed functions which vary slowly over space (large Λ_c), yet will preserve a multitude of possibilities for Λ_ρ. We will derive later on, from this scaled differential equation, asymptotic dispersion relations which correlate with that of the constant–coefficient Klein–Gordon equation. It may seem reasonable that this correlation will be the outcome, since constant coefficients in equation (3) coincide with constant c (large Λ_c) and constant damping coefficient b—not constant ρ.

Taking

$$\boldsymbol{x}_2 \stackrel{\text{def}}{=} \eta \boldsymbol{x}_1 \,, \tag{25}$$

$$\Delta_2 p(\tfrac{\Lambda_c}{2\pi}\boldsymbol{x}_2) - \left(\frac{\nabla_2\tilde{\rho}}{\tilde{\rho}(\frac{\mu}{\eta}\boldsymbol{x}_2)}\right)\cdot\nabla_2 p - \nabla_2\cdot\left(\frac{\nabla_2\tilde{\rho}}{\tilde{\rho}}\right)p + \frac{\lambda^2}{\eta^2}\tilde{\omega}^2\tilde{n}^2(\boldsymbol{x}_2)p = 0 \tag{26}$$

if

$$\nabla_2 \stackrel{\text{def}}{=} \frac{1}{\eta}\nabla_1 \,.$$

Equations (21) and (24) render

$$\frac{\mu}{\eta} = \frac{\Lambda_c}{\Lambda_\rho} \,, \qquad \frac{\lambda}{\eta} = \frac{\omega_o \Lambda_c}{(2\pi)c_o} \,. \tag{27}$$

Realizing that

$$\left|\frac{\nabla_2\tilde{\rho}(\frac{\mu}{\eta}\boldsymbol{x}_2)}{\tilde{\rho}}\right| = O(\frac{\mu}{\eta})$$

we substitute

$$\frac{\nabla_2\tilde{\rho}}{\tilde{\rho}} = \alpha\frac{\mu}{\eta}\hat{\gamma}_o \tag{28}$$

into equation (26), insisting that $|\alpha| = O(1)$ and interpreting $\hat{\gamma}_o$ as a constant direction vector of the gradient of density, as in equation (13).

Equation (26) becomes

$$\Delta_2 p(\tfrac{\Lambda_c}{2\pi}\boldsymbol{x}_2) - \left(\alpha\frac{\mu}{\eta}\hat{\gamma}_o\right)\cdot\nabla_2 p + \frac{\lambda^2}{\eta^2}\tilde{\omega}^2\tilde{n}^2(\boldsymbol{x}_2)p = 0. \tag{29}$$

The symbol α represents an arbitrary scalar constant, to be determined. Equation (28) makes the simplest interesting assumption about the fractional density function, assigning it to be constant. Though this assignment is consistent with that of equation (13), one could also consider spatially varying fractional densities for more generality. With that degree of generality the divergence of fractional density in equation (26) does not vanish necessarily, as in this treatment.

A nonvanishing divergence (of fractional density) term contributes to the traveltime of waves in that it enters into the acoustic damping coefficient, and thus the Klein–Gordon dispersion relation. Its absence alters the damping, as was pointed out when the Klein–Gordon form was introduced. Though not at all obvious at this point, one would conclude during ray analysis that, if nonvanishing, that term may also contribute to the traveltime of rays.

Indeed, one may proceed straightway with ray analysis on equation (29). We shall develop, instead, yet another scaled wave equation. This equation will be simpler and easier to work with than equation (29). In particular, we observe that equation (29) has a constant coefficient on its ∇_2 (first order) term, and eliminate that gradient on p in favor of a zeroth order term (with no gradient). Try

$$p(\tfrac{\Lambda_c}{2\pi}\boldsymbol{x}_2) = e^{\frac{1}{2}\alpha\frac{\mu}{\eta}\hat{\boldsymbol{\gamma}}_o\cdot\boldsymbol{x}_2} q(\tfrac{\Lambda_c}{2\pi}\boldsymbol{x}_2) \tag{30}$$

in equation (29). One obtains

$$\Delta_2 q - \left[\left(\frac{1}{2}\alpha\frac{\mu}{\eta}\right)^2 - \left(\frac{\lambda}{\eta}\tilde{\omega}\tilde{n}(\boldsymbol{x}_2)\right)^2\right] q(\tfrac{\Lambda_c}{2\pi}\boldsymbol{x}_2) = 0, \tag{31}$$

a Klein–Gordon differential equation. Let us establish several points concerning equations (30) and (31).

We first emphasize that the q of equation (31) is one and the same as that of equations (3). One establishes that equivalency by scaling equations (3) as above, then identifying $\alpha(\mu/\eta)$ as

$$\alpha\frac{\mu}{\eta} = \frac{\Lambda_c}{\pi}\frac{b_o}{c_o}. \tag{32}$$

Equation (32) holds by virtue of equations (13) and (28).

Moreover, equation (32) establishes that p really is $p(\frac{\Lambda_c}{2\pi}\boldsymbol{x}_2)$ as advertised in equation (30). Substitution into equation (30) gives

$$p(\tfrac{\Lambda_c}{2\pi}\boldsymbol{x}_2) = e^{\frac{b_o}{c_o}\hat{\boldsymbol{\gamma}}_o\cdot(\frac{\Lambda_c}{2\pi}\boldsymbol{x}_2)} q(\tfrac{\Lambda_c}{2\pi}\boldsymbol{x}_2), \tag{33}$$

a function of the proper argument. Finally, we see from equation (14) that our new solution form (equations (30) or (33)) merely makes the statement $p = \sqrt{\rho}\ q$, like equation (2).

What have we accomplished through scaling the wave equation? It is well known that finite difference modeling with equation (1) simulates wavefield dispersion associated with rapid variation in medium properties. Asymptotic ray solutions must be derived from scaled equations (29) or (31) to account for rapid ($\mu = \lambda$) density variation. (From equations (27), density varies at the scale of the seismic wavelength when $\mu = \lambda$.)

Finite differencing accounts automatically for large or small time and length scales. Those scales are implicit in the dimensional operators and coefficients of equations (1)

or (3). On the other hand an analytical, asymptotic treatment relies on the *analyst* to identify a balance of terms, based on selection of the scaling constants. Those scales must be made *explicitly* available for the choosing. We will discover in what follows that analysis, directly on equation (18), corresponds implicitly to choosing $\mu/\eta = 1$. Implicitly, the density and speed functions are assumed to vary at the same (slow) rate over space.

RAY ANALYSIS

We shall unveil through equation (31) a hierarchy of *eikonal* and *transport* equations as the ray theoretical analogs of the preceding wave theory. The classical eikonal and transport results (e.g., Cerveny et al., 1977 and Bleistein, 1984) occupy one position in the hierarchy—and thus are subsumed by this approach. This pair of equations provides analytical means for calculating traveltime and amplitude, respectively. For this reason, the eikonal equation may be thought of as an "asymptotic dispersion relation".

We will discover that rapid density variation influences traveltime through the appearance of the acoustic damping coefficient in a new eikonal equation. The Klein–Gordon wave theory gave the same prediction, yet through expressions for group or phase velocities (equations (9) and (10)). Slow variation belongs with the transport equation, which governs ray amplitudes.

The asymptotic *ansatz* made is that

$$q(\tfrac{\Lambda_c}{2\pi}\boldsymbol{x}_2;\tfrac{\lambda}{\eta}) \sim A(\tfrac{\Lambda_c}{2\pi}\boldsymbol{x}_2;\tfrac{\lambda}{\eta})e^{i\frac{\lambda}{\eta}\tilde{\tau}(\frac{\Lambda_c}{2\pi}\boldsymbol{x}_2)} \tag{34}$$

with A having the formal expansion

$$A = A_0 + \frac{A_1}{i\lambda/\eta} + \frac{A_2}{(i\lambda/\eta)^2} + \ldots. \tag{35}$$

Here $\tilde{\tau}$ is a (dimensionless) traveltime, the conjugate variable of dimensionless frequency λ/η. The character A symbolizes the full amplitude, A_0 the leading order amplitude, etc. Inserting the ansatz into equation (31) gives

$$\begin{aligned} &-\frac{\lambda^2}{\eta^2}[\nabla_2\tilde{\tau}\cdot\nabla_2\tilde{\tau} - \tilde{\omega}^2\tilde{n}^2]A - \frac{\mu^2}{\eta^2}[\frac{1}{2}\alpha]^2 A \\ &+ i\frac{\lambda}{\eta}[2\nabla_2\tilde{\tau}\cdot\nabla_2 A + A\Delta_2\tilde{\tau}] + \Delta_2 A \sim 0. \end{aligned} \tag{36}$$

We see from equation (36) that—through our efforts to scale the wave equation—we have built in the freedom to weight variously the ratio of μ to η in an asymptotic balance of terms. That is to say, we are free to choose a wavelength for density variation relative to speed variation (equations (27)). From equation (28), different choices also amount to different magnitudes of fractional density.

A continuum of possible ratios μ/η is available. However, inspection of equation (36) indicates $\mu/\eta = (\lambda/\eta)^j$, $j = \ldots, -1, 0, 1, \ldots$, are positions in that continuum where fundamental reordering of terms occurs. It is at those positions where the μ/η term exactly matches, surpasses, or recedes from the other terms with regard to their ordering in λ/η, the expansion parameter. We discuss below the two most interesting cases, $\mu/\eta = (\lambda/\eta)^0$ and $\mu/\eta = (\lambda/\eta)^1$. From those one can characterize generally the nature of rayfields over the entire spectrum of values for μ/η.

$\mu = \eta$

We choose $\mu/\eta = 1$ in equation (36) and, consistent with the asymptotic expansion of equation (34), take λ/η large enough (by taking ω_o and Λ_c large enough) such that

$$\nabla\tilde{\tau} \cdot \nabla\tilde{\tau} = \tilde{\omega}^2 \tilde{n}^2(\boldsymbol{x}_2) \,. \tag{37}$$

By reverting to dimensional coordinates and variables one identifies equation (37) as the familiar eikonal equation. Dimensional time τ is

$$\tau \stackrel{\text{def}}{=} \frac{\Lambda_c}{2\pi c_o \tilde{\omega}} \tilde{\tau} \,. \tag{38}$$

We refer back to equations (19), (20), (24) and (25) to obtain the dimensional analog

$$\nabla\tau \cdot \nabla\tau = \frac{1}{c^2(\boldsymbol{x})} \,. \tag{39}$$

Thus, traveltime through a "$\mu = \eta$" medium is governed by the classical eikonal equation, equation (39). From equations (27), $\mu = \eta$ corresponds to $\Lambda_\rho = \Lambda_c$. Density varies at the same slow rate of spatial variation at which speed varies, as required by large λ/η. Bleistein (1984) demonstrates that one may also obtain equation (39) through asymptotic analysis directly on unscaled wave equations, taking ω to be the expansion parameter. We conclude, by comparison with our result from a scaled equation, that the direct approach corresponds implicitly to choosing $\mu = \eta$.

Similar analyses give the same eikonal equation and

$$2\nabla\tau \cdot \nabla A_{(0)} + A_{(0)}\Delta\tau = 0 \qquad \forall\ \mu/\eta = (\lambda/\eta)^j,\ \ j \leq 0. \tag{40}$$

This leading order transport result is identical to the one for constant density media (Bleistein, 1984). Thus, the case $\mu = \eta$ serves as a transition point ($j = 0$) for variable density acoustic media—below which ($j < 0$) rays propagate as if in a constant density medium.

$\mu = \lambda$

The choice $\mu/\eta = \lambda/\eta$ corresponds, from their definitions, to choosing $\Lambda_\rho = 2\pi c_0/\omega_o$. In words, this is a situation where density varies on the same scale as a

reference wavelength for the medium. Hence, a "$\mu = \lambda$" medium is thinbedded with respect to density. Equation (36) gives, by dominant balance in powers of λ/η,

$$\begin{aligned} \nabla\tau \cdot \nabla\tau &= \frac{1}{c^2(\boldsymbol{x})} - \frac{b_o^2}{c_o^2}\frac{1}{\omega^2} \\ &= \frac{1}{c^2(\boldsymbol{x})} - \left(\frac{\Delta\sqrt{\rho}}{\sqrt{\rho}}\right)_o \frac{1}{\omega^2} \,. \end{aligned} \tag{41}$$

(In addition to dimensionalization, we have used equations (27) and (32) to solve for α.) This new eikonal equation provides the basis for predicting a rayfield traveltime distortion due to density gradients, distinct from the influence exerted through c. Moreover, equation (41) shows traveltime τ to vary not only with space but also with frequency, as it should in a dispersive medium.

Define the wavenumber $\tilde{k} \stackrel{\text{def}}{=} |\nabla\tau|\omega$ to see that equation (41) is the asymptotic equivalent of a Klein–Gordon dispersion relation. With that definition we obtain

$$\tilde{k}^2 = \frac{\omega^2}{c^2(\boldsymbol{x})} - \frac{b_o^2}{c_o^2} \,, \tag{42}$$

a form quite similar to that of equation (8). Let us compare the two.

The ray–theoretical result in equation (42) permits speed functions that vary slowly with space, unlike equation (8). That generality was bought at the price of requiring, effectively, that ω be large. On the other hand, the wave–theoretical result in equation (8) is valid for all ω. Differences notwithstanding, these dispersion relations have identical forms when c is constant.

We complete the ray investigation by identifying $\mu/\eta = \lambda/\eta$ as another transition position ($j = 1$). Equation (36) requires the trivial solution $A \sim 0$ for all $\mu/\eta = (\lambda/\eta)^j$, $j > 1$. Apparently, waves of the type proposed in equation (34) cannot propagate in a medium where density varies still more rapidly.

CONCLUSIONS

Theory, wave and ray, predicts that rapid density variation induces a dispersive traveltime distortion for signals propagating in an acoustic medium. That dispersion is of the Klein–Gordon variety, originating through an acoustic damping related to the gradient and curvature of the density function.

Consequently, Klein–Gordon modeling and imaging algorithms should correctly treat variable–density acoustic traveltimes. Moreover, because a nonzero damping coefficient implies a nonconstant density function, those algorithms avoid entirely the usual need to compute density gradients.

Rather, a Klein–Gordon algorithm may be designed naturally as a repeated implementation, once for each layer, of the canonical constant–speed, constant–damping

problem. For full execution of the theory, algorithms should include spatially–variable scaling (by $\sqrt{\rho}$) of Klein–Gordon amplitudes to obtain variable–density amplitudes.

ACKNOWLEDGMENTS

This project was supported by the Consortium Project of the Center for Wave Phenomena, Colorado School of Mines.

REFERENCES

Abramowitz, M., and Stegun, I.A., 1965, Handbook of mathematical functions: Dover Publications Inc.

Bleistein, N., 1984, Mathematical methods for wave phenomena: Academic Press Inc.

Cerveny, V., Moltkov, I.A., and Psencik, I., 1977, Ray methods in seismology: Praha, Karlova Universita.

Claerbout, J.F., 1985, Imaging the earth's interior: Blackwell Scientific Publications.

DeSanto, J.A., 1989, Boundary value problems for scalar waves – part I: CWP–078, Consortium Project on Seismic Inverse Methods for Complex Structures, Colorado School of Mines.

Wapenaar, C.P.A., and Berkhout, A.J., 1989, Elastic wave field extrapolation: Elsevier.

Zemansky, M.W., 1968, Heat and thermodynamics: McGraw–Hill Kogakusha, Ltd.

APPENDIX A: VARIABLE DENSITY WAVE EQUATION

In this appendix we derive a linear wave equation for inhomogeneous acoustic media. The derived equation contains a *fractional density* term which is neglected normally. This term is important to acoustic propagation times when the wavelength of the seismic wave is similar to the wavelength of density variation.

Our derivation strategy comes from first principles. We write exact expressions for conservation of mass and linear momentum and choose an equation of state appropriate for fluids. Perturbation of these expressions gives a pair of linear differential field equations; a wave equation on pressure is derived from this system.

Exact equations

Consider a fixed volume V of fluid surrounded by a surface S. An outward pointing unit normal vector $\boldsymbol{n}$ gives the orientation of the surface at each point. Conservation of linear momentum is described for this fluid volume by

$$\frac{d}{dt}\int_V \rho \boldsymbol{v}\, dV \;=\; -\oint_S p\boldsymbol{n}\, dS - \int_V \boldsymbol{f}\, dV - \oint_S \boldsymbol{v}\rho\boldsymbol{v}\cdot\boldsymbol{n}\, dS$$

$$= -\int_V \nabla p \, dV - \int_V \boldsymbol{f} \, dV - \int_V \nabla \cdot (\boldsymbol{v}\rho\boldsymbol{v}) \, dV, \tag{A-1}$$

where p, $\boldsymbol{v}$, ρ, and $\boldsymbol{f}$ respectively symbolize pressure, particle velocity, fluid density, and an acoustic source (body force density). The first two integrals on the right side of the equation calculate momentum gained per unit of time t. The last integral accounts for fluid flux out of the volume (momentum lost per unit time).

Since V is arbitrary, equation (A-1) can be written in equivalent differential form as

$$\frac{\partial(\rho\boldsymbol{v})}{\partial t} + \nabla \cdot (\boldsymbol{v}\rho\boldsymbol{v}) + \nabla p = -\boldsymbol{f}.$$

Expansion of the divergence gives

$$\frac{\partial(\rho\boldsymbol{v})}{\partial t} + \boldsymbol{v} \cdot \nabla \cdot (\rho\boldsymbol{v}) + \rho\boldsymbol{v} \cdot \nabla\boldsymbol{v} + \nabla p = -\boldsymbol{f}$$

as recorded in Wapenaar and Berkhout (1989). Expansion of the time derivative shows that

$$\boldsymbol{v}\left[\frac{\partial\rho}{\partial t} + \nabla \cdot (\rho\boldsymbol{v})\right] + \rho\left[\frac{\partial\boldsymbol{v}}{\partial t} + \boldsymbol{v} \cdot \nabla\boldsymbol{v}\right] + \nabla p = -\boldsymbol{f}(\boldsymbol{x}, t). \tag{A-2}$$

The second bracketed term is referred to as a *material* or *Lagrangian* derivative on $\boldsymbol{v}$. Conservation of mass requires that the first bracketed term be zero.

In particular,

$$\begin{aligned} \frac{d}{dt}\int_V \rho \, dV &= -\oint_S \rho\boldsymbol{v} \cdot \boldsymbol{n} \, dS \\ &= -\int_V \nabla \cdot (\rho\boldsymbol{v}) \, dV \end{aligned} \tag{A-3}$$

expresses mass conservation for the fluid volume as a whole. At a point, the differential equivalent

$$\frac{\partial\rho}{\partial t} + \nabla \cdot (\rho\boldsymbol{v}) = 0 \tag{A-4}$$

holds. This treatment assumes no sources or sinks of mass within the volume.

Collecting results, conservation of linear momentum is written exactly (albeit, nonlinearly) as

$$\rho\left[\frac{\partial\boldsymbol{v}}{\partial t} + \boldsymbol{v} \cdot \nabla\boldsymbol{v}\right] + \nabla p = -\boldsymbol{f}(\boldsymbol{x}, t). \tag{A-5}$$

Equation (A-5) gives three scalar relations in five unknown functions. Mass conversation (equation (A-4)) adds a fourth equation. An equation of state

$$p = p(\rho) \tag{A-6}$$

provides the necessary fifth, modeling compression/expansion of the fluid as an adiabatic process (Zemansky, 1968).

Linear equations

To proceed toward a linear wave equation, we linearize the system of five equations (A-4)—(A-6) by expanding all functions in perturbation series, as did DeSanto (1989). That is,

$$\begin{aligned} \rho(\boldsymbol{x},t) &= \rho^{(0)} + \epsilon\rho^{(1)}, \\ p(\boldsymbol{x},t) &= p^{(0)} + \epsilon p^{(1)}, \qquad \text{and} \\ \boldsymbol{v}(\boldsymbol{x},t) &= \boldsymbol{v}^{(0)} + \epsilon\boldsymbol{v}^{(1)}, \end{aligned} \tag{A-7}$$

where ϵ is a small, dimensionless parameter. Background functions (those with a $^{(0)}$) are interpreted as descriptions of the medium before waves are introduced. Perturbations from the background state are due to waves.

Substitution of equations (A-7) into equation (A-4) gives linear, ordered expressions for mass conservation. That is to say, to zeroth order in ϵ

$$\frac{\partial\rho^{(0)}}{\partial t} + \nabla\cdot(\rho^{(0)}\boldsymbol{v}^{(0)}) = 0 \tag{A-8}$$

and, to $O(\epsilon^1)$,

$$\frac{\partial\rho^{(1)}}{\partial t} + \nabla\cdot(\rho^{(0)}\boldsymbol{v}^{(1)}) + \nabla\cdot(\rho^{(1)}\boldsymbol{v}^{(0)}) = 0. \tag{A-9}$$

Substitution of equations (A-7) into the expression for momentum conservation (equation (A-5)) produces

$$\rho^{(0)}\frac{\partial\boldsymbol{v}^{(0)}}{\partial t} + \nabla p^{(0)} = \boldsymbol{0} \tag{A-10}$$

to $O(1)$ (where $\boldsymbol{f}^{(0)} \equiv \boldsymbol{0}$) and

$$\rho^{(0)}\frac{\partial\boldsymbol{v}^{(1)}}{\partial t} + \rho^{(1)}\frac{\partial\boldsymbol{v}^{(0)}}{\partial t} + \nabla p^{(1)} = -\boldsymbol{f}^{(1)} \tag{A-11}$$

to $O(\epsilon^1)$.

Quadratic velocity terms were neglected to obtain linear expressions. However, $\boldsymbol{v}^{(0)}$ was not taken to be zero, as is typically the case (Wapenaar and Berkhout, 1989). Analysis of the equation of state (A-6) reveals $\boldsymbol{v}^{(0)} \equiv \boldsymbol{0}$ to be inconsistent with a variable–density acoustic medium, as we now show.

We follow the analysis of DeSanto (1989). Taking $p^{(0)} = p^{(0)}(\rho^{(0)})$ the chain rule gives

$$\nabla p^{(0)} = c^2\nabla\rho^{(0)} \tag{A-12}$$

with

$$c^2 \stackrel{\text{def}}{=} \frac{\partial p^{(0)}}{\partial\rho^{(0)}}\,. \tag{A-13}$$

The assumption $\boldsymbol{v}^{(0)} \equiv \mathbf{0}$ requires $\nabla p^{(0)} \equiv \mathbf{0}$ from equation (A-10), and equation (A-12) in turn requires $\nabla \rho^{(0)} \equiv \mathbf{0}$. That is to say, an inhomogeneous fluid medium is, to zeroth order, in hydrodynamic equilibrium. Hydrostatic equilibrium ($\boldsymbol{v}^{(0)} \equiv \mathbf{0}$) is not permissible for media with arbitrary density variations over space.

Equation (A-12) will be used to trade background pressure gradients for density gradients, density being the quantity measured routinely in exploration geophysics. Again, we follow DeSanto (1989) to derive another substitution. Expanding pressure about the background state $p^{(0)}(\rho^{(0)})$ and using equations (A-7),

$$\begin{aligned} p^{(0)} + \epsilon p^{(1)} &= p^{(0)} + \frac{\partial p^{(0)}}{\partial \rho^{(0)}}(\rho - \rho^{(0)}) \\ &= p^{(0)} + \epsilon \frac{\partial p^{(0)}}{\partial \rho^{(0)}} \rho^{(1)}. \end{aligned}$$

Therefore,

$$p^{(1)} = c^2 \rho^{(1)} \tag{A-14}$$

to $O(\epsilon^1)$. This result gives a substitution for density perturbations in terms of pressure perturbations.

One additional physical simplification is assumed customarily for exploration geophysics problems. One normally assumes $\partial \rho^{(0)}/\partial t \equiv 0$ (or, $\rho^{(0)} = \rho^{(0)}(\boldsymbol{x})$ at most). This implies that, to zeroth order, the fluid is incompressible and can not flux out of the volume. Proof of these physical consequences depends on liberal use of the divergence theorem. From equation (A-8), $\nabla \cdot (\rho^{(0)} \boldsymbol{v}^{(0)}) \equiv 0$ implies $\oint_S (\boldsymbol{v}^{(0)} \cdot \boldsymbol{n})\, dS \equiv 0$ and equation (A-9) simplifies to

$$\frac{\partial \rho^{(1)}}{\partial t} + \nabla \cdot (\rho^{(0)} \boldsymbol{v}^{(1)}) = 0. \tag{A-15}$$

Also, if $p^{(0)} = p^{(0)}[\rho^{(0)}(\boldsymbol{x})]$ then $c = c(\boldsymbol{x})$ at most, from equation (A-13).

Equations (A-10) through (A-15) constitute the system of linearized expressions needed to write a linear wave equation on a single field (perturbation) quantity. We choose to write the equation for pressure. Density perturbation terms are replaced with pressure perturbations in equations (A-15) and (A-11) using equation (A-14). All background functions are then expressed in terms of background density through equations (A-10) and (A-12). These substitutions give

$$\frac{1}{c^2} \frac{\partial p^{(1)}}{\partial t} + \nabla \cdot (\rho^{(0)} \boldsymbol{v}^{(1)}) = 0 \tag{A-16}$$

and

$$\rho^{(0)} \frac{\partial \boldsymbol{v}^{(1)}}{\partial t} - \frac{\nabla \rho^{(0)}}{\rho^{(0)}} p^{(1)} + \nabla p^{(1)} = -\boldsymbol{f}^{(1)}(\boldsymbol{x}, t). \tag{A-17}$$

The above pair of differential equations are the *field equations* for linear waves in inhomogeneous acoustic media. The *wave equation*

$$\Delta p^{(1)} - \nabla \cdot \left[\frac{\nabla \rho^{(0)}}{\rho^{(0)}} p^{(1)} \right] - \frac{1}{c^2(\boldsymbol{x})} \frac{\partial^2 p^{(1)}}{\partial t^2} = -\nabla \cdot \boldsymbol{f}^{(1)}(\boldsymbol{x}, t) \tag{A-18}$$

results from the divergence of equation (A-17) minus the time derivative of equation (A-16). This result is recognized to be the wave equation for a constant–density medium but, with an additional term, the term with brackets.

Another form of the variable density wave equation is also common. Expand the bracketed term in equation (A-18) and factor out $\rho^{(0)}$ from terms containing differentiated pressure. These manipulations produce the form

$$\rho^{(0)}(\boldsymbol{x}) \nabla \cdot \left[\frac{\nabla p^{(1)}}{\rho^{(0)}} \right] - \nabla \cdot \left[\frac{\nabla \rho^{(0)}}{\rho^{(0)}} \right] p^{(1)} - \frac{1}{c^2(\boldsymbol{x})} \frac{\partial^2 p^{(1)}}{\partial t^2} = -\nabla \cdot \boldsymbol{f}^{(1)}(\boldsymbol{x}, t), \tag{A-19}$$

where

$$\left[\frac{\nabla \rho^{(0)}}{\rho^{(0)}} \right]$$

is a *fractional density*. Though this term is often neglected (Claerbout, 1985; Wapenaar and Berkhout, 1989), we showed that the differentiated equation of state (A-12) and equation (A-10) require, strictly speaking, that it be included.

Traditionally, background and perturbation superscripts are dropped. This simplification gives

$$\rho(\boldsymbol{x}) \nabla \cdot \left[\frac{\nabla p}{\rho} \right] - \nabla \cdot \left[\frac{\nabla \rho}{\rho} \right] p - \frac{1}{c^2(\boldsymbol{x})} \frac{\partial^2 p}{\partial t^2} = -f(\boldsymbol{x}, t), \tag{A-20}$$

with $f(\boldsymbol{x}, t) \stackrel{\text{def}}{=} \nabla \cdot \boldsymbol{f}^{(1)}(\boldsymbol{x}, t)$. Equation (A-20) is the final wave equation form sought in this development.

Network Parallel 3-D FFT

Tong Chen and Dave Hale

Center for Wave Phenomena
Colorado School of Mines
Golden, Colorado 80401
(303) 273-3557

Network parallel 3-D FFT

Tong Chen and Dave Hale

ABSTRACT

The use of network-connected workstations to do parallel computing is attractive due to the good performance-to-cost ratio. The deciding factor of the performance is the ratio of computation to communication costs. In 3-D seismic processing, the communication cost can be frustratingly high.

By distributing the 3-D data set, which may be too big to be stored on any one disk attached to one workstation, to several disks, each attached to its own workstation, we may perform the data input/output operations in parallel. However, when data flow between disks is needed, the cost of communication may be high.

The communication cost can be reduced by controlling the data flow and making it also run in parallel. Some experimental tests involving network communication suggest an optimal strategy of data flow. Using this strategy, a 3-D turning wave migration of $1000 samples \times 1000 traces \times 1000 lines$, for example, can be performed in 18 hours on five network-connected IBM RS/6000 workstations.

INTRODUCTION

The use of network-connected computers to do parallel computing is of current interest to geoscientists (Koshy, 1991; Black and Su, 1991). By running many high-performance workstations, such as the IBM RS/6000, in parallel, we may achieve speeds comparable to those of supercomputers, while the performance-to-cost ratio is much higher. Advances in the processing power of workstations and communication speed of networks make network parallel computing (NPC) feasible today. Further improvements of the communication speed using optical fibers will make NPC even more attractive (Almasi et al., 1991). Meanwhile software systems such as Linda (Carriero and Gelernter, 1989) and PVM (Parallel Virtual Machine) (Beguelin et al., 1991) make NPC easy to implement.

For any application, the deciding factor in NPC is the ratio of computation to communication costs. Geoscience applications such as seismic modeling and imaging seem to be quite fit for NPC, because they have high computation to communication ratios. A detailed discussion of speedups relative to single-workstation computation for a 2-D migration application, under different circumstances, can be found in Almasi(1991).

For many 2-D seismic applications, where the data set can reside in memory, NPC implementations are not difficult. Figure 1 illustrates the diagram for this kind of implementation using a message-passing system such as PVM. A prototype program using PVM in this way can be found in the Appendix.

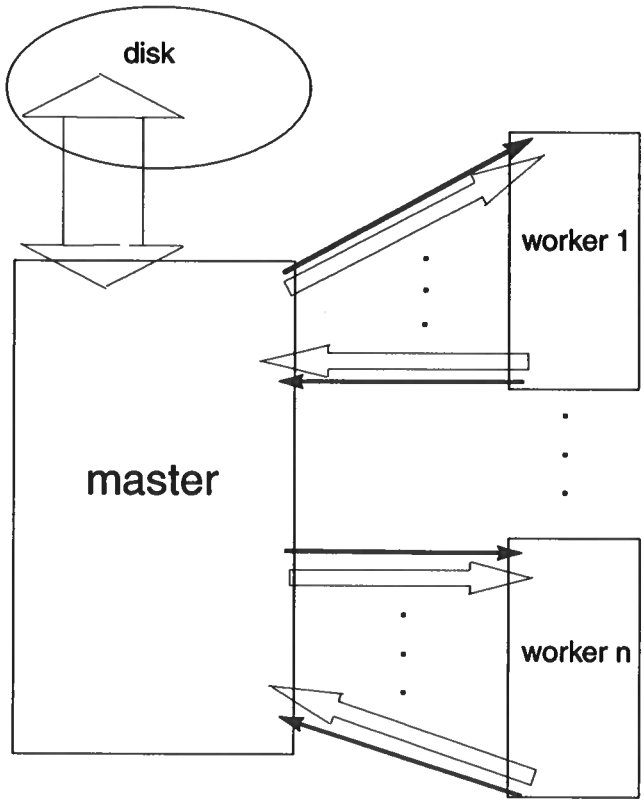

FIG. 1. Working scheme for a message-passing system in NPC when data can reside in memory. The black arrows denote commands, and the clear ones, data. The master reads data from the disk and sends them out to the workers. After being processed, the data are sent back to the master, which writes them to the disk. Notice that all the disk I/O is carried out by the master.

In 3-D seismic processing, however, the situation is different. For many 3-D applications, besides so-called *inline* processing, *crossline* processing is also required,

which in turn requires that the data set be accessed from different directions. The data set is typically so large that it cannot reside in memory, which necessitates a lot of disk I/O, both sequential and random access. The cost for disk I/O, especially random access I/O, is so high in 3-D seismic processing that high speedup can hardly be achieved using parallel computing, even with some supercomputers. Also, a 3-D data set may be too large to be stored on one disk of a workstation, which makes NPC implementation a bit difficult. Black and Su (1991) suggested using a larger machine capable of managing the large volume of data. A different strategy is to use several workstations, each with its own disk (Figure 2). Fortunately, having several disks available is a sufficiently common situation in network environments. Also, using several disks makes it possible to perform disk I/O in parallel.

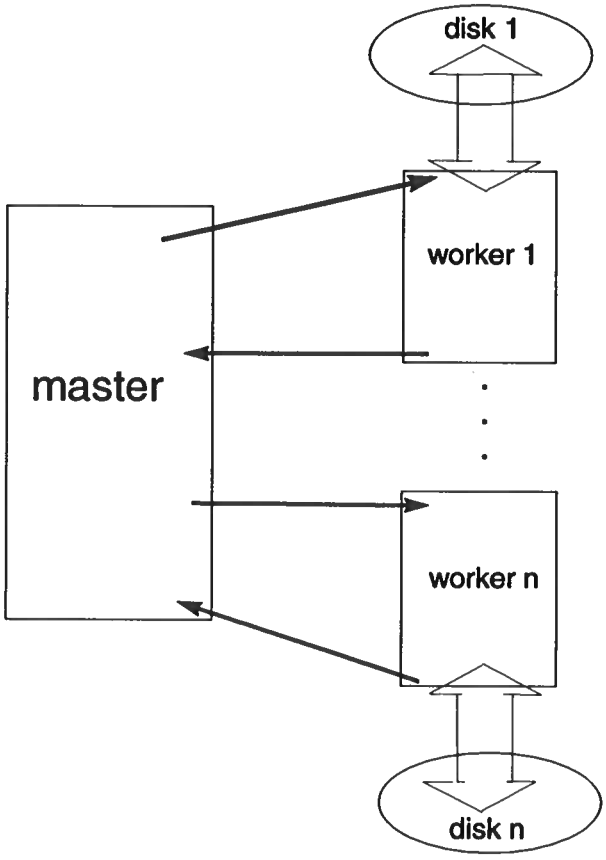

FIG. 2. Working scheme for a message-passing system in NPC when data are distributed among several disks. The black arrows denote commands, and the clear ones, data. The master functions only to coordinate the workers. Every worker reads data from its own disk and writes data to its own disk. In this case, disk I/O is performed in parallel by different workers.

For NPC implementations of 3-D seismic processing, distribution of the data among several disks is necessary. The strategy for data distribution can dominate

the efficiency of processing. Using 3-D FFT as an example, we suggest a strategy of data distribution.

3-D FFT is an example where accessing of data on different disks is needed. This accessing requires network communication, which is expensive using network hardware and software now available. Noticing that we have several disks, we tried to make the data flow in parallel. Some experimental results allowed us to design an effective strategy to control the data flow.

By following the selected strategy above, we can perform a 3-D turning wave migration for a data set of size $1000 \times 1000 \times 1000$ on five IBM RS/6000 workstations in 18 hours.

DATA DISTRIBUTION

In 3-D seismic processing, the data set is typically too big to be stored on one disk attached to one workstation. A 3-D seismic survey of dimension $1000 samples \times 1000 traces \times 1000 lines$, for example, requires 4 Gbytes of storage. The disks we usually have for our workstations each have 1.2 Gbytes capacity, so that we must distribute the data to several disks. We seek an optimum strategy for the data distribution.

In some applications, such as deconvolution, which is a one-dimensional process, the distribution is simple. We can store a piece of data (many seismic lines) on each disk. Each workstation processes only its own piece of data. After all the workstations have finished their own processing, the results are composited. Little data communication is necessary.

In many other cases, however, since we have both inline and crossline processing, a lot of data communication is needed. One example is the 2-D FFT along inline and crossline dimensions in 3-D seismic migration or modeling programs. A flow chart of the example is as follows:

FFT $f(t,x,y)$ *to* $F(t,k_x,y)$
Transpose $F(t,k_x,y)$ *to* $F(t,y,k_x)$
FFT $F(t,y,k_x)$ *to* $F(t,k_y,k_x)$
For all k_x {
    For all k_y {
        ⋮
    }
}
IFFT $F(t,k_y,k_x)$ *to* $F(t,y,k_x)$
Transpose $F(t,y,k_x)$ *to* $F(t,k_x,y)$
IFFT $F(t,k_x,y)$ *to* $f(t,x,y)$

Let's consider several strategies for this example.

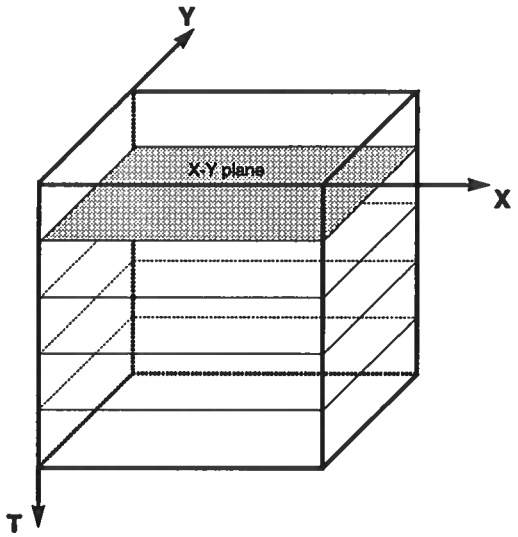

FIG. 3. T slice data distribution. This choice will benefit the 2-D FFT, but requires transposition of the entire data set.

T slice

Since 2-D FFT is a two-dimensional process, the seemingly ideal method of data distribution would be to let each workstation store a set of time slices (Figure 3). For every time slice, each workstation reads the X-Y data plane and performs a 2-D FFT. In this way, each workstation can process its own piece of data. No network communication seems necessary, but this strategy requires that time T be the slowest computational dimension, while in real applications, it is typically the fastest dimension. Transposition of the entire data set is thus needed, which is difficult due to its requirements for huge storage and long running time.

Y slice

According to the format of the data recorded, we can make Y slices. Every workstation stores some Y slices (X-T sections) (Figure 4). Obviously, in this way, an FFT along the X direction is easy. For every Y slice, each workstation reads the X-T data plane and performs an FFT along the X direction. But, FFT along the Y direction is difficult, since it requires data on different disks. This indicates much network communication. Furthermore, it is difficult for the FFT along the Y direction to run in parallel, since at one moment, several workstations may access the data on one disk, resulting in I/O conflict.

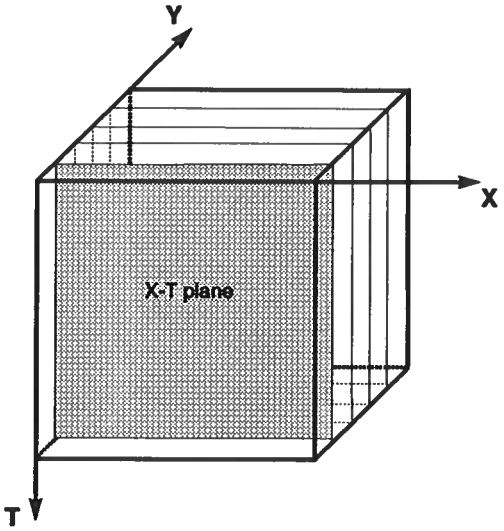

FIG. 4. Y slice data distribution. This choice is a natural way of data distribution. It will benefit the FFT along the X direction, but the FFT along the Y direction is difficult.

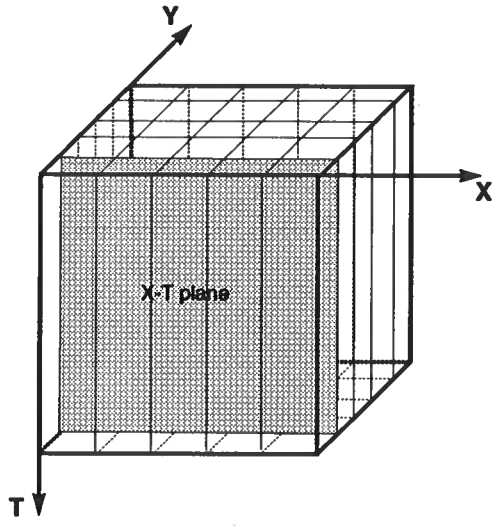

FIG. 5. XY slice data distribution, which chops the data set into several block files. It will benefit FFT along both X and Y directions, but requires swapping of the block files after FFT along the X direction.

XY slice

From the discussion above, we have seen that the Y slice makes FFT along the X direction easy to implement. To deal with the problem in computing FFT along the Y direction, we make additional X slices (Figure 5). In this way, we actually chop the data set into several block files. For the FFT along the X direction, each workstation reads data from the block files on its local disk and forms an X-T data plane. For FFT along the Y direction, we would like for the workstations to read data from their local disks also. One way to satisfy this is to swap the block files and put the data for one Y-T data plane on one disk. This is why the X slice is necessary. Since the data for FFT along the Y direction are now on one disk, I/O conflict is avoided.

DATA COMMUNICATION

Using the 2-D FFT as an example, we examined different strategies of data distribution. The XY slice method seems to be the best in this case. However, in this strategy, after FFT along the X direction, swapping of the block files is needed, which requires network communication. Figure 6 illustrates the distribution of the block files when we use five workstations. Since we use five workstations, we have 5×5 block files. Swapping the block files is like transposing a matrix, in this case, a 5 by 5 matrix.

$$\begin{pmatrix} (0,0) & (0,1) & (0,2) & (0,3) & (0,4) \\ (1,0) & (1,1) & (1,2) & (1,3) & (1,4) \\ (2,0) & (2,1) & (2,2) & (2,3) & (2,4) \\ (3,0) & (3,1) & (3,2) & (3,3) & (3,4) \\ (4,0) & (4,1) & (4,2) & (4,3) & (4,4) \end{pmatrix} \Rightarrow \begin{pmatrix} (0,0) & (1,0) & (2,0) & (3,0) & (4,0) \\ (0,1) & (1,1) & (2,1) & (3,1) & (4,1) \\ (0,2) & (1,2) & (2,2) & (3,2) & (4,2) \\ (0,3) & (1,3) & (2,3) & (3,3) & (4,3) \\ (0,4) & (1,4) & (2,4) & (3,4) & (4,4) \end{pmatrix}$$

The block files on the diagonal of the matrix need no swapping. The other 20 files are to be swapped. Choosing NFS file read/write, to implement the swap of block files, we can obtain a transfer rate of about 250 Kbytes/s. For a typical 3-D seismic survey of size $1000 \times 1000 \times 1000$, and using five workstations, we can estimate the cost of the swap. The size of each block file is $4 \times 1000 \times 1000 \times 1000/25$ bytes. A transfer rate of 250 Kbytes/s is assumed when swapping, and 20 swaps are needed. The cost of the swap, if done sequentially, is therefore:

$$\begin{aligned} T &= number\ of\ swaps \times \frac{size\ of\ each\ block\ file}{transfer\ rate} \\ &= 20 \times \frac{4 \times 1000 \times 1000 \times 1000/25}{250 \times 1000} \\ &\approx 3.6 \text{ hr.} \end{aligned} \tag{1}$$

This estimate shows that swapping the block files sequentially is very expensive. Notice that when swapping in this way, only one workstation and one disk are busy

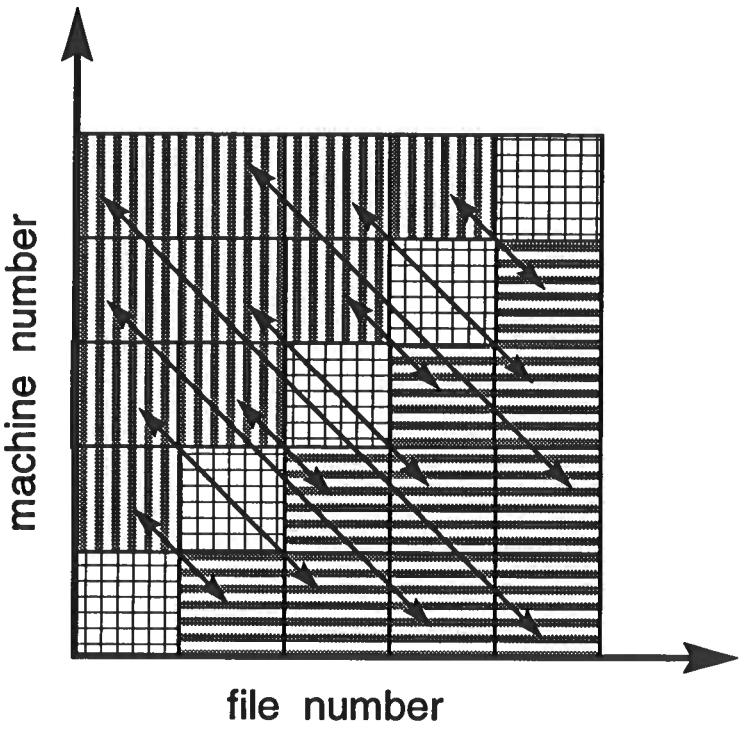

FIG. 6. Swapping of block files. In the case of using five workstations, there are 25 block files. Since the block files on the diagonal need no swapping, 20 block files are to be swapped.

at any given time. The other workstations and disks are idle waiting for the swap to finish. This suggests the possibility of doing the swapping in parallel. Since swapping the block files requires network communication as well as disk read/write, the performances of all of these operations will determine our parallel strategy. We did some experiments to estimate the costs of network communication and disk read/write, since, unfortunately, theoretical analysis of these costs is difficult.

Local disk read/write

We did some tests for local disk read and write. Making sure that the disk is a local disk, we did some timing for writing to a file and reading from it. The transfer rate as a function of the package size of each read/write operation is shown in Figure 7. From this figure, we find that the cost changes little when the package size varies. We obtained rates of about 2 Mbytes/s for read and about 1.6 Mbytes/s for write.

Remote disk read/write

We did a similar test for a remote disk. We did the test in NFS environment with a token ring. The result is shown in Figure 8. Again, the cost does not change too much when we varied the package size. One impressive feature about this result is that reading from a remote disk is much faster than writing to it. This suggests one

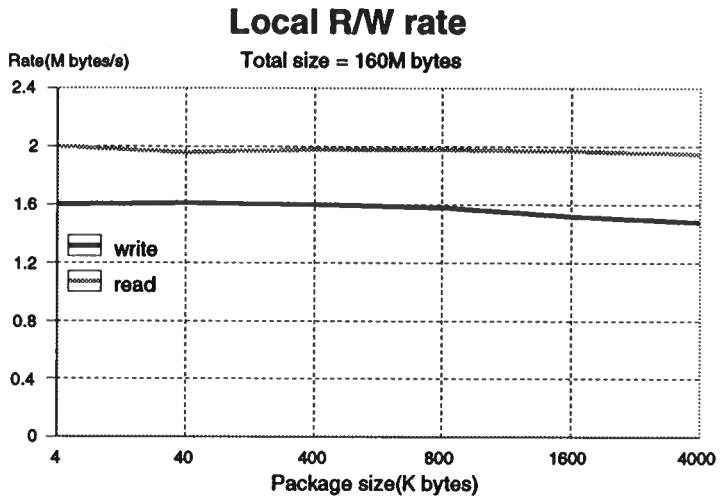

FIG. 7. Transfer rate of local disk read and write. The black line is for write and the grey one for read. Notice that the performance changes little when the size of each read/write changes.

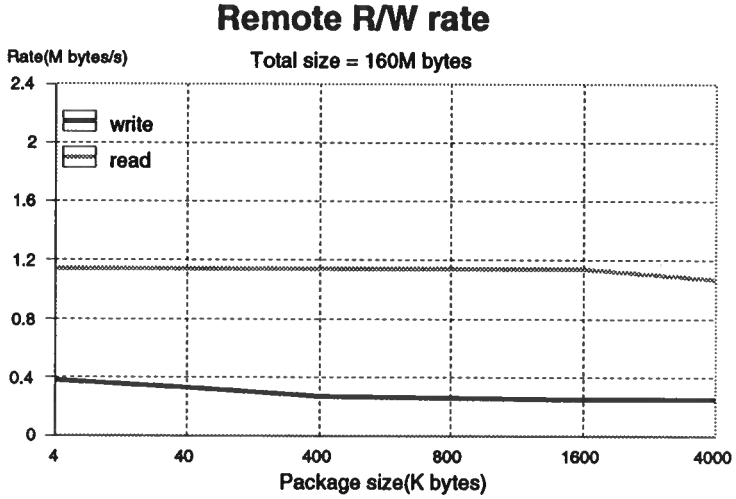

FIG. 8. Transfer rate for remote disk read and write. The black line is for write, and the grey one for read. Notice that the performance changes little when the size of each read/write changes. Also notice that read from a remote disk is significantly faster than writing to it.

way to reduce the communication cost, that is, making every write operation local when swapping the block files. Figure 9 illustrates the strategy.

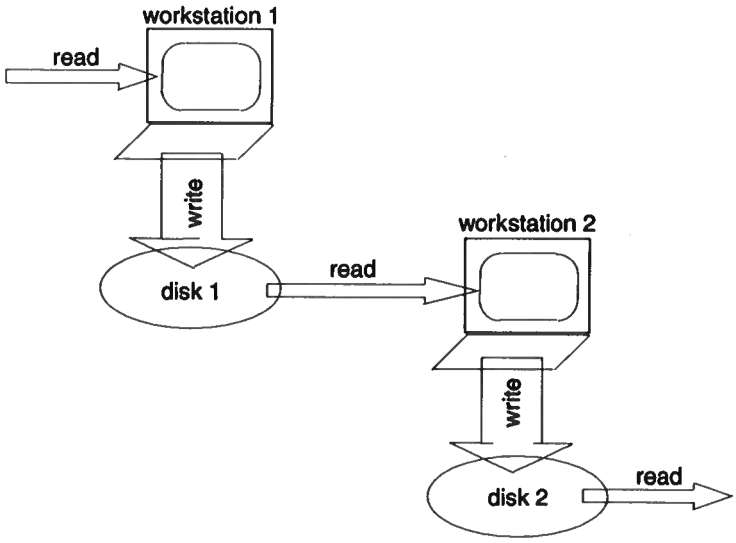

FIG. 9. Reading from a remote disk and writing to the local one can reduce the communication cost.

I/O conflict

From Figure 9, we can see that to swap the block files in parallel, several workstations may have to access the disks simultaneously. This, of course, will cause I/O conflict. One way to avoid this is to synchronize the read and write operations. We call it synchronous strategy. We can wait for all the read operations to finish, and then write. But this will take a lot of time, not only waiting to synchronize the read and write operations, but also on the extra messages to synchronize. Another way is to try to reduce the severity of the I/O conflict. We call it asynchronous strategy. From the results of our experiments, we found that having one read operation and one write operation to a disk is possible, where the read is performed by a remote workstation and the write by the local one. Figure 10 shows the combined transfer rate for reading from a remote disk and writing to the local one, done sequentially and in parallel. Here, doing sequentially means we perform only one remote read and local write at a time, where there is no I/O confilct. And doing in parallel means we have more than one (in our case two) workstations doing remote read and local write at a given time, which may cause I/O conflict. From this result, we find that doing remote read and local write in parallel is even a bit faster than doing it sequentially, which indicates little problem of I/O conflict. We also tried the synchronous strategy. The result turns out that the synchronous strategy is no faster that the asynchronous one.

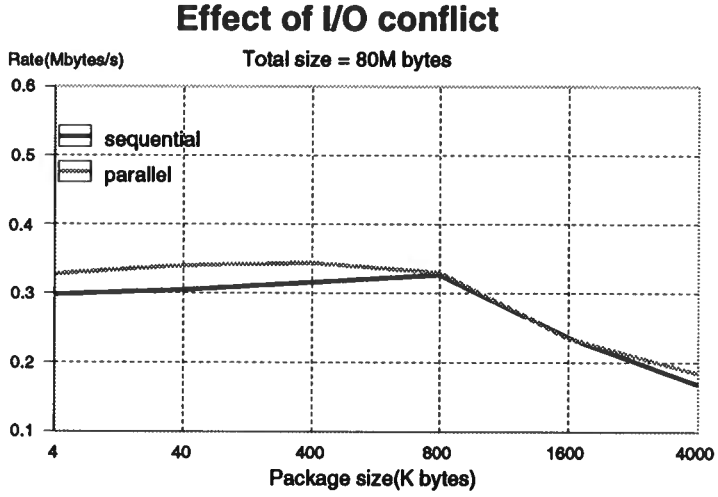

FIG. 10. Combined transfer rate for remote read and local write. The black line is for doing sequentially, and the grey one for doing in parallel. Notice that the rate for the parallel one is even a bit higher than that for the sequential one.

Network capacity

Another factor to be considered, when swapping the block files in parallel, is the capacity of the network—the total size of data that can be transferred at the same time in the network. According to our experimental results, five packages of message, each of size up to 800 Kbytes in the network have little effect on the transfer rate. This indicates that we can swap the block files in parallel without thrashing the network.

NETWORK PARALLEL SWAP

The above experimental results indicate that swapping the block files in parallel is feasible. The remaining problem is how to design a strategy to satisfy the constraints from the above experimental results. The constraints are:

1. making every write operation local
2. for a given disk, having only one read operation by a remote workstation and one write operation by the local workstation occur at a time
3. only generating one temporary file at each step when swapping

Figure 11 illustrates the strategy for the swap. The block files on the NE-SW diagonal need no swapping. Our strategy is to start from the diagonal. First, swap the block files on the sub-diagonal and super-diagonal. Notice that for n workstations, only $n-1$ elements are on the sub-diagonal and $n-1$ on super-diagonal. In a periodic

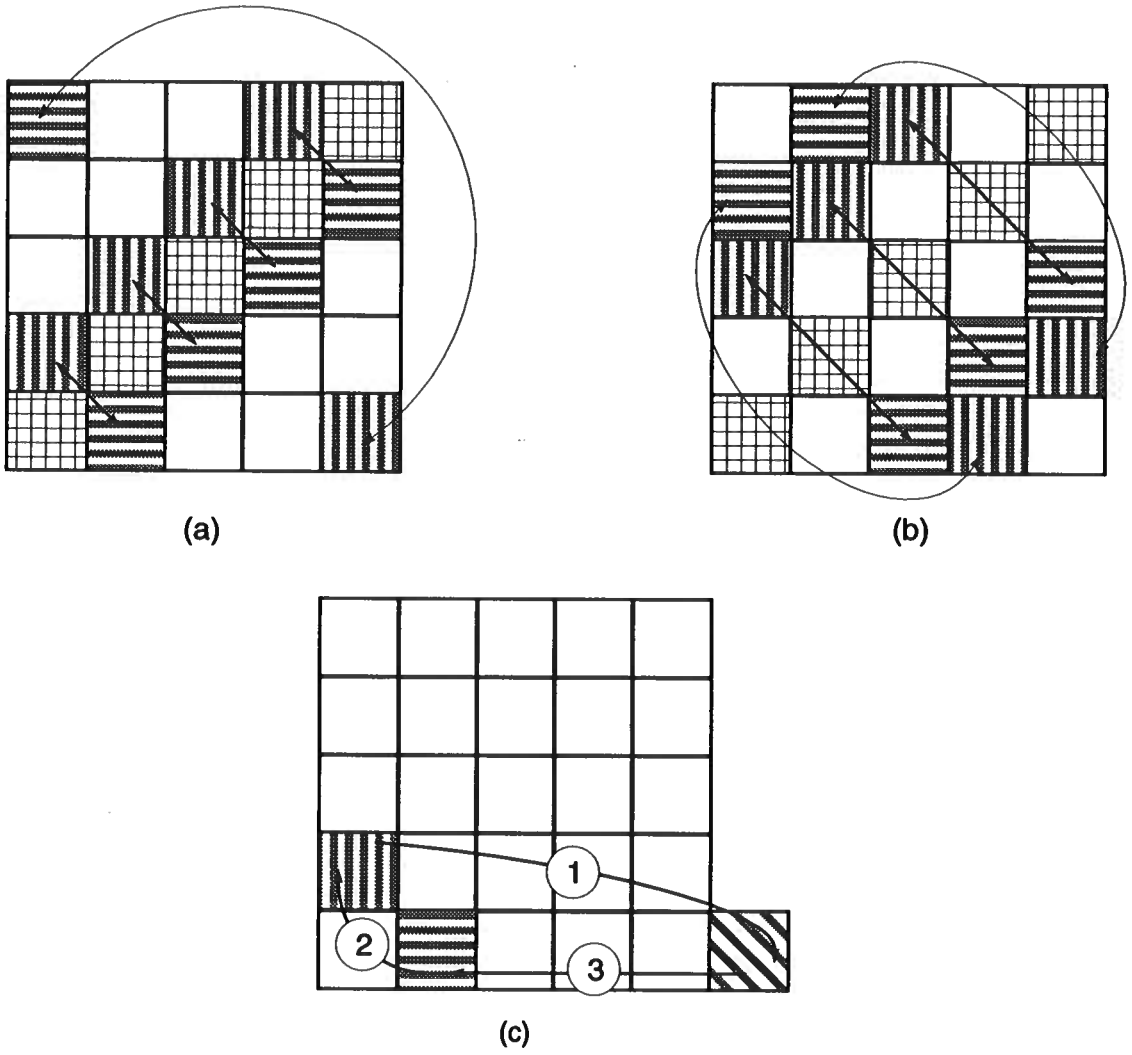

FIG. 11. Strategy of parallel swapping of block files. In this 5×5 case, the swap is done in two steps. (a) is the first step, where the block files along the sub- and super-diagonals of the matrix get swapped. Those along the diagonal need no swapping. Also, the files at the corners of the matrix, which can be considered as along the sub- and super-diagonals in terms of modulo, are swapped. These swaps are done in parallel. (b) is the second step, which finishes all the swaps in this case. (c) is the detail of each swap. First read from a file and write it to a temporary file. Then write the file to be swapped to the file just read. Finally, rename the temporary file to the file swapped.

sense (modulo n), two more block files are also on the sub- and super-diagonals. We can swap the $2n$ block files in parallel. Second, swap the block files one more step from the diagonal. And then, the next time, one more step, and so on. For example, in the first step, on workstation m, we read from file $([m+1]_n, m)$, which is on the disk of workstation $[m+1]_n$, and write it to $(m, [m+1]_n)$, which is on the local disk. In this way, we can satisfy all three above constraints. In this way, instead of swapping two elements of the matrix at each step, we actually swap two colums. For $n = 5$ and $n = 4$, the processes are shown as follows:

$n = 5$

$$\begin{pmatrix} (0,1) \\ (1,2) \\ (2,3) \\ (3,4) \\ (4,0) \end{pmatrix} \Rightarrow \begin{pmatrix} (1,0) \\ (2,1) \\ (3,2) \\ (4,3) \\ (0,4) \end{pmatrix}, \quad \begin{pmatrix} (0,2) \\ (1,3) \\ (2,4) \\ (3,0) \\ (4,1) \end{pmatrix} \Rightarrow \begin{pmatrix} (2,0) \\ (3,1) \\ (4,2) \\ (0,3) \\ (1,4) \end{pmatrix}$$

$n = 4$

$$\begin{pmatrix} (0,1) \\ (1,2) \\ (2,3) \\ (3,0) \end{pmatrix} \Rightarrow \begin{pmatrix} (1,0) \\ (2,1) \\ (3,2) \\ (0,3) \end{pmatrix}, \quad \begin{pmatrix} (0,2) \\ (1,3) \\ (2,0) \\ (3,1) \end{pmatrix} \Rightarrow \begin{pmatrix} (2,0) \\ (3,1) \\ (0,2) \\ (1,3) \end{pmatrix}$$

When using n workstations, we need $P(n,2) = n(n-1)$ read and the same number of write operations, to swap the block files. Doing it in parallel, we need only the time for $P(n,2)/n = n-1$ read and the same number of write operations, where the read is from a remote disk and the write is to the local one. The parallel operation can reach a combined transfer rate of about 300 Kbytes/s, according to our experimental results. For $n = 5$, only two steps of swaps are needed, where one swap includes two read and two write operations. When $n = 4$, only 1.5 steps of swaps are needed, since in the second step of the swap, the upper half of the swap is actually identical to the lower one.

For comparison with the sequential solution, we can estimate the cost of this strategy, for the problem of $1000 \times 1000 \times 1000$ with five workstations. The cost of swap is now:

$$\begin{aligned} T &= 4 \times \frac{4 \times 1000 \times 1000 \times 1000/25}{300 \times 1000} \\ &\approx 0.6 \text{ hr.} \end{aligned} \tag{2}$$

CONCLUSION

For the flow chart of the 3-D migration or modeling, we can estimate the cost, for the size of $1000 \times 1000 \times 1000$, using five workstations.

For FFT along the X direction, disk I/O needed is almost sequential. (It is not sequential since we have to read data from several files.) The combined rate for read and write is about 600 Kbytes/s. The I/O time is

$$\begin{aligned} T_{io} &= \frac{4 \times 1000 \times 1000 \times 1000/5}{600 \times 1000} \\ &\approx 1333 \text{ sec.} \end{aligned} \tag{3}$$

The time for computation, assuming that the workstations run at speed of 10 MFLOPS, and the constant factor α in the cost of FFT equals to five, is

$$\begin{aligned} T_{cmp} &= \frac{\alpha \times 1000 \times 1000 \times 1000 \times \log_2 1000/5}{10 \times 1000 \times 1000} \\ &= 1000 \text{ sec.} \end{aligned} \tag{4}$$

We can estimate the time for FFT along the X direction very roughly as

$$\begin{aligned} T_x &= T_{io} + T_{cmp} \\ &\approx 1333 + 1000 \\ &\approx 0.6 \text{ hr.} \end{aligned} \tag{5}$$

Similarly, we can estimate the time for FFT along the Y direction. In this case, random disk I/O from different files is needed. The combined rate for read and write is about 150 Kbytes/s.

$$\begin{aligned} T_{io} &= \frac{4 \times 1000 \times 1000 \times 1000/5}{150 \times 1000} \\ &\approx 5333 \text{ sec.} \end{aligned} \tag{6}$$

The time for computation should be almost the same as that of FFT along the X direction.

These give the time for FFT along the Y direction as

$$\begin{aligned} T_y &= T_{io} + T_{cmp} \\ &\approx 5333 + 1000 \\ &\approx 1.8 \text{ hr.} \end{aligned} \tag{7}$$

The time for the inverse transformations should be almost the same as for the FFT's, except the time for scaling.

Using turning wave migration (Hale et al., 1991) as an example, we can estimate the cost for a 3-D data set of size $1000 \times 1000 \times 1000$, running on five IBM RS/6000

workstations. From our preliminary result, migration or modeling takes about 12 hours. Using the estimate for the time of the swap and the FFT's, we can get the total time as

$$\begin{aligned} T &= T_x + T_{sw} + T_y + T_{mg} + T_y + T_{sw} + T_x \\ &= 0.6 + 0.6 + 1.8 + 12 + 1.8 + 0.6 + 0.6 \\ &= 18 \text{ hr.} \end{aligned} \tag{8}$$

ACKNOWLEDGMENTS

Thanks to Dr. Ken Larner for his review of this paper. A lot of thanks also go to Gina Boice of Center for Geoscience Computing for providing us with the test environment. Financial support for this work was provided by the members of the Consortium Project on Seismic Inverse Methods for Complex Structures at the Center for Wave Phenomena, Colorado School of Mines.

REFERENCES

Koshy, M., Pereyra, V., and Meza, J., 1991, Distributed computing application in forward and inverse geophysical modeling: Extended Abstracts, 61st Annual International SEG Meeting, 349-352.

Black, J., and Su, C., 1991, Networked parallel 3-D depth migration: Extended Abstracts, 61st Annual International SEG Meeting, 349-356.

Hale, D., Hill, N. R., and Stefani, J. P., 1991, Imaging salt with turning seismic waves: Extended Abstracts, 61st Annual International SEG Meeting, 1171-1174.

Almasi, G., McLuckie, T., Bell, J., Gordon, A., and Hale, D., 1991, Parallel distributed seismic migration: IBM Research Report, RC17323.

Beguelin, A., Dongarra, J., Geist, A., Manchek, R., and Sunderam, V., 1991, A Users' Guide to PVM–Parallel Virtual Machine.

Carriero, N., and Gelernter, D., 1989, Linda in context: Communications of the ACM, **32**, 4(April), 444-458.

APPENDIX: PROTOTYPE PROGRAM USING PVM

A prototype program using PVM is shown below. This program illustrates a PVM implementation of master-worker mode, where only the master stores the original data. The workers get both data and instructions from the master. This is different from what we mainly discussed in the paper. But it is usefull for most 2-D PVM implementations.

The program computes the sum of $a \times x[i]$, $for\ i = 0, 1, ..., n-1$. Notice that we have a master and a worker program. The master program distributes the data

among several workers, which compute their partial sums. The master then collects the partial sums and adds them up.

The include file sum.h defines the messages used in the program. The names of the master and worker processes (called components in PVM), are also defined.

The include file sum.h is as follows:

```
/* define message types for simple PVM program */
#define MASTER 0
#define SCALAR 1
#define NEEDWORK 2
#define INT 3
#define NEEDSUM 4
#define SUM 5

/* master and worker components */
#define CMASTER "summaster"
#define CWORKER "sumworker"
```

The master program is as follows:

```
/*
PVM application - a simple example of an approach that might be used to
parallelize migration of different frequencies.The program computes the
sum of a*x[i], for i=0,1,...,n-1.  The computation is distributed over a
user-specified number of workers, which compute partial sums.  The main
(master) program adds up these partial sums and prints the result.

In the migration analogy, the scale factor a corresponds to velocity
information required by each worker.  The number x[i] corresponds to the
data for the i'th frequency, and n corresponds to the number of frequencies.
*/

#include <stdio.h>
#include "pvm.h"
#include "sum.h"

main (int argc, char **argv)
{
        int master,a=2,one=1,total=0,sum;
        int n,nw,iw;

        /* get parameters */
        if (argc!=3) {
                printf("Usage:  %s <# of values> <# of workers>\n",*argv);
                exit(-1);
        }
        n = atoi(*++argv);
        nw = atoi(*++argv);


        /* enroll in pvm */
        master = pvmEnroll(CMASTER);

        /* create nw instances of sumworker */
        for (iw=0; iw<nw; iw++) {
                if (pvmInitiate(CWORKER,NULL)<0) {
                        fprintf(stderr,"cannot initiate worker %d\n",iw);
                        pvmLeave();
                        exit(-1);
                }
        }
        fprintf(stderr,"%d workers started\n",nw);

        /* send master instance to all workers */
        pvmBeginMessage();
        pvmPutNInt(1,&master);
```

```
        pvmSend(MASTER,CWORKER,-1);

        /* send scale factor to all workers */
        pvmBeginMessage();
        pvmPutNInt(1,&a);
        pvmSend(SCALAR,CWORKER,-1);

        /* while integers remain to be summed */
        while (n>0) {

                /* get request for work */
                pvmReceive(NEEDWORK);
                pvmMessageInfo(NULL,NULL,NULL,&iw);

                /* send an integer to worker that requested work */
                pvmBeginMessage();
                pvmPutNInt(1,&one);
                pvmSend(INT,CWORKER,iw);

                /* decrement number of integers */
                n--;
        }

        /* request sums from workers */
        pvmBeginMessage();
        pvmSend(NEEDSUM,CWORKER,-1);

        /* while workers remain */
        while (nw>0) {

                /* get sum */
                pvmReceive(SUM);
                pvmMessageInfo(NULL,NULL,NULL,&iw);
                pvmGetNInt(1,&sum);
                /* fprintf(stderr,"worker %d sum=%d\n",iw,sum); */

                /* accumulate sums */
                total += sum;

                /* terminate worker */
                pvmTerminate(CWORKER,iw);
                nw--;
        }

        /* leave pvm */
        pvmLeave();
}
```

The worker program is as follows:

```
/* simple worker program */

#include <stdio.h>
#include "pvm.h"
#include "sum.h"

static int msgtypes[2]={INT,NEEDSUM};

main()
{
        int instance,master,msgtype,a,x,sum=0;

        /* enroll in pvm */
        instance = pvmEnroll(CWORKER);

        /* receive master instance number */
        pvmReceive(MASTER);
        pvmGetNInt(1,&master);

        /* receive scale factor */
        pvmReceive(SCALAR);
```

```
        pvmGetNInt(1,&a);

        /* loop while integers remain to be summed */
        do {
                /* request work from master */
                pvmBeginMessage();
                pvmSend(NEEDWORK,CMASTER,master);

                /* get message from master */
                msgtype = pvmNReceive(2,msgtypes);

                /* if integer received */
                if (msgtype==INT) {

                        /* accumulate in sum */
                        pvmGetNInt(1,&x);
                        sum += a*x;

                /* else if sum requested */
                } else if (msgtype==NEEDSUM) {

                        /* send sum */
                        pvmBeginMessage();
                        pvmPutNInt(1,&sum);
                        pvmSend(SUM,CMASTER,master);
                }

        } while (msgtype!=NEEDSUM);

        /* leave pvm */
        pvmLeave();
}
```

CWP-114

Seismic Wave Propagation in Thinly-Layered Media with Steep Reflectors

H. Lydia Deng

Excerpt from

— Master of Science Thesis —

Center for Wave Phenomena
Colorado School of Mines
Golden, Colorado 80401
(303) 273-3557

Seismic wave propagation in thinly layered media with steep reflectors

H. Lydia Deng

ABSTRACT

Seismic waves reflected from steep interfaces beneath layered sediments spend a significant amount of time travelling more or less horizontally. Therefore, accurate imaging of steep geologic structure requires knowledge of the behavior of these horizontally propagating waves. In particular, the role of evanescence and tunneling of seismic waves propagating in thinly-layered media must be understood.

For thinly-layered media, reflected seismic waves show frequency-dependent amplitude and phase behavior that varies with reflection dip. This dip-dependent attenuation and dispersion is not well understood and is ignored in conventional seismic processing.

Waves propagating vertically in a sequence of thin layers are known generally to lose high frequencies by *stratigraphic filtering*. However, waves reflected from steep reflectors in a thinly-layered medium are additionally attenuated and dispersed by the less well-known *evanescent filtering*. Seismic waves become evanescent when they arrive at a high-velocity layer at post-critical angle. When the high-velocity layer is thin relative to a seismic wavelength, a significant amount of low-frequency energy *tunnels* through to an adjacent low-velocity layer. Compounded loss of evanescent energy through high-velocity layers yields attenuation and dispersion of seismic waves reflected from steep reflectors.

An improved understanding of this filtering action may help us to improve seismic processing techniques used to image steep geologic structures.

INTRODUCTION

Only recently, seismologists have begun to directly image steep geologic structures, such as overhanging salt domes intruding into a sequence of thin sedimentary layers

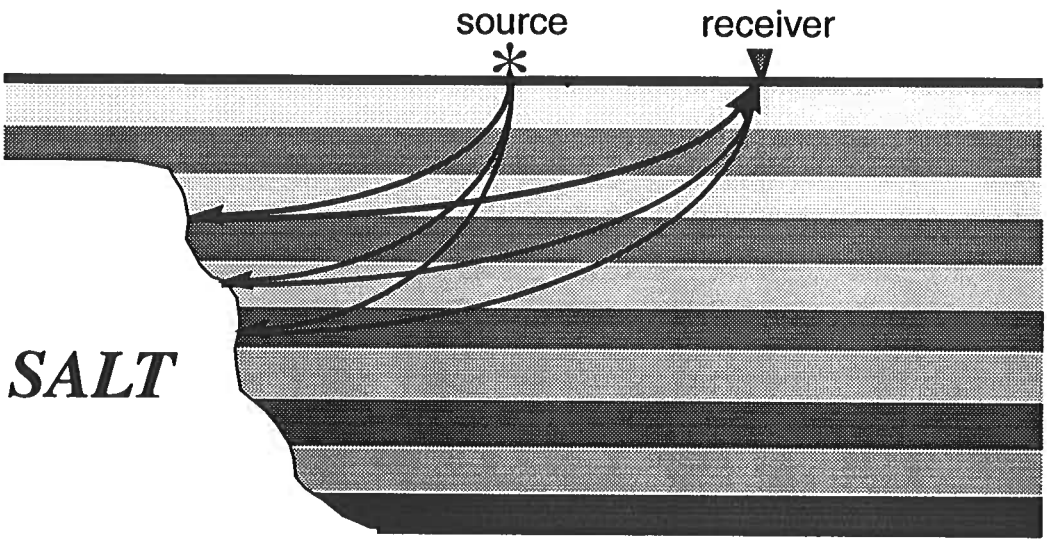

FIG. 1. Seismic waves reflected from a steep interface spend a significant amount of time traveling more or less horizontally in a layered medium with a trend of velocity with depth.

in the Gulf of Mexico. While reflection seismic data can give a good indication of the presence of salt, accurate imaging of the flanks of salt bodies requires both a good understanding of seismic waves in thinly-layered media and adequate processing techniques.

Studies of acoustic well logs show that a major portion of the stratigraphic column of the Gulf of Mexico is made up of a somewhat binary sequence of alternating layers of sand and shale (e.g., Velzeboer, 1981). As velocities in such media usually tend to increase with depth, such a medium is referred as an *increasing-trend, velocity-layered* medium in this paper. It is also common to find massive salt structures, such as is depicted in Figure 1, in that area. In an increasing-trend, velocity-layered medium, seismic rays taking off from the Earth's surface exhibit generally increasing propagation angle (i.e. angles as measured with respect to the vertical) with increasing depth. At some depth, some of the rays travel horizontally along sedimentary layers before being reflected from an overhanging interface.

Observation of synthetic seismograms shows that seismic waves traveling in thinly-layered media are attenuated and dispersed differently for different interface dips. This dip-dependent wavelet shaping may be largely related to the difference of propagation angles of seismic waves traveling in a sequence of sedimentary layers. Figure 2 shows a snapshot of waves propagating in a velocity-alternating medium; this synthetic seismogram is generated by the frequency-wavenumber domain finite-difference

(FKFD) algorithm described in Appendix A. In figure 2, we can see that waves are attenuated differently for different angles of propagation in such a velocity-alternating medium.

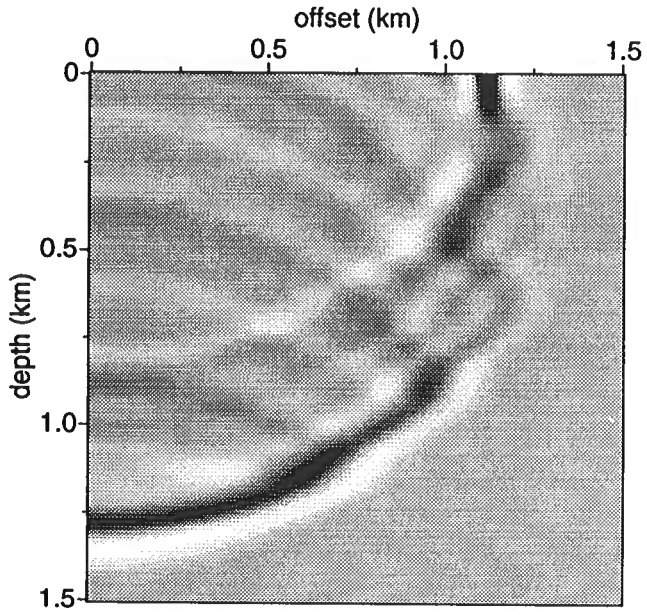

FIG. 2. A snapshot of seismic waves propagating from a 2-D point source at the origin. The velocity of the medium alternates between 1.6 km/s and 2.26 km/s; the bed thickness of the medium is 120 m.

Stratigraphic filtering (e.g., O'Doherty and Anstey, 1971; Banik and Shuey, 1985a; Banik, et al., 1985b; White, et al., 1990), caused by destructive interference of short-period multiples, is well known to attenuate high frequencies of the seismic signal. Waves traveling in a sequence of thin, sedimentary layers may also lose their high frequencies through *evanescent filtering*, because only the low-frequency energy *tunnels* through the high-velocity layers (e.g., Fuchs and Schulz, 1976). Attenuation of seismic waves reflected from steep interfaces in thinly-layered media likely can be attributed to a combination of stratigraphic and evanescent filtering, both of which vary with propagation direction. This dip dependence is typically ignored in seismic data processing. A good understanding of the behavior of horizontal traveling waves may thus help us to improve our processing of seismic reflections from steep interfaces.

Reflection synthetic seismograms used in this study are computed by the FKFD scheme (Korn, 1988) followed by the Born approximation (e.g., Bleistein and Gray, 1985); the implementation is described in Appendix A.

ATTENUATION OF SEISMIC WAVES IN THIN LAYERS

Amplitudes of seismic waves are altered in a frequency-dependent way while they propagate. For example, it is well known that seismic waves lose their high frequencies because some of the high-frequency energy is absorbed by the medium due to inelasticity. Therefore, seismic data lose temporal resolution at late recording times. This frequency-dependent attenuation is quantitatively described by the "Q" of the medium. The change in the frequency content of seismic data with increase of recording time is a form of *non-stationarity.*

Observations of seismic data indicate that attenuation of seismic waves can be caused by other mechanisms, as well. Figure 3 shows reflections from a horizontal interface beneath two different sedimentary media, one with a linear velocity variation without layering, and the other an increasing-trend, velocity-layered medium. Figure 3a shows the reflection for the linear-velocity medium. The layered medium, corresponding to Figure 3b, has a bed thickness smaller than the dominant wavelength of the seismic signal. The reflection wavelet for the layered medium is broader than that for the medium without layering. Broadening of the wavelet shows that some of the high-frequency energy is lost through multiple reflection as waves travel in the thinly-layered medium. This phenomenon can be seen clearly in Figure 3c, which shows the frequency spectra of these two reflections.

O'Doherty and Anstey (1971) observed that the high-frequency content of seismic waves appears to be attenuated by the superposition of short-period multiples. When seismic waves travel through a sequence of sedimentary layers, a series of multiples is produced at velocity discontinuities. These multiples cannot be distinguished individually if thicknesses of the layers are smaller than the seismic wavelength. Seismic wavelets, which are the superpositions of both primaries and multiples, are thereby broadened in time. As a result of these interferences, seismic waves lose their high frequencies as they travel through a sequence of thin layers. This phenomenon is known as *stratigraphic filtering.* Though this effect on seismic signals is similar to that caused by inelasticity, the stratigraphic-filtering effect is due to destructive interference, not to absorption of seismic energy.

Following O'Doherty and Anstey (1971), much progress has been made toward understanding the attenuation behavior of seismic waves due to thin layers. Banik and Shuey (1985a) derived formulas to describe quantitatively the apparent attenuation and time delay caused by stratigraphic filtering in a statistical sense. In addition, they studied this filtering for sedimentary sequences typically logged in oil and gas wells (Banik et al., 1985b).

However, their work was based on an assumption that seismic waves propagate vertically through sedimentary layers (i.e., perpendicular to the reflecting boundaries). Seismic waves reflected from a steep interface spend a significant amount of time traveling more or less horizontally. These waves, traveling at large incident angles may be attenuated and dispersed by another, not well-known reason. Successful

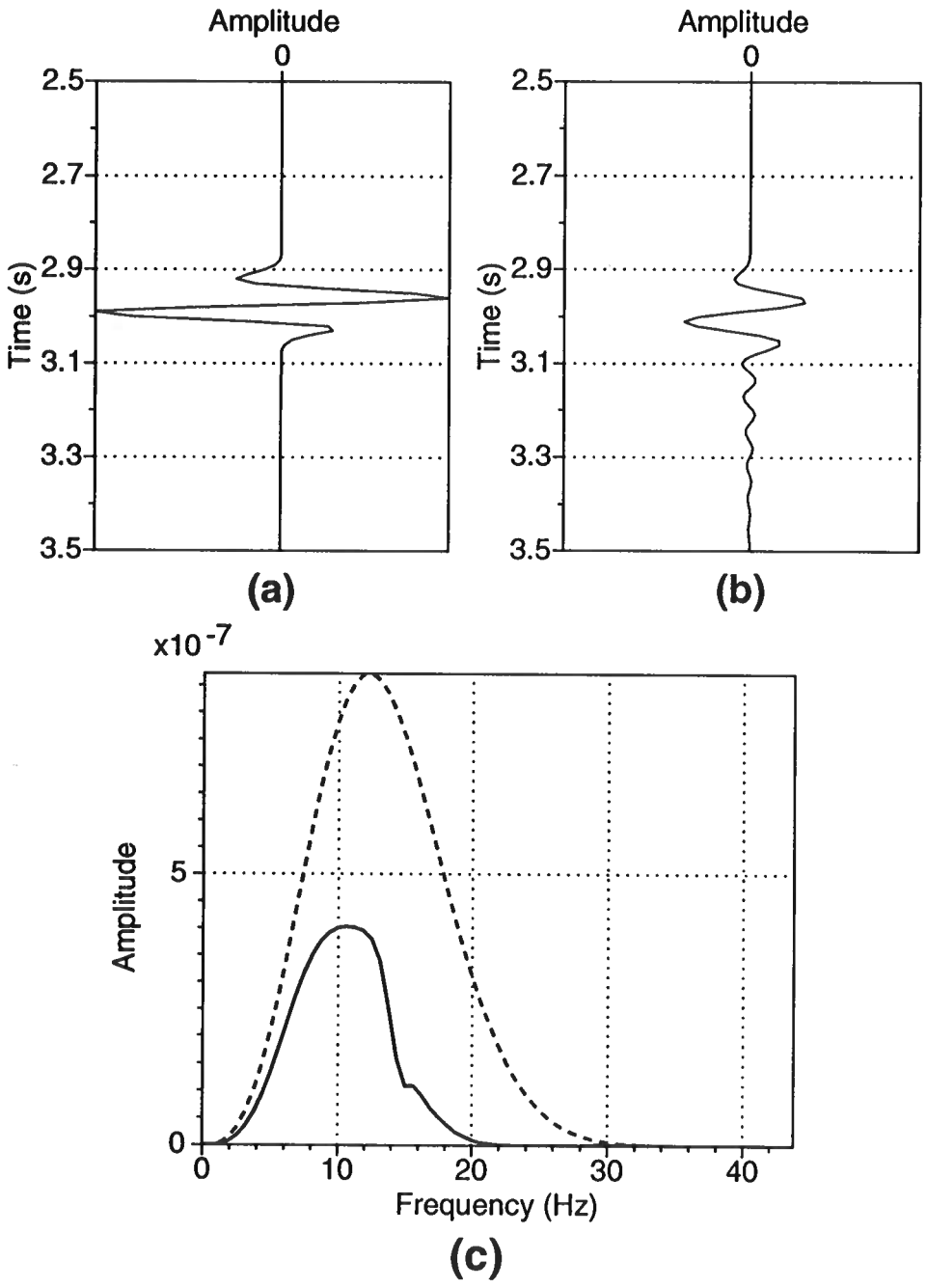

FIG. 3. Zero-offset reflections from a horizontal interface beneath (a) a linear-velocity medium ($v(z) = 1.6 + 0.5z$ (km/s)) and (b) an increasing-trend, velocity-layered medium where the velocity has a linear trend of $1.6 + 0.5z$ (km/s) plus a sinusoidal variation with a bed thickness 60 m. The dominant frequency of the source signal is 10 Hz. (c) shows the frequency spectra of these seismic traces, the dotted line corresponds to the trace in (a) and the solid line corresponds to the trace in (b).

imaging of steep geologic subsurfaces likely requires that the behavior of horizontally traveling waves be understood.

Figure 4 shows reflections from a vertical interface in two different sedimentary media, a linear-velocity medium without layering (Figure 4a) and an increasing-trend, velocity-layered medium (Figure 4b) with a bed thickness comparable to the dominant wavelength of the seismic signal. As was the case for vertical incidence, the reflection wavelet for the layered-medium arrives at the same time as that for the linear velocity medium, but is broader. In addition, the wavelet for the layered medium has lower amplitude than that for the linear-velocity medium. The frequency spectra shown in Figure 4c highlight differences in these two reflections. High frequencies in the waves that travels nearly horizontally in the layered medium are largely attenuated - more so than are those in vertically propagating waves.

As observed in Figures 3 and 4, seismic waves reflected from horizontal and vertical interfaces are attenuated and dispersed differently. Because of ray bending, those waves reflected from vertical interfaces spend more time travelling in each layer and travel through fewer layers than do those reflected from horizontal interfaces. Therefore, the stratigraphic filtering of waves reflected from steep interfaces will be different, and perhaps less severe. Therefore, the severe loss of high frequencies observed for waves reflected from vertical interfaces implies that there must be another mechanism that contributes to the attenuation of seismic waves that propagate with large, non-vertical angles.

EVANESCENT FILTERING

When seismic waves arrive at a high-velocity layer with their incident angle larger than the critical angle, the propagating waves become evanescent. Amplitudes of these evanescent waves decay exponentially away from the layer boundary, with slower amplitude decay with distance for long-wavelength waves than for short-wavelength. When evanescent waves arrive at the boundary of a low-velocity layer before their amplitudes have exponentially decayed to negligible values within the high-velocity layer, the transmitted waves become propagating again. These long wavelength waves are known as *tunnel* waves; they have *tunnelled* through the thin, high-velocity layer.

Extended travel as evanescent waves attenuates the high-frequency content of seismic waves that travel through a sequence of alternating layers with large propagation angles. Figure 5 schematically illustrates the frequency-dependence of this *evanescent filtering*, a low-pass filtering of seismic waves that are evanescent over a portion of their travel paths. The increasing angle of ray paths with depth increases the amount of evanescent energy with a faster decaying rate. Therefore, it is the propagation angle and the thickness of high-velocity layers at the bottom of the travel path of waves, where has the most significant evanescence, largely determine the amount of energy survives the evanescent filtering.

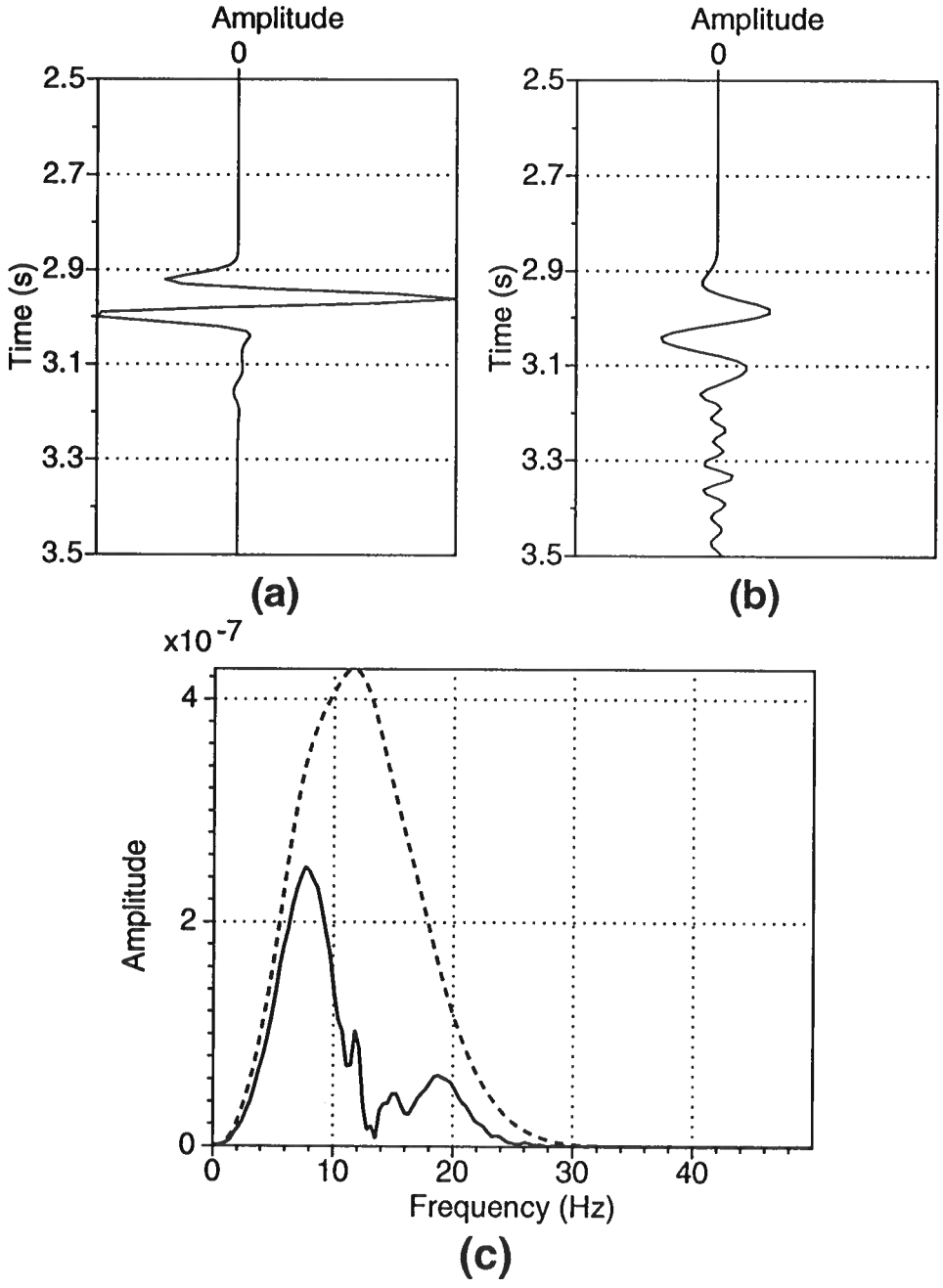

FIG. 4. Zero-offset reflections from a vertical interface. (a) is the reflection for a linear-velocity medium. The velocity function is $v(z) = 1.6 + 0.5z$ (km/s). (b) is the reflection for an increasing-trend layered-velocity medium. The velocity function has a linear trend of $1.6 + 0.5z$ (km/s) plus a sinusoidal variation with a bed thickness 150 m. The dominant frequency of the source signal is 10 Hz. The horizontal distance from the source to the vertical interface is 2.5 km. (c) shows the frequency spectra of these seismic traces, the dotted line corresponds to the trace in (a) and the solid line corresponds to the trace in (b).

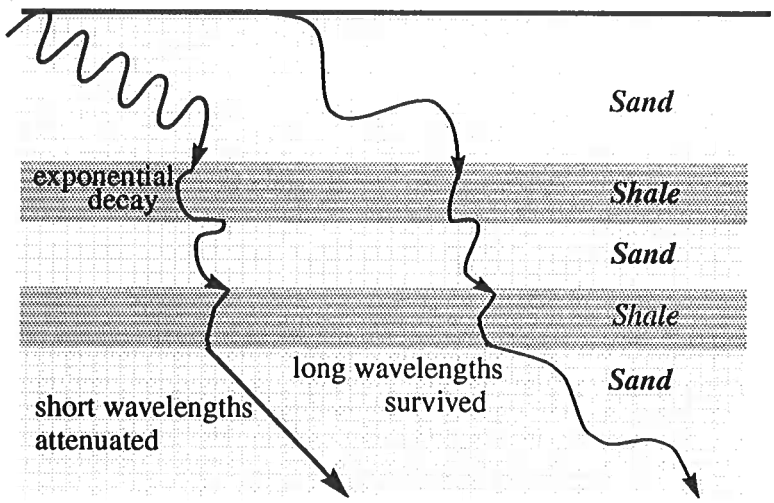

FIG. 5. Seismic waves become evanescent when they reach the boundary of a high-velocity layer beyond critical angle. In the high-velocity layer, the amplitudes of high-frequency components decay faster than do those of low-frequency components. Some of the low frequencies tunnel through the high-velocity layer while high frequencies do not.

REFLECTIONS FROM VERTICAL INTERFACES

Due to evanescent filtering, seismic waves reflected from a vertical interface embedded in a layered medium are attenuated and dispersed. As zero-offset reflections end at a vertical reflector with a 90-degree propagation angle, the amount of energy loss due to evanescent filtering is related to the thickness of sedimentary layers and the velocity contrast between low- and high-velocity media. Keeping the velocity contrast of the sedimentary layers a constant, changes in the bed thickness of the sediments greatly alters the evanescent filtering of seismic waves.

Figure 6 shows frequency-dependent behavior of waves reflected from a vertical interface in layered media with different bed thicknesses. When the sedimentary layers are thick relative to the wavelength of seismic waves, repeated evanescent decay greatly attenuates the high-frequency energy. The low resolution and weak amplitudes of the waves in Figure 6a shows that only very low frequencies survive the evanescent filtering in the medium where velocity varies slowly with respect to the seismic wavelength. When the bed thickness of the sediments decreases, more and more energy tunnels through the thin, high-velocity layers, especially at the bottom of the travel path of waves. Figure 6 illustrates that resolution of the seismograms in-

creases with a decrease in bed thickness of the sediments. Figure 6d has the sharpest reflections of all four seismograms. When the bed thickness of the layered medium is smaller than the minimum wavelength of the seismic signal, most of the seismic energy survives the repeated thin high- and low-velocity alternating layers.

Figure 7 shows frequency spectra of reflections from vertical interfaces, which verify the observations from Figure 6 that frequency-dependent attenuation is more severe for larger ratio of bed thicknesses to wavelength . When bed thicknesses are comparable to the seismic wavelength, only low frequencies can survive the evanescent filtering. As layers of sedimentary media become thinner, progressively more high-frequency energy survives the thin, high-velocity layers. If the bed thickness of the medium is smaller than the minimum wavelength of the seismic signal, the shape of the frequency spectrum is similar to that for a medium without velocity-layering; seismic waves tunnel through the thin, high-velocity layers for all frequencies.

DIP-DEPENDENT ATTENUATION

Both stratigraphic filtering and evanescent filtering cause high-frequency loss of seismic waves reflected from a geologic structure beneath a sequence of sedimentary layers. The amount of high-frequency loss is determined to both the bed thickness of the sediments and the dip of the interface.

Figure 8 illustrates the geometry of zero-offset waves reflected from interfaces with different dips. The high-frequency loss of waves reflected from horizontal interfaces is caused by only stratigraphic filtering because no evanescent energy is produced. The increase of reflector dip weakens the stratigraphic filtering; evanescent filtering cannot attribute to the loss of seismic energy until the reflector is steep enough to produce evanescent energy. The high-frequency loss is mainly attributed to evanescent filtering for waves reflected from vertical interfaces because of their large propagation angles. Therefore, for intermediate dips between 0 and 90 degrees, reflections have their high frequencies attenuated by the possible combination of the two filtering effects depending on the bed thickness of the sediments and the dip of the interface.

Figure 9 shows the scaled frequency spectra of synthetic seismic reflections from vertical and horizontal interfaces embedded in an increasing-trend, velocity-layered medium. The bed thickness is 150 m, comparable to a typical wavelength of the seismic signal. Waves reflected from the vertical interface are more bandlimited than are those reflected from the horizontal interface. This observation demonstrates the strong evanescent filtering of seismic signals when the bed thickness of the medium is comparable to the spatial wavelength of the seismic signal, while stratigraphic filtering is weak in this particular medium.

As the sedimentary layers of the medium get thinner, more high-frequency energy tunnels through high-velocity layers. However, shortening of the time-delay of short-period multiples increases the likelihood of losing high frequencies due to stratigraphic filtering. Therefore, the decrease in the bed thickness of the sediments

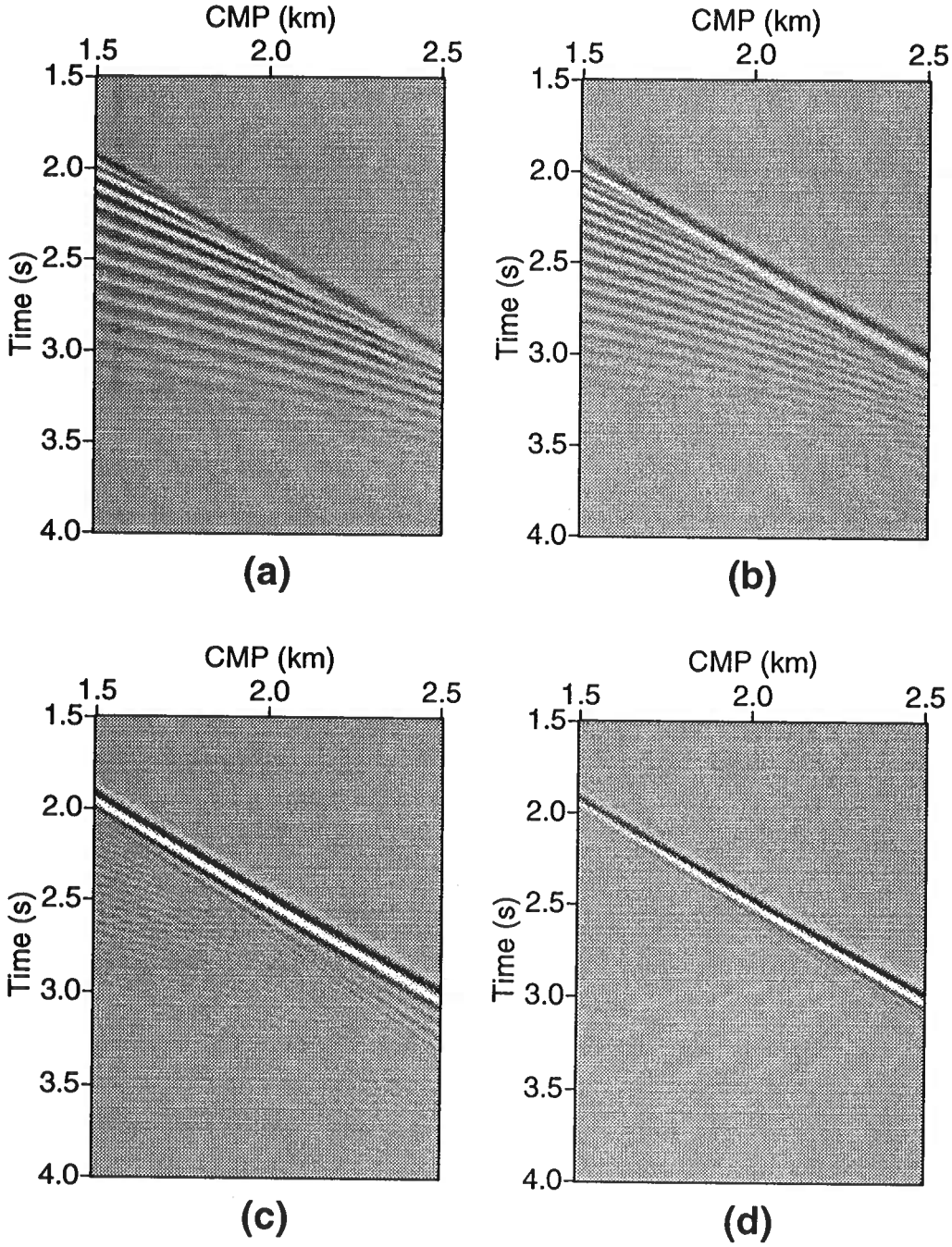

FIG. 6. Zero-offset reflections from a vertical interface in four layered media. The velocity in each medium has a linear trend of $1.6 + 0.5z$ (km/s) and a sinusoidal variation with bed thickness (a) 250 m, (b) 150 m, (c) 100 m and (d) 60 m, respectively. The dominant frequency of the source signal is 10 Hz.

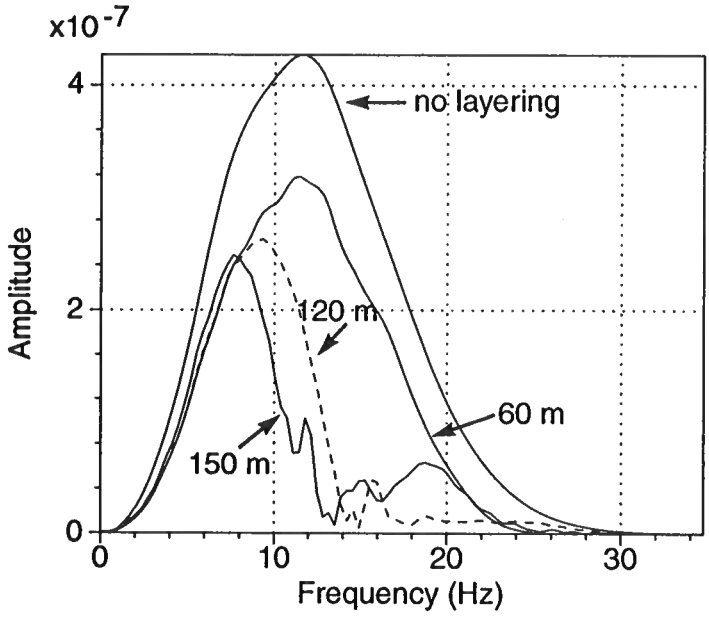

FIG. 7. Frequency spectra of the reflections from a vertical interface in four different layered media. The dominant frequency of the source signal is 10 Hz. The velocity in each of the media has a linearly increasing trend of $1.6 + 0.5z$ (km/s). One medium has no velocity-layering. The bed thicknesses of the other three media are 150 m, 120 m and 60 m, respectively.

decreases the high-frequency loss due to evanescent filtering but increases the loss due to stratigraphic filtering.

Figure 10 shows the scaled frequency spectra of waves reflected from different dipping interfaces with the same travel time, where the ratio of changes of the medium to the typical wavelength is less than 0.5. I use the frequency $f_{0.6}$, where the corresponding amplitude drops to 60% of the peak amplitude, to measure the frequency content of the reflection. The spectrum corresponding to the vertical interface contains more high frequencies than that for the horizontal interface, i.e. $f_{0.6}$ for the vertical interface is higher than $f_{0.6}$ for the horizontal interface. The $f_{0.6}$ for the 45° interface is higher than does that for the horizontal interface, and lower than that for the vertical interface. This dip-dependent phenomenon tells us that the high-frequency loss of waves reflected from a dipping interface is dominated by stratigraphic filtering if the thickness of layers in the medium is much smaller than the seismic wavelength.

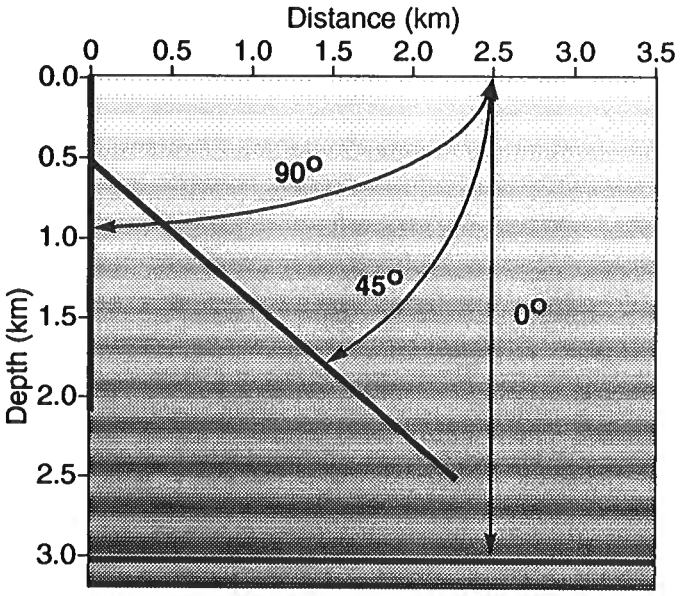

FIG. 8. Geometry of zero-offset reflections from interfaces with different dips. In a medium with a sequence of sedimentary layers, reflections from a steeper interface spend more time travelling in each layer.

CONCLUSION

Velocity layering may cause two possible forms of low-pass filtering on reflection seismic waves: stratigraphic filtering and evanescent filtering. The action of these different filters depends on the dip of the reflecting interface as well as the bed thickness. Figure 11 summarizes the general dependence of the action of these two filters on reflector dip and bed thickness.

The frequency content of waves reflected from a dipping interface beneath a layered medium depends on the combined action of stratigraphic filtering and evanescent filtering. When the layers are thick relative to the seismic wavelength, the high-frequency loss is dominated by evanescent filtering; high frequencies are more severely attenuated with increase of reflector dip. However, when the layers are thin relative to

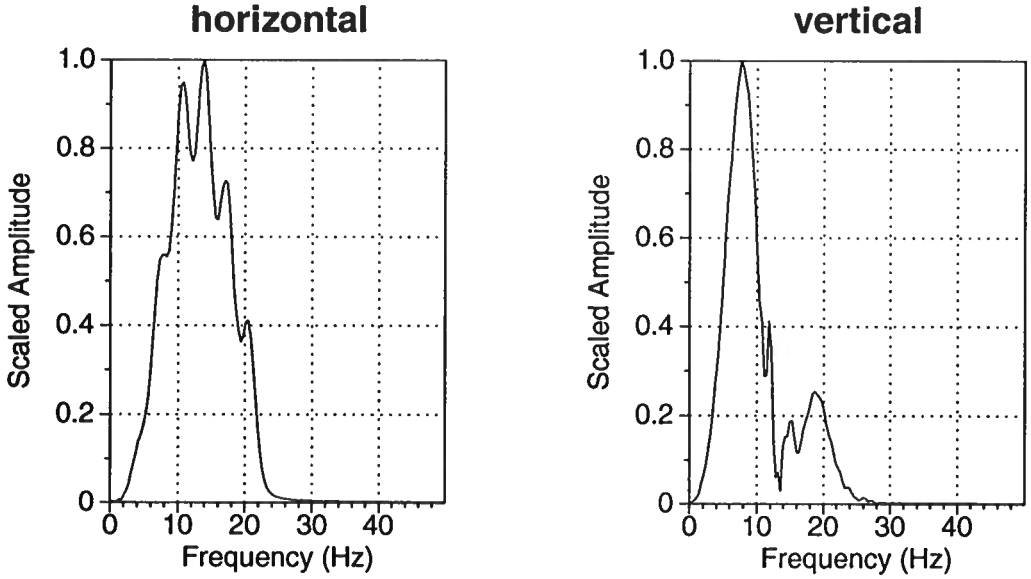

FIG. 9. Scaled frequency spectra of the reflections from a horizontal (left) and vertical (right) interface embedded in a sequence of thin layers. Both reflections have the same travel time. The velocity of the medium has a linear trend of $1.6+0.5\,z$ (km/s) and a sinusoidal variation with a bed thickness of 150 m. The source signal has a dominant frequency of 10 Hz.

the seismic wavelength, the high-frequency loss is dominated by stratigraphic filtering; that filtering becomes less severe with increase of reflector dip.

The research in this paper is based on a qualitative observation and analysis of the dip-dependent attenuation of synthetic seismograms. Reflections recorded in these seismograms correspond to increasing-trend, velocity-layered media. For a further study of this behavior, stochastic-velocity background media may need to be used for a quantitative understanding of evanescent filtering.

The loss of high-frequency signal in seismic waves reflected from geologic structures is important. Improved imaging of structures may require a dip-dependent deconvolution to regain those high frequencies.

ACKNOWLEDGEMENT

I am very grateful to Dr. Dave Hale who proposed this project, initiated the modeling code, and gave his direct and enlightened advice throughout the research. Dr. Dave Hale and Dr. Ken Larner provided many helpful comments and gave much of their time in the proofreading and editing of my writing, which is especially appreciated.

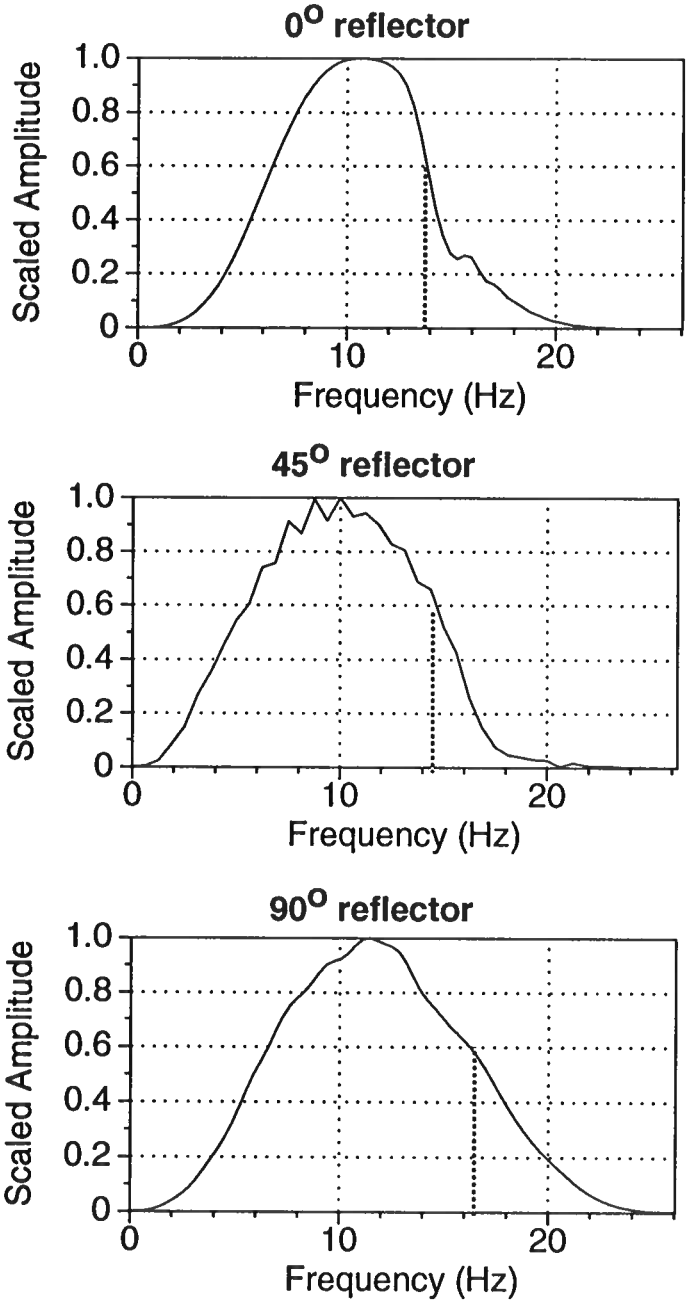

FIG. 10. Dip-dependent frequency distribution of zero-offset reflections with the same travel time. The velocity of the sedimentary medium has a linearly increasing trend of $1.6 + 0.5z$ (km/s), and a sinusoidal variation with a bed thickness of 60 m. The dominant frequency of source signal is 10 Hz. The dotted lines show frequencies which corresponding to 60% of peak amplitudes.

filtering		stratigraphic	evanescent
REFLECTOR	steep	weak	strong
	less steep	strong	weak (or none)
LAYERS	thick	weak	strong
	thin	strong	weak

FIG. 11. The dependence of stratigraphic filtering and evanescent filtering on reflector dip and bed thickness.

The financial support of this project was provided by Department of Energy of the United States. The project was also supported by the Consortium Project of the Center for Wave Phenomena, Colorado School of Mines. The computing facilities were provided by the Center for Geoscience Computing, Colorado School of Mines.

REFERENCES

Banik, I. L., Shuey, R.T., 1985a, Stratigraphic filtering, Part I: Derivation of the O'Doherty-Anstey formula: Geophysics **50**, 2768–2774.

Banik, I. L., Resnick, J.R. Shuey, R.T., 1985b, Stratigraphic filtering, Part II: Model spectra: Geophysics **50**, 2768–2774.

Bleistein, 1984, Mathematical methods for wave phenomena: Academic Press Inc.

Bleistein, N., Gray, S.H., 1985, An extension of the Born inversion method to a depth dependent reference profile: Geophysical Prospecting, **33** 999–1022.

Deng, H. L., 1992, Seismic wave propagation in thinly layered media with steep reflectors: Master's thesis, Colorado School of Mines; also published as **CWP-114**.

Fuchs, K., Schulz, K., 1976, Tunneling of low-frequency waves through the subcrustal lithosphere: J. Geophysics **42**, 175–190.

Korn, M., 1987, Computation of a wavefields in vertically inhomogeneous media by a frequency domain finite-difference method and application to wave propagation in earth models with random velocity and density perturbations: Geophysics J.R.astr.Soc. **88**, 345–377.

O'Doherty, R. F., and Anstey, N. A., 1971, Reflections on amplitudes: Geophys. Prosp., **19**, 430–458.

White, B., Sheng, P., Nair, B., 1990, Localization and backscattering spectrum of seismic waves in stratified lithology: Geophysics **55**, 1158–1165.

Velzeboer, C.J., 1981, The theoretical seismic reflection response of sedimentary sequences: Geophysics **46**, 843–853.

APPENDIX A: MODELING OF SEISMIC WAVES IN THIN LAYERS

To reduce the complexity of dealing with both steep interfaces and thinly-layered sedimentary media, the modeling algorithm used to generate reflection synthetic seismograms in this research is performed in two steps,

1. Calculate the Green function for a sequence of thin sedimentary layers, ignoring the existence of geologic structure. A *frequency-wavenumber finite-difference*(FKFD) scheme (Korn, 1988) is used to compute this Green function.

2. Using the Green function, compute reflections from dipping interfaces via the *Born approximation* (Bleistein, 1985).

Waves propagating in thin layers - Green's function

Due to high-frequency assumptions, conventional methods based on the WKBJ approximation fail to predict even the first arrival times for waves traveling in *thinly* layered media. Commonly used reflectivity methods become prohibitively expensive for media where the velocity is continuously changing, or media that contain many thin layers. The basic assumption for reflectivity methods is that the medium is made up of homogeneous layers, and interfaces of each layers must be dealt with individually. The FKFD algorithm introduced by Korn (1988) has no high-frequency approximation, and the seismic wavefield is computed for all depths simultaneously.

The FKFD algorithm is a combination of integral transformations and a finite-difference technique. The wavefield for each frequency and wavenumber, the *frequency-wavenumber response* of the medium, is calculated by a one-dimensional finite-difference scheme. The summation of these frequency-wavenumber responses yields the seismic wavefield in the medium.

The acoustic wave equation may be reduced to a second-order ordinary differential equation when the wavefield is decomposed for each frequency (ω) and wavenumber

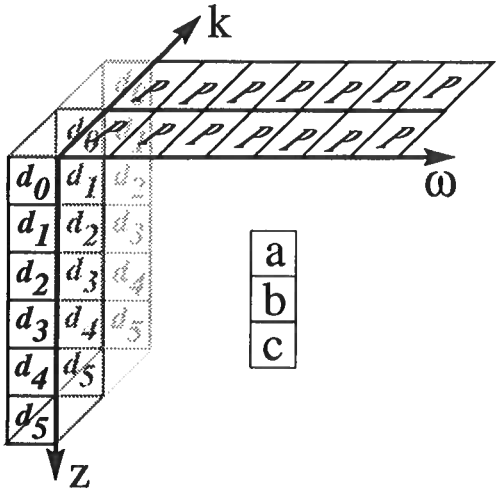

FIG. A-1. The finite-difference mesh used in the modeling. The wavefield is computed by finite-differencing for each frequency and wavenumber.

(k).

$$\rho\frac{d}{dz}\frac{1}{\rho}\frac{d}{dz}P+\left(\frac{\omega^2}{v^2}-k^2\right)P=-\frac{\omega^2}{v^2}\delta(z-z_s)S(\omega), \tag{A-1}$$

where $\rho(z)$ is bulk density, z is depth, $v(z)$ is the medium velocity, $S(\omega)$ is the Fourier transformed signature of a source located at depth z_s, and $P(\omega,k,z)$ is the pressure field. Equation (A-1) may be solved by a second-order implicit finite-difference scheme (Deng, 1992). Figure A-1 shows the finite-difference "star" used to calculate $P(\omega,k,z)$ for a single frequency and wavenumber. For each frequency and wavenumber, the finite-differencing is performed for all depths by solving a tri-diagonal linear system (Deng, 1992).

The seismic wavefield is obtained by integrating frequency-wavenumber responses computed by the finite-differencing. For a line-source, or *a two-dimensional (2-D) point source*, the integration is a 2-D inverse Fourier transform of the frequency-wavenumber responses,

$$p(t,r,z)=\frac{1}{4\pi^2}\int_{-\infty}^{\infty}d\omega e^{-i\omega t}\int_{-\infty}^{\infty}dke^{ikr}P(\omega,k,z), \tag{A-2}$$

where r is the horizontal distance from the source, $k=k_x$ is the horizontal wavenumber, and $p(t,r,z)$ is the wavefield corresponding to a 2-D point source.

To satisfy the condition of causality, the integration over frequencies in equation (A-2) is taken above the singularities on the real axis,

$$\omega=\nu+i\epsilon,\quad \text{where } \epsilon>0. \tag{A-3}$$

The frequency-wavenumber response $P(\omega, k, z)$ is thus computed for complex frequencies ω. As a result of using complex frequencies, the wavefield is exponentially attenuated by an amplitude factor $e^{-\epsilon t}$. This attenuation avoids the possible alias of seismic traces, wherein signals of late times appear at early times on a seismogram. $P(\omega, k, z)$ is obtained by solving a complex-coefficient, tri-diagonal linear system (Deng, 1992). Therefore, the wavefield corresponding to a 2-D point source is represented by

$$\begin{aligned} p(t,r,z) &= \frac{1}{4\pi^2}\int_{-\infty}^{\infty} d\omega e^{-i\omega t}\int_{-\infty}^{\infty} dk\, e^{ikr}P(\omega,k,z) \\ &= \frac{1}{4\pi^2}e^{\epsilon t}\int_{-\infty}^{\infty} d\nu e^{-i\nu t}\int_{-\infty}^{\infty} dk\, e^{ikr}P(\omega,k,z). \end{aligned} \tag{A-4}$$

As shown in equation (A-4), the frequency integral is performed by a Fourier transform followed by an amplitude correction that compensates for the use of complex ω by an exponential factor $e^{\epsilon t}$ in the time domain. Hence, use of a large imaginary part of frequency can result in boosted noises at late times. An imaginary part $\epsilon = log_e(100)/T$, where T is the maximum recording time, keeps the amplitude factor to be at most 100 at the latest time; this choice of ϵ is used in this research.

Reflection from dipping interfaces

The reflected wavefield is often referred to as the *scattered wavefield*, while the wavefield corresponding to the Green function is the *incident wavefield* (e.g., Bleistein, 1984). Under the assumption of small reflection coefficients, a first-order Born approximation (e.g., Bleistein and Gray, 1985) gives zero-offset reflections from a dipping interface using the incident wavefield.

For our problem, the velocity of the sedimentary medium is taken as the *background velocity*, and the presence of an interface perturbs the velocity function. As a result of this perturbation, the real velocity of the model, which is made up of a sequence of sedimentary layers and the interface, may vary laterally as well as vertically. If the background velocity function is $c(z)$ and the real velocity function of the model is $v(x,z)$, the perturbation $\alpha(x,z)$ due to the interface is defined by the expression

$$\frac{1}{v^2(x,z)} = \frac{1}{c^2(z)}\left[1+\alpha(x,z)\right]. \tag{A-5}$$

The wavefield for a single frequency, $P(\omega, x, z)$, is the solution of the 2-D Helmholtz equation

$$\rho\frac{\partial}{\partial z}\left(\frac{1}{\rho}\frac{\partial}{\partial z}P\right)+\frac{\partial^2}{\partial x^2}P+\frac{\omega^2}{v^2(x,z)}P=-\frac{\omega^2}{v^2(x_s,z_s)}\delta(x-x_s)\delta(z-z_s)S(\omega), \tag{A-6}$$

where $S(\omega)$ is the Fourier transformed signature of a source located at (x_s, z_s).

For an interface which has a perturbation $\alpha < 5\%$, the zero-offset reflection field $P_s(\omega, x, z)$ can be obtained by an area integral (Bleistein and Gray, 1985),

$$P_s(\omega,x_s,z_s)=\omega^2 S(\omega)\int_0^{\infty} d\eta\frac{1}{c^2(\eta)}\int_{-\infty}^{\infty} d\xi\alpha(\xi,\eta)G^2(\omega,|\xi-x_s|,|\eta-z_s|). \tag{A-7}$$

In this research, I have assumed that the perturbation exists only on the interface,

$$\alpha(x,z) = \tilde{\alpha}(x,z)\delta(x-x_r)\delta(z-z_r),$$

where (x_r, z_r) lies on the interface. Under this assumption, the double integral in equation (A-7) is reduced to a line integral along the interface L,

$$P_s(\omega, x_s, z_s) = \omega^2 S(\omega) \int_L dl(\xi,\eta)\, \frac{1}{c^2(\eta)}\, \tilde{\alpha}(\xi,\eta)\, G^2(\omega, |\xi - x_s|, |\eta - z_s|), \qquad \text{(A-8)}$$

where $l(\xi,\eta)$ is the arc length of the interface at (ξ,η). This delta-function perturbation assumption reduces the computation from the area integral to a line integral.

However, the use of a delta function introduces a spatial differentiation to wavelets because of the reduction from an areal integration to a line integration. Since the purpose of this research is to study the behavior of seismic waves caused by velocity layering, and as the same differentiation will occur with or without the layering, this differentiation of wavelets does not affect the result of this research.

A Small Dip, Small Offset Representation of the DMO Operator in a Medium with a Constant Velocity Gradient

Michel Dietrich

Center for Wave Phenomena
Colorado School of Mines
Golden, Colorado 80401
(303) 273-3557

A small dip, small offset representation of the DMO operator in a medium with a constant velocity gradient

Michel Dietrich

ABSTRACT

A small dip, small offset approximation of the dip moveout (DMO) operator is derived in a medium with a constant velocity gradient in the vertical direction. The DMO impulse response is defined by four parameters: the vertical time t_n, the half source-receiver offset h, and two "squeeze" functions $\gamma_x(t_n)$ and $\gamma_y(t_n)$ which are directly related to the central curvature of the DMO operator in the inline and crossline directions.

The expressions obtained show that the DMO operator depends only weakly on the velocity function considered: for a fixed value t_n, the squeeze factors γ_x and γ_y depend solely on the gradient k and are notably independent of the reference velocity V_0. Furthermore, the γ_x factor in the inline direction shows only little sensitivity to variations of the velocity gradient k. However, the γ_y factor in the crossline direction is directly proportional to k.

It is also shown that the approximate representation of the DMO operator remains accurate for large source-receiver offsets. The relative error in curvature in the inline direction is usually less than 10%, even for the largest offsets used in conventional seismic surveys. The curvature of the DMO operator in the crossline direction can be exactly computed for any offset h.

INTRODUCTION

Dip moveout is a simple and cost-effective seismic processing which is usually applied to the data by assuming that the seismic wave velocity is constant. DMO processing in inhomogeneous media is more difficult to implement, because the DMO operator is then a two-dimensional, complex-shaped function of the zero-offset traveltime. In a recent paper (Dietrich and Cohen, 1992, hereafter referred to as Paper I), we derived an *exact* formulation of the DMO operator in a medium characterized by a constant velocity gradient in the vertical direction. Our analytical formulation gives a complete solution of the problem, but does not permit to study (analytically) the overall behaviour and properties of the DMO impulse response in a simple way. In particular, it is often desirable (and instructive) to represent a complex seismic processing operator by a truncated power series to obtain its simplest possible expression. The complexity of the parametric definition of the DMO operator given in Paper I prevents such an analysis.

In this paper, I derive an approximate representation of the DMO operator for a linear velocity-depth function, which is valid for small source-receiver offsets and small dips. The DMO impulse response is basically defined by the curvature at the origin (in two orthogonal directions), and by the vertical time corresponding to a horizontal reflector. The expressions of the curvature are obtained from the normal moveout velocity in the inline and crossline directions.

The central curvature in the inline direction is obtained as a particular case of the general formula derived by Hale (1988) for a vertically inhomogeneous media. The curvature in the crossline direction requires more calculations, but can be derived by extending Hale's approach in the strike direction. The final formulas obtained emphasize the relative insensitivity of the DMO impulse response relative to the velocity profile considered, and confirm the high degree of accuracy of the approximate DMO formula proposed by Hale (1988) in the inline direction, for an arbitrarily complex $V(z)$ medium.

I. GENERAL PROCEDURE

The DMO mapping operator in a depth-dependent medium can be approximately represented by the function

$$t_0 = t_n \left[1 - \frac{x_0^2}{\gamma_x(t_n) h^2} - \frac{y_0^2}{\gamma_y(t_n) h^2} \right] \quad , \tag{1}$$

where t_0 is the two-way traveltime along the normal incidence ray, and (x_0, y_0) are the coordinates of the point of emergence of the ray at the surface of the ground.

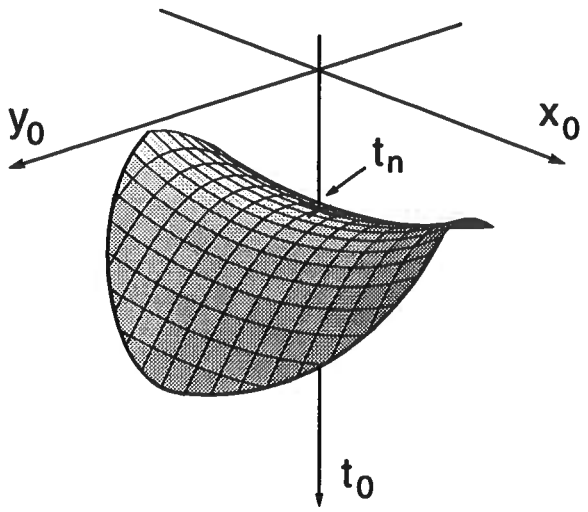

FIG. 1. Small dip, small offset representation of the DMO impulse response in a vertically inhomogeneous medium. The operator is defined by the normal moveout time t_n, and by the central curvature in the inline (x_0) and crossline (y_0) directions.

$\gamma_x(t)$ and $\gamma_y(t)$ are time-variable squeeze functions in the inline and crossline directions respectively, and are related to the curvature of the DMO operator through the relations

$$\left.\frac{\partial^2 t_0}{\partial x_0^2}\right|_{x_0=0} = -\frac{t_n}{\gamma_x(t_n)h^2} \quad \text{and} \quad \left.\frac{\partial^2 t_0}{\partial y_0^2}\right|_{y_0=0} = -\frac{t_n}{\gamma_y(t_n)h^2} \quad . \tag{2}$$

Since γ_x is usually positive, and γ_y, negative, equation (1) generally represents a saddle-shaped operator, as depicted in Figure 1. It can also be noticed that equation (1) differs from the constant velocity DMO ellipse by an additional contribution in the crossline direction, and by the squeeze factors γ_x and γ_y.

The general procedure to derive a small dip, small offset approximation of the DMO operator consists in writing the dip-*dependent* and dip-*independent* NMO equations, and in eliminating the finite-offset time T between these two equations. This procedure has been employed by Hale (1988) in the inline direction, but remains valid in any direction.

The dip-independent NMO equation relating the finite-offset time T to the vertical time t_n is given by

$$T^2 = t_n^2 + \frac{4h^2}{V_2^2(t_n)} \quad , \tag{3}$$

where

$$V_2(t) \equiv \left[\frac{1}{t} \int_0^t v^2(u)du \right]^{1/2} \tag{4}$$

is the root mean square velocity at traveltime t.

The dip-dependent NMO equation relating the finite-offset time T to the zero-offset time T_0 is similarly given by

$$T^2 = T_0^2 + \frac{4h^2}{V_{dip}^2(T_0, \boldsymbol{p})} \quad , \tag{5}$$

where $V_{dip}(T_0, \boldsymbol{p})$ is the moveout velocity at time T_0 and in the direction $\boldsymbol{p}$ traveled by the zero offset ray.

Combining equations (3) and (5), we obtain the expression

$$T_0^2 = t_n^2 + 4h^2 \left[\frac{1}{V_2^2(t_n)} - \frac{1}{V_{dip}^2(T_0, \boldsymbol{p})} \right] \tag{6}$$

which can be written in the form

$$T_0^2 = t_n^2 + \gamma(t_n, \boldsymbol{p}) h^2 \lambda^2(\boldsymbol{p}) \quad , \tag{7}$$

where $\gamma(t_n, \boldsymbol{p})$ is the correction factor at time t_n and in the direction $\boldsymbol{p}$, and λ is the "two-way" ray parameter of the zero offset ray in the direction $\boldsymbol{p}$.

The equivalence between equations (1) and (7) can then be easily established by noting that

$$\lambda_x = \frac{\partial t_0}{\partial x_0} \quad ; \quad \lambda_y = \frac{\partial t_0}{\partial y_0} \tag{8}$$

and

$$T_0^{(x)} = t_0^{(x)} + |\lambda_x x_0| \quad ; \quad T_0^{(y)} = t_0^{(y)} + |\lambda_y y_0| \quad . \tag{9}$$

(T_0 denotes the two-way traveltime along the zero offset ray emerging at the source-receiver midpoint, whereas t_0 represents the two-way traveltime along the normal incidence ray corresponding to a particular reflection point in the subsurface).

Hale (1988) demonstrated that the γ_x factor in the inline direction can be expressed in the form

$$\gamma_x(t_n) = \frac{3}{2} \frac{V_4^4(t_n)}{V_2^4(t_n)} - \frac{t_n}{V_2(t_n)} \frac{\mathrm{d}V_2(t_n)}{\mathrm{d}t_n} - \frac{1}{2} \quad , \tag{10}$$

where

$$V_4(t) \equiv \left[\frac{1}{t} \int_0^t v^4(u) du \right]^{1/4} \quad . \tag{11}$$

The derivation of expression γ_y in the crossline direction can be obtained from equation (7) and requires the knowledge of the moveout velocity V_{dip} in the strike direction.

II. MOVEOUT VELOCITY IN THE STRIKE DIRECTION

According to Levin (1971), the normal moveout velocity for a dipping reflector in a constant velocity medium is given by

$$V_{dip}(\phi,\theta) = V_0[1 - \sin^2\phi\cos^2\theta]^{1/2} \quad , \tag{12}$$

where ϕ is the dip angle of the reflector, and θ, the angle between the profile line and the dip line. In the strike direction $\theta = \pi/2$, the moveout velocity is simply equal to the contant velocity V_0 of the medium.

The general expression of the moveout velocity in the crossline direction for a vertically inhomogeneous medium can be obtained from the three-dimensional traveltime equation for dipping layers derived by Diebold (1987). Diebold showed that the traveltime equation along a raypath between a source S and receiver R in a stack of homogeneous layers with interfaces of arbitrary dip and strike can be written as

$$T = \boldsymbol{p}_S \cdot \boldsymbol{X}_S \; + \; \boldsymbol{p}_R \cdot \boldsymbol{X}_R \; + \; \sum_j (q_{S_j} + q_{R_j}) z_j \quad , \tag{13}$$

where $\boldsymbol{X}_S$ is the horizontal position vector from the source S to a vertical reference line on which the layer thicknesses z_j are defined; $\boldsymbol{X}_R$ is the horizontal position vector from the reference line to the receiver R; $\boldsymbol{p}_S$ and $\boldsymbol{p}_R$ are the horizontal slowness vectors of the rays departing from the source S, and arriving to the receiver R; and q_{S_j} and q_{R_j} are the vertical slowness components of the source and receiver rays in layer j. The summation is over the layers j traversed by the rays (Figure 2).

The reference line is fixed, but can be chosen anywhere, e.g., through the source, at the receiver, at the reflection point, or elsewhere. The choice of the reference line determines the layer thicknesses z_j and the horizontal vectors $\boldsymbol{X}_S$ and $\boldsymbol{X}_R$, but does not influence the slowness components $\boldsymbol{p}_S$, $\boldsymbol{p}_R$ and q_j.

Diebold's formula is particularly elegant because it is a mere generalization of the well-known traveltime formulas in one- and two-dimensional layered media. Moreover, Richards (1990) showed that the trigonometric proof of equation (13) given in the original paper of Diebold (1987) is hardly needed when the raypath is decomposed in a particular way.

In our problem, it is convenient to put the reference line at the reflection point in the crossline direction $x = 0$. With the assumption that the half source-receiver offset h is small, we can write

$$T_0 = 2\,[\,\boldsymbol{p}_0 \cdot \boldsymbol{X}_0 \; + \; \tau_0\,] \quad = \quad 2\,\left[\,p_0^{(y)} y_0 \; + \; \tau_0\,\right] \quad , \tag{14}$$

$$T = 2\,[\,\boldsymbol{p}_S \cdot \boldsymbol{X}_S \; + \; \tau\,] \quad \simeq \quad T_0 \; + \; 2\,\left[\,p_0^{(y)} \frac{h^2}{y_0} \; + \; \delta\tau\,\right] \quad , \tag{15}$$

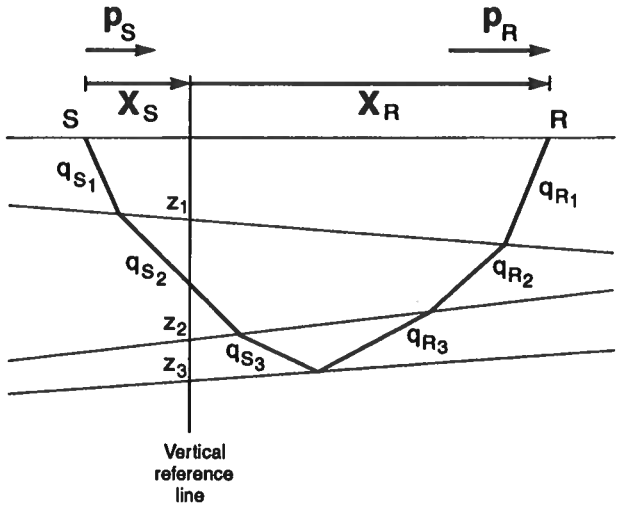

FIG. 2. 2-D schematic of a 3-D raypath from source S to receiver R which is composed of line segments that in general are not co-planar. Dipping interfaces are planar, but are not presumed to share a common strike. The local layer thicknesses z_j are defined by the intersection of the interfaces with the vertical reference line. The q_{S_j}'s and q_{R_j}'s denote the vertical slownesses in each layer, $\mathbf{p}_S$ and $\mathbf{p}_R$ are the horizontal slowness vectors at the source and at the receiver, and $\mathbf{X}_S$ and $\mathbf{X}_R$ represent the horizontal distances traveled along the source and receiver raypaths (after Richards, 1990).

where

$$\tau_0 = \sum_j q_{0_j} z_j \quad ; \quad \tau = \sum_j q_{S_j} z_j \quad \text{and} \quad \delta\tau = -\frac{(p_0^{(y)} h)^2}{2y_0^2} \sum_j \frac{z_j}{q_{0_j}} \quad . \tag{16}$$

We then obtain

$$T^2 = T_0^2 + \frac{4h^2}{V_{dip}^2(T_0, y_0)} + O(h^4) \tag{17}$$

with

$$V_{dip}^2(T_0, y_0) = \frac{2y_0}{p_0^{(y)} T_0}. \tag{18}$$

The above expression for $V_{dip}(T_0, y_0)$ was also given by Witte (1991). When the horizontal distance y_0 traveled along the zero-offset ray is small, it can be shown that

$$V_{dip}(T_0, y_0) \simeq V_2(t_{mig}) \quad , \tag{19}$$

where t_{mig} is the two-way migration (vertical) time corresponding to the reflection at time T_0.

III. THE LINEAR $V(z)$ CASE

In a medium characterized by a velocity function $V(z) = V_0 + kz$, the expressions of $V(t)$, $V_2(t)$ and $V_4(t)$ at the two-way traveltime t are respectively given by

$$V(t) = V_0 e^{kt/2} \quad , \quad V_2(t) = V_0 \left[\frac{e^{kt}-1}{kt}\right]^{1/2} \quad \text{and} \quad V_4(t) = V_0 \left[\frac{e^{2kt}-1}{2kt}\right]^{1/4} \quad . \tag{20}$$

When these expressions are substituted in equation (10), we find

$$\gamma_x(t_n) = \frac{kt_n\,(e^{kt_n}+3)}{4\,(e^{kt_n}-1)} \quad . \tag{21}$$

In addition, the closed form expression of the traveltime T_0 given in Paper I allows us to write equation (18) in the form

$$V_{dip}^2(T_0, y_0) = V_0 V(t_{mig}) \frac{\sinh kT_0/2}{kT_0/2} \quad , \tag{22}$$

and, after some approximations,

$$V_{dip}^2(T_0, y_0) \simeq V_2^2(t_n) \left[1 - \frac{kt_n \lambda_y^2 V_2^2(t_n)}{16}\right] \quad . \tag{23}$$

The expression of γ_y can then be obtained from equations (6) and (7), and is simply written

$$\gamma_y(t_n) = -\frac{kt_n}{4} \quad . \tag{24}$$

Equations (21) et (24) clearly show that the squeeze functions γ_x and γ_y are independent of the velocity V_0 and depend only on the velocity gradient k. Moreover, it can be demonstrated from equation (21) that

$$\frac{\mathrm{d}\gamma_x}{\gamma_x} \ll \frac{\mathrm{d}k}{k} \quad , \tag{25}$$

which shows that γ_x depends only weakly on k. On the other hand, since γ_y is directly proportional to k, the curvature of the DMO operator in the crossline direction will be affected by errors in the velocity gradient k. (However, it should be recalled that the most energetic contributions of the DMO operator are concentrated along the inline direction – see Paper I).

The behavior of the DMO impulse response predicted by equations (21) and (24) is entirely confirmed by the curves displayed in Figures 3 and 4. Figures 3 and 4 respectively show the *exact* inline and crossline components of the DMO operator (calculated from the equations given in Paper I), for several values of V_0 and k.

(a)

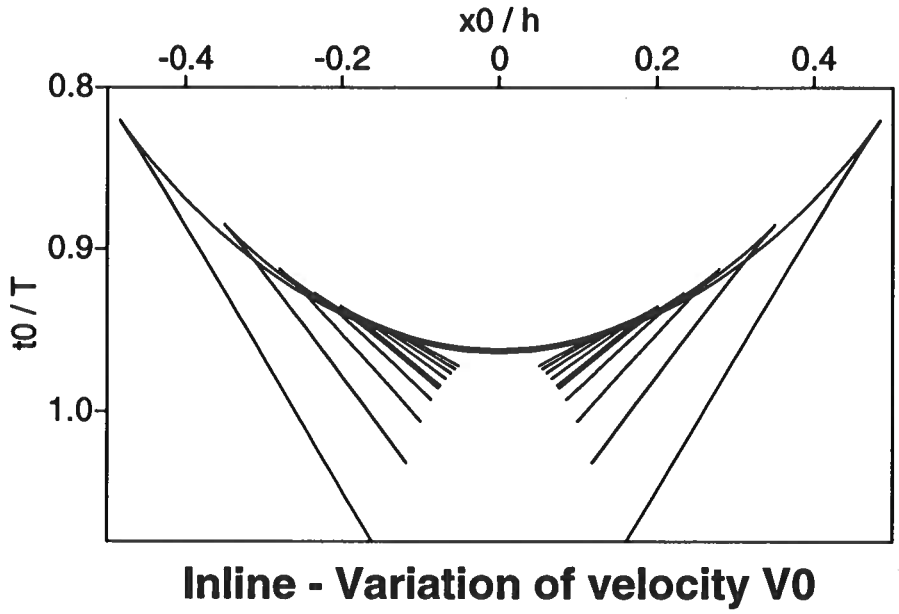

(b)

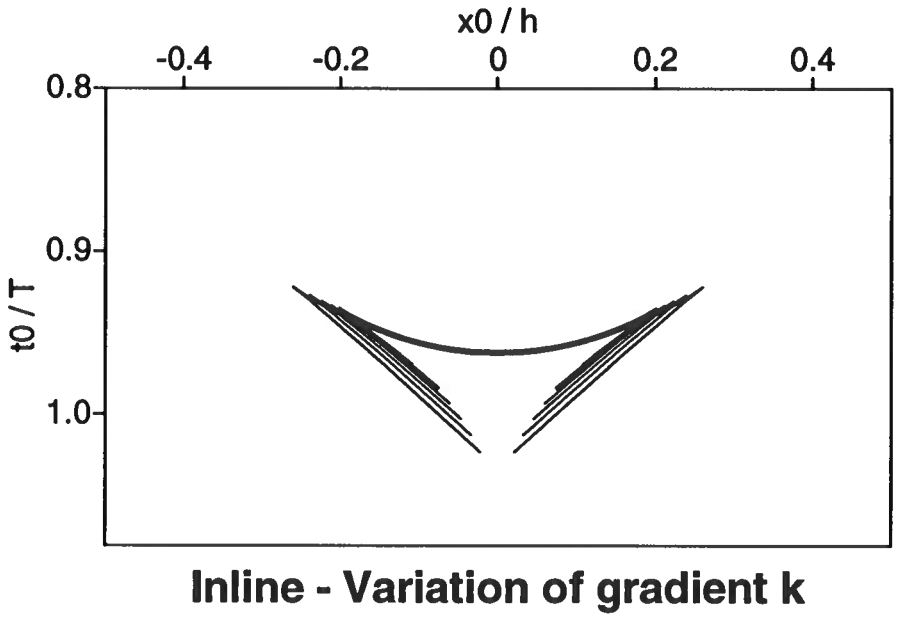

FIG. 3. DMO operators in the inline direction for variations of $\pm 10\%, \pm 20\%, \pm 30\%, \pm 40\%, \pm 50\%$ of velocity V_0 (a), and gradient k (b). The standard values used in this calculation are $V_0 = 1.5$ km/s, $k = 0.3$ /s, $h = 2$ km and $T = 6$ s. The curves have been superposed by using the normal moveout time t_n corresponding to the standard values.

(a)

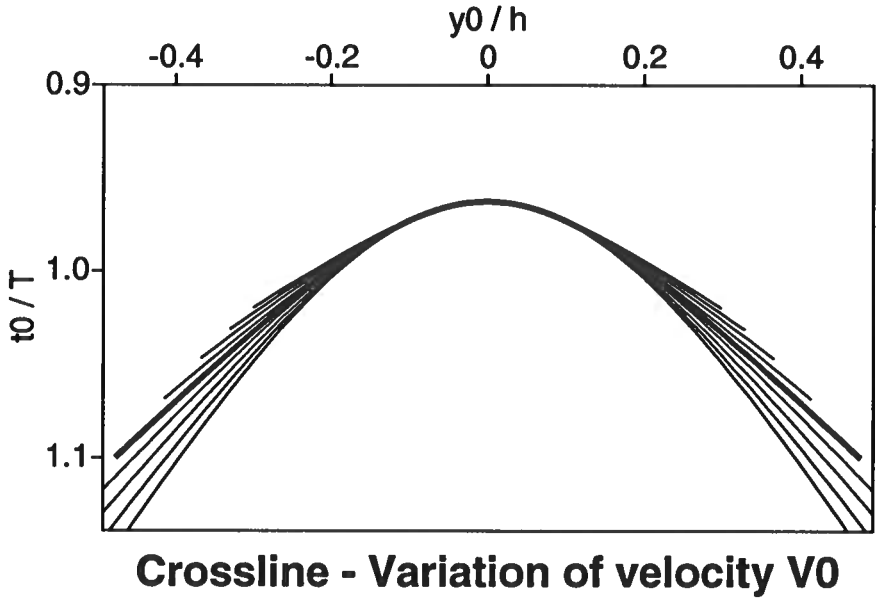

(b)

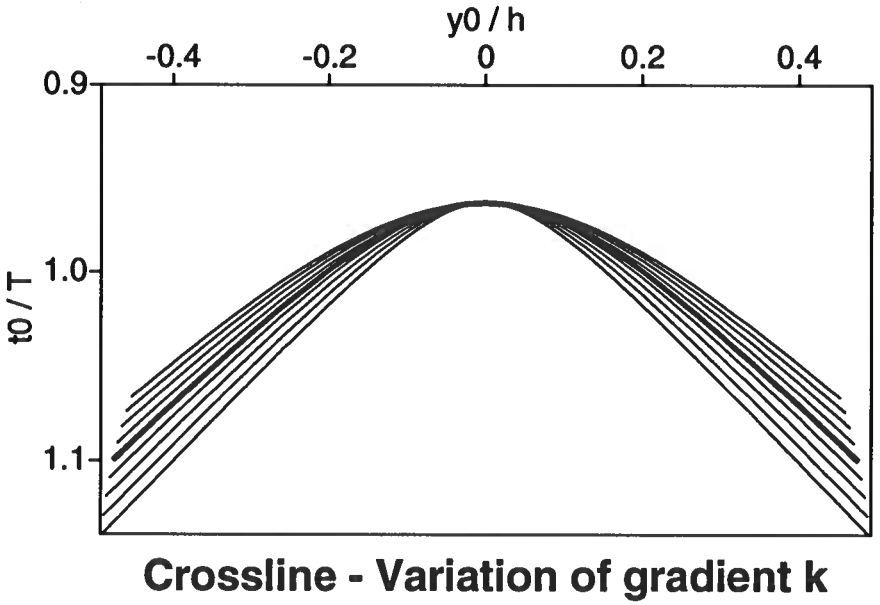

FIG. 4. Same as Figure 3, but in the crossline direction.

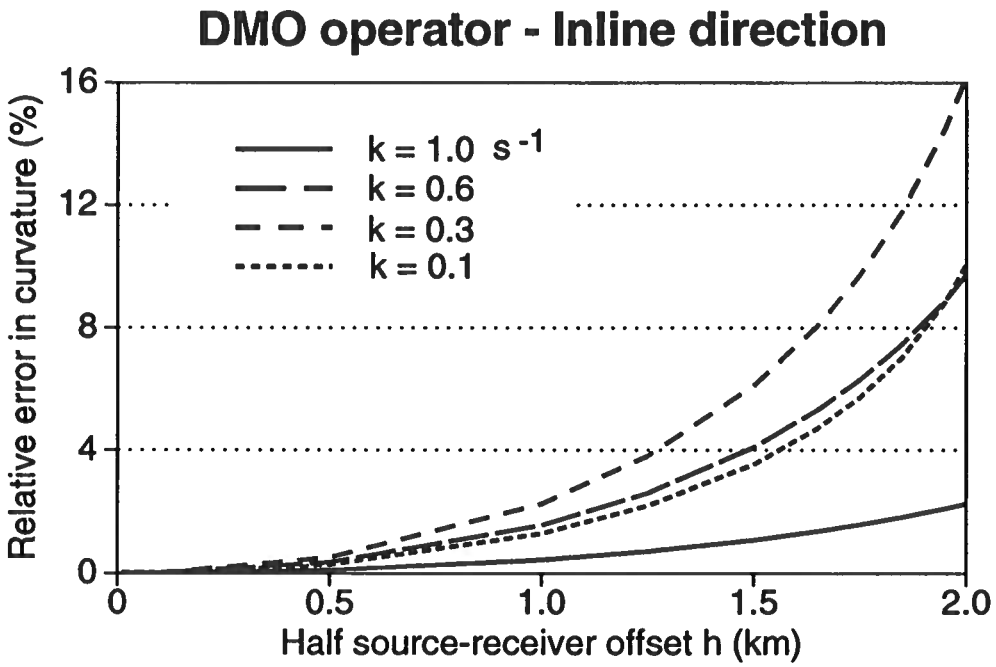

FIG. 5. Accuracy of the DMO approximation in the inline direction. The curves show the relative error in curvature as a function of the half source-receiver offset h, for four different values of the velocity gradient k. The other parameters used in this calculation are $V_0 = 1.5$ km/s and $T = 3$ s .

Besides, it may be noticed from equations (2) and (24) that the curvature in the crossline direction is independent of t_n, and can be exactly computed for any offset h. Figure 5 shows that the curvature computed from equations (2) and (21) in the inline direction remains very accurate when the source-receiver offset is increased.

CONCLUSIONS

An approximate representation of the DMO operator in a medium with a constant velocity gradient has been derived. The approximate operator can be used for any velocity gradient, and remains accurate even for rather large source-receiver offsets. The DMO correction in the inline direction is almost independent of the velocity function considered.

ACKNOWLEDGMENTS

This work was done while the author was a visiting scientist at the Center for Wave Phenomena of the Colorado School of Mines. The author is grateful for the financial support of the Société Nationale Elf Aquitaine.

REFERENCES

Diebold, J. B., 1987, Three-dimensional traveltime equation for dipping layers: Geophysics, **52**, 1492-1500.

Dietrich, M., and Cohen, J. K., 1992, 3-D migration to zero offset for a constant velocity gradient: an analytical formulation: CWP-113, Colorado School of Mines, 26p.

Hale, D., 1988, Dip moveout processing, *in* Domenico, S. N., Ed., Course notes series, **4**: Soc. Expl. Geophys.

Levin, F. K., 1971, Apparent velocity from dipping interface reflections: Geophysics, **36**, 510-516.

Richards, P. G., 1990, A short course on theoretical seismology, *in* Desaubies, Y., Tarantola, A., and Zinn-Justin, J., Eds., Oceanographic and geophysical tomography: Les Houches 1988, NATO ASI Session L, North Holland, 29-134.

Witte, D., 1991, Dip moveout in vertically varying media: 61st SEG Annual Meeting, Houston, 10-14 November, Expanded Abstracts, 1181-1183.

CWP-116

A Dip-Dependent Divergence Correction

Francesca Fazzari

Excerpt from

— Master of Science Thesis —

Center for Wave Phenomena
Colorado School of Mines
Golden, Colorado 80401
(303) 273-3557

A dip-dependent divergence correction

Francesca Fazzari

ABSTRACT

A divergence correction is conventionally applied to zero-offset data in an effort to obtain reflection amplitude information. The conventional divergence correction compensates for the geometrical spreading of a point source in a horizontally layered medium where velocity varies with depth only. The dip-dependent divergence correction extends the conventional correction for improved amplitude processing of dipping beds.

The dip-dependent divergence correction is computed by dynamic ray tracing, and is applied to stacked data using a dip decomposition technique. This correction decreases amplitudes relative to those obtained from the conventional correction. The difference in amplitude is greatest for large reflector dips. In a data example from the Gulf of Mexico, the conventional correction over-amplified the reflection off a salt dome flank by a factor of 1.5.

High amplitudes near salt flanks are also associated with the presence of hydrocarbons. Applying the dip-dependent divergence correction ensures that 'bright spots' are not erroneously caused by over-amplification of steep dips by the conventional correction.

In areas like the Gulf of Mexico, where the velocity function varies with depth, and steep reflectors are commonplace, the poststack dip-dependent divergence correction is an inexpensive way to improve the amplitude information in seismic images.

INTRODUCTION

The divergence correction is applied to compensate for the decay in amplitude due to the geometrical spreading of the wavefront generated by a seismic source. When transmission losses can be neglected, the amplitudes in divergence-corrected seismic data are proportional to reflection coefficients of interfaces within the subsurface.

After appropriate divergence correction, properties of the subsurface become more interpretable in terms of seismic amplitudes.

The divergence correction for a particular seismic event depends upon the location of its subsurface reflection point relative to the source location, and upon the structural configuration of the overburden. For zero-offset reflections from horizontal beds in a $v(z)$ medium, where the velocity v varies only with depth z, the reflection point is specified by the vertical traveltime of the seismic energy and the velocity of the medium. Traveltime and velocity therefore determine the zero-offset divergence correction for horizontal reflectors.

Newman (1973) derived the zero-offset divergence correction $v_{\rm rms}^2 t/v_0$, for a horizontally layered homogeneous earth, where t is the two-way vertical traveltime to the reflector, v_0 is the velocity at the surface, and $v_{\rm rms}$ is the root-mean-square average velocity along the vertical path between surface and reflector. This correction is routinely applied to stacked seismic data.

Newman also derived the divergence correction for finite-offset reflections from horizontal beds in a $v(z)$ medium. For finite offset reflections, the divergence correction, and the reflection point depend on horizontal slowness (reflection slope), and traveltime. These quantities are measurable in finite-offset seismic data. The finite-offset divergence correction for horizontal reflectors, which is generally not applied in practice, does not require two-point ray tracing.

For media with dipping and curved interfaces, other authors (e.g., Červený, et al., 1977) have employed asymptotic ray theory to determine a general expression for the wave amplitude, including divergence effects. Červený, et al., described how to evaluate the divergence for finite offset and dipping reflectors using the dynamic ray tracing equations. The divergence is computed by using two-point ray tracing to find the subsurface reflection point, and then solving the dynamic ray tracing equations for the raypath to that reflection point.

I use the dynamic ray tracing equations to determine the divergence correction for any reflector in a medium where the velocity varies with depth only. This is the dip-dependent divergence correction. For zero-offset data, the reflection point and the divergence correction depend only on reflection slope and traveltime. The dip-dependent divergence correction is applied to stacked data without the computational cost of two-point ray tracing.

DERIVATION

Červený and Hron (1980) showed that for a seismic line recorded from a $v(z)$ medium, the three-dimensional divergence due to a point source reduces to the product of two two-dimensional components: an in-plane component $\sqrt{q}$, and an out-of-plane component $\sqrt{\sigma}$. The in-plane dimensions are defined by a subsurface depth slice beneath the seismic line, and the out-of-plane dimensions by a depth slice taken perpendicular to the seismic line.

Consider an in-plane raypath from a shotpoint to a subsurface reflection point. Let γ define the initial (take-off) angle between ray and vertical z axis. The divergence correction along the raypath is a ratio of the normal distance at time t between the ray with angle γ and the nearby ray with angle $\gamma + d\gamma$, to the initial normal distance.

The normal distance is described by the dynamic ray tracing equations, which are based on the ray centered coordinate system (e.g., Červený and Hron, 1980).

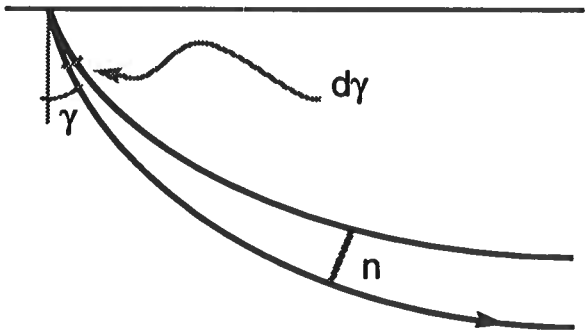

FIG. 1. The normal distance n between a ray characterized by take-off angle γ and a nearby ray characterized by take-off angle $\gamma + d\gamma$.

In ray centered coordinates, every point along a central ray i.e., the in-plane ray from shot point to subsurface reflection point, has direction vector **s** and normal **n**. **s** has magnitude equal to the distance travelled along the ray. The magnitude of **n** is equal to the distance between the central ray (with angle γ) and a nearby ray (with angle $\gamma + d\gamma$), when s is held fixed. The relationship of n to s is described by the dynamic ray tracing equations (Červený, 1981a)

$$\frac{dn}{ds} = vp_n \qquad \frac{dp_n}{ds} = -\frac{v_{,nn}}{v^2}n, \tag{1}$$

where p_n is the component of the slowness in the direction of the normal, and $v_{,nn}$ is the second derivative of velocity with respect to n.

The divergence correction is a ratio of the normal distance at traveltime t to the initial normal distance. The initial normal is measured when the wavefront is at unit distance from the source center i.e., when the distance travelled along the ray is equal to one. As both normal distances become small, the normal at traveltime t is approximated by the differential dn and the initial normal distance by $1 \cdot d\gamma$ (Červený, 1981b). The divergence correction is therefore $dn/d\gamma$. It is evaluated by taking the derivative of the dynamic ray tracing equations (1) with respect to γ. Define q and p so that

$$q \equiv \frac{dn}{d\gamma} \qquad p \equiv \frac{dp_n}{d\gamma}.$$

In terms of these new variables, the derivative of equations (1) with respect to γ is

$$\frac{dq}{dt} = v^2 p \qquad \frac{dp}{dt} = -\frac{v_{,nn}}{v} q. \tag{2}$$

The relationship $s = vt$ was used to replace distance along the ray s by traveltime t.

Equations (2) govern the in-plane divergence $\sqrt{q}$. A similar expression governs the out-of-plane divergence $\sqrt{\sigma}$, the only difference being the value of the normal curvature of the velocity function $v_{,nn}$. For a one-dimensional velocity function which varies with depth only, $v_{,nn}$ in the in-plane direction is equal to $v_{,zz} p_x^2 v^2$. $v_{,zz}$ is the second derivative of velocity with respect to depth, and p_x is the horizontal slowness (reflection slope). The equivalent expression for the normal curvature in the out-of-plane direction is $v_{,zz} p_y^2 v^2$, where p_y is the horizontal slowness in the direction perpendicular to the seismic line (crossline reflection slope). For a 2-D seismic line, however, p_y is assumed to be zero. In the out-of plane direction, the normal curvature of the velocity function is therefore zero. Thus p is a constant, and equal to its initial value of $1/v_0$. The differential equations for σ and q are

$$\begin{aligned} \frac{d\sigma}{dt} &= \frac{v^2}{v_0}; \\ \frac{dq}{dt} = v^2 p \qquad & \frac{dp}{dt} = -v_{,zz}\, p_x^2 v\, q, \end{aligned} \tag{3}$$

where both σ and q are initially zero.

The in-plane divergence, and the out-of-plane divergence contribute to the total divergence correction D,

$$D(p_x, t) = \sqrt{\sigma(t)}\sqrt{q(p_x, t)}.$$

For a horizontally layered medium down to the reflector, the dip-dependent divergence correction depends upon the interval velocity of the medium through which the seismic wave travels, reflection slope, and traveltime.

IMPLEMENTATION

I use finite differences to numerically solve equations (3) for σ and q by marching forward in traveltime along the ray. Given a particular velocity function, a divergence correction table is generated for all traveltimes τ and all possible reflection slopes p_x.

For zero-offset reflections from dipping beds, the horizontal slowness (reflection slope) and traveltime of a ray from shotpoint to reflection point are the same as for a ray from reflection point to receiver. Further, the horizontal slowness that characterizes the raypath of a particular reflection corresponds to reflection slope, which is measured on a zero-offset section. Note that for finite-offset reflections from dipping beds, the horizontal slowness and traveltime of a ray from shotpoint to reflection point differ from those for a ray from reflection point to receiver. In the finite-offset

case, these quantities require two-point ray tracing. For zero-offset data, however, the raypath to a reflection point and the divergence correction are specified by a particular combination of reflection slope and traveltime; no ray tracing is required.

The dip-dependent divergence correction is equivalent to a time-varying dip filter because of its simultaneous dependence on reflection slope and traveltime. Although dip-dependent processing is most easily implemented in the frequency-wavenumber domain, the time dependent attributes of the table cannot be considered once the 2-D Fourier transform is made. To apply the divergence correction, I use a dip decomposition technique similar to Jakubowicz's (1990) method for efficient DMO. The dip-dependent divergence correction is applied, for all times, to each reflection slope in the wavenumber-time domain. The dip filtered data are then transformed to the wavenumber-frequency domain. In this domain, only the frequencies near the slope-wavenumber combination $\omega = k/p_x$ are included in the output. The dip decomposition algorithm can be summarized:

Zero out $Q(k,\omega)$
Transform the stacked data $p(x,t)$ to $P(k,t)$
For all wavenumbers k {
    For all slopes p_x {
        Apply the divergence correction for all times t so that:
            $s(k,t) = D(p_x,t) \times P(k,t)$
        Transform $s(k,t)$ to $S(k,\omega)$
        For all frequencies ω near k/p_x {
            Add $S(k,\omega)$ to the output $Q(k,\omega)$
        }
    }
}
Transform the divergence-corrected data $Q(k,\omega)$ to $q(x,t)$

DIVERGENCE CORRECTION TABLE

The conventional divergence correction over-amplifies reflections from dipping beds. The amount of over-amplification depends on reflection slope, unmigrated traveltime, and interval velocity function. For interval velocity functions that increase with depth, the divergence correction is largest for energy that travels the farthest and penetrates most deeply into the medium; i.e., at large times and at small values of p_x, where the raypath is nearly vertical.

Consider a dipping reflector and a nearly horizontal reflector in a medium where the velocity increases with depth (Figure 2). If the unmigrated traveltime to these reflectors along the normal incidence raypath is held constant, the dipping reflector must be shallower than the nearly horizontal reflector. The average velocity along the normal incidence raypath to the dipping reflector is therefore less than that for

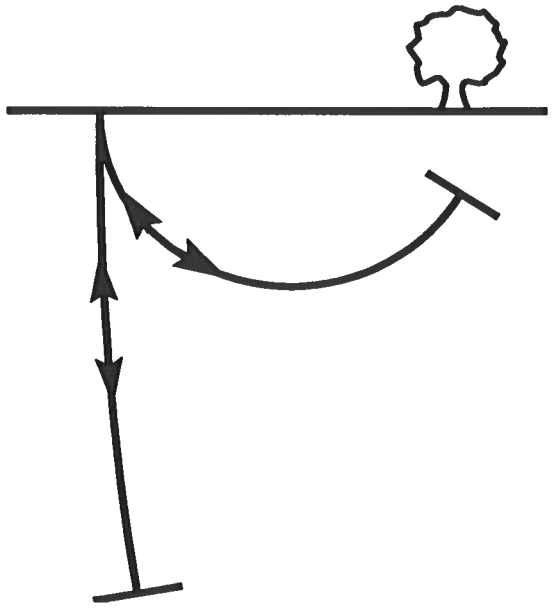

FIG. 2. A shallow, overhung reflector and a deep, nearly horizontal reflector in a medium where the velocity increases with depth. The traveltimes of the two normal incidence raypaths are equal. The divergence correction is greater for the nearly horizontal reflector than for the dipping reflector.

the nearly horizontal reflector. Consequently, for fixed traveltime, the divergence correction decreases as reflection slope increases. The maximum value of the divergence correction occurs at zero reflection slope or for horizontal reflectors, where the conventional divergence correction, $v_{\rm rms}^2 t/v_0$ is valid.

For small traveltimes, the difference between conventional and dip-dependent divergence correction is small. The difference increases with traveltime. For large traveltimes, an event with small reflection slope, such as the nearly horizontal reflector in Figure 2 must be located at depth in the subsurface. An event with large reflection slope at late time, however, corresponds to a much shallower reflector, and thus requires a smaller divergence correction. The divergence correction for the shallow reflector is much smaller than that for the deep, nearly horizontal reflector. As traveltime increases, for events with large reflection slopes, the amount of amplitude exaggeration after conventional divergence correction increases.

Figure 3 shows contours of the ratio of the conventional divergence correction to the dip-dependent divergence correction, for the velocity function $v = 1.5 + 0.6z$. The conventional divergence correction exaggerates amplitudes by less than three percent for events whose reflection slope and traveltime fall above the contour labeled 1.03. For events that fall on the 1.66 contour, including the dipping events in Figure 4b, the conventional correction over-amplifies those events by approximately 70 percent. The amount of over-amplification after conventional divergence correction increases with reflection slope and traveltime.

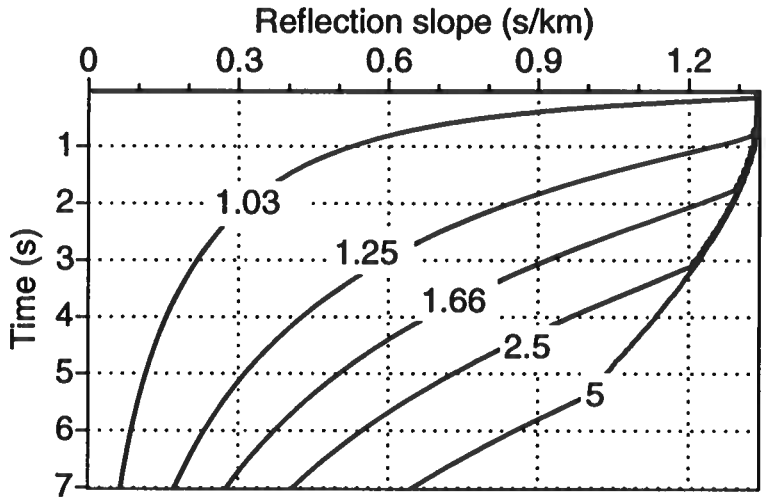

FIG. 3. Contours of amplitude error that result from applying the conventional divergence correction to a medium characterized by the velocity function $v = 1.5+0.6z$ km/s. For the reflection slopes and times that fall along a given contour, such as the 1.66 contour, the conventional correction over-amplifies dipping events by about 1.7 times.

RESULTS

The examples in Figures 4 and 5 demonstrate the amplitude effect of the dip-dependent divergence correction. The amount of over-amplification caused by the conventional correction is shown in the difference plots, Figures 4c and 5d, where the amplitudes of dip-dependent divergence-corrected data are subtracted from those of conventionally corrected data. Both divergence corrections are normalized by the initial correction for zero reflection slope i.e., $v^2_{\rm rms}(t_1)t_1$, where t_1 is the time sampling interval.

The synthetic data were generated by a modeling program based upon the Kirchhoff approximation (e.g., Bleistein, 1986). The modeling program produced a stack that was migrated by a finite difference migration process (Hale, 1991), which yields amplitudes proportional to the reflection coefficients. Reflection coefficients of the model reflectors were held constant throughout the model; this constancy is preserved (Figure 4b) after applying the dip-dependent divergence correction.

The difference plot in Figure 4c demonstrates that the conventional divergence correction has exaggerated the amplitudes of dipping reflections. For nearly horizontal reflectors, the dip-dependent divergence correction and the conventional divergence correction have the same action.

The dip-dependent divergence correction is applied to a Gulf of Mexico seismic line in Figure 5. In the Gulf of Mexico, an interval velocity function that varies with

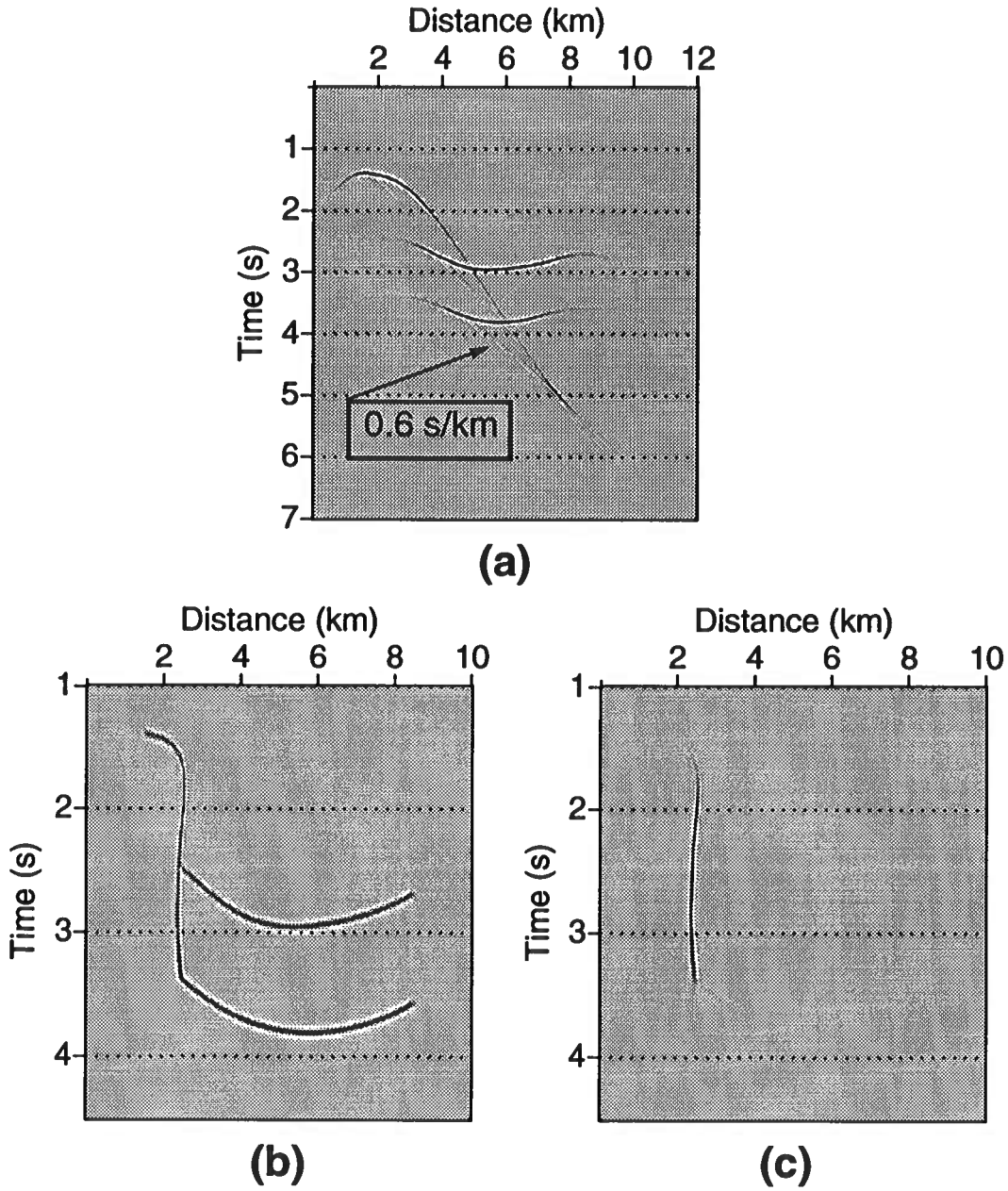

FIG. 4. (a) Zero-offset synthetic data generated from an interval velocity model $v = 1.5 + 0.6z$. The amplitude error contours are those shown in Figure 2. The dipping event at 4.5 s has a reflection slope of 0.6 s/km. This event falls upon the 1.66 contour of Figure 2. (b) Migration of dip-dependent divergence-corrected data. (c) The difference: conventionally corrected amplitudes minus dip-dependent divergence corrected amplitudes.

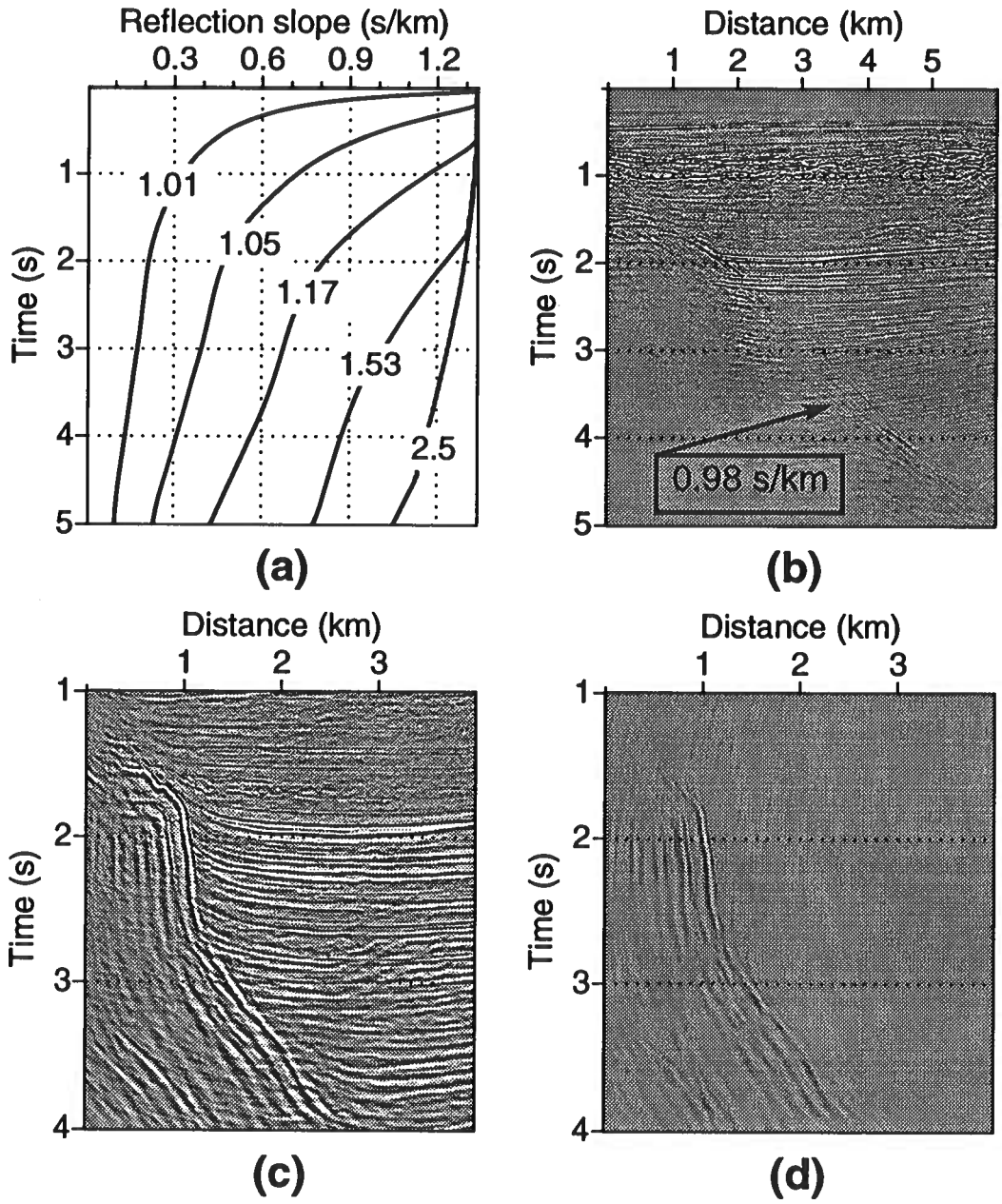

FIG. 5. (a) Contours of amplitude error that results from applying the conventional divergence correction to a medium described by the interval velocity used to migrate the data. (b) The stack. (c) Migrated data with amplitudes adjusted by the dip-dependent divergence correction. (d) The difference: conventionally corrected amplitudes minus dip-dependent divergence corrected amplitudes.

depth is a good approximation to the velocity of sediments through which seismic waves propagate. The arrow on the stacked data points to the salt flank, with a reflection slope of 0.98 s/km at a time of about 3.5 s. This event falls on the 1.53 contour of Figure 5a. The conventionally corrected amplitudes along the salt flank are thus over amplified by 50 percent.

Because the velocity increase is less rapid than in the model studied above, the amplitude difference in Figure 5d is less dramatic than for the synthetic example shown above. In this medium, the conventional divergence is valid over a larger range of dips and traveltimes. As before, the dip-dependent divergence correction has decreased the amplitudes of dipping beds at late times, and steeply dipping beds at early times.

CONCLUSIONS

The error in amplitude due to the conventional divergence correction is most significant for events with large reflection slope at late times. The conventional divergence correction has been shown to over-amplify dipping events by 50 percent on stacked data (Figure 5). The dip-dependent divergence correction improves the processing of amplitudes of dipping reflectors in a medium where the velocity varies only with depth. Gulf of Mexico data, which often contain steep reflectors and where the velocity profiles have little lateral variation, are particularly suited for the application of this correction.

The dip-dependent divergence correction could be applied to prestack data if two-point ray tracing is performed to determine raypaths to and from the reflection point for each event. This is a topic for further study; however, I expect that the amplitude effects of the dip-dependent divergence correction applied to finite-offset data, which are subsequently stacked, will not differ significantly from those of the poststack divergence correction.

ACKNOWLEDGMENTS

Thanks to Dave Hale for his suggestion of the project and his ongoing guidance. Thanks to Ken Larner for his helpful critique of the paper. The author is grateful for the support of the members of the Consortium Project of the Center for Wave Phenomena, Colorado School of Mines.

REFERENCES

Bleistein, N., 1986, Two-and-one-half dimensional in-plane wave propagation: Geophys. Prosp., **34**, 686–703.

Červený, V., 1981a, Ray tracing in a vicinity of a central ray: Stanford Exploration Project, **28**, 39–48.

Červený, V., 1981b, Computation of geometrical spreading by dynamic ray tracing: Stanford Exploration Project, **28**, 49–59.

Červený, V., and Hron, F., 1980, Ray series method and dynamic ray tracing system for three-dimensional inhomogeneous media: Bul. Seis. Soc., **70**, 47–77.

Červený, V., Molotkov, I. A., and Pšenčik, I., 1977, Ray method in seismology: Univerzita Karlova Praha.

Hale, D., 1991, Migration in the time-wavenumber domain: **CWP-107**, Project Review, Colorado School of Mines.

Jakubowicz, H., 1990, A simple efficient method of dip-moveout correction: Geophys. Prosp., **38**, 221–245.

Newman, P., 1973, Divergence effects in a layered earth: Geophysics **38**, 481–488.

Reverse-Time Depth Migration with the Full Wave Equation

Tong Fei

Center for Wave Phenomena
Colorado School of Mines
Golden, Colorado 80401
(303) 273-3557

Reverse-time depth migration with full wave equation

Tong Fei

ABSTRACT

Where the subsurface is inhomogeneous, lateral and vertical variation in velocity and density should be considered when doing seismic migration. Reverse-time depth migration based on the full wave equation is one general approach that takes such velocity variation into account.

By changing dependent variables, I replace the second-order acoustic wave equation by four first-order partial differential equations. A two-step explicit finite-difference method was used to solve these equations. Results of application to synthetic data indicate that this method can image the reflectors beyond 90 degrees with accuracy.

INTRODUCTION

Finite-difference migration has been widely implemented following approaches of Claerbout (1985). His method employs a one-way wave equation that allows energy to propagate only downward. Although successful in many situations, the method is limited by the assumptions made in deriving the one-way wave equation. In particular, it is assumed that the spatial derivatives of the velocity field can be ignored. However, such terms are significant in the presence of strong velocity contrasts. Most finite-difference schemes based on the one-way wave equation contain a limit on the maximum dip angle of the reflector. To deal with a variable velocity field, Kosloff and Baysal (1983) developed a two-dimensional migration scheme in the frequency and space domain based on a direct integration in depth of the acoustic wave equation.

Here, I introduce a two-step explicit finite-difference, reverse-time depth migration scheme. The method is based on a set of first-order partial differential equations derived from the second-order acoustic wave equation. This method can be applied

with full consideration of variable velocity and density, and their gradients, and it can accurately image the positions of the dipping reflector beyond 90 degrees.

THEORY

The key steps in deriving equations used for reverse-time depth migration here are (1) to define the new dependent variables, and (2) to form the new first-order equations in these variables, based on the second-order acoustic wave equation.

For velocity and density fields that are functions of space, the acoustic wave equation is

$$\frac{1}{\rho}\frac{\partial^2 P}{\partial^2 t} = c^2\left[\frac{\partial}{\partial x}\left(\frac{1}{\rho}\frac{\partial P}{\partial x}\right) + \frac{\partial}{\partial y}\left(\frac{1}{\rho}\frac{\partial P}{\partial y}\right) + \frac{\partial}{\partial z}\left(\frac{1}{\rho}\frac{\partial P}{\partial z}\right)\right] + f(x,y,z,t), \tag{1}$$

where $\rho = \rho(x,y,z)$ is the density function, $c = c(x,y,z)$ is the wave velocity and $f(x,y,z,t)$ is the source function.

With new dependent variables defined as

$$q(x,y,z,t) = \frac{1}{\rho(x,y,z)}\frac{\partial P}{\partial t}, \tag{2}$$

$$u(x,y,z,t) = \frac{c(x,y,z)}{\rho(x,y,z)}\frac{\partial P}{\partial x}, \tag{3}$$

$$v(x,y,z,t) = \frac{c(x,y,z)}{\rho(x,y,z)}\frac{\partial P}{\partial y}, \tag{4}$$

$$w(x,y,z,t) = \frac{c(x,y,z)}{\rho(x,y,z)}\frac{\partial P}{\partial z}, \tag{5}$$

the second-order acoustic wave equation (1) can be reduced to a new first-order partial differential equation, and three additional first-order partial differential equations can be derived from the definition (2) – (5). This gives a complete set of the first-order partial differential equations for finding the migration images. These equations take the form

$$\frac{\partial q}{\partial t} = c\left(\frac{\partial u}{\partial x} + \frac{\partial v}{\partial y} + \frac{\partial w}{\partial z}\right) - \alpha u - \beta v - \gamma w + f(x,y,z,t), \tag{6}$$

$$\frac{\partial u}{\partial t} = c\left(\frac{\partial q}{\partial x} + Aq\right), \tag{7}$$

$$\frac{\partial v}{\partial t} = c\left(\frac{\partial q}{\partial y} + Bq\right), \tag{8}$$

$$\frac{\partial w}{\partial t} = c\Big(\frac{\partial q}{\partial z} + Cq\Big), \tag{9}$$

where α, β and γ are the three components of wave velocity gradient, and A, B and C are the three components of the normalized density gradient. These gradients are function of space, and can be written as

$$(\alpha, \beta, \gamma) = \nabla c, \tag{10}$$

$$(A, B, C) = \frac{1}{\rho} \nabla \rho. \tag{11}$$

From equation (2) it is seen that the new dependent variable $q(x, y, z, y)$ has a 90-degree phase shift relative to the variable P.

ALGORITHM

The set of equations (6)–(9) may now be solved by using the two-step Lax-Wendroff finite-difference method, which has the second-order accuracy.

At each time step n, the variable q is defined on the main grid points, while u, v and w are defined at the centers between the main grid points in the x, y and z directions respectively. In the Lax-Wendroff finite-difference method, temporary variables are defined at auxiliary points at the half-time steps $n + \frac{1}{2}$.

auxiliary calculation:

$$\begin{aligned} q^{n+\frac{1}{2}}_{i,j,k} = q^n_{i,j,k} \; + \; & \frac{\triangle t}{2} c_{i,j,k} \Big[\frac{u^n_{i+\frac{1}{2},j,k} - u^n_{i-\frac{1}{2},j,k}}{\triangle x} + \frac{v^n_{i,j+\frac{1}{2},k} - v^n_{i,j-\frac{1}{2},k}}{\triangle y} \\ & + \frac{w^n_{i,j,k+\frac{1}{2}} - w^n_{i,j,k-\frac{1}{2}}}{\triangle x} \Big] \\ & - \frac{\alpha_{i,j,k}}{2} \Big[u^n_{i+\frac{1}{2},j,k} + u^n_{i-\frac{1}{2},j,k} \Big] \frac{\triangle t}{2} \\ & - \frac{\beta_{i,j,k}}{2} \Big[v^n_{i,j+\frac{1}{2},k} + v^n_{i,j-\frac{1}{2},k} \Big] \frac{\triangle t}{2} \\ & - \frac{\gamma_{i,j,k}}{2} \Big[w^n_{i,j,k+\frac{1}{2}} + w^n_{i,j,k-\frac{1}{2}} \Big] \frac{\triangle t}{2} + f^n_{i,j,k} \frac{\triangle t}{2}, \end{aligned} \tag{12}$$

$$u^{n+\frac{1}{2}}_{i,j,k} = u^n_{i,j,k} + \frac{\triangle t}{2} c_{i,j,k} \Big[\frac{q^{n+\frac{1}{2}}_{i+1,j,k} - q^{n+\frac{1}{2}}_{i,j,k}}{\triangle x} + \frac{A_{i,j,k}}{2} (q^{n+\frac{1}{2}}_{i+1,j,k} + q^{n+\frac{1}{2}}_{i,j,k}) \Big], \tag{13}$$

$$v_{i,j,k}^{n+\frac{1}{2}} = v_{i,j,k}^{n} + \frac{\triangle t}{2} c_{i,j,k}\left[\frac{q_{i,j+1,k}^{n+\frac{1}{2}} - q_{i,j,k}^{n+\frac{1}{2}}}{\triangle y} + \frac{B_{i,j,k}}{2}(q_{i,j+1,k}^{n+\frac{1}{2}} + q_{i,j,k}^{n+\frac{1}{2}})\right], \tag{14}$$

$$w_{i,j,k}^{n+\frac{1}{2}} = w_{i,j,k}^{n} + \frac{\triangle t}{2} c_{i,j,k}\left[\frac{q_{i,j,k+1}^{n+\frac{1}{2}} - q_{i,j,k}^{n+\frac{1}{2}}}{\triangle x} + \frac{C_{i,j,k}}{2}(q_{i,j,k+1}^{n+\frac{1}{2}} + q_{i,j,k}^{n+\frac{1}{2}})\right], \tag{15}$$

where i, j and k are the space indices of x, y and z, $\triangle x, \triangle y$ and $\triangle z$ are the spatial steps, and $\triangle t$ is the negative time step used for migration.

These auxiliary variables are then used in the main calculation to determine the variables at the time step $n+1$:

main calculation:

$$\begin{aligned} q_{i,j,k}^{n+1} = q_{i,j,k}^{n} \quad &+ \quad \triangle t c_{i,j,k}\left[\frac{u_{i+\frac{1}{2},j,k}^{n+\frac{1}{2}} - u_{i-\frac{1}{2},j,k}^{n+\frac{1}{2}}}{\triangle x} + \frac{v_{i,j+\frac{1}{2},k}^{n+\frac{1}{2}} - v_{i,j-\frac{1}{2},k}^{n+\frac{1}{2}}}{\triangle y}\right. \\ &+ \quad \left.\frac{w_{i,j,k+\frac{1}{2}}^{n+\frac{1}{2}} - w_{i,j,k-\frac{1}{2}}^{n+\frac{1}{2}}}{\triangle x}\right] \\ &- \quad \frac{\alpha_{i,j,k}}{2}\left[u_{i+\frac{1}{2},j,k}^{n+\frac{1}{2}} + u_{i-\frac{1}{2},j,k}^{n+\frac{1}{2}}\right]\triangle t \\ &- \quad \frac{\beta_{i,j,k}}{2}\left[v_{i,j+\frac{1}{2},k}^{n+\frac{1}{2}} + v_{i,j-\frac{1}{2},k}^{n+\frac{1}{2}}\right]\triangle t \\ &- \quad \frac{\gamma_{i,j,k}}{2}\left[w_{i,j,k+\frac{1}{2}}^{n+\frac{1}{2}} + w_{i,j,k-\frac{1}{2}}^{n+\frac{1}{2}}\right]\triangle t + f_{i,j,k}^{n+\frac{1}{2}}\triangle t, \end{aligned} \tag{16}$$

$$u_{i,j,k}^{n+1} = u_{i,j,k}^{n} + \triangle t c_{i,j,k}\left[\frac{q_{i+1,j,k}^{n+\frac{1}{2}} - q_{i,j,k}^{n+\frac{1}{2}}}{\triangle x} + \frac{A_{i,j,k}}{2}(q_{i+1,j,k}^{n+\frac{1}{2}} + q_{i,j,k}^{n+\frac{1}{2}})\right], \tag{17}$$

$$v_{i,j,k}^{n+1} = v_{i,j,k}^{n} + \triangle t c_{i,j,k}\left[\frac{q_{i,j+1,k}^{n+\frac{1}{2}} - q_{i,j,k}^{n+\frac{1}{2}}}{\triangle y} + \frac{B_{i,j,k}}{2}(q_{i,j+1,k}^{n+\frac{1}{2}} + q_{i,j,k}^{n+\frac{1}{2}})\right], \tag{18}$$

$$w_{i,j,k}^{n+1} = w_{i,j,k}^{n} + \triangle t c_{i,j,k}\left[\frac{q_{i,j,k+1}^{n+\frac{1}{2}} - q_{i,j,k}^{n+\frac{1}{2}}}{\triangle z} + \frac{C_{i,j,k}}{2}(q_{i,j,k+1}^{n+\frac{1}{2}} + q_{i,j,k}^{n+\frac{1}{2}})\right]. \tag{19}$$

Stability of the difference scheme is subject to the dimensions of the time and space steps. To ensure stability, the time step should satisfy

$$|\triangle t| \leq \frac{min(\triangle x, \triangle y, \triangle z)}{\sqrt{3}|c_{max}|}. \tag{20}$$

The absorbing boundary condition (Clayton and Engquist, 1980) has been applied to the two side boundaries and the lower boundary.

With this two-step calculation, we can obtain the depth migration image for spatially variable characteristics of the media.

NUMERICAL EXAMPLES

I have tested this two-step explicit method on problems of two-dimensional depth migration, in the case where $\frac{\partial}{\partial y} = 0$. Input data in one set of tests consisted of unit impulses for two media: one with constant velocity and the other with constant velocity gradient in depth. In other tests involving a reflector model, both constant velocity and variable velocity fields are considered. Tests were also made with density that varies linearly with depth. The results show that the density factor influences only the amplitude of the image.

Impulse response

Figure 1 shows the impulse responses of the two-step algorithm where velocity is a constant 2.0 km/s. Here, density is also constant, the spatial steps are equal to 0.02 km ($\triangle x = \triangle z = 0.02$ km), and the time step is -2 ms ($\triangle t$ = -2 ms). From the figure, it can be seen that three clear semicircular reflectors are in the right positions with the highest dip close to 90 degrees. The weakening in amplitude at higher dips is probably caused by insufficient data recorded (i.e., insufficient migration aperture). For comparison, the one-step explicit finite-difference scheme applied to equation (1) yields the impulse responses given in Figure 2. Strong dispersion arises in that finite-difference scheme. Another test for lower frequency (5 times lower) gives the result that the dispersion becomes weakening.

Figure 3 shows impulse responses for the case where velocity is linearly increasing with depth, $c = 2.0 + 0.6z$ km/s, with density kept constant. For this velocity model, the two-step explicit method can image reflectors beyond 90 degrees.

Other tests made for density linearly increasing with depth give the same image positions as for the constant density field (Figures 1 and 3), but the density factor influences the amplitude of the image.

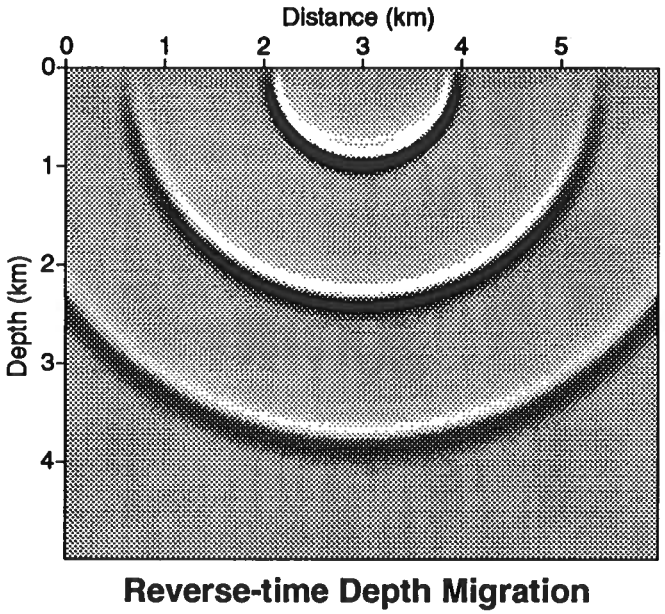

FIG. 1. Impulse response for a constant background velocity of 2.0 km/s by using two-step explicit method.

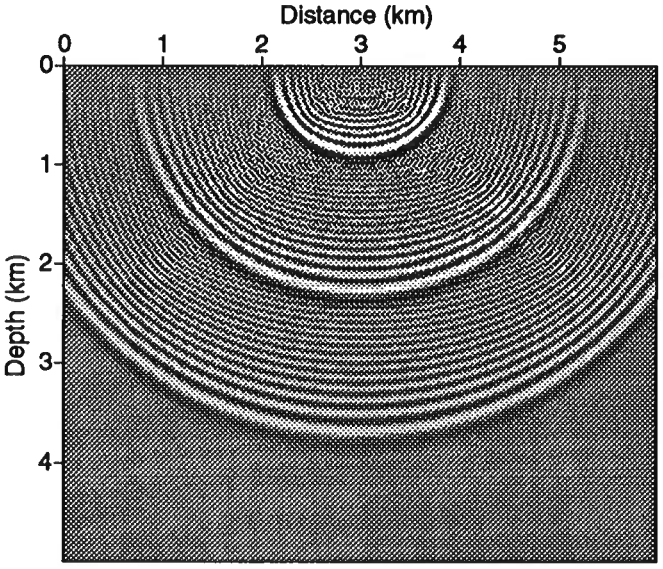

FIG. 2. Impulse response for a constant background velocity of 2.0 km/s by directly applying the one-step explicit finite-difference scheme to wave equation (1).

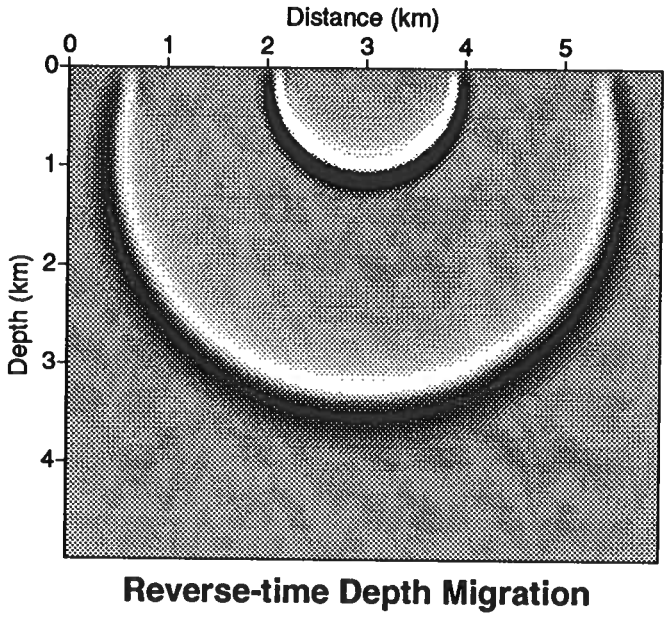

FIG. 3. Impulse response for the velocity which linearly increasing with depth, $c = 2.0 + 0.6z$ km/s.

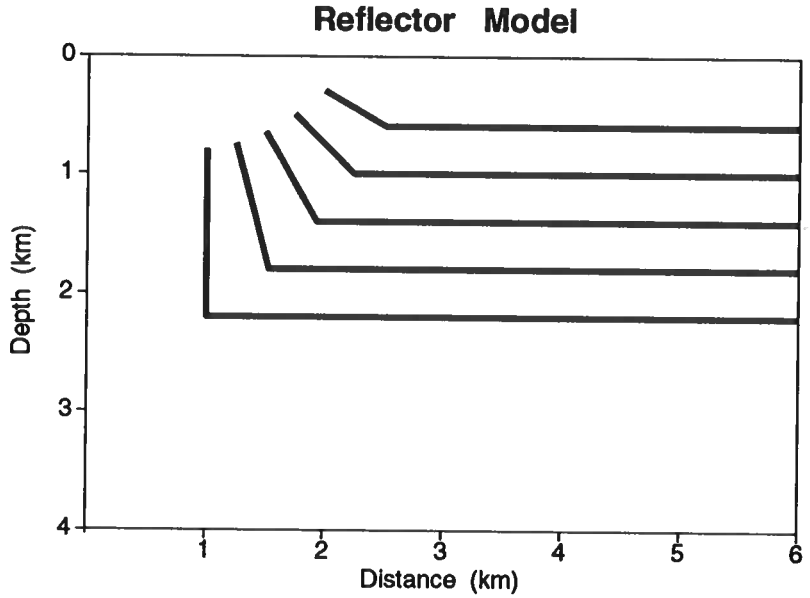

FIG. 4. Reflector model used to generate synthetic data for the tests described in Figures 5 through 9.

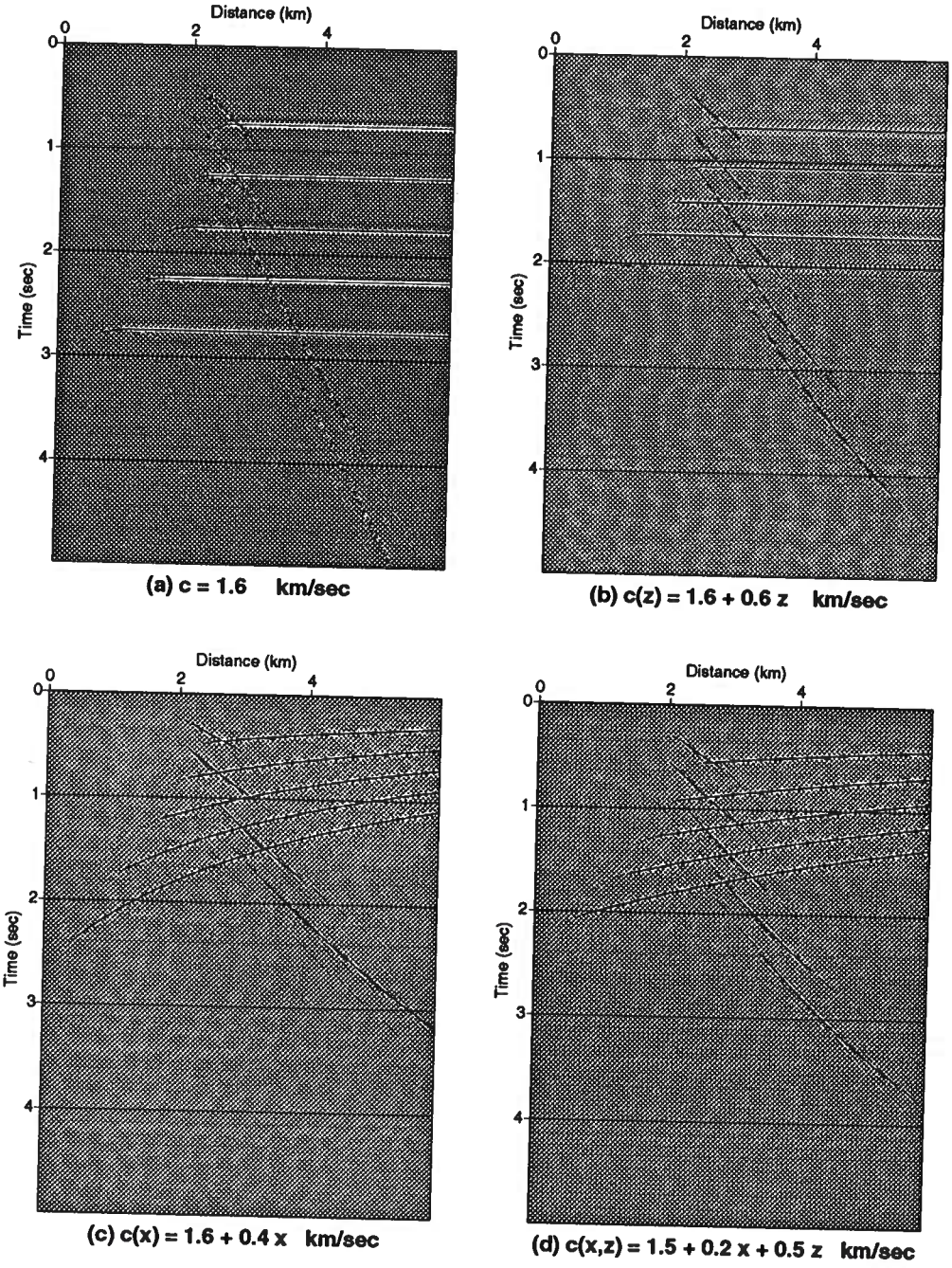

FIG. 5. Zero-offset synthetic time sections generated by Kirchhoff modeling (Hale, 1991) (a) for constant velocity $c = 1.6$ km/s, (b) for velocity linearly increasing with depth, $c(z) = 1.6 + 0.6z$ km/s, (c) for velocity linearly increasing in the horizontal direction, $c(x) = 1.6 + 0.4x$ km/s, (d) for velocity model $c(x, z) = 1.5 + 0.2x + 0.5z$ km/s.

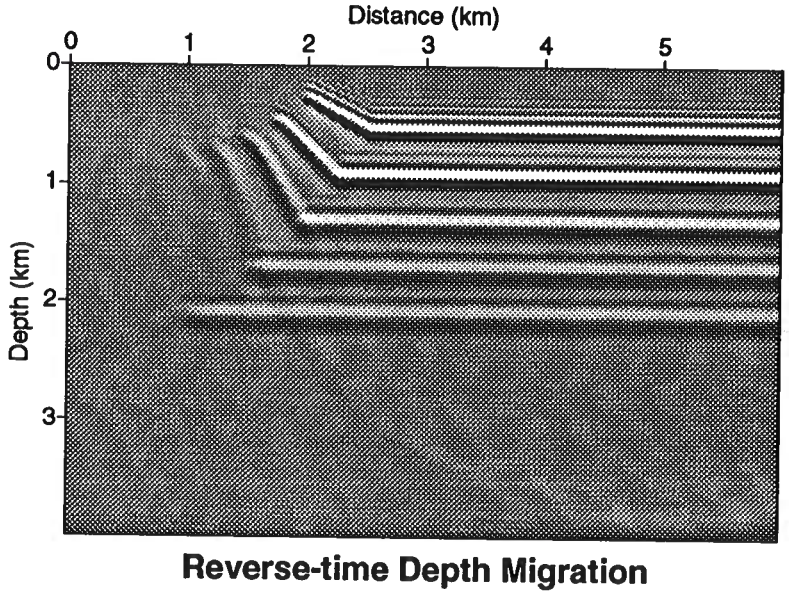

FIG. 6. Migrated section with constant velocity, $c = 1.6$ km/s.

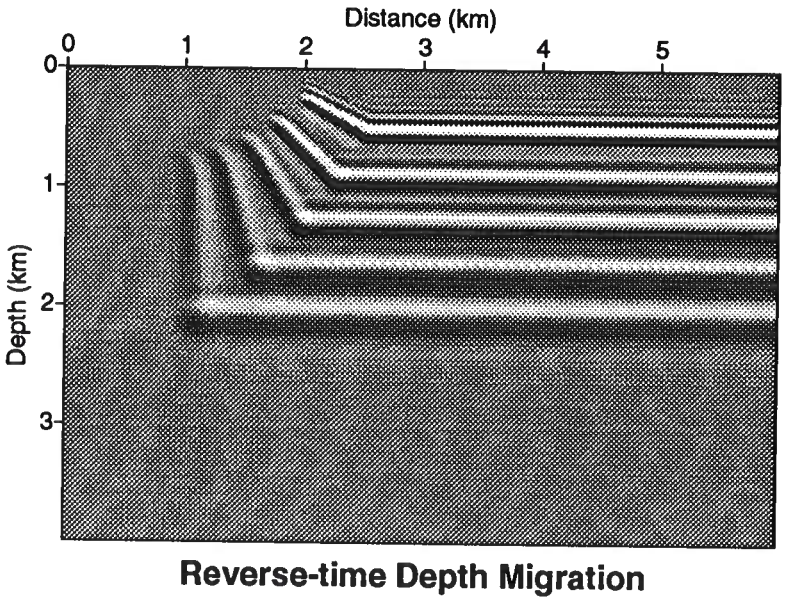

FIG. 7. Migrated section with velocity model $c(z) = 1.6 + 0.6z$ km/s.

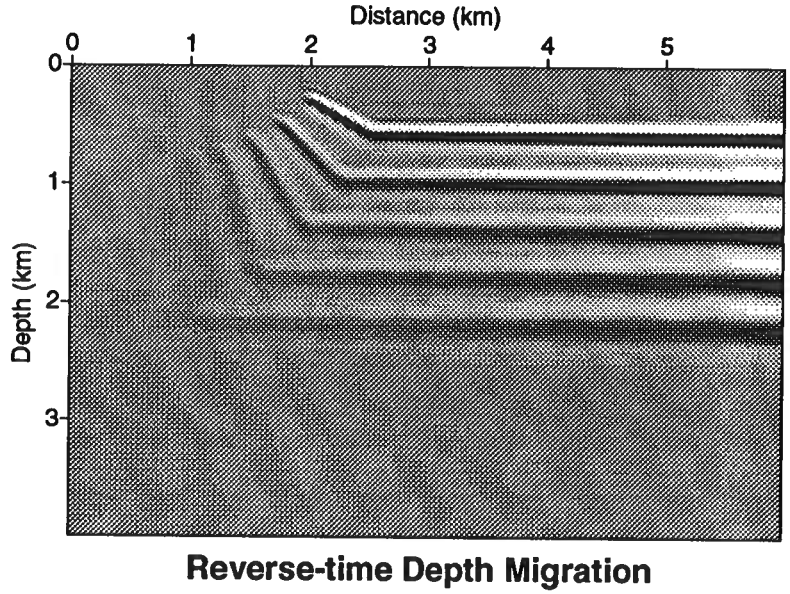

FIG. 8. Migrated section with velocity model $c(x) = 1.6 + 0.4x$ km/s.

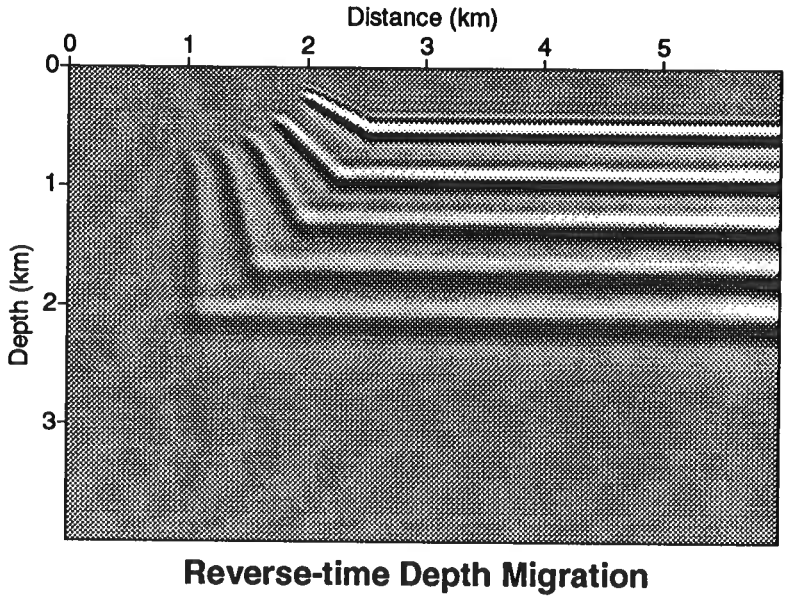

FIG. 9. Migrated section with velocity model $c(x, z) = 1.5 + 0.2x + 0.5z$ km/s.

Reflector model

The model shown in Figure 4 has five horizontal reflectors and five dipping reflectors with dips varying from 30 degrees to 90 degrees in 15-degree increments. The input zero-offset time section was obtained by a Kirchhoff modeling program developed by Hale (1991).

The first example is for a constant velocity of 2.0 km/s. The synthetic data are shown in Figure 5a. The migrated section (Figure 6) shows that a good image is obtained for horizontal reflectors and for reflectors with dip up to 60 degrees. For steeper reflectors the image is poor because insufficient data were recorded. For a vertical reflector, synthetic data cannot be recorded in constant velocity media, so no migrated image is obtained.

The second example illustrates the migrated image for velocity linearly increasing with depth, $c(z) = 1.6+0.6z$ km/s. Figure 5b gives the synthetic data for this velocity model. The migrated section (Figure 7) indicates that this two-step explicit method can accurately image the 90-degree dipping reflector.

The third example is for variable velocity which is increasing horizontally, $c(x) = 1.6 + 0.4x$ km/s. The synthetic time section is given in Figure 5c. The migrated result (Figure 8) indicates that with laterally varying velocity the two-step explicit method can give correct reflector positions for all dips. For the 90-degree event, the recorded synthetic data are insufficient (Figure 5c), so we can hardly see the image. The amplitudes appear weak for deep events and for the events in the slow velocity region. Another test for a velocity field decreasing horizontally, $c(x) = 4.0 - 0.4x$ km/s, gives the same behavior. The reason for this is not fully understood yet, further research is required.

For a velocity field that is changing both vertically and horizontally, $c(x, z) = 1.5+0.2x+0.5z$ km/s, the synthetic time section is given in Figure 5d. The migrated section (Figure 9) shows that we can accurately locate the horizontal, dipping, and vertical reflectors. In this case, the result is qualitatively somewhere between that for the two preceding cases. For the same reason as in the third example, the amplitudes are weak for the events in the slow velocity region and at greater depth.

CONCLUSIONS

A two-step explicit reverse-time depth migration method is presented which can be applied to arbitrary velocity and density fields (2-D in this application). Starting with the acoustic wave equation, the new set of first-order partial differential equations involves no additional assumptions. The migrated results show that this method can accurately image the positions of reflectors with up to 90-degree dips for constant velocities if sufficient data have been recorded, and beyond 90 degrees for variable velocities, but the amplitude are weakening for the deep events and the events in the slow velocity region. Strong dispersion in Figure 2 suggests that directly applying the

one-step explicit finite-difference scheme to the wave equation (1) cannot correctly get the migrated images. Other results suggest that when the density varies linearly with depth, this variable density field does not influence the imaged positions of the reflectors.

ACKNOWLEDGMENTS

Thanks to Ken Larner for his critical reading of this paper. I also thank Dave Hale for helpful discussions and comments. I gratefully acknowledge the support of the members at the Center for Wave Phenomena, Colorado School of Mines.

REFERENCES

Claerbout, J. F., 1985, Imaging of the earth's interior: Blackwell Scientific Publications, Inc.

Clayton, R.W., and Engquist, B., 1980, Absorbing side boundary conditions for wave equation migration: Geophysics, **45**, 895-904.

Hale, D., 1991, Synthetic seismograms for linear velocity function: CWP software, Colorado School of Mines.

Kosloff, D. Dan and Baysal, Edip, 1983, Migration with the full acoustic wave equation: Geophysics, **48**, 677-687.

Migration by the Kirchhoff, Slant Stack, and Gaussian Beam Methods

Dave Hale

Center for Wave Phenomena
Colorado School of Mines
Golden, Colorado 80401
(303) 273-3557

Migration by the Kirchhoff, slant stack, and Gaussian beam methods

Dave Hale

ABSTRACT

Gaussian beam migration offers features that are unmatched by any other single depth migration method. Unfortunately, computer algorithms for Gaussian beam migration are more complicated and difficult to understand than those for most other methods.

One way to simplify Gaussian beam migration is to understand how it is related to other methods that may be more familiar. In particular, Gaussian beam migration is similar to Kirchhoff integral migration. It is also similar to the phase-shift (or slant stack) migration method. In a sense, the Gaussian beam approach to depth migration is to combine the best of these more familiar methods to obtain an efficient, robust, and flexible method for seismic imaging.

INTRODUCTION

Computer programs for Gaussian beam migration tend to be more complicated than those for migration via Kirchhoff, finite-difference, or Fourier transform methods. The software development effort required to implement Gaussian beam migration is substantial, and it is difficult to know whether or not the effort is worthwhile unless you have already made it. Or unless someone else has.

Fortunately, enough research on Gaussian beam migration has recently been published and presented that newcomers to the method (like me) should expect to be rewarded for the time and money invested in understanding and implementing it. In particular, work by Costa, et al. (1989), Lazaratos and Harris (1990), and Hill (1990, 1991) suggests that Gaussian beam migration provides desirable features that are not available with any other single method commonly used today. Among these features are computational efficiency, robustness with respect to ray caustics and shadows, the ability to image reflector dips greater than 90 degrees with turning waves, and straightforward extensions for migration of non-zero-offset sections and 3-D seismic

data. Table 1 provides a brief comparison of several depth migration methods, with respect to these features.

Method	Domain	Efficiency	Robustness	TW?	NZO?
Reverse-time	(t, x, z)	Poor	Good	Yes	No
Finite-difference	(ω, x, z)	Good	Good	No	No
Kirchhoff	(t, x, z)	Good	Poor	Yes	Yes
Slant stack	(τ, p_x, x, z)	Good	Poor	Yes	Yes
Gaussian beam	(τ, p_x, x, z)	Good+	Good	Yes	Yes

Table 1. A subjective comparision of depth migration methods. TW and NZO denote abilities to handle turning waves and non-zero-offset (constant-offset) sections, respectively.

This paper is an introduction to Gaussian beam migration, targeted for readers who are already familiar with migration methods commonly used today, who can appreciate analogies drawn between Gaussian beam migration and more familiar methods. In particular, Gaussian beam migration is shown here to lie somewhere between the Kirchhoff and slant stack migration methods. Slant stack migration, while perhaps the least familiar method listed in Table 1, is shown below to be a variant of the well-known phase-shift (Gazdag, 1978) method.

This paper is not intended to be a substitute for Hill's (1990) paper, which contains several figures and examples that are particularly useful for understanding Gaussian beam migration. Also, this paper does not introduce curvilinear, ray-centered coordinates and their use in Gaussian beam migration, not because these subjects are intuitive or irrelevant, but rather because they have been well presented by others (e.g., Červený et al., 1982). Here, only Cartesian coordinates are used.

Parts of this paper are intended to clarify some parts of Hill's (1990) paper that I found difficult to follow, such as equations (23) through (27) of that paper. Also, this paper derives equations, analogous to Hill's equations (34a) and (34b), for two key sampling parameters that must be computed in Gaussian beam migration.

KIRCHHOFF MIGRATION

Migration in this paper will be discussed in the context of the simplest 2-D, acoustic, constant-density wave equation:

$$\frac{\partial^2 w}{\partial x^2} + \frac{\partial^2 w}{\partial z^2} - \frac{1}{v^2}\frac{\partial^2 w}{\partial t^2} = 0, \tag{1}$$

where $w = w(t, x, z)$ denotes a pressure wavefield, a function of time t, horizontal distance x, and depth z. For migration of zero-offset (stacked) seismic data, based on the exploding reflectors principle (e.g., Claerbout, 1985), the velocity $v = v(x, z)$ in this equation must be replaced with half-velocity $v/2$. For simplicity, I will assume that v in equation (1) has already been halved.

The Kirchhoff integral method of poststack migration (e.g., Schneider, 1978) can be summarized by the simple equation:

$$g(x,z) = \int dx'\, A(x',x,z) f[t = t(x',x,z), x'], \tag{2}$$

where $g(x,z)$ denotes the subsurface image, and $f(t,x)$ denotes the seismic data recorded at the surface $z = 0$.

The functions $t(x',x,z)$ and $A(x',x,z)$ represent the traveltime and amplitude of a seismic wave that travels from the point $(x', z = 0)$ to the point (x,z). In actual implementations of Kirchhoff migration, some additional filtering of the seismic data $f(t,x)$ must be performed; this filtering is not relevant here and has been omitted in equation (2).

Computations implied by equation (2) can be performed in several ways, depending on the order in which one loops through the variables x', x, and z. Perhaps the most efficient implementation is

Kirchhoff migration:

for all points (x,z) {
    $g(x,z) = 0$
}

for all x' *(all seismic traces)* {
    for all points (x,z) {
        compute $t(x',x,z)$ *and* $A(x',x,z)$
        accumulate contribution to $g(x,z)$ *of* $f(t,x')$
    }
}

The most difficult part of this algorithm is the accurate and efficient computation of the time and amplitude functions $t(x',x,z)$ and $A(x',x,z)$. This problem is difficult, in part, because these functions may be multi-valued; i.e., more than one seismic wave may arrive at the surface location $(x', z = 0)$ from the same subsurface point (x,z).

This problem is illustrated in Figure 1, which shows the contribution to the migrated image of a single (synthetic) seismic trace "recorded" at surface location $x' = 5\,\text{km}$. The velocity function $v(x,z)$ used in this example has a low-velocity zone centered at horizontal distance $x = 4\,\text{km}$ and depth $z = 1.5\,\text{km}$, embedded in a linearly increasing velocity function $v(x,z) = 1.5 + 0.6z$. Rays traced from the surface location x' are superimposed on the image to highlight the multiple wavefronts at points in the lower left corner of the image. Rays that intersect at subsurface locations (x,z) imply multi-valued functions $t(x',x,z)$ and $A(x',x,z)$.

Ray tracing, such as that illustrated in Figure 1, is often used to compute the functions $t(x',x,z)$ and $A(x',x,z)$. In this example, many of the rays traced from

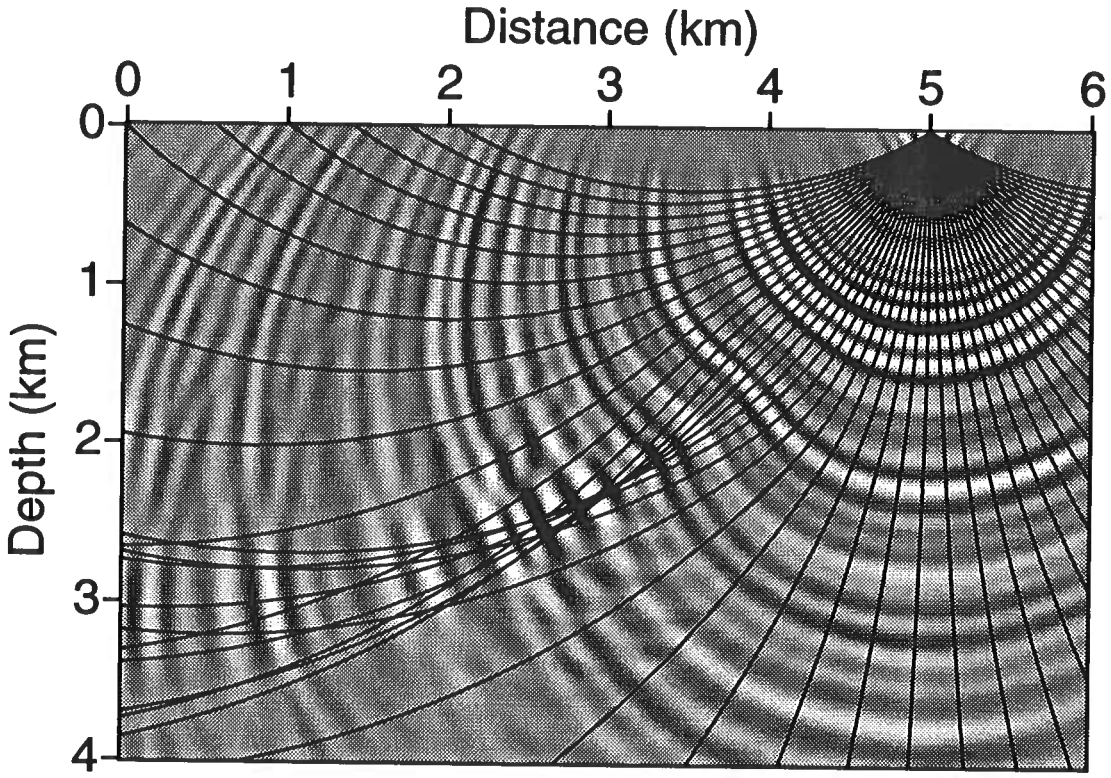

FIG. 1. Contribution of one (synthetic) seismic trace in depth migration. Note (1) the complicated behavior in the lower left corner caused by a low-velocity zone, and (2) that one trace has contributed to almost every point in this subsurface image. In Kirchhoff migration, the complete image is obtained by summing the contributions from all traces.

the surface location $x' = 5\,\text{km}$ pass through or near the low-velocity lens and cross in the lower left corner of the model. Asymptotic (WKBJ, high-frequency) ray theory erroneously yields infinite amplitudes where rays cross. Even if the amplitude factor A is omitted from equation (2), it is difficult and computationally expensive to find all of the rays and their corresponding traveltimes t between two points (x, z) and $(x', z = 0)$.

A recent and popular alternative to ray tracing is the direct solution of a non-linear partial differential equation (the eikonal equation) for the traveltime function t (e.g., Vidale, 1988; Van Trier and Symes, 1991). This method and other similar alternatives to ray tracing yield only the shortest traveltime t between any two points (x, z) and $(x', z = 0)$. Such methods fail to account for the multiple arrivals in the lower left corner of Figure 1.

The problems caused by multi-valued time and amplitude functions (and infinite amplitudes) tend to make Kirchhoff migration less robust in handling lateral velocity variations than the other methods listed in Table 1. In fact, a Gaussian beam method was used to compute the single-trace contribution shown in Figure 1. I did not

attempt to reproduce this result with a Kirchhoff depth migration, primarily because of the computational difficulties described above.

The computational cost of Kirchhoff migration is easy to estimate, given the algorithm outlined above. The cost is proportional to the number of traces (number of x') times the number of subsurface points (x, z) to be imaged. Assuming that the number of samples in each dimension (time or space) is proportional to, say, the number of time samples N in each seismic trace, the cost of Kirchhoff migration goes as N^3. This estimate is based on the assumption that $t(x', x, z)$ and $A(x', x, z)$ can be computed in constant time for any given x', x, and z. As shown below, a cost proportional to N^3 is typical of depth migration methods.

SLANT STACK MIGRATION

The second depth migration method considered in this paper is one that, to my knowledge, is never used. It is useful only because it is similar to migration methods that are used, and because it represents one extreme in a spectrum of migration methods that includes Gaussian beam migration.

Phase-shift migration

First, recall Gazdag's (1978; Claerbout, 1985, 30–33) phase-shift method for depth extrapolation of a seismic wavefield in the frequency-wavenumber (ω, k_x) domain:

$$W(\omega, k_x, z) = W(\omega, k_x, z=0)\, A(k_x/\omega, z)\, e^{-i\omega \int_0^z d\zeta \frac{\cos\theta(k_x/\omega,\zeta)}{v(\zeta)}}, \tag{3}$$

where $\theta(p_x, z)$ is the angle defined by

$$\sin\theta(p_x, z) = v(z)p_x,$$

and

$$A(p_x, z) = \left[\frac{v(z)\cos\theta_0}{v_0\cos\theta(p_x, z)}\right]^{1/2}. \tag{4}$$

Equation (3) is the WKBJ solution (e.g., Aki and Richards, 1980, 416) to the differential equation,

$$\frac{d^2W}{dz^2} + \left[\frac{\omega^2}{v^2(z)} - k_x^2\right] W = 0,$$

which is the wave equation (1), expressed in the frequency-wavenumber domain. Although velocity $v(z)$ is here restricted to be a function of depth z only, this limitation will be removed below.

The angle $\theta(p_x, z)$ defined above is the propagation angle at depth z of a plane wave that emerges at the earth's surface with angle θ_0 and velocity v_0 satisfying $\sin\theta_0 = v_0 p_x$.

In phase-shift migration, the amplitude function $A(p_x, z)$ is often omitted, in part because it goes to infinity as z approaches the turning point, that depth where

$\theta(p_x, z) = \pm 90$ degrees. This erroneous infinite amplitude is similar to that encountered when performing Kirchhoff migration with WKBJ amplitudes determined by ray tracing.

For migration of zero-offset seismic data $f(t,x)$, we identify $W(\omega, k_x, z=0)$ as the Fourier transformed data $F(\omega, k_x)$. Inverse Fourier transform equation (3) from wavenumber k_x to distance x,

$$W(\omega, x, z) = \frac{1}{2\pi} \int dk_x \, A(k_x/\omega, z) \, e^{-i\omega \int_0^z d\zeta \frac{\cos\theta(k_x/\omega,\zeta)}{v(\zeta)} + ik_x x} \, F(\omega, k_x), \tag{5}$$

and then evaluate the inverse Fourier transform from frequency ω to time t at $t=0$ to obtain the subsurface image

$$\begin{aligned} g(x,z) &= \frac{1}{2\pi} \int d\omega \, e^{-i\omega t=0} \, W(\omega, x, z) \\ &= \frac{1}{4\pi^2} \int d\omega \int dk_x \, A(k_x/\omega, z) \, e^{-i\omega \int_0^z d\zeta \frac{\cos\theta(k_x/\omega,\zeta)}{v(\zeta)} + ik_x x} \, F(\omega, k_x). \end{aligned} \tag{6}$$

Equation (6) concisely summarizes the phase-shift migration method.

From wavenumber k_x to reflection slope p_x

The ratio $p_x = k_x/\omega$ that appears in phase-shift migration corresponds to the slope of a reflection recorded in the seismic data $f(t,x)$. Equation (5) implies that each reflection slope p_x can be extrapolated in depth independently. This motivates a change in integration variable from k_x to p_x:

$$\begin{aligned} W(\omega, x, z) &= \frac{1}{2\pi} \int dp_x \, |\omega| A(p_x, z) e^{-i\omega \int_0^z d\zeta \frac{\cos\theta(p_x,\zeta)}{v(\zeta)} + i\omega p_x x} \, F(\omega, k_x = \omega p_x) \\ &= \int dp_x \, A(p_x, z) e^{-i\omega\tau(p_x,x,z)} B(\omega, p_x), \end{aligned} \tag{7}$$

where

$$B(\omega, p_x) \equiv \frac{|\omega|}{2\pi} F(\omega, k_x = \omega p_x), \tag{8}$$

and

$$\tau(p_x, x, z) \equiv \int_0^z d\zeta \, \frac{\cos\theta(p_x, \zeta)}{v(\zeta)} - p_x x. \tag{9}$$

With this change of variables, equation (6) becomes

$$g(x,z) = \int dp_x \, A(p_x, z) \, \frac{1}{2\pi} \int d\omega \, e^{-i\omega\tau(p_x,x,z)} \, B(\omega, p_x).$$

Recognizing that the integral over frequency ω is just an inverse Fourier transform, we obtain the following expression for the subsurface image:

$$g(x,z) = \int dp_x \, A(p_x, z) \, b[\tau = \tau(p_x, x, z), p_x]. \tag{10}$$

An appropriate name for equation (10) is *slant stack migration* because the function $b(\tau, p_x)$ is a filtered slant stack of the surface seismic data $f(t, x)$. Specifically,

$$b(\tau, p_x) = \rho(\tau) * \int dx\, f(t = \tau + p_x x, x),$$

where $\rho(\tau)$ is the so-called "rho" filter defined by

$$\rho(\tau) \equiv \frac{1}{2\pi} \int d\omega\, e^{-i\omega\tau} \frac{|\omega|}{2\pi}.$$

To verify this relationship between $b(\tau, p_x)$ and $f(t, x)$, Fourier tranform $b(\tau, p_x)$ to obtain

$$\begin{aligned} B(\omega, p_x) &= \frac{|\omega|}{2\pi} \int d\tau\, e^{i\omega\tau} \int dx\, f(t = \tau + p_x x, x) \\ &= \frac{|\omega|}{2\pi} \int dx\, e^{-i\omega p_x x}\, F(\omega, x) \\ &= \frac{|\omega|}{2\pi} F(\omega, k_x = \omega p_x), \end{aligned}$$

which matches the definition of $B(\omega, p_x)$ given by equation (8) above.

Although the derivation of slant stack migration above began with the restriction that velocity varies with depth only, equation (10) can be generalized to account for lateral velocity variations, as suggested by the work of Sinton and Frazer (1982). In the general case of $v = v(x, z)$, the amplitude function A depends on horizontal distance x as well as reflection slope p_x and depth z, and both functions $A(p_x, x, z)$ and $\tau(p_x, x, z)$ are more difficult to compute than for the laterally homogeneous case.

However, as in Kirchhoff migration, these functions can be computed by ray tracing. In particular, the function $\tau(p_x, x, z)$ can be computed by

$$\tau(p_x, x, z) = t(p_x, x, z) - p_x x', \tag{11}$$

where $t(p_x, x, z)$ denotes the time required for a ray to travel from the subsurface point (x, z) to the surface with emergence angle $\theta_0 = \arcsin(v_0 p_x)$. v_0 denotes the velocity at the surface location x' where the ray intersects the surface. Substitution of the traveltime function $\tau(p_x, x, z)$ defined by equation (11) and a corresponding amplitude function $A(p_x, x, z)$ into equation (10) yields *slant stack depth migration.*

The most straightforward algorithm for slant stack migration is analogous to that for Kirchhoff migration:

Slant stack migration:

compute filtered slant stack $b(\tau, p_x)$ *of seismic data* $f(t, x)$

for all points (x, z) {
    $g(x, z) = 0$
}

for all p_x *(all reflection slopes)* {
    for all points (x, z) {
        compute $\tau(p_x, x, z)$ *and* $A(p_x, x, z)$
        accumulate contribution to $g(x, z)$ *of* $b(\tau, p_x)$
    }
}

As for Kirchhoff migration, the most difficult part of this algorithm is the accurate and efficient computation of the time and amplitude functions $\tau(p_x, x, z)$ and $A(p_x, x, z)$. Again, these functions may be multi-valued. Figure 2 shows the contribution to the migrated image of a single reflection slope p_x, corresponding to an emergence angle of 20 degrees. The velocity function $v(x, z)$ used in this example is the same as that of Figure 1. Rays with the same emergence angle, but different emergence locations, are superimposed on the image. Where rays intersect at a subsurface point (x, z), the functions $\tau(p_x, x, z)$ and $A(p_x, x, z)$ are multi-valued.

Even when velocity varies with depth only, the time (and amplitude) functions may be multi-valued. To see why, simply trace two rays with the same emergence angle, but different emergence locations, backwards into a subsurface in which velocity increases with depth. The rays will intersect after one of them has turned beyond 90 degrees. When velocity varies with depth only, just two times $\tau(p_x, x, z)$ are feasible — one corresponds to the ray that has not yet reached its turning point, and the other corresponds to the turned ray.

Assuming that ray tracing is used to compute the necessary time (and amplitude) functions, the difference between the ray tracing for Kirchhoff depth migration and that for slant stack depth migration is interesting. In Kirchhoff migration, we require the time $t(x', x, z)$, which we may determine by tracing rays with different emergence angles θ_0 backwards from the emergence location x', until we find all of the rays that pass through the subsurface point (x, z). In this approach, given x', x, and z, we search for the appropriate emergence angles θ_0, or equivalently, reflection slopes p_x. In slant stack migration, we require the time $\tau(p_x, x, z)$. Given p_x, x, and z, we search for the emergence locations x' required by equation (11).

In a computer implementation of slant stack migration, we must convert the integral over reflection slope p_x in equation (10) to a sum, which implies that we must determine how finely to sample p_x. The definition of $p_x = k_x/\omega$ suggests that we

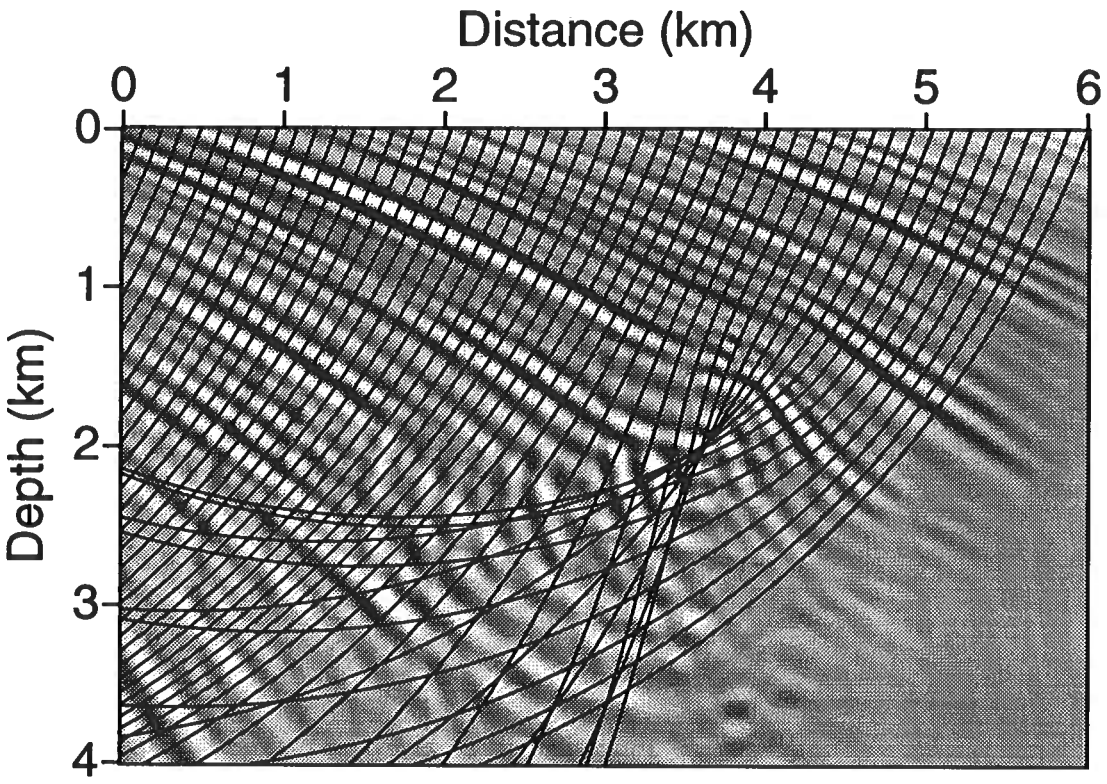

FIG. 2. Contribution of one reflection slope p_x in depth migration. Note (1) the complicated behavior in the lower left corner caused by a low-velocity zone, and (2) that one slope p_x contributes to almost every point in the subsurface image. In slant stack migration, the complete image is obtained by summing the contributions from all reflection slopes.

choose $\Delta p_x = \Delta k_x/\omega$, where Δk_x is the sampling of wavenumber k_x we would use in phase-shift migration. To avoid aliasing, we would choose $\Delta k_x = 2\pi/X$, where X denotes the horizontal width of the seismic data to be migrated. To implement equation (10) we must use a sampling interval p_x that is independent of frequency. Therefore, we choose

$$\Delta p_x = \frac{2\pi}{\omega_h X}, \tag{12}$$

to avoid aliasing frequencies less than the highest frequency of interest, ω_h.

Because of the similarities between the algorithms for Kirchhoff and slant stack migrations, it is easy to verify that slant stack migration, like Kirchhoff migration, has a computational cost proportional to N^3, where N is again the number of time samples. The number of slopes p_x that must be imaged is, from equation (12), proportional to the number of seismic traces, which tends to grow in proportion to N. The cost of computing the filtered slant stacks $b(\tau, p_x)$ via FFTs [equation (8)] is proportional to $N^2 \log N$ and is, therefore, likely to be a negligible part of the total cost proportional to N^3.

Given their similar computational costs, one might wonder why slant stack migration is used less often than Kirchhoff migration. Perhaps the best explanation is that *slant stack migration is less straightforward and no better than Kirchhoff migration.* Slant stack migration is certainly no more robust than Kirchhoff migration. Because of the difficulties in computing the multi-valued time and amplitude functions $\tau(p_x, x, z)$ and $A(p_x, x, z)$, the single-slope contribution shown in Figure 2 was computed via a robust Gaussian beam algorithm, rather than the slant stack algorithm outlined above.

One way to obtain a robust depth migration would be to combine the Kirchhoff and slant stack methods, blending the single-trace and single-slope contributions together to obtain the image at any given subsurface point (x, z). For any (x, z), we might choose the blending weights to emphasize the contribution that is most accurate. For example, where the Kirchhoff method implies infinite amplitude at a point (x, z), we would use the slant stack method to compute the contribution at that point. This blending approach is analogous to that proposed for seismic modeling by Chapman and Drummond (1982). That approach, which is based on Maslov asymptotic theory, depends on the fact (not proven here) that the Kirchhoff and slant stack methods are guaranteed not to fail simultaneously at any point (x, z).

As shown in the following section, Gaussian beams provide another technique for combining the Kirchhoff and slant stack methods to obtain a robust depth migration algorithm.

GAUSSIAN BEAM MIGRATION

Recall that the first step in slant stack migration is the computation of the filtered slant stack $b(\tau, p_x)$ of the seismic data $f(t, x)$ recorded at the surface. This slant stacking decomposes $f(t, x)$ into plane waves, with each reflection slope p_x corresponding to a different plane wave component. In contrast, Kirchhoff migration requires no preliminary decomposition of the seismic data $f(t, x)$; the decomposition into individual seismic traces at unique surface locations x' was performed when the data were recorded.

Gaussian beam migration is similar to slant stack migration, in that it too requires that $f(t, x)$ be decomposed with slant stacking. The difference is that Gaussian beam migration computes many *local slant stacks (beams)*, each computed from small overlapping subsets of the seismic data. As in slant stack migration, each plane wave component of each subset contributes to the migrated image independently, and all contributions are summed to obtain the complete subsurface image.

Local slant stacks

First, we extract a window of the data $f(t, x)$ by applying a lateral shift and a frequency-dependent Gaussian taper:

$$F_j(\omega, x) \equiv e^{-\frac{1}{2}\left|\frac{\omega}{\omega_l}\right|\frac{x^2}{l^2}} F(\omega, x + x_j), \tag{13}$$

where x_j is the center of the Gaussian window, and l is the width (standard deviation) of the Gaussian when frequency $\omega = \omega_l$. It is convenient to choose ω_l to be the lowest frequency of interest, so that l is related to the maximum width of the Gaussian. If we assume a Gaussian amplitude of 1/100 is negligible, then the width of the data window after Gaussian tapering is approximately $X = 6l\sqrt{|\omega_l/\omega|}$.

The local slant stack of $F_j(\omega, x)$ is defined as in equation (8) by

$$\begin{aligned} B_j(\omega, p_x) &\equiv C\frac{|\omega|}{2\pi}\int dx\, e^{-i\omega p_x x}\, F_j(\omega, x) \\ &= C\frac{|\omega|}{2\pi}\, F_j(\omega, k_x = \omega p_x). \end{aligned} \tag{14}$$

The extra scale factor C in this local slant stack will be determined below to normalize the sum of overlapping Gaussian windows.

Local slant stacks, like the slant stacks of the preceding section, must be adequately sampled in p_x. Using the criterion of equation (12), but with X determined by the width of the Gaussian window, we obtain

$$\Delta p_x = \frac{2\pi}{\omega_h X} = \frac{\pi}{3l\sqrt{|\omega_l \omega_h|}}, \tag{15}$$

which guarantees that frequencies less than the highest frequency of interest ω_h will not be aliased. Although the derivation here of Δp_x is quite different, the result is similar to that in Hill's (1990) equation (34b). The only difference is that Hill has a factor of 4 in the denominator where equation (15) has a factor of 3.

Depth extrapolation

Depth extrapolation of the locally slant stacked (beam-formed) data window can be performed as suggested by equation (7):

$$W_j(\omega, x, z) = \int dp_x\, A_j(p_x, x, z) e^{-i\omega\tau_j(p_x, x, z)} B_j(\omega, p_x). \tag{16}$$

The function $W_j(\omega, x, z)$ is only a part of the complete wavefield, because it is computed for a single Gaussian window of data. The complete wavefield is given by summing up contributions from many overlapping windows of data; i.e.,

$$W(\omega, x, z) = \sum_j W_j(\omega, x, z).$$

The key problem here, as in slant stack migration, is to compute the time and amplitude functions $\tau_j(p_x, x, z)$ and $A_j(p_x, x, z)$. The dynamic ray tracing solution to this problem is:

1. Trace *one* ray, with emergence location x_j and emergence angle $\theta_j = \arcsin[v(x_j, 0)p_x]$.

2. Solve *dynamic ray tracing* equations along the ray for both point and plane-wave sources.

3. Combine solutions for both point and plane-wave sources to obtain *complex-valued* time and amplitude functions $\tau_j(p_x, x, z)$ and $A_j(p_x, x, z)$.

A complete explanation of these three steps requires the introduction of concepts such as curvilinear ray-centered coordinates, which in this paper would be an unnecessary distraction. Hill's (1990) paper summarizes these three steps concisely, and more complete discussions are provided by Červený, et al. (1982) and Červený and Pšenčík (1984).

Were it not for the fact that both $\tau_j(p_x, x, z)$ and $A_j(p_x, x, z)$ are complex-valued, depth extrapolation for local slant stacks would be no more robust than that for the global slant stacks of the previous section. The complex combination of solutions to the dynamic ray tracing equations for both point and plane-wave sources ensures that amplitudes will be well-behaved. In particular, the complex-valued amplitude function $A_j(p_x, x, z)$ never goes to infinity, unlike the WKBJ amplitude functions for Kirchhoff, phase-shift, or slant-stack migrations.

Another important feature of the complex times and amplitudes computed by dynamic ray tracing for Gaussian beams is that they are single-valued, unlike those computed for Kirchhoff or slant stack migration.

Matching the surface seismic data

As in slant stack migration, we must ensure that the seismic wavefield at the surface $W(\omega, x, z = 0)$ matches the seismic data $F(\omega, x)$. To this end, we arrange for the complex-valued time and amplitude functions evaluated at $z = 0$ to be

$$\begin{aligned} \tau_j(p_x, x, z = 0) &= p_x(x - x_j) - \frac{i}{2}\frac{\text{sgn}(\omega)}{|\omega_l|}\frac{(x - x_j)^2}{l^2} \\ A_j(p_x, x, z = 0) &= 1. \end{aligned} \tag{17}$$

The choice of the Gaussian width l determines the weighting of the point source and plane-wave source solutions to the dynamic ray tracing equations. Specifically, a tiny l corresponds to a point source, and a huge l corresponds to a plane-wave source.

Inserting the times and amplitudes given by equations (17) into the expression for the seismic wavefield given by equation (16), we obtain

$$\begin{aligned} W_j(\omega, x, z = 0) &= e^{-\frac{1}{2}\left|\frac{\omega}{\omega_l}\right|\frac{(x-x_j)^2}{l^2}} \int dp_x\, e^{i\omega p_x(x-x_j)}\, B_j(\omega, p_x) \\ &= C\, e^{-\frac{1}{2}\left|\frac{\omega}{\omega_l}\right|\frac{(x-x_j)^2}{l^2}}\, F_j(\omega, x - x_j) \\ &= C\, e^{-\left|\frac{\omega}{\omega_l}\right|\frac{(x-x_j)^2}{l^2}}\, F(\omega, x). \end{aligned}$$

The complete wavefield at the surface is

$$\begin{aligned} W(\omega,x,z=0) &= \sum_j W_j(\omega,x,z=0) \\ &= F(\omega,x)\,C\sum_j e^{-\left|\frac{\omega}{\omega_l}\right|\frac{(x-x_j)^2}{l^2}} \\ &\approx F(\omega,x). \end{aligned}$$

Hill (1990) showed that the error in the last approximation is about 1 percent if

$$\begin{aligned} x_j &= j\Delta \\ \Delta &< \left|\frac{2\omega_l}{\omega}\right|^{1/2} l \\ C &= \left|\frac{\omega}{\pi\omega_l}\right|^{1/2}\frac{\Delta}{l}. \end{aligned} \tag{18}$$

Here, Δ is the spacing between the beam center location x_j, the centers of the overlapping Gaussian windows. In order for this spacing to be independent of frequency, we choose

$$\Delta = \left|\frac{2\omega_l}{\omega_h}\right|^{1/2} l, \tag{19}$$

where ω_h is again the highest frequency of interest. The frequency-dependent scale factor C given by equation (18) is most conveniently applied when filtering the local slant stacks, as suggested by equation (14).

Hill's (1990) recommended value for Δ is similar to that given above by equation (19). The only difference is that Hill's equation (34a) has a factor 2 where equation (19) has a factor $\sqrt{2}$. Thus, Hill recommends a somewhat larger spacing between beam center locations and a somewhat finer sampling of p_x [recall equation (15)] than are derived here. The differences between the values for Δ and p_x in this paper and those recommended by Hill are likely due to the application of a Gaussian taper in equation (13) above. A different, non-Gaussian taper is implied by Hill's equation (27).

The subsurface image

Given equation (16), which describes one contribution $W_j(\omega,x,z)$ to the complete seismic wavefield, we need only sum these contributions and integrate over frequency ω, as in slant stack migration, to obtain the subsurface image. Specifically, the complete image is obtained by

$$g(x,z) = \sum_j g_j(x,z),$$

where

$$\begin{aligned} g_j(x,z) &= \frac{1}{2\pi}\int d\omega\, W_j(\omega,x,z) \\ &= \int dp_x\, A_j(p_x,x,z)\,\frac{1}{2\pi}\int d\omega\, e^{-i\omega\tau_j(p_x,x,z)} B_j(\omega,p_x). \end{aligned} \tag{20}$$

If the time and amplitude functions τ_j and A_j in equation (20) were real-valued, then it would be straightforward to identify the integral over frequency as an inverse Fourier transform, and to obtain an equation analogous to equation (10) for slant stack migration. Complex-valued τ_j and A_j make Gaussian beam amplitudes well behaved, but they complicate our implementation of equation (20). In particular, we require that $g_j(x,z)$ be real-valued, which means that we must preserve conjugate symmetry in the frequency domain. Specifically, the sign of the imaginary parts of τ_j and A_j must depend on the sign of ω.

To see how to implement equation (20), we should express τ_j and A_j in terms of their real and imaginary parts:

$$\begin{aligned} \tau &= \tau_R + i\text{sgn}(\omega)\tau_I \\ A &= A_R + i\text{sgn}(\omega)A_I. \end{aligned}$$

Remember that τ_R, τ_I, A_R, and A_I are all functions of the beam center location x_j, the reflection slope p_x, and the subsurface image coordinates (x,z), even though this dependence has not been stated explicitly in order to simplify notation below. In terms of these real and imaginary parts, equation (20) may be written more precisely as

$$g_j(x,z) = \int dp_x \, \frac{1}{2\pi} \int d\omega \, [A_r + i\text{sgn}(\omega)A_I] \, e^{-i\omega\tau_R + |\omega|\tau_I} B_j(\omega, p_x). \tag{21}$$

Note that, to avoid exponential growth of the integrand, we require $\tau_I \leq 0$, which is consistent with equations (17).

Straightforward implementation of equation (21) would require numerous costly integrations over frequency ω. Therefore, we seek an equivalent time-domain expression by first defining

$$\tilde{B}(\omega, \tau_I) \equiv e^{|\omega|\tau_I} B_j(\omega, p_x), \tag{22}$$

followed by its time-domain equivalent

$$\tilde{b}(\tau_R, \tau_I) = \frac{1}{2\pi} \int d\omega \, e^{-i\omega\tau_R} \tilde{B}(\omega, \tau_I). \tag{23}$$

Both $\tilde{B}$ and $\tilde{b}$ are functions of beam center location x_j and reflection slope p_x, although this dependence has been suppressed to simplify notation. To account for the complex amplitude function A in equation (21), recall that multiplication by $-i\text{sgn}(\omega)$ in the frequency domain is equivalent to a Hilbert transform in the time domain. Therefore, equation (21) becomes

$$g_j(x,z) = \int dp_x \, \left[A_R \tilde{b}(\tau_R, \tau_I) - A_I \tilde{b}_H(\tau_R, \tau_I) \right], \tag{24}$$

where $\tilde{b}_H$ denotes the Hilbert transform of $\tilde{b}$. Equation (24) is similar to equation (10) for slant stack migration; the differences are due entirely to the use of complex time and amplitude functions in Gaussian beam migration.

Algorithm and cost

Equation (24), with all of the steps necessary to evaluate the integrand, accounts for most of the computational effort in Gaussian beam migration. It describes the contribution to the subsurface image of one Gaussian-tapered window of seismic data. The complete image is obtained by summing all such contributions, as in the following algorithm for Gaussian beam migration:

Gaussian beam migration:

for all points (x,z) {
    $g(x,z) = 0$
}

for all $x_j = j\Delta$ *(all beam center locations)* {
    compute $f_j(t,x)$ *by shifting and tapering data* $f(t,x)$
    compute filtered slant stack $b_j(\tau,p_x)$ *of* $f_j(t,x)$
    for all p_x *(all reflection slopes)* {
        for all points (x,z) *within beam* {
            compute complex-valued $\tau_j(p_x,x,z)$ *and* $A_j(p_x,x,z)$
            accumulate contribution to $g(x,z)$ *of* $b_j(\tau,p_x)$
        }
    }
}

This algorithm for Gaussian beam migration is similar to both the Kirchhoff and slant stack migration algorithms. One obvious difference is that Gaussian beam migration has two loops outside the innermost loop over subsurface image coordinates (x,z), whereas the Kirchhoff and slant stack methods have only one. This observation might lead us to suspect that Gaussian beam migration is more costly than either Kirchhoff or slant-stack migration. If the cost of the latter algorithms is proportional to N^3, is the cost of Gaussian beam migration proportional to N^4?

The answer to this question is that although the computational cost of Gaussian beam migration is somewhat difficult to estimate, it is certainly no greater than N^3. The cost of the outer two loops is proportional to the number of beam center locations x_j times the number of reflection slopes p_j, which is proportional to N, not N^2. This is because the spacing between beam center locations Δ is proportional to the beam width l at the surface, whereas the sampling interval Δp_x is inversely proportional to l. [Recall equations (15) and (19).] For large beam widths, we have many reflection slopes but few Gaussian windows of data to migrate. For small beam widths, we have more Gaussian windows, but fewer reflection slopes to migrate. Therefore, the cost of the outer two loops in Gaussian beam migration is proportional to N.

Consider now the cost of the innermost loop over subsurface image coordinates (x, z). For Kirchhoff and slant-stack migration, the cost of the innermost loop is proportional to N^2. Each trace or each reflection slope contributes to almost every sample in the subsurface image, a computational grid that tends to grow as the square of the number of time samples N in a seismic trace. For Gaussian beam migration, the cost of the innermost loop is proportional to N times the width of a Gaussian beam. Depending on the beam width, this product may be significantly less than the comparable product for Kirchhoff or slant-stack migration, which accounts for the "Good+" efficiency rating of Gaussian beam migration in Table 1.

Figure 3 illustrates the contribution of one beam in the innermost loop of Gaussian beam depth migration. Although the width of the beam grows with distance from the surface in this example, the area within the beam is less than the area affected by a single trace in Kirchhoff migration or a single reflection slope in slant stack migration.

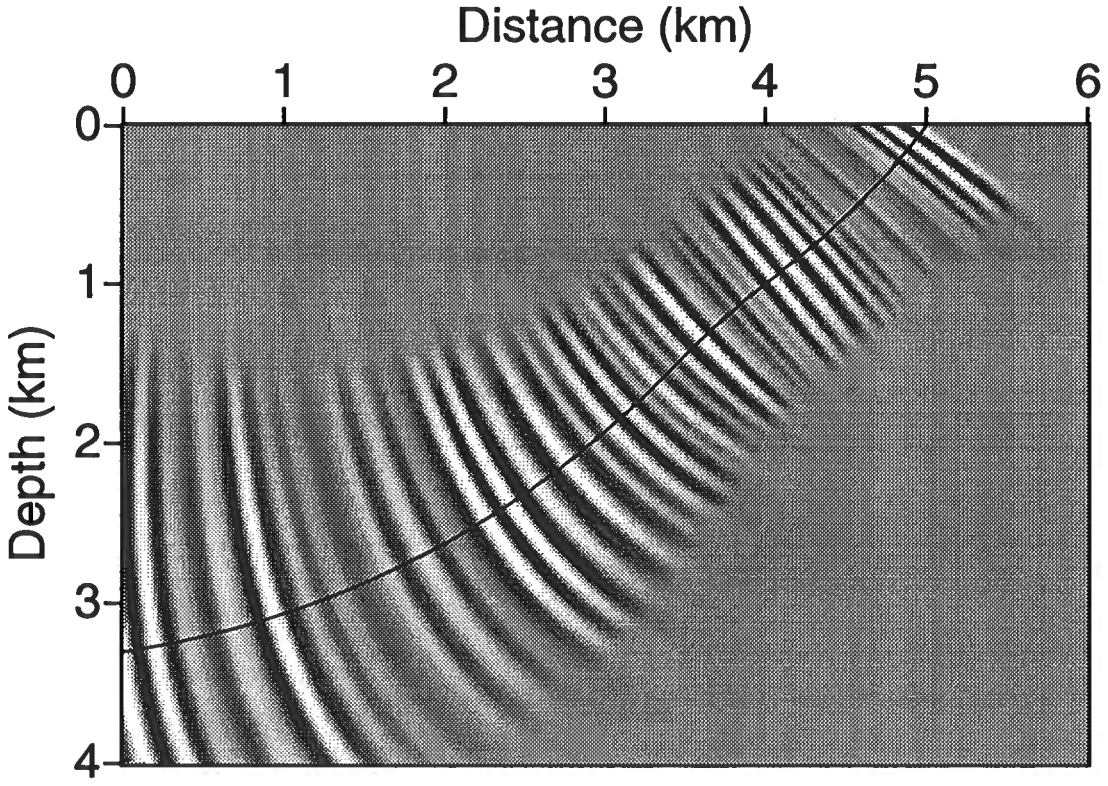

FIG. 3. Contribution of one Gaussian beam in depth migration. Note (1) the distortion of the beam caused by a low-velocity zone, and (2) that one beam contributes to fewer subsurface image points than one trace in Kirchhoff migration or one reflection slope in slant stack migration. The complete image is obtained by accumulating many such contributions.

The difficulty in estimating the cost of Gaussian beam migration lies in the difficulty in estimating the width of the beam, for a given width l at the surface. At great distances from the surface, the beam width becomes asymptotically proportional to N. The important issue is how quickly the beam width approaches its asymptotic

value. However, even in the worst case, where the beam widens rapidly away from the surface, the computational cost of the innermost loop is proportional to N^2. Therefore, the total cost of Gaussian beam migration grows at a rate no greater than N^3.

Note that the wavefronts in the Gaussian beam of Figure 3 are simple, because dynamic ray tracing for a single ray was used to compute the complex-valued time and amplitude functions that describe the beam. Dynamic ray tracing makes these functions single-valued, so that the contribution of a single Gaussian beam to the migrated image is simpler to compute than that of a single trace in Kirchhoff migration or of a single reflection slope in slant stack migration.

CONCLUSION

Kirchhoff integral migration images each seismic trace independently. Because a single trace is very localized in space, it contributes significant energy at all wave propagation angles to the subsurface image. For a single trace, more than one propagation angle can contribute to a single image point.

Slant stack migration images each reflection slope independently. A single reflection slope contributes to a narrow range of propagation angles, but each slope consists of all traces, resulting in extremely wide wavefronts that extend from one end of the seismic section to the other. For a single reflection slope, more than one trace can contribute to a single image point.

Gaussian beam migration lies somewhere between the Kirchhoff and slant stack methods. Instead of migrating one trace at a time for all reflection slopes (as in Kirchhoff migration) or one reflection slope for all traces (as in slant stack migration), Gaussian beam migration independently images each reflection slope in overlapping, Gaussian-tapered subsets of traces. The innermost loop of Gaussian beam migration is the accumulation of a relatively narrow beam that represents a narrow range of propagation angles. Each beam contributes no more than once to each image point.

ACKNOWLEDGMENTS

Support for this work was provided by the members of the Consortium Project on Seismic Inverse Methods for Complex Structures at the Center for Wave Phenomena, Colorado School of Mines.

REFERENCES

Aki, K., and Richards, P. G., 1980, Quantitative seismology, theory and methods: W. H. Freeman and Company.

Červený, V., Popov, M. M., and Pšenčík, I., 1982, Computation of wave fields in inhomogeneous media — Gaussian beam approach: Geophys. J. R. astr. Soc., **70**, 109–128.

Červený, V., and Pšenčík, I., 1984, Gaussian beams in elastic 2-D laterally varying layered structures: Geophys. J. R. astr. Soc., **78**, 65–91.

Chapman, C. H., and Drummond, R., 1982, Body-wave seismograms in inhomogeneous media using Maslov asymptotic theory: Bull. Seis. Soc. Am., **72**, no. 6, S277–S317.

Claerbout, J. F., 1985, Imaging the Earth's interior: Blackwell Scientific Publications.

Costa, C. a., Raz, S., and Kosloff, D., 1989, Gaussian beam migration: Presented at the 59th Ann. Internat. Mtg. Soc. Expl. Geophys., Expanded Abstracts, 1169–1171.

Gazdag, J., 1978, Wave equation migration with the phase-shift method: Geophysics, **43**, 1342–1351.

Hill, N. R., 1990, Gaussian beam migration: Geophysics, **55**, 1416–1428.

Hill, N. R., Watson, T. H., Hassler, M. H., and Sisemore, L. K., 1991, Salt-flank imaging using Gaussian beam migration: Presented at the 61st Ann. Internat. Mtg. Soc. Expl. Geophys., Expanded Abstracts, 1178–1180.

Lazaratos, S. K., and Harris, J. M., 1990, Radon transform / Gaussian beam migration: Presented at the 60th Ann. Internat. Mtg. Soc. Expl. Geophys., Expanded Abstracts, 1314–1317.

Schneider, W. A., 1978, Integral formulation for migration in two and three dimensions: Geophysics, **43**, 49–76.

Sinton, J. B., and Frazer, L. N., 1981, A method for the computation of finite frequency body wave synthetic seismograms in laterally varying media: Geophys. J., **71**, 35–55.

van Trier, J., and Symes, W. W., 1991, Upwind finite-difference calculation of traveltimes: Geophysics, **56**, 812–821.

Vidale, J., 1988, Finite-difference calculation of traveltimes: Bull. Seis. Soc. Am. **78**, no. 6, 2062–2076.

Computational Aspects of Gaussian Beam Migration

Dave Hale

Center for Wave Phenomena
Colorado School of Mines
Golden, Colorado 80401
(303) 273-3557

Computational aspects of Gaussian beam migration

Dave Hale

ABSTRACT

The computational efficiency of Gaussian beam migration depends on the solution of two problems: (1) computation of complex-valued beam times and amplitudes in Cartesian (x, z) coordinates, and (2) limiting computations to only those (x, z) coordinates within a region where beam amplitudes are significant.

The first problem can be reduced to a particular instance of a class of closest-point problems in computational geometry, for which efficient solutions, such as the Delaunay triangulation, are well known. Delaunay triangulation of sampled points along a ray enables the efficient location of that point on the raypath that is closest to any point (x, z) at which beam times and amplitudes are required. Although Delaunay triangulation provides an efficient solution to this closest point problem, a simpler solution, also presented in this paper, may be sufficient and more easily extended for use in 3-D Gaussian beam migration.

The second problem is easily solved by decomposing the subsurface image into a coarse grid of square cells. Within each cell, simple and efficient loops over (x, z) coordinates may be used. Because the region in which beam amplitudes are significant may be difficult to represent with simple loops over (x, z) coordinates, I use recursion (a function that calls itself) to move from cell to cell, until the entire region defined by the beam has been covered.

Benchmark tests of a computer program implementing these solutions suggest that the cost of Gaussian beam migration is comparable to that of migration via explicit depth extrapolation in the frequency-space domain. For the data sizes and computer programs tested here, the explicit method was faster. However, as data size was increased, the computation time for Gaussian beam migration grew more slowly than that for the explicit method.

INTRODUCTION

Gaussian beam migration may be summarized concisely (Hale, 1992) by

$$g(x,z) = \sum_j \int dp_x \, A_j(p_x,x,z) \, b_j[\tau = \tau_j(p_x,x,z), p_x], \tag{1}$$

where $g(x,z)$ denotes the subsurface image, a function of horizontal distance x and depth z, and $b_j(\tau,p_x)$ denotes a local slant stack of seismic data recorded at the surface $z = 0$, a function of time τ for each reflection slope p_x. The time and amplitude functions $\tau_j(p_x,x,z)$ and $A_j(p_x,x,z)$ are complex-valued, and they determine the mapping of each local slant stack (beam) onto the subsurface image. The sum over beam centers x_j and the integral over reflection slopes p_x simply accumulate the contributions of each beam.

Figure 1 illustrates the contribution of one Gaussian beam formed from synthetic seismic data. This beam corresponds to a beam center $x_j = 5\,\text{km}$ and a reflection slope p_x that is equivalent to an emergence angle of 36 degrees. The beam is refracted by a gradual increase in velocity with depth and by a low-velocity zone centered at $x = 4\,\text{km}$ and $z = 1.5\,\text{km}$.

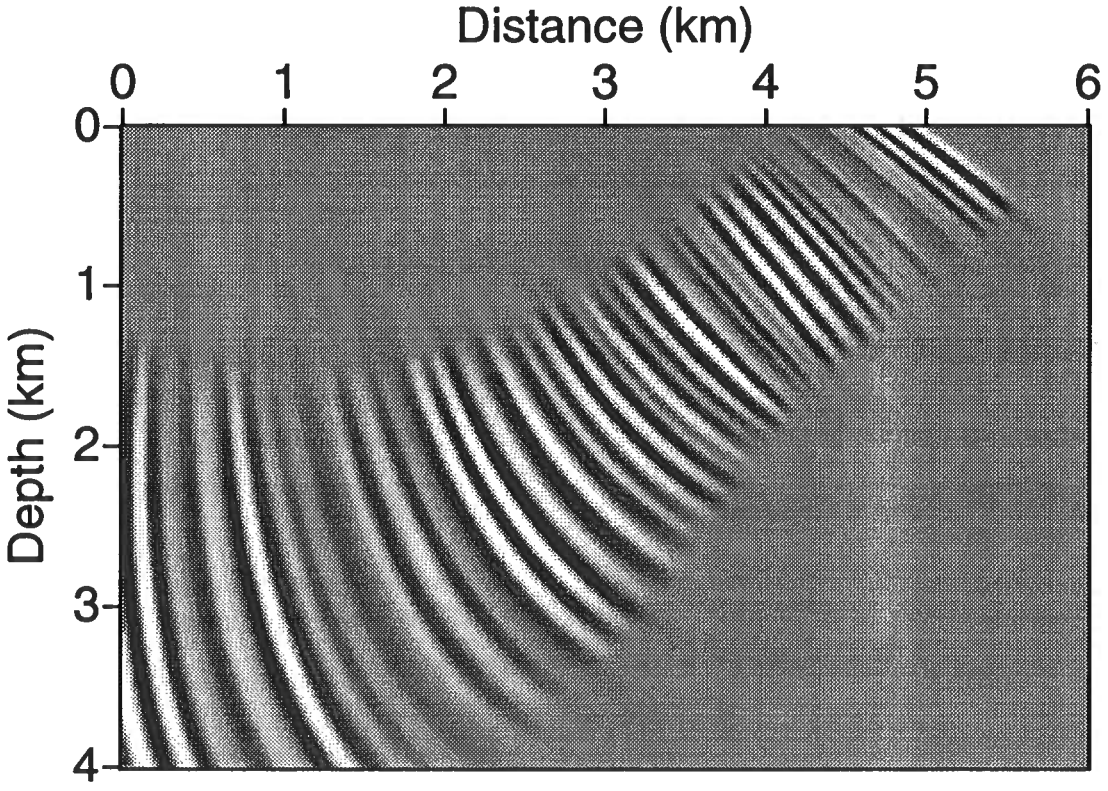

FIG. 1. Contribution of one Gaussian beam to a subsurface image. The fundamental task in Gaussian beam migration is to efficiently compute many such contributions, the sum of which yields the complete image.

The fundamental task in Gaussian beam migration is to efficiently compute the contribution, like that shown in Figure 1, of each beam to the subsurface image. The prerequisite task of computing $b_j(\tau, p_x)$ (beam forming) can be accomplished simply by slant stacking a Gaussian-tapered window of data, and this tapering and slant stacking can be performed efficiently via fast Fourier transforms. However, once the data have been beam-formed, one must then efficiently map each beam onto the subsurface image, and this mapping is complicated by two problems.

The first problem is due to the fact that the complex-valued functions $\tau_j(p_x, x, z)$ and $A_j(p_x, x, z)$ are difficult (although not impossible) to compute in the Cartesian coordinates x and z. They are more easily and typically computed as functions of ray-centered coordinates (s, n) (Červený, et al., 1982; Hill, 1990; Figure 2 below). Transformation from ray-centered coordinates to Cartesian coordinates requires that we determine the point on a ray [the ray that defines the coordinates (s, n)] that is nearest to a given point (x, z). As noted by Hill (1990), "the transformation from ray-centered (s, n) to Cartesion (x, z) coordinates and ... are time-consuming computations."

The second problem in efficiently mapping each beam is that computations should be performed for only those subsurface points (x, z) where the contribution of the beam is significant. As illustrated in Figure 1, not all subsurface points are affected by a given beam. In Gaussian beam migration of recorded seismic data, each beam may contribute significantly to only a small fraction of the sampled subsurface points (x, z). (See Hill, 1990, for some particularly good examples.) However, the subset of samples affected by a single beam forms a region that may be quite irregular and not easily translated into bounds for simple loops over x and z in computer programs.

This paper proposes solutions to these two computational problems: (1) finding the nearest point on a ray and (2) working only within a beam. Following the discussion below of these two problems and their solutions, the results of benchmark tests of a computer program implementing these solutions are presented.

NEAREST POINT ON A RAY

In this section, I assume that dynamic ray tracing (Červený, et al., 1982; Hill, 1990) has been performed to compute complex-valued time and amplitude functions in ray-centered coordinates (s, n). Equation (1) requires that these functions be evaluated in Cartesian coordinates (x, z). Therefore, we need a method to determine (s, n) coordinates from (x, z) coordinates.

Figure 2 illustrates the two different coordinate systems for the raypath used to compute the beam of Figure 1. This raypath was computed by integrating the dynamic ray tracing equations via a simple 4th-order Runge-Kutta method (e.g., Press, et al., 1986, 550–554). Solutions to these equations were thereby obtained at points uniformly sampled in time along the raypath.

Solution of the dynamic ray tracing equations requires evaluation of velocity and its derivatives along the raypath. Here, velocity was uniformly sampled in Cartesian

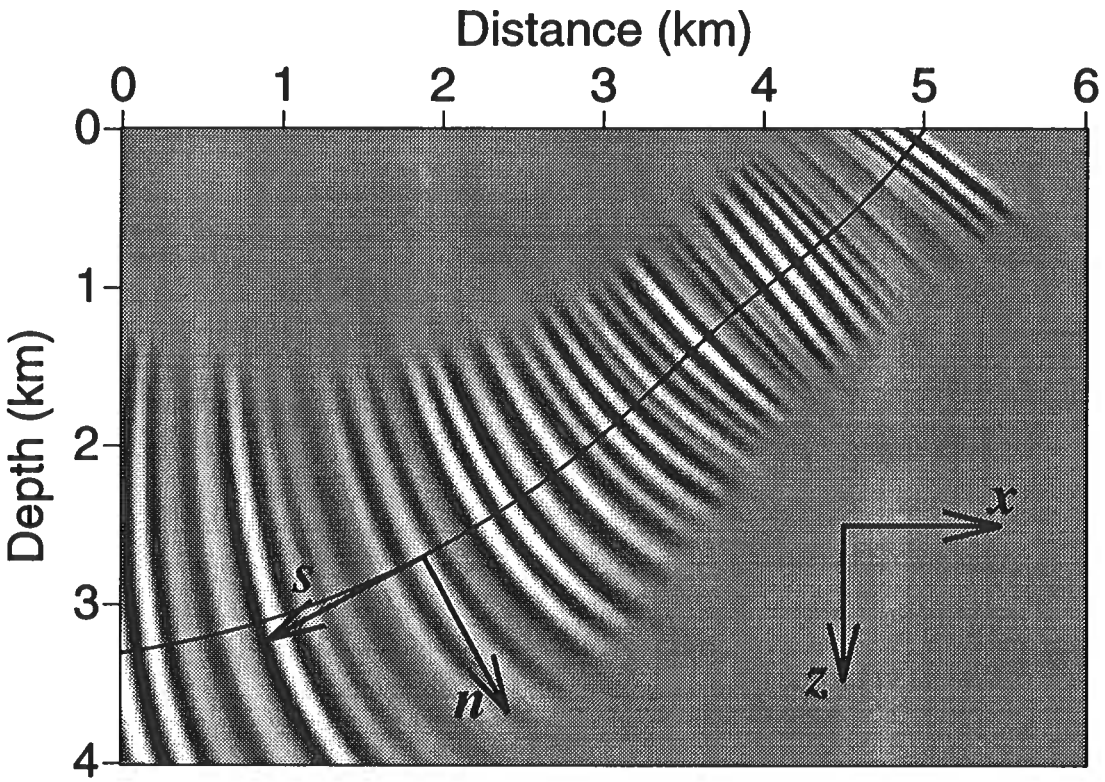

FIG. 2. Time and amplitude functions for this Gaussian beam were first computed in ray-centered coordinates (s, n) and then transformed to Cartesian coordinates (x, z). s denotes distance along the raypath and n denotes normal distance to the raypath.

coordinates x and z. Piecewise Hermite bi-cubic interpolation with continuous first (but not second) derivatives (e.g., Thomson and Gubbins, 1982) was used to interpolate velocity and its derivatives at points along the raypath. An attractive feature of bi-cubic interpolation in two dimensions is that it is easily extended to tri-cubic interpolation in three dimensions, as required for Gaussian beam migration of 3-D seismic data.

Although more sophisticated ray tracing methods might be used, the simple ray tracing method described above is efficient in the context of Gaussian beam migration. Accumulation of each beam requires evaluation of the seismic wavefield at many subsurface points (x, z). If N time steps are used in the solution of the dynamic ray tracing equations, then the computational cost of ray tracing is proportional to N. However, the cost of *using* the results of this ray tracing, the cost of accumulating a beam, is proportional to N times the nominal width N_w of the beam. As illustrated in Figure 2, N_w varies along the raypath. However, for typical beam widths, the $O(N)$ cost of simple Runge-Kutta ray tracing is insignificant compared with the $O(N \times N_w)$ cost of accumulating the corresponding Gaussian beam.

For any given coordinates (x, z), corresponding coordinates (s, n) can be determined simply by finding that point on the raypath that is nearest to (x, z). s is then the distance along the ray to the nearest point, and n is the distance from (x, z) to that nearest point. For the Runge-Kutta ray tracing described above, which yields a raypath discretely sampled in time, we need only find the sample that is nearest to the specified (x, z). Once we know the nearest sampled point, the complex time and amplitude functions can be determined easily from quantities computed during dynamic ray tracing (Červený and Pšenčík, 1984).

As noted by Červený, et al. (1982), normals to a curved raypath will intersect at large distances from the raypath, so that a single set of (x, z) coordinates will correspond to more than one set of (s, n) coordinates. Fortunately, as illustrated in Figure 2, Gaussian beam amplitudes tend to be largest at points (x, z) that are nearest the raypath. Therefore, by choosing the smallest normal distance to the raypath, we choose that set of (s, n) coordinates that tends to yield the largest contribution to the subsurface image. In the special case that two or more points on the raypath are nearest and equidistant to (x, z), we will find only one of them, so that only one contribution of the Gaussian beam will be accumulated at that point (x, z).

The simplest way to find the nearest point on the raypath is to compute the distance from the specified (x, z) to all sampled points along the raypath, remembering the sample that corresponds to the minimum distance. However, this approach is inefficient, requiring a computational cost proportional to N for every point (x, z). This $O(N)$ cost is significant, because the number of points for which the nearest point problem must be solved is proportional to the area within the beam, $N \times N_w$, which implies an $O(N^2 \times N_w)$ cost per beam.

The reason that the simplest solution to the nearest point problem is so costly is that it fails to take advantage of the fact that the nearest point on the raypath for one (x, z) is likely to be close to the nearest point for a neighboring (x, z). As one iterates over the points (x, z) within a beam in some ordered fashion, the nearest point on the raypath is unlikely to jump wildly from end of the raypath to the other.

Unfortunately, it is difficult to guarantee that such wild behavior will never occur, particularly in the cases of turned rays and rapid velocity variations. The simplest method, while inefficient, is guaranteed to yield the nearest point.

In the remainder of this section, two more efficient solutions to the nearest point problem are presented. Both are guaranteed to yield the nearest point on the raypath. The first is highly efficient, but difficult to extend to 3-D ray tracing. The second is less efficient, but easily extended to 3-D ray tracing. Both solutions have a computational cost that is significantly less than the $O(N)$ cost of the simplest solution.

Triangles

Voronoi tessellation (e.g., Preparata and Shamos, 1985) provides a natural solution to the nearest point problem. The region bounded by the Voronoi polygon corresponding to any vertex in a Voronoi tessellation is, by definition, the locus of

points that are nearer to that vertex than to any other vertex. If we let each sampled point on a raypath be a vertex in a Voronoi tessellation, then to find the point on the raypath nearest to an arbitrary point (x, z), we need only find that vertex with a Voronoi polygon containing the point (x, z). Preparata and Shamos (1985) show that the worst-case computational cost of constructing the Voronoi tessellation is $O(N \times \log N)$ and that the cost of finding the nearest vertex is $O(\log N)$.

Rather than constructing a Voronoi tessellation of the sampled points on a raypath, it is simpler to build its dual, a Delaunay triangulation of the Voronoi vertices (Watson, 1981). Figure 3 shows the Delaunay triangulation of sampled points along the raypath in Figure 2. For clarity in this figure, only one tenth of the sampled points that are actually computed during ray tracing are shown in the triangulation. The Delaunay triangulation, like the Voronoi tessellation, may be computed with a cost of $O(N \times \log N)$.

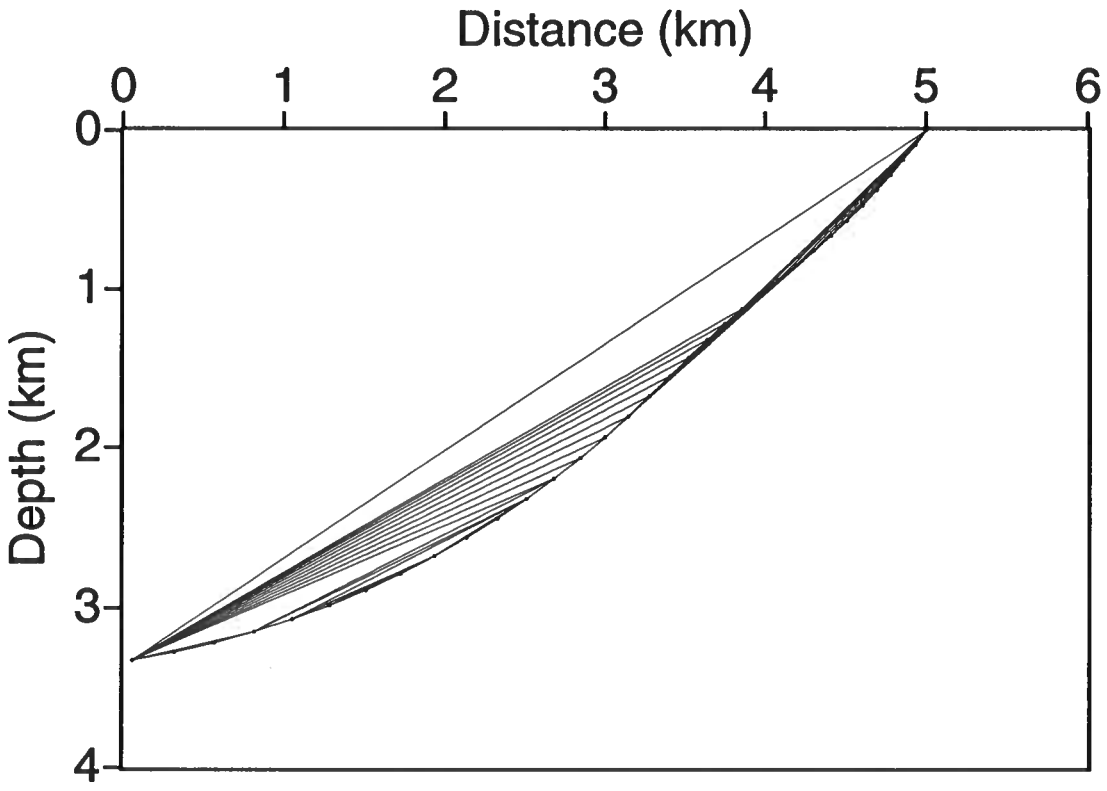

FIG. 3. Delaunay triangulation of sampled points along a raypath. By following the edges of this triangulation, one can efficiently determine that point on the raypath that is nearest to an arbitrary point (x, z).

Given the Delaunay triangulation of a set of vertices, like that shown in Figure 3, one can easily find the vertex that is nearest to any point (x, z). Starting from any vertex, follow the edges of the triangulation, moving from vertex to vertex. When moving from a vertex to one of its neighbors, always choose the neighbor that is

closest to the point (x, z). Eventually, a vertex will be reached that is nearer to (x, z) than any of its neighbors. That vertex is the nearest vertex in the triangulation.

This algorithm is efficient when iterating over numerous (x, z) coordinates. The nearest vertex (nearest point on the raypath) for one (x, z) is likely to be close to the nearest vertex for a nearby (x, z). However, this algorithm will successfully find the nearest point on the raypath, even when that nearest point jumps from one end of the raypath to the other as (x, z) changes. As illustrated in Figure 3, the edges of the Delaunay triangulation make such large jumps possible, although they will rarely be taken.

In the special case of a straight ray (as for constant velocity), triangulation of the collinear points along the raypath is impossible. However, the sampled points can still be connected with edges such that the vertex-to-vertex search can be performed as described above for a Delaunay triangulation. One way to avoid handling this special case is to always include in the triangulation three artificial vertices that form a large equilateral triangle containing the entire raypath. These fake vertices must be far enough away from the raypath that they will never be the closest vertex in the triangulation to any point (x, z) of interest.

The main drawback of the Delaunay triangulation solution to the nearest point problem is that it is difficult to extend to three dimensions for use in Gaussian beam migration of 3-D seismic data. Although such an extension is possible (the triangles become tetrahedra), it is not trivial. Watson's (1981) triangulation algorithm is perhaps the easiest to extend to three dimensions, but the cost of triangulation with Watson's method is $O\left(N^{3/2}\right)$ for two dimensions and $O\left(N^{5/3}\right)$ for three dimensions. Therefore, in keeping with the goal of using only computational methods that may be easily extended for use in 3-D imaging, an alternative solution to the nearest point problem is proposed below.

Circles

Figure 4 illustrates another solution to the nearest point problem. Here, the N sampled points along the raypath are grouped into N_c clusters bounded by circles. Each circle contains only a subset (roughly N/N_c) of the N sampled points. To find the point on the raypath that is nearest to a specified point (x, z), begin by choosing one of the circles. A good choice is the circle that contains a point previously found to be closest to a nearby (x, z). Interrogate (find the nearest point inside) this first circle, and remember the minimum distance. Then, for all remaining circles, interrogate the circle only if the circle's radius plus the minimum distance found so far is less than the distance from the circle's center to the point (x, z). In other words, look inside only those circles that could possibly contain a point closer to (x, z) than the closest point found so far.

The cost of this method depends on the number of circles and on the number of sampled points inside each circle. If we make one ($N_c = 1$) big circle containing all of the sample points, then the cost of finding the nearest point is $O(N)$, which is no more efficient than the simplest search. Alternatively, if we choose $N_c = N$ tiny

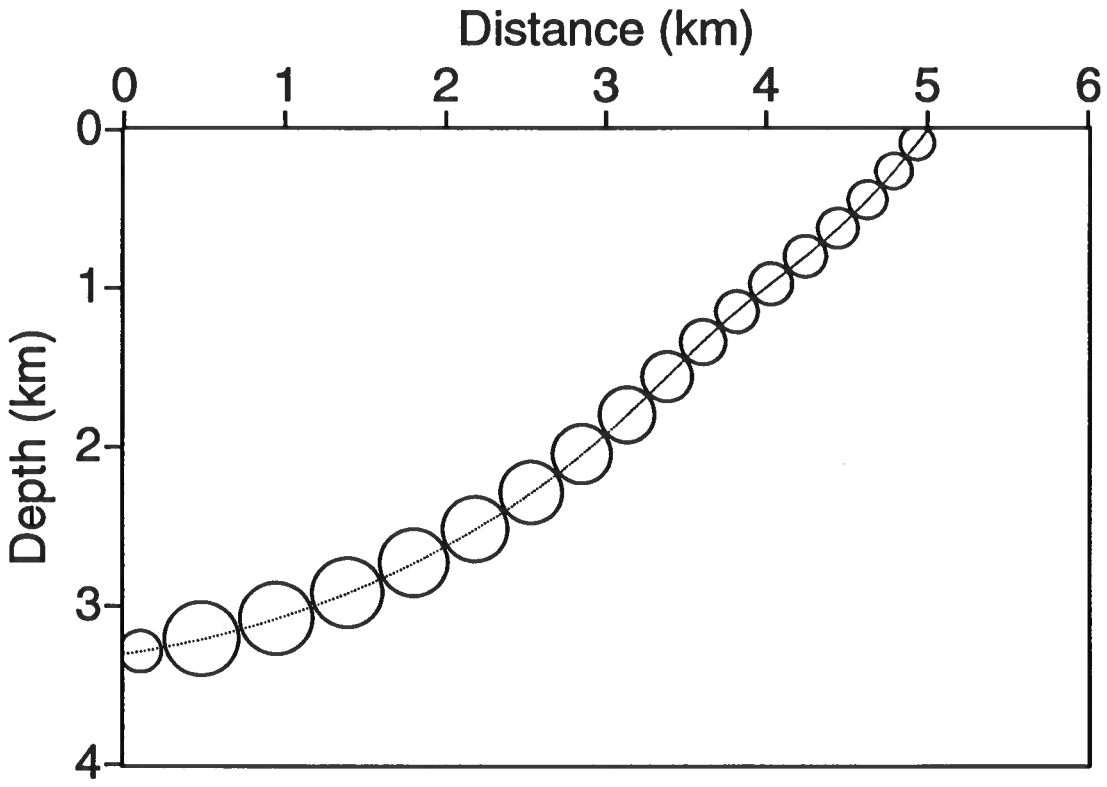

FIG. 4. Sampled points along a raypath are grouped into circular clusters to facilitate the search for that point on the raypath that is nearest to an arbitrary point (x, z). The points inside any given circle can be ignored during this search if the minimum distance found so far is less than the distance from (x, z) to the circle's boundary.

circles, each containing only one sampled point, then the cost is again $O(N)$, because we must interrogate all N circles. The most efficient use of the circles lies between these two extreme choices.

In general, the cost of the circle-based solution to the nearest point problem is roughly $O(N_c + kN/N_c)$, where k is the number of circles that must be interrogated. If the first circle interrogated contains the desired nearest point, then perhaps none of the remaining circles need to be interrogated. If we suppose that this $k = 1$ ideal case occurs frequently as we iterate over (x, z) coordinates, then the cost of the circle-based search is minimized by choosing $N_c = \sqrt{N}$, and the cost becomes $O(\sqrt{N})$. For large N (say, $N > 100$), this cost is significantly less than the $O(N)$ cost of the simplest search method.

The raypath in Figure 4 was sampled at $N = 316$ points. Therefore, there are $\sqrt{N} \approx 18$ circles in Figure 4, and each contains 18 samples of the raypath, except for the last circle at the end of the raypath, which contains only 10 samples. To find the sample nearest to a point (x, z), each of the 18 circles must be checked to determine whether or not it could possibly contain the nearest sample.

The most attractive feature of the circle-based search method is that it can be trivially extended to three dimensions, in which the circles become spheres.

For either two or three dimensions, the circle-based search method adds a factor $\sqrt{N}$ to the total cost of accumulating a beam. To keep this $\sqrt{N}$ factor from becoming significant for typical N, the nearest point problem should be solved for only a subset of the (x, z) samples within a Gaussian beam. As suggested by Hill (1990), the complex time and amplitude functions may be computed on a relatively coarse grid of (x, z) coordinates, and then bilinearly interpolated for use in equation (1). My experiments suggest that these functions can be sampled about 8 times more coarsely in each spatial dimension than the beam itself, which implies an $8^2 = 64$ fold reduction in the cost of time and amplitude calculations for 2-D grids, and an $8^3 = 512$ fold reduction for 3-D grids. These reductions make the cost of the circle-based search an insignificant portion of the total cost of accumulating the contribution of a Gaussian beam.

WORKING INSIDE THE BEAM

One of the most useful properties of Gaussian beams is their compactness. The amplitude of the beam in Figure 2 decays exponentially with distance-squared (n^2) from the central ray (Hill, 1990). For efficient Gaussian beam migration, we should exploit this compactness by ignoring points (x, z) where the exponential decays to less than, say, one percent of its peak value. In other words, we should solve the nearest point problem and compute each beam's contribution to the subsurface image for only those points (x, z) where that contribution is significant.

Figure 5 shows the superposition of a coarsely sampled grid on the Gaussian beam of Figure 1. Note that this grid does not include all points (x, z); rather, it includes only those points where the beam amplitude is significant. As discussed in the preceding section, complex times and amplitudes should be computed at the corners of each cell of such a grid and then bilinearly interpolated for use in equation (1). Computations should be restricted to only those cells having significant amplitudes at all four corners. In other words, we should work only inside the beam.

As Figure 5 illustrates, the grid of cells within the beam may be irregularly shaped, so that it may be difficult to determine the bounds of simple loops over these cells in computer programs. For this particular beam, one might determine bounds in depth z for each horizontal distance x within the beam. For other beams, however, multiple loops over disjoint sets of z coordinates might be required for a single x coordinate. Such loops over cells within an irregularly shaped beam become even more difficult to organize in three dimensions.

A simple solution to the problem of working within the beam is to use recursion instead of loops over cells. Begin with the corner of the cell that is nearest to the point where the raypath intersects the surface $z = 0$. This corresponds to the cell corner at a distance of about 5 km in Figure 5. For any reasonable beam width, the Gaussian beam amplitude at this first cell corner is guaranteed to be significant. Compute the

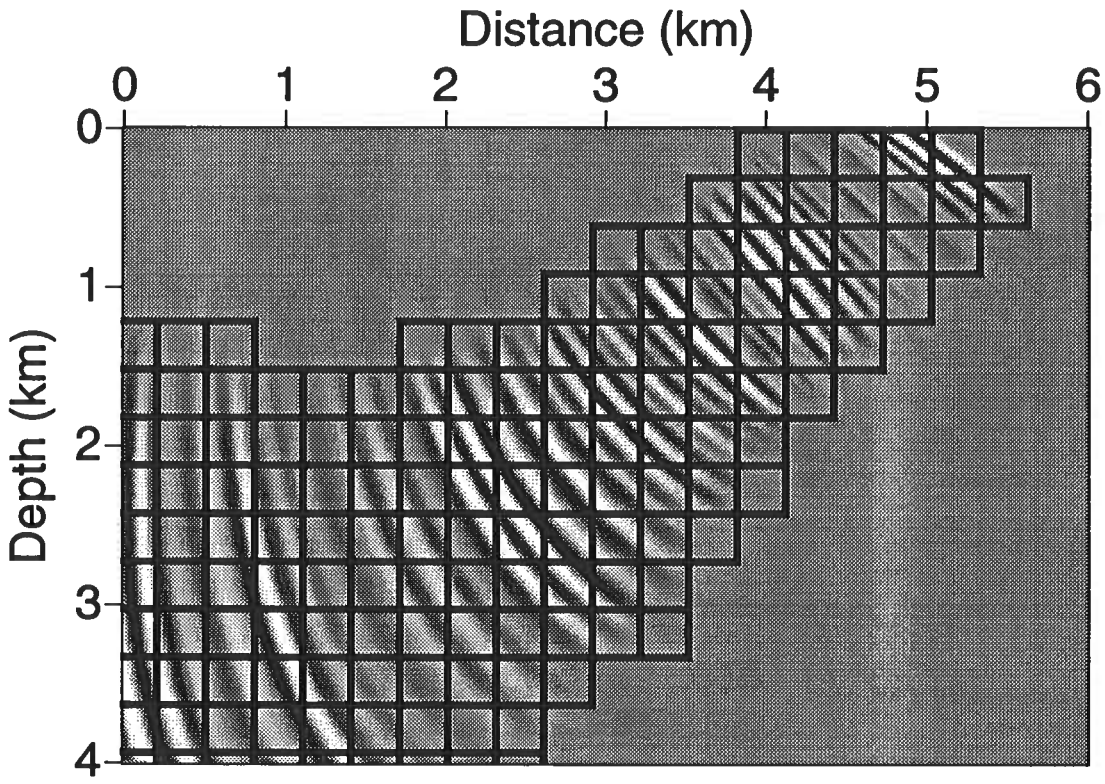

FIG. 5. Coarse grid of cells for which the amplitude of the Gaussian beam is significant. The irregular shape of this grid suggests that a recursive algorithm should be used to move from cell to cell, while accumulating the contribution of the beam within each cell.

complex time and amplitude for this first cell corner. Then, compute the times and amplitudes for the neighboring cell corners left, right, and below the first one. If the amplitude at a neighbor is significant, then compute times and amplitudes for that neighbor's neighbors. Repeat this recursive process until times and amplitudes for all cell corners with significant amplitudes have been computed.

The computer software that I use to set the complex time and amplitude at each cell corner is written in the C programming language as follows:

```
void setCell (Cells *cells, int jx, int jz)
/*****************************************************************************
Set a cell by computing the Gaussian beam complex time and amplitude of
its upper left corner.  If the amplitude is non-zero, set neighboring
cells recursively.
*****************************************************************************
Input:
cells           pointer to cells
jx              x index of the cell to set
jz              z index of the cell to set
*****************************************************************************
Notes:
To reduce the amount of memory required for recursion, the actual
computation of complex time and amplitude is performed by the function
cellTimeAmp(), so that no local variables are required in this
function, except for the input arguments themselves.
```

```
*****************************************************************************/
{
        /* If cell is out of bounds, return. */
        if (jx<0 || jx>=cells->mx || jz<0 || jz>=cells->mz) return;

        /* If cell is live, return. */
        if (cells->cell[jx][jz].live==cells->live) return;

        /* Make cell live. */
        cells->cell[jx][jz].live = cells->live;

        /* Compute complex time and amplitude.  If amplitude is
         * big enough, recursively set neighboring cell. */
        if (cellTimeAmp(cells,jx,jz)) {
                setCell(cells,jx+1,jz);
                setCell(cells,jx-1,jz);
                setCell(cells,jx,jz+1);
                setCell(cells,jx,jz-1);
        }
}
```

This `setCell` function "sets a cell" by computing the complex time and amplitude of its upper left corner. The first statement in this function ensures that the cell lies within an array of cells that spans the entire subsurface image. The second statement checks to see whether or not the cell has already been set. The third statement marks the cell as being "live". A live cell is a cell that has been (or, more precisely, soon will be) set. The actual work of computing the complex time and amplitude is done by the function `cellTimeAmp`. If the amplitude is significant, `cellTimeAmp` returns `True` and the function `setCell` calls itself four times, once for each of its neighbors left, right, below, and above.

The type `Cells` has been defined elsewhere to be a C structure containing all of the information required to compute times and amplitudes, including the results of dynamic ray tracing sampled at points along the raypath, the circular clusters used to find the nearest point on the raypath, as well as the grid of cells itself. The variable `cells` is a pointer to (i.e., address of) this structure.

The `live` flag is used to avoid redundant computations and, even more importantly, to ensure that the recursion ends. Note that at least one of the four calls to the function `setCell` is unnecessary, in principle, because the only way to set any cell (except for the first cell) is to have already set one of its four neighbors. However, rather than testing to see which of the four neighbors is live, it is simpler to have the function `setCell` return if the cell has already been set.

For convenience, the grid of cells is represented by a two-dimensional array that spans the entire subsurface image, not just the region within the beam. To avoid having to initially turn off the live flag in every cell, which would require working *outside* the beam, a pseudo-random integer is used to denote a live cell. For each beam, a unique pseudo-random integer is generated. That integer is then used as the live flag for every cell within the beam. A new and different integer is used for each beam so that the live flags do not need to be turned off before processing the next beam.

In my computer program that performs Gaussian beam migration, the function `setCell` is called explicitly only once for each beam to start the recursion. All other calls to `setCell` are made by the function `setCell` itself.

After complex times and amplitudes have been computed at the corners of each cell within the beam, we may then accumulate the contribution of the beam to the subsurface image. Again, recursion is used to visit all of the cells that contribute significantly, starting with the cell nearest the raypath at the surface. Only cells with four live corners are used. Within each cell, simple loops over finely sampled x and z coordinates are used to accumulate the cell's contribution. Cells that have been processed in this way are marked with another psuedo-random flag (different from the live flag) that is unique for each beam.

BENCHMARKS

To analyze the cost of Gaussian beam depth migration, a series of benchmark tests were conducted using a computer program based on the computational methods described above. All tests were conducted for equal numbers of time, horizontal distance, and depth samples, so that computation time could be measured as a function of a single size N. In this way, the time required for Gaussian beam migration was measured for sizes $N = 100$, 200, 400, and 800. All tests were performed on an IBM POWERstation 520 workstation.

For comparison, the same sizes N were used to measure the cost of depth migration via explicit depth extrapolation filters applied in the frequency domain, as described by Hale (1991). This explicit method has a highly optimized inner loop, which in these tests consisted of 20 complex multiplies and 38 complex adds. This inner loop must be executed for all frequencies, horizontal distances, and depths. Therefore, the number of times that this innermost loop is executed is proportional to N^3.

The results of these tests are plotted in Figure 6. As indicated in Figure 6a, for all sizes N tested, the explicit extrapolation method requires less computation time than the Gaussian beam method. However, Figure 6b shows that the cost of the explicit method grows at a faster rate than that of the Gaussian beam method. The slopes of the almost linear curves in the log-log plots of Figure 6b indicate that the cost of the explicit method is roughly proportional to $N^{2.7}$, while the cost of the Gaussian beam method is approximately proportional to $N^{2.2}$, for the range of N used in these tests.

To highlight the relative costs of the two computer programs, the ratios of the times required for the explicit program to the times required for the Gaussian beam program are plotted in Figure 7. For the largest size tested here, $N = 800$, the Gaussian beam program is about 20 percent slower than the explicit program.

We must be careful not to conclude from these benchmark tests that Gaussian beam migration is inherently slower than migration via explicit extrapolation filters. Rather, we should only conclude that, for the sizes tested, my current computer program for Gaussian beam migration is slower than my current program for the explicit method.

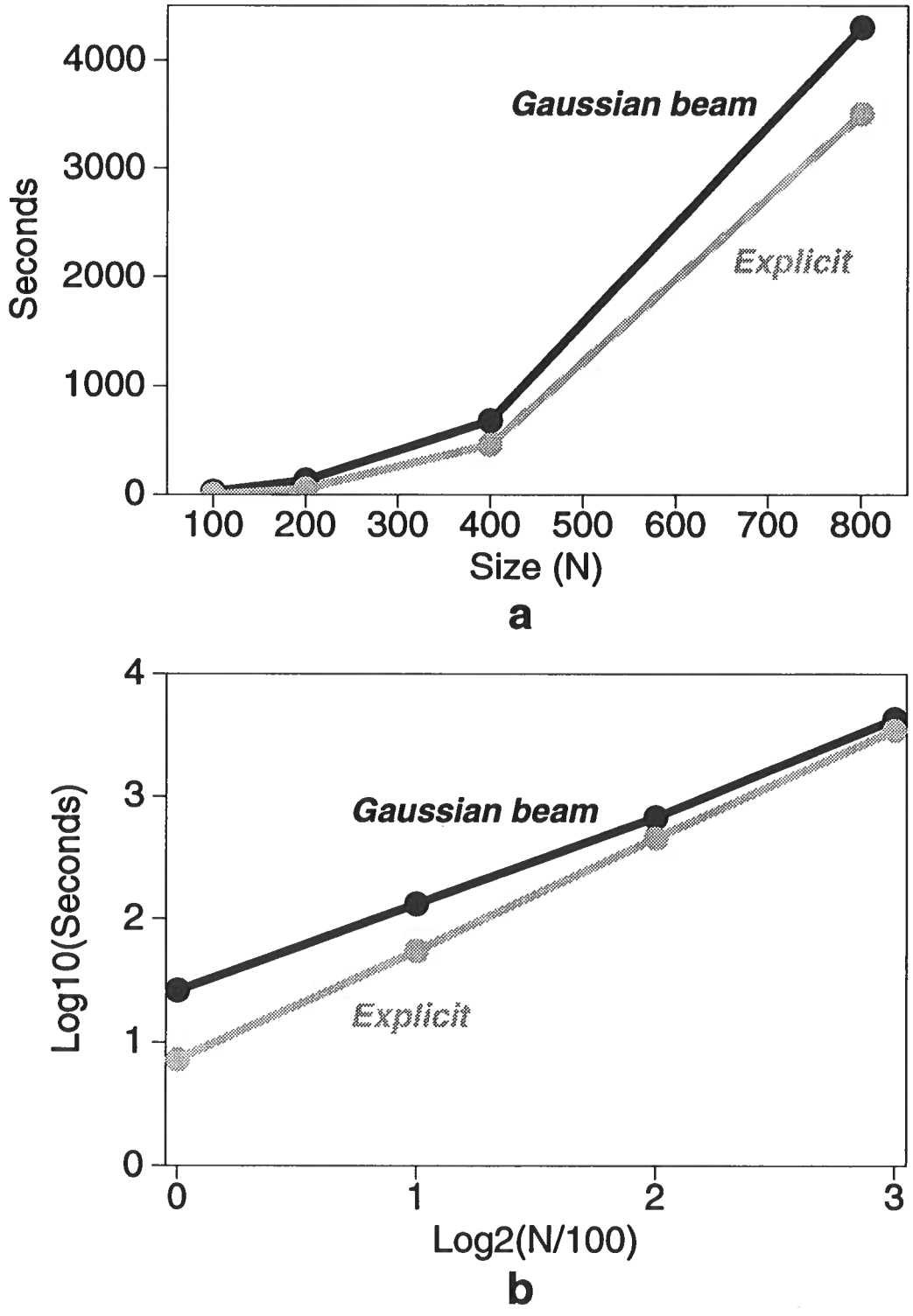

FIG. 6. Benchmark tests of two computer programs for depth migration. Computation times for the Gaussian beam program are (a) greater than, but (b) increase at a slower rate than those for the explicit extrapolation program. Log10 and Log2 denote logarithms for bases 10 and 2, respectively.

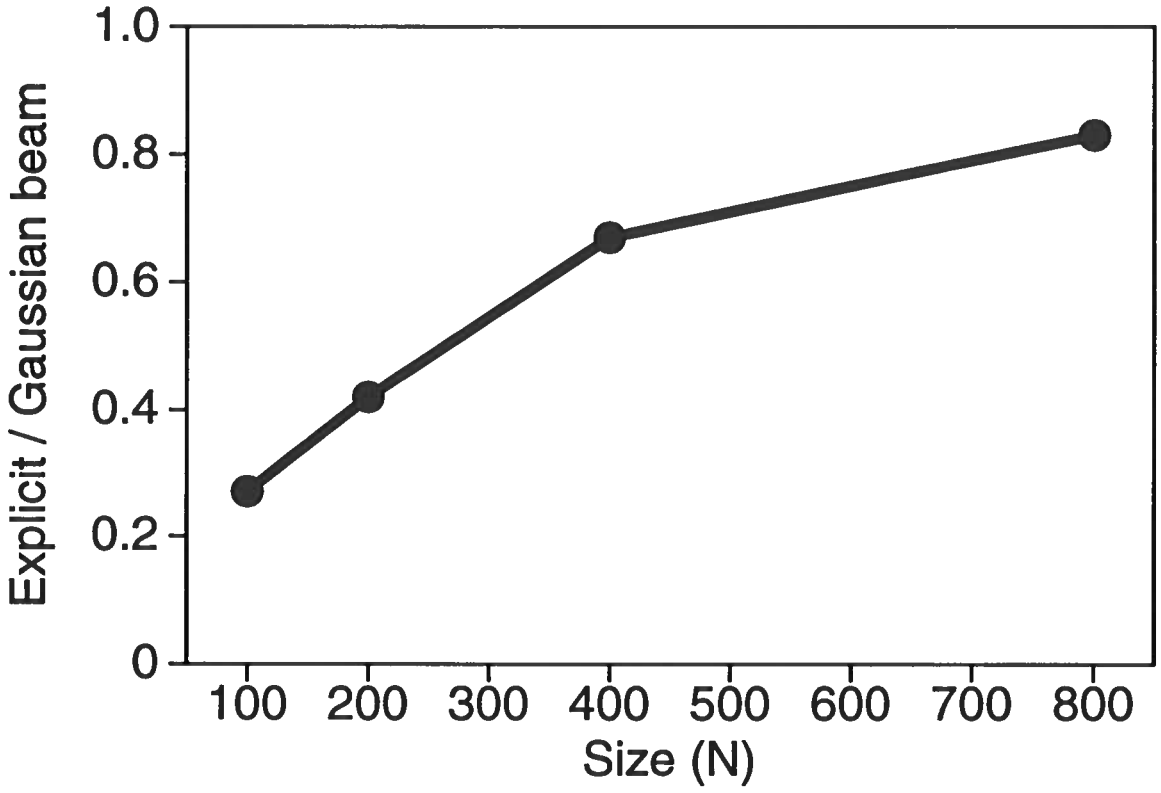

FIG. 7. Ratios of the computation times plotted in Figure 6a.

The most interesting results of these tests are the slopes of the almost linear curves in Figure 6b, not their intercepts. Optimization of the innermost loops of either computer program may significantly change the intercepts, but is unlikely to change the slopes of these curves significantly.

CONCLUSION

Two of the most difficult (or at least awkward) computational problems in Gaussian beam migration are (1) computation of complex-valued beam times and amplitudes in Cartesian (x, z) coordinates, and (2) performing calculations for only those (x, z) coordinates within the region where beam amplitudes are significant.

One way to simplify these problems might be to restrict the use of Gaussian beam migration to special velocity functions. For example, subsurface models with layers in which velocity or the velocity gradient is constant might facilitate the mapping from ray-centered (s, n) coordinates to Cartesian (x, z) coordinates, because the raypath within each such layer could be expressed analytically.

The algorithms proposed in this paper were selected, in part, to make such restrictions unnecessary. For example, an efficient solution to the first problem requires only that the results of dynamic ray tracing be well-sampled along rays traced from

the surface. The algorithms proposed here do not depend on a specific representation of velocity or a particular method for ray tracing.

The algorithms were also chosen to facilitate their extension to 3-D migration and 2-D prestack migration of non-zero-offset sections. The square cells used in 2-D migration simply become cubic cells in 3-D migration. For non-zero-offset data, beam times and amplitudes must be computed for both source and receiver beams (Hill, et al., 1991). By computing the required times and amplitudes on a coarse grid of cells, as suggested by Hill (1990), we can reduce the cost of these computations. Furthermore, by using recursion to move from cell to cell, we can limit subsequent computations to only those cells where both source and receiver beam amplitudes are significant. Extensions to 3-D poststack depth migration and 2-D prestack depth migration, while not trivial, are straightforward.

The results of benchmark tests suggest that Gaussian beam migration is competitive with the most efficient depth migration methods. Although my current implementation of Gaussian beam migration is slower than a highly optimized depth migration based on explicit extrapolation filters, benchmark timings suggest that Gaussian beam migration may be most efficient for large data sizes (requiring more than one hour on a typical computer workstation). As data dimensions increase, the computational cost of Gaussian beam migration grows more slowly than that of the explicit method.

ACKNOWLEDGMENTS

Support for this work was provided by the members of the Consortium Project on Seismic Inverse Methods for Complex Structures at the Center for Wave Phenomena, Colorado School of Mines.

REFERENCES

Červený, V., Popov, M. M., and Pšenčík, I., 1982, Computation of wave fields in inhomogeneous media — Gaussian beam approach: Geophys. J. R. astr. Soc., **70**, 109–128.

Červený, V., and Pšenčík, I., 1984, Gaussian beams in elastic 2-D laterally varying layered structures: Geophys. J. R. astr. Soc., **78**, 65–91.

Hale, D., 1991, Stable explicit depth extrapolation of seismic wavefields: Geophysics, **56**, 1770–1777.

Hale, D., 1992, Migration by the Kirchhoff, slant stack and Gaussian beam methods: this report.

Hill, N. R., 1990, Gaussian beam migration: Geophysics, **55**, 1416–1428.

Hill, N. R., Watson, T. H., Hassler, M. H., and Sisemore, L. K., 1991, Salt-flank imaging using Gaussian beam migration: Presented at the 61st Ann. Internat. Mtg. Soc. Expl. Geophys., Expanded Abstracts, 1178–1180.

Preparata, F. P., and Shamos, M. I., 1985, Computational geometry — an introduction: Springer-Verlag.

Press, W. H., Flannery, B. P., Teukolsky, S. A., and Vetterling, W. T., 1986, Numerical recipes — the art of scientific computing: Cambridge University Press.

Thomson, C. J., and Gubbins, D., 1982, Three-dimensional lithospheric modelling at NORSAR: linearity of the method and amplitude variations from the anomalies: Geophys. J. R. astr. Soc., **71**, 1–36.

Watson, D. F., 1981, Computing the n-dimensional Delaunay tessellation with application to Voronoi polytopes: The Computer Journal, **24**, no. 2, 167–172.

CWP-118

Migration Error in Transversely Isotropic Media with Linear Velocity Variation in Depth

Ken Larner and Jack K. Cohen

Center for Wave Phenomena
Colorado School of Mines
Golden, Colorado 80401
(303) 273-3557

Migration error in transversely isotropic media with linear velocity variation in depth

Ken Larner and Jack K. Cohen

ABSTRACT

Given the sensitivity of imaging accuracy to the velocity used in migration, migration founded (as in practice) on the erroneous assumption that a medium is isotropic can be expected to be inaccurate for steep reflectors. Here, we estimate errors in interpreted reflection time and lateral position as a function of reflector dip for transversely isotropic models in which the axis of symmetry is vertical and the medium velocity varies linearly with depth. we limit consideration to media in which ratios of the various elastic moduli are independent of depth.

Tests with reflector dips up to 120 degrees on a variety of anisotropic media show errors that are tens of wavelengths for dips beyond 90 degrees when the medium (unrealistically) is homogeneous. For a given anisotropy, the errors are smaller for inhomogeneous media; the larger the velocity gradient, the smaller the errors. For gradients that are representative of the subsurface, lateral-position errors tend to be minor for dips less than about 60 degrees, growing to two to five wavelengths as dip passes beyond 90 degrees.

These errors are independent of reflector depth and rms velocity to the reflector, but depend significantly on their ratio; i.e., on migrated reflection time. Migration error, which is found to be unrelated to the ratio of horizontal to vertical velocity, is such that reflections with later migrated reflection times tend to be more severely over-migrated than are those with earlier migrated reflection times.

Over a large range of dips, migration errors that arise when anisotropy is ignored but inhomogeneity is honored tend to be considerably smaller than those encountered when inhomogeneity is ignored in migrating data from isotropic, inhomogeneous media.

INTRODUCTION

Difficult and unreliable as it is to measure anisotropy in the field, and as infrequently as it is done, it is nevertheless currently recognized and accepted that the Earth's subsurface is anisotropic—often, considerably so. For example, a frequently used measure of anisotropy for p-waves, the ratio of velocity in the horizontal direction to that in the vertical direction, is commonly found to be 1.05 to 1.1, and is often as large as 1.2 and higher (Seriff, 1986). For typical seismic wavelengths, the anisotropy may be either an intrinsic property of the rocks or the result of thin layering of different rock types. The distinction here is immaterial—the essential result is that waves travel with different speeds in different directions.

Given the general increase in wave speed with depth in the subsurface, reflections from steep interfaces—dips of 90 degrees and beyond—involve ray paths that sweep through a wide range of angles from vertical. Consequently, for inhomogeneous, anisotropic media, the energy propagates at different speeds due not only to variation in velocity with position but also to its variation with direction of propagation. Given the sensitivity of imaging accuracy to the velocity used in migration and given that migration, in practice, is founded on the assumption that the subsurface is isotropic, it is useful to analyze the positioning errors that arise from using migration algorithms that assume isotropy when the subsurface medium is not. This issue should be particularly relevant to use of steep-dip algorithms such as those that use turning waves (Hale, Hill, and Stefani, 1991) to image flanks of overhanging salt domes.

While anisotropy exists for both p-waves and s-waves, and s-wave anisotropy has been given the greater attention in the literature, most imaged reflection seismic data involves p-waves, and that is what we treat here. Moreover, although anisotropy can take on all manner of complexity, we assume the relatively simple, but plausible, form of transverse isotropy with a vertical axis of symmetry. That is, the velocity of plane waves (i.e., *phase velocity*) varies only with angle from the vertical; velocity is the same in all azimuthal directions.

Also, since the Earth's subsurface is not homogeneous (otherwise, among other things, turning waves would not exist), studies of migration error restricted to anisotropic models that are homogeneous can yield conclusions that, as we shall see, are greatly misleading. Again, actual subsurface inhomogeneity can be complicated and endlessly varied, so we limit consideration to a particularly simple form—media in which the pertinent elastic moduli vary only with depth z. Moreover, the allowed spatial variation will be such that ratios among the moduli remain independent of depth. Červený (1989) refers to such media as *factorized anisotropic inhomogeneous* (FAI), and shows simplifications that arise when ray tracing in FAI media. Furthermore, following Shearer and Chapman (1988), we gain considerable efficiency in ray-trace modeling of travel times with our assumption that velocity variations are linear with depth.

Here, we do numerical studies of errors in interpreted reflection time and lateral position as a function of reflector dip for models of the type described above. We treat only post-stack migration, and do so by considering only errors in the imaged position of dipping reflections for media with no lateral velocity variation. Those positioning errors are estimated from analysis of diffraction traveltime curves obtained by ray tracing.

Anisotropy and inhomogeneity can have a pronounced influence on the shape of diffraction curves, as evidenced by the comparison of diffraction curves for four models shown in Figure 1. All four curves pertain to a scatterer at depth $D = 1500$ m, beneath midpoint $y = 0$ m, in media having the same vertical root-mean-square (rms) velocity. They differ in that the different subsurface models represent the four combinations of homogeneous/inhomogeneous and isotropic/anisotropic. Here and throughout this paper, the anisotropy is FAI transverse isotropy, with vertical axis of symmetry. The two inhomogeneous models (solid curves) involve linear $v(z)$, where v represents any of the velocity-equivalents of the four elastic moduli describing p-wave behavior in a transversely isotropic medium.

For those models, the vertical p-wave velocity is given by

$$v(z) = v_0 + kz, \tag{1}$$

with the gradient $k = 0.6$ s^{-1}, and the vertical-direction velocity at the surface v_0 is such that the vertical rms velocity down to $D = 1500$ m is 3306 m/s, the vertical velocity for shale-limestone listed in Table 1. For the homogeneous, transversely isotropic model, the four elastic moduli [A, C, F, and L, in the notation of White (1983)] are those of the shale-limestone medium listed in Table 1). Actually listed in the table are *velocities* associated with the various moduli (i.e., $V_C = \sqrt{C/\rho}$—where ρ is bulk density—is the p-wave velocity in the vertical direction; V_A is the p-wave velocity in the horizontal direction; V_L is the s-wave velocity in the vertical direction; and V_F is a velocity-like quantity associated with the elasticity modulus F). For the anisotropic model with linear $v(z)$, the moduli are such that their associated *rms* velocities are equal to their constant-velocity counterparts in the homogeneous model.

In Figure 1, the curve for the homogeneous, isotropic model is a hyperbola, as expected, and the curves for the two inhomogeneous models are clearly non-hyperbolic, with inflection points at midpoints beyond which reflections pertain to turning waves (Hale, et al., 1992). While the diffraction curve for the homogeneous, anisotropic model differs from that for the homogeneous, isotropic one, it is not evident from this figure whether or not the curve is hyperbolic. As it happens, it is not: a plot of the instantaneous slope of the T^2 versus y^2 line indicates that, while the T^2 versus y^2 is almost straight, it is not strictly so. Instantaneous "stacking" velocity based on the instantaneous slope of $T^2(y^2)$ increases with increasing midpoint value y, from a value close to the velocity in the vertical direction at $y = 0$ to one that is close to that for propagation in the horizontal direction as y/D becomes large.

Medium	$\sqrt{C/\rho}$ m/s	$\sqrt{A/\rho}$ m/s	$\sqrt{F/\rho}$ m/s	$\sqrt{L/\rho}$ m/s
Berea sandstone	4206	4210	1961	2664
Shale-limestone	3306	3721	2076	1819
Cotton Valley shale	4721	5320	3095	2890
Pierre shale	2202	2235	1803	969

Table 1. Velocity-type quantities related to the four elastic moduli that are pertinent to p-waves in transversely isotropic media. The four media listed are the same as those studied by Levin (1990).

It is not obvious that the differences seen in the curves of Figure 1 would give rise to sizeable errors in migration when the wrong curve is used for the migration. As we shall see, however, for reflections from steep reflectors (i.e., for regions of the diffraction curves where y is large), the migration errors can be large—even tens of wavelengths. As it happens, the largest errors arise when isotropy is assumed for media that are anisotropic and *homogeneous*, rather than inhomogeneous.

ERROR COMPUTATION

The quality of a migration algorithm is usually assessed by applying the algorithm to synthetic and, ultimately, field data. Typical test data consist of reflections from plane-dipping reflectors, diffractions from point scatterers, and impulses. With data from plane reflectors, one measures the position of the migrated reflection relative to its known true location; with diffractions, one qualitatively assesses how well or poorly the diffractions *collapse* about the apex; and with impulses, one studies the shape of the impulse response.

Here, we are interested less in the quality of a particular migration algorithm than in errors that arise when the migration is based on an erroneous assumption (e.g., isotropy) about the velocity model. In the context of the Kirchhoff-summation view of migration, errors arise because the wrong diffraction curve is used to do the migration: points on sloping reflections are migrated to the wrong apex location.

Consider migration of the schematic, zero-offset, sloping reflection shown in Figure 2. In migrating the portion of the reflection in the vicinity of point (T, y), where T is unmigrated reflection time, we first find the diffraction curve that is tangent to the reflection at (T, y). If the velocity model is correct, migration will image the point (T, y) at the correct migrated position (T_m, y_m). Suppose, instead, that the wrong velocity model is used for the migration. Then, as depicted in Figure 3, after migration the point (T, y) goes to the erroneous position (T_e, y_e) instead of (T_m, y_m).

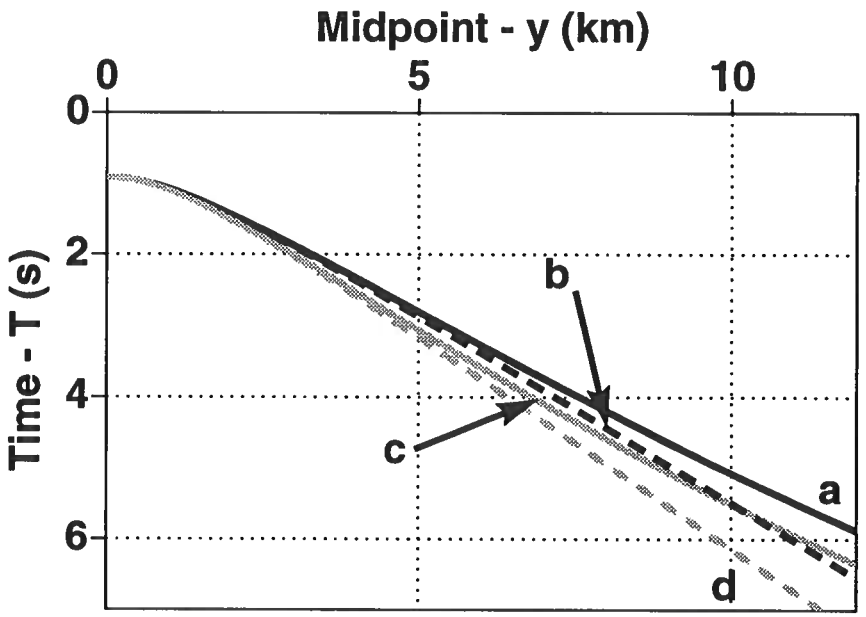

FIG. 1. Diffraction curves $T(y)$, where T is two-way time between a surface source at midpoint y and a scatterer at depth $D = 1500$ m beneath $y = 0$, for four related media characterized by the same vertical rms velocity. (a) transversely isotropic, with linear $v(z)$—black solid, (b) homogeneous, transversely isotropic—black dash, (c) isotropic with linear $v(z)$—gray solid, and (d) homogeneous, isotropic—gray dash. The latter curve is the only hyperbolic one.

Note that the point (T_e, y_e) is at the apex of the erroneous diffraction curve that is tangent to *both* the correct diffraction curve and the reflection at the unmigrated position (T, y). For the numerical estimates of migration error as a function of reflector dip, we do not actually compute reflections from plane-dipping reflectors. Instead, we work with just diffraction curves, recognizing that any point along a diffraction curve may be associated with a dipping reflector whose reflection is tangent to the diffraction curve at that point. The estimation of migration error involves three steps.

1. Compute diffraction curves associated with a buried point scatterer (such as those shown in Figure 1).

2. Estimate the erroneous position (T_e, y_e) to which any given point on the diffraction curve for the anisotropic medium migrates when an algorithm that erroneously assumes isotropy is used for the migration.

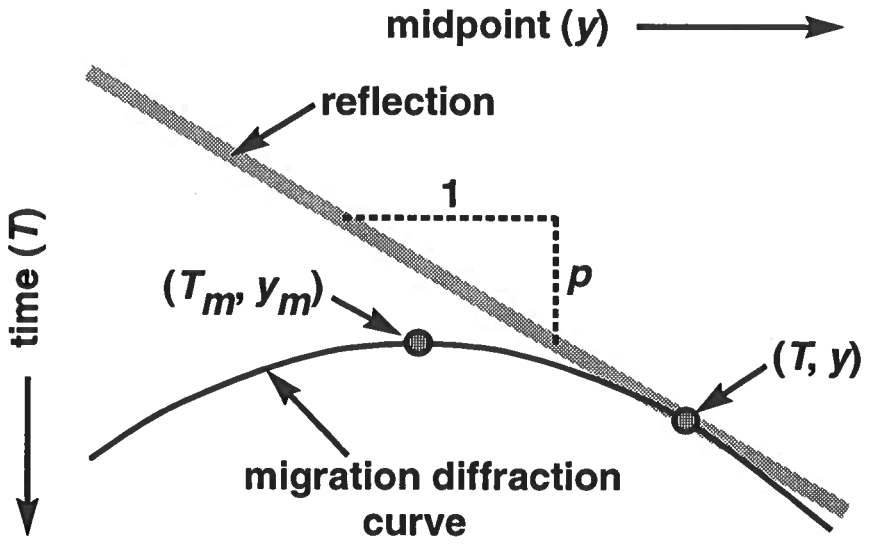

FIG. 2. Schematic time section showing the relationship between the unmigrated position (T, y) on a sloping reflection and the position (T_m, y_m) to which it should migrate. The migrated position is at the apex of the diffraction curve that is tangent to the reflection (slope = p) at the unmigrated position.

3. Estimate the error in interpreted temporal and lateral position of a migrated reflection by determining the departures in position and time of the erroneously migrated point from the correctly migrated reflection.

Computation of Diffraction Curves

While travel-time computation in inhomogeneous media generally first requires computationally intensive numerical integration to obtain ray paths, such numerical integration can be averted for special classes of media. For example, in isotropic media with constant gradient in velocity, ray paths are circular so that two-point ray tracing and travel-time computation can be done analytically. Shearer and Chapman (1988) have developed an efficient method for ray tracing in the type of media considered here—FAI media with constant velocity gradient. For transversely isotropic media, the core of their result is the remarkable property that ray paths are simply scaled, rotated versions of the polar plot of slowness as a function of angle from the axis of symmetry.

With this observation, Larner (1992) shows that, when the axis of symmetry for the transverse isotropy is parallel to the velocity gradient, two-point ray tracing can be done efficiently as the solution of a quadratic equation for x_1^2 as a function of (x_3^2) followed by a secant search to determine the ray parameter p_1. As shown in Figure 4, (x_1, x_3) is position along the ray path, where x_3 is the coordinate in the gradient direction, with $x_3 = 0$ being the line along which the linear velocity function is zero, and x_1 is the coordinate in the orthogonal direction, such that $x_1 = 0$ at the ray's

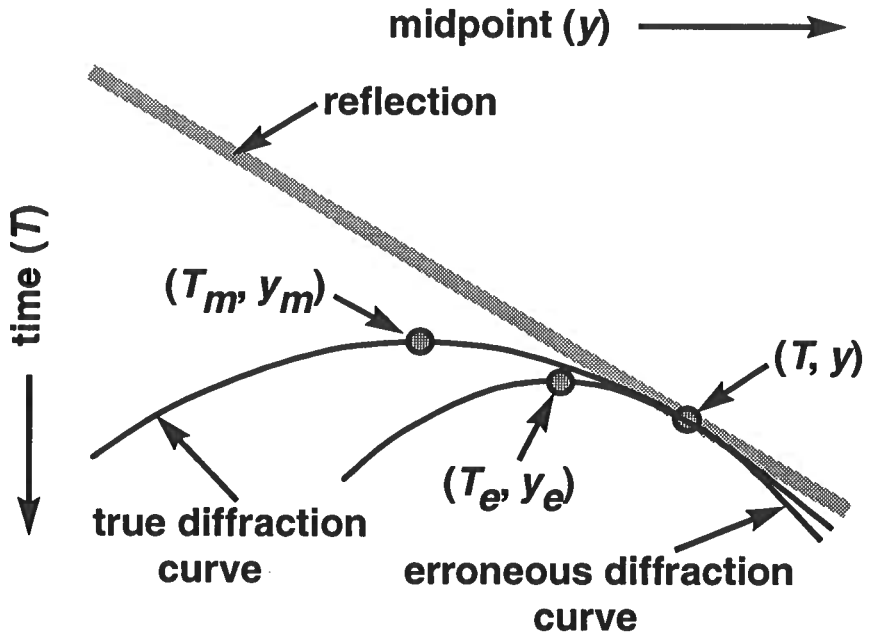

FIG. 3. Schematic time section showing the relationship between the unmigrated position (T, y) on a sloping reflection, the position (T_m, y_m) to which it should migrate, and the position (T_e, y_e) at which it is actually imaged when the data are migrated with an erroneous velocity function.

turning point. The coordinate x_3 is just a translated version of the depth z obtained by rewriting equation (1) as

$$v(z) = k(z + \frac{v_0}{k}) = kx_3,$$

where

$$x_3 = z + \frac{v_0}{k}. \tag{2}$$

Note, in Figure 4, that reflectors such as the one shown, in general, are not perpendicular to zero-offset ray paths when the medium is anisotropic. For anisotropic media, reflectors are orthogonal to the *phase* direction rather than the *ray* direction (Byun, 1984).

Different solutions of the quadratic equation for x_1^2 [see Larner (1992)] give ray paths for p-waves and for sv-waves. Here, we are interested in only the p-wave solutions. Once the ray parameter is determined, numerical integration is still required to obtain travel time; Červený (1989), however, shows the form of the integrand to be particularly simple, and the integration thus efficient, for the particular type of anisotropic medium under consideration here. The full procedure for computing $T(y_j)$ at uniformly sampled midpoint distances y_j is described in Larner (1992). There, it is also shown that, for zero-offset rays in media of the type studied here, reflector dip ϕ

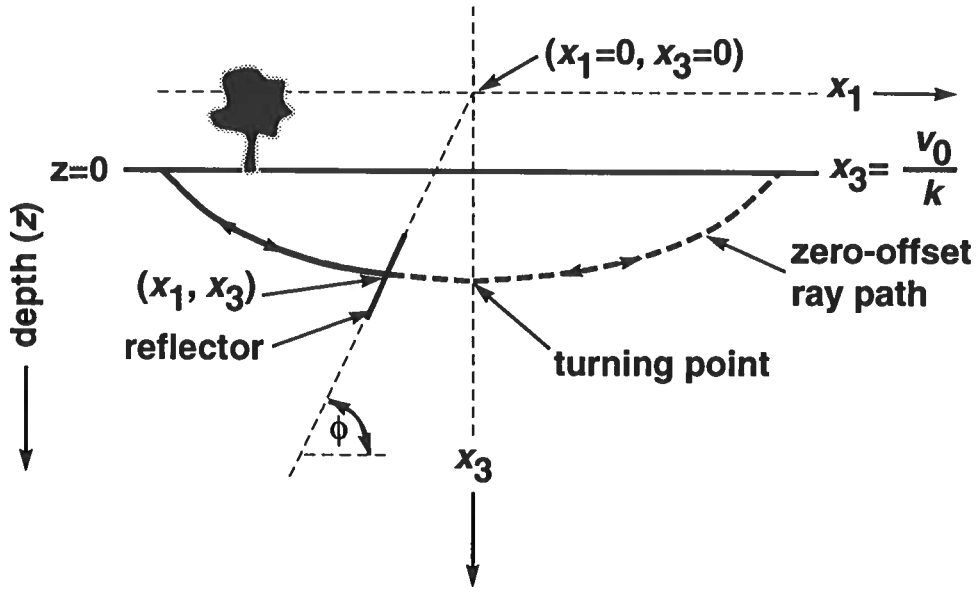

FIG. 4. Ray path in an FAI transversely isotropic, linear $v(z)$ half-space, shown in (x_1, x_3) coordinates. The medium's surface, $z = 0$, is equivalent to $x_3 = v_0/k$. Also, $x_1 = 0$ at the turning point. If this is a zero-offset ray path, then the line shown with dip ϕ represents a hypothetical reflector; the solid portion of the ray path pertains to a source-receiver location to the left of the reflector, and the dashed portion contains a turning ray that would image the underside of the reflector from the right. Note that the reflector is not perpendicular to the ray path except at the turning point.

at any point (x_1, x_3) is given by

$$\tan\phi = -\frac{x_3}{x_1}, \tag{3}$$

as indicated in Figure 4.

Estimation of Erroneous Migrated Position (T_e, y_e)

As illustrated in Figure 3, to find the erroneous migrated position (T_{ej}, y_{ej}) at which a point (T_j, y_j) is imaged, we must find the diffraction curve that is associated with the migration-velocity model and is tangent to the true diffraction curve $T(y)$ at (T_j, y_j). Specifically, the erroneous diffraction curve should have slope p_j at (T_j, y_j), where p_j is computed as

$$p_j = \frac{T_{j+1} - T_{j-1}}{y_{j+1} - y_{j-1}}.$$

This would be no problem if the migration process were based on the assumption that the medium were homogeneous and isotropic. Then, the migration diffraction curve would be a hyperbola, given by

$$T_j^2 = T_{ej}^2 + \frac{4(y_j - y_{ej})^2}{V_m^2},$$

where V_m is the migration velocity. Differentiating this equation gives the slope at (T_j, y_j)

$$p_j \equiv \frac{dT_j}{dy_j} = \frac{4(y_j - y_{ej})}{V_m^2 T_j},$$

or

$$y_{ej} = y_j - \frac{p_j V^2 T_j}{4}.$$

Also, the erroneously migrated time would be given by

$$T_{ej} = T_j \cos\theta_j,$$

where

$$\sin\theta_j = \frac{p_j V}{2}. \tag{4}$$

Assume instead that the data are migrated with an algorithm that honors vertical variation in velocity, but is founded on the assumption that the subsurface medium is isotropic [e.g., the phase-shift method of Gazdag (1978)]. Then, at the outset, the depth z_j of the scatterer that would give rise to the migration diffraction curve with slope p_j at (T_j, y_j) is unknown, and hence, the migration velocity required to generate that migration diffraction curve is initially unknown.

To find that scatterer depth and associated velocity, we match the slopes of the true and migration diffraction curves at the point (T_j, y_j), as follows. Let the erroneous, migration diffraction curve be given by $t(x)$, where, referring to Figure 3,

$$x = y - y_e \tag{5}$$

is the migration distance. We assume that the velocity model used for migration is isotropic, with velocity given by equation (1). That is, the velocity at any depth z is identical to the velocity in the vertical direction in the true, transversely isotropic medium. (Below, we shall modify this assumption somewhat.) For such a medium, ray paths are circles, and, using the expression of Dietrich and Cohen (1992), the two-way time t between a surface point at midpoint y and a scatterer at depth (y_e, z) is given by

$$\begin{aligned} t &= \frac{2}{k}\cosh^{-1}\left(\frac{k^2x^2 + v_0^2 + v^2(z)}{2v_0 v(z)}\right) \\ &= \frac{2}{k}\cosh^{-1}(\alpha x^2 + \beta) \\ &= \frac{2}{k}\cosh^{-1}\eta, \end{aligned} \tag{6}$$

where

$$\begin{aligned} \alpha &\equiv \frac{k^2}{2v_0 v(z)} \\ \beta &\equiv \frac{v_0^2 + v^2(z)}{2v_0 v(z)} \\ \eta &\equiv \alpha x^2 + \beta = \cosh\frac{kt}{2}. \end{aligned} \tag{7}$$

Differentiating equation (6) gives the slope of the diffraction curve

$$p \equiv \frac{dt}{dx} = \frac{4\alpha x}{k\sqrt{\eta^2 - 1}}. \tag{8}$$

Given measurements of T_j $(= t)$ and p_j, and assuming that the constants v_0 and k in equation (1) are known, we eliminate x from equations (7) and (8). There results a quadratic equation for $v(z_j)$, whose appropriate solution is

$$v(z_j) = \frac{v_0(\cosh\delta + \sinh\delta\sqrt{1-g^2})}{1 + g^2\sinh^2\delta}, \tag{9}$$

where

$$\begin{aligned} \delta &= \frac{kt_j}{2} \\ g &= \frac{p_j v_0}{2}. \end{aligned} \tag{10}$$

Once $v(z_j)$ has been determined, the depth z_j is obtained from equation (1), x_j from equation (8), and y_{ej} from equation (5). Finally, the vertical reflection time to the scatterer is given by

$$T_{ej} = 2\int_0^{z_j} \frac{d\sigma}{v_0 + k\sigma} = \frac{2}{k}\log\frac{v(z_j)}{v_0}. \tag{11}$$

Estimation of Migration Error

We have just seen how the erroneous migrated position (T_{ej}, y_{ej}) is computed. In addition, the correct position (T_m, y_m) is known to be just the apex of the diffraction curve (T_j, y_j) obtained from by tracing in the FAI transversely isotropic medium. At first thought, it might seem from Figure 3 that the sought-after errors in migrated time and position are just $(T_e - T_m)$ and $(y_e - y_m)$, respectively (from here on, the subscript j is dropped). While, in a sense that is true, such measures will not suffice for assessing errors in position of the reflections that would confront interpreters. Interpreters rarely identify how individual *points* in data move when data are migrated. Instead,

they generally focus attention on *reflections* that, if not planar, are often locally approximately so.

Consider the sloping reflections in the schematic, migrated zero-offset section shown in Figure 5a. In practice, the incorrectly migrated reflection through migrated point (T_e, y_e) would be approximately parallel to the correctly migrated reflection through (T_m, y_m), as depicted in the figure. The quantities Δy and ΔT shown in the figure are the measures of error that would be apparent to the interpreter. Note that given (T_e, y_e) and (T_m, y_m), Δy and ΔT vary with the slope p_m of the migrated reflection. That is, one has to know, or estimate, p_m in order to compute Δy and ΔT. This fact becomes obvious when Figures 5a and 5b are compared. Figure 5b depicts a situation where the apex positions (T_e, y_e) and (T_m, y_m) are identical to those in Figure 5a, but the slopes of the reflections differ greatly in the two figures. One might pertain to a reflector dip that is less than 90 degrees, and the other to one that exceed 90 degrees. As a result, the migration errors Δy and ΔT differ considerably in the two figures.

The dependence of Δy and ΔT on the slope p_m is readily seen in the geometry of Figure 5. We have

$$\begin{aligned} \Delta y &= (y_e - y_m) - \frac{T_e - T_m}{p_m} \\ \Delta T &= -p_m \Delta y. \end{aligned} \tag{12}$$

So, these two inter-related measures of migration error can be fully estimated once we know the slope p_m of the correctly migrated reflections. That slope is readily computed from knowledge of $v(z)$ and the reflector dip ϕ. Such a reflector is depicted in Figure 6. Also shown are vertical "paths" from two surface points separated by the distance Δy down to the reflector. Migrated reflection time at the two surface points is just the two-way time along these vertical paths. Locally, the migrated-reflection slope is taken as constant, given by

$$\begin{aligned} p_m &\equiv \frac{\Delta T_m}{\Delta y} \approx \frac{dT_m}{dy} \\ &= \frac{dT_m}{dz}\frac{dz}{dy} = \tan\phi \frac{dT_m}{dz}. \end{aligned}$$

But, for any $v(z)$ medium,

$$T_m = 2\int_0^z \frac{d\sigma}{v(\sigma)},$$

so

$$\frac{dT_m}{dz} = \frac{2}{v(z)},$$

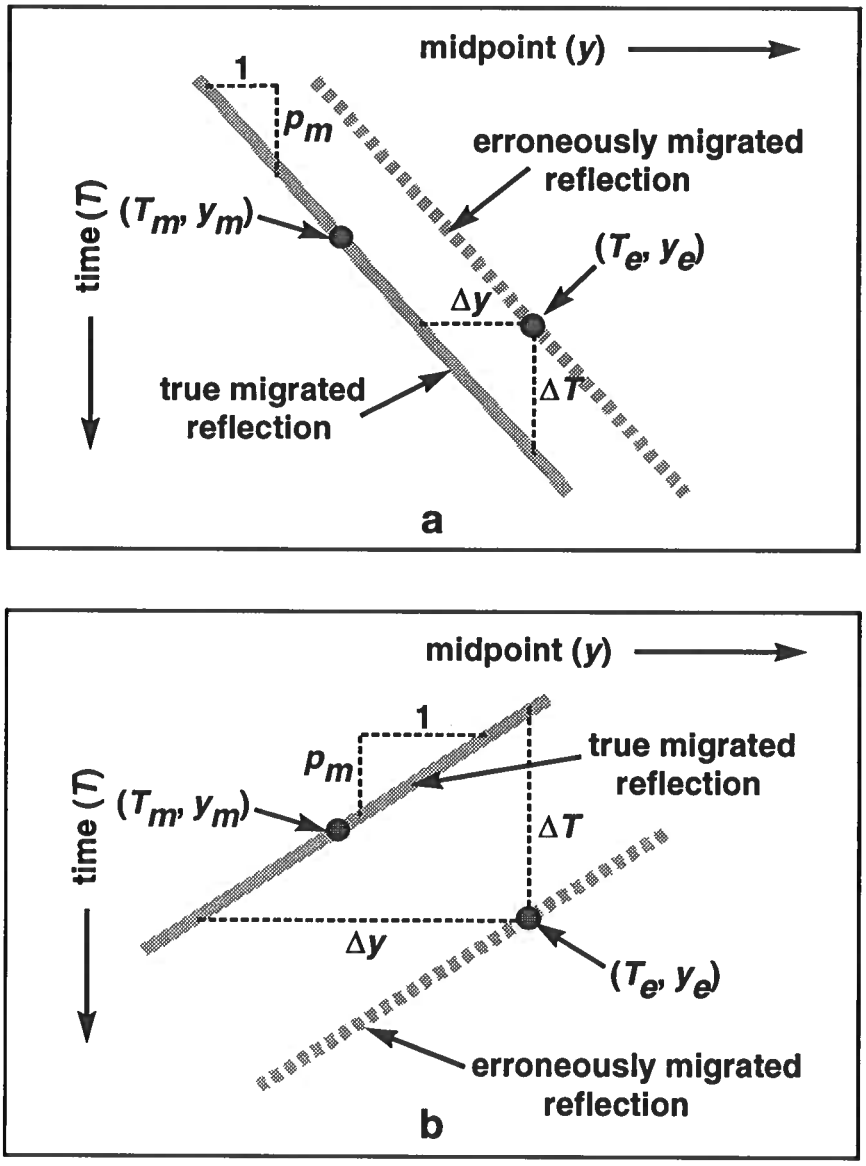

FIG. 5. Schematic time sections showing the erroneously migrated (dashed) and correctly migrated (solid) reflections through the erroneously and correctly imaged positions (T_e,y_e) and (T_m,y_m). The lateral error in imaged reflection position is Δy, and the time error is ΔT. Figures 5a and 5b differ only in that the slope p_m of the migrated reflection differs in the two cases.

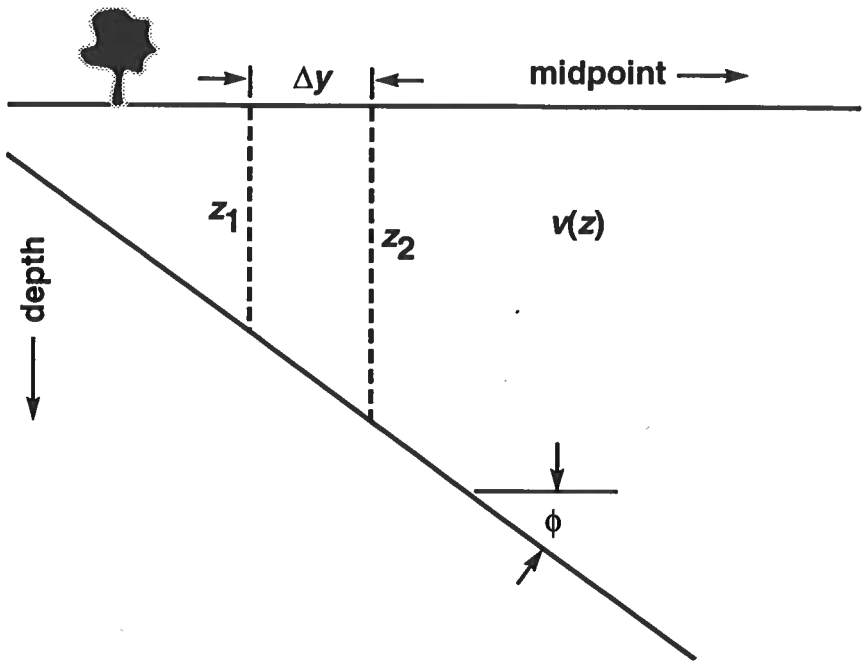

FIG. 6. Schematic depth section showing a dipping reflector beneath a $v(z)$ medium. Migrated reflection times at two neighboring points on the surface are simply two-way times along the vertical paths.

from which we get

$$p_m = \frac{2\tan\phi}{v(z)}. \tag{13}$$

Note that this result, which is familiar for homogeneous media, holds for any $v(z)$ medium, even a generally anisotropic one. For our error studies, then, we have all the information required to compute the migration errors Δy and ΔT once we can associate any point (T_j, y_j) along the true diffraction curve (for a scatterer at depth z) with a reflector dip ϕ_j. That dip is available from the ray-tracing result, equation (3).

WHAT FORM OF VELOCITY TO USE FOR MIGRATION?

Reiterating, our estimates of migration error come from relating the true diffraction curve (i.e., that for an FAI transversely isotropic medium with linear $v(z)$ dependence) to the diffraction curve associated with the time-migration process used, and, almost universally in practice, that migration process is based on the assumption that the subsurface is isotropic and vertically inhomogeneous. As is known, if the medium were homogeneous and isotropic, no issue would arise as to which form of velocity to use in the migration—migration velocity = rms velocity = stacking velocity (assuming horizontal reflectors) = medium velocity. Equally well known, for vertically inhomogeneous, isotropic media, stacking velocity (obtained by $T^2 - X^2$ analysis over a finite spread-length X) exceeds rms velocity, approaching it as the spread-length

approaches zero. When the medium is anisotropic (even when it is homogeneous), the situation becomes more complex.

Levin (1979) has shown that, in a transversely isotropic medium with vertical axis of symmetry, stacking velocity for p-wave reflections from horizontal interfaces differs from the vertical velocity, even in the limit as spread-length X approaches zero. The limiting stacking velocity can be larger or smaller than the vertical velocity, depending on ratios among the four pertinent elastic moduli. Moreover, Thomsen (1986) shows that, for so-called *weak* anisotropy, the relationship between these two types of velocity is *totally independent* of the ratio of horizontal-direction velocity to vertical-direction velocity, V_A/V_C—the most commonly quoted measure of degree of anisotropy. As we shall see, this same discrepancy between zero-offset-limit stacking velocity and vertical velocity in homogeneous media carries over into a difference between zero-offset-limit stacking velocity and vertical *rms* velocity for inhomogeneous media.

Given this complexity, for studies of migration error and, indeed, when doing migration in practice, which form of velocity should we use—vertical rms velocity, stacking velocity based on finite spread-length, or the limiting stacking velocity as offset approaches zero?

Figure 7 shows computed lateral position errors Δy for reflector dip ranging from 0 to 120 degrees, for four different choices of migration velocity. Results are shown for the shale-limestone and Cotton Valley shale tabulated in Table 1 [the quantities shown in Table 1 are computed from the parameters of Thomsen (1986)]. The media treated in Figure 7 have linear velocity increase with depth, with vertical rms velocity matching the $V_C = \sqrt{C/\rho}$ values in Table 1 (e.g., the vertical rms velocity for the inhomogeneous shale-limestone medium is 3306 m/s). For these tests, the reflector depth is 1500 m, and the gradient $k = 0.6$ s^{-1} in the vertical-velocity expression $v(z) = v_0 + kz$.

Not surprising, as seen in Figure 7, the position errors depend on the velocity function used for the migration. For both the shale-limestone and Cotton Valley shale, migration errors are smallest for the migration-velocity function $v(z)$ that is based on stacking velocity computed when the spread-length is comparable to reflector depth—a satisfying result since, in practice, velocity is most often estimated in this way. From the figure, the poorest choice of velocity function for migration is that based on the vertical rms velocity, such as might be obtained from sonic-log data.

Perhaps most striking in the Figure 7 is the dramatically anomalous error behavior for the Cotton Valley shale when the migration velocity is based on the rms velocity. For the shale-limestone, errors for stacking velocity approach those for rms velocity as the spread-length shrinks to zero. Such is not the case for the Cotton Valley shale. This behavior for migration error is consistent with Thomsen's (1986) predictions that small spread-length stacking velocity for transversely isotropic media can depart significantly from vertical velocity.

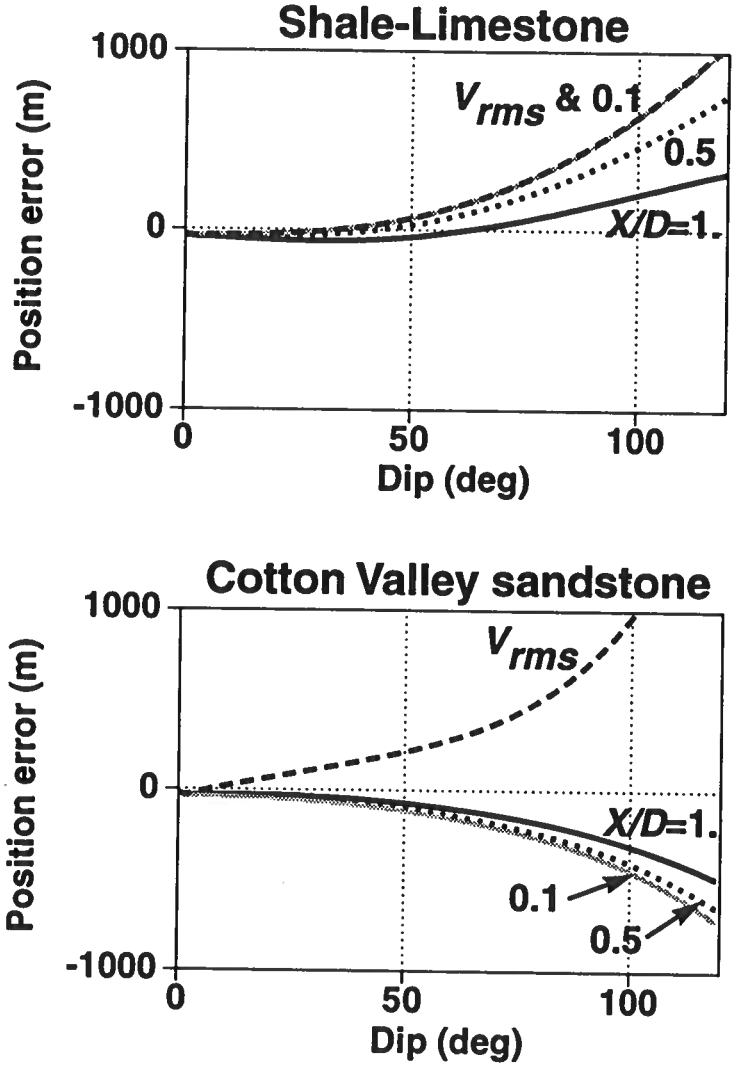

FIG. 7. Position error Δy versus reflector dip for shale-limestone (top) and Cotton Valley shale (bottom). For each, the reflector depth is $D = 1500$ m and the vertical velocity gradient is $k = 0.6$ s^{-1}. For the dashed curve, the $v(z)$ velocity function used for migration is derived from the vertical rms velocity to the reflector. For the other three curves, the $v(z)$ velocity function used for migration is derived from the stacking velocity to a horizontal reflector at depth D, with different choices of ratio of spread-length to depth X/D used in the stacking-velocity computation.

Medium	V_A/V_C	V_{stack}/V_{rms}			
		$X/D = 1.0$	$X/D = 0.5$	$X/D = 0.1$	Thomsen
Berea sandstone	1.001	1.01	1.02	1.02	1.02
Shale-limestone	1.126	1.06	1.02	1.00	1.00
Cotton Valley shale	1.127	1.16	1.18	1.19	1.19
Pierre shale	1.015	1.04	1.05	1.06	1.06

Table 2. For the four media treated in this study, columns 3–5 list the ratio of stacking velocity to vertical rms velocity for three values of the ratio of the spread-length to reflector depth. For comparison, column 6 contains the ratio of zero-offset stacking velocity to rms velocity predicted by Thomsen (1986). Column 2 lists the ratio of horizontal to vertical medium velocity—the most frequently quoted measure of degree of anisotropy.

Table 2 gives a summary of the ratio V_{stack}/V_{rms} measured in my studies with transversely isotropic, linear $v(z)$ media. For comparison are shown Thomsen's predictions, which were derived for *homogeneous* transversely isotropic media. The equality of values in columns 5 and 6 of the table shows that Thomsen's predictions extend to inhomogeneous media. Moreover, also in agreement with Thomsen's predictions, note the considerable differences between the values in column 6 for the shale-limestone and Cotton Valley shale despite the fact that the ratios of horizontal to vertical velocity for the two media (column 2) are nearly identical.

Repeating, based on the curves shown in Figure 7, along with those for the other media studied (Berea sandstone and Pierre shale; not shown here), the migration-velocity function that is derived from stacking velocity computed when the spread-length is comparable to reflector depth yields the smallest of the errors. Thus, both in accord with these results and mimicking common practice, the velocity function that we use for all the migration-error tests below is based on stacking velocity (for horizontal reflectors) with $X/D = 1$, and the migration action simulated fully takes into account velocity variation with depth.

MIGRATION-ERROR RESULTS

Anisotropy versus Inhomogeneity

Figure 8 shows position error Δy (top) and time error ΔT (bottom) as a function of reflector dip ranging from 0 to 120 degrees for three different models, all of which have properties related to those of the transversely isotropic shale-limestone listed in Table 1. For all three curves, the reflector depth is 1500 m. The solid gray curves pertain to a homogeneous medium with just the properties listed in Table 1. The solid black curves are for a $v(z) = v_0 + kz$ medium with gradient $k = 0.6\ \mathrm{s}^{-1}$, and with

v_0 such that the vertical rms velocity to the reflector is 3306 m/s. Consider, first, just the position errors. The gray curve exhibits large error for dips greater than about 60 degrees. Clearly if we limited our analysis to just *homogeneous* media, we would conclude that failure to take anisotropy into account would lead to migration errors that are intolerably large for steep reflectors. However, we find that the combination of anisotropy *and* velocity variation with depth (solid black curve) leads to much more tolerable errors—even for dips as large as 120 degrees. As we shall see below, in some sense the shale-limestone is the most extreme of the four types of media studied here. For the other media, the errors, even for the homogeneous models, are not so large as those shown here. In all cases, nevertheless, errors are smaller for the inhomogeneous models than for their (unrealistic) homogeneous counterparts.

Now, consider the dotted curve in the top part of the figure. This curve pertains to an *isotropic* medium with $v(z)$ identical to the vertical-velocity function in the transversely isotropic shale-limestone. If we were to migrate data from such a medium with an algorithm that honors the $v(z)$ behavior, such as the phase-shift method of Gazdag (1978) as extended for turning waves by Hale, et al. (1992), then we would get near-zero error for all dips. The dotted curve, however, simulates errors that would arise if the data were migrated with a simplistic Kirchhoff-type time-migration algorithm (Schneider, 1978) that uses a hyperbolic diffraction curve based on the stacking velocity. Such a limited algorithm is known to yield unacceptable errors for steep reflectors; the dotted curve, then, shows the size of error that is corrected when a phase-shift-type migration approach is used.

Stated differently, the dotted curve gives the errors when inhomogeneity is not properly treated in the migration of an inhomogeneous, isotropic medium, while the gray curve gives the errors when anisotropy is not taken into account in the migration of a homogeneous, transversely isotropic medium with the shale-limestone properties. Significantly, for dip less than about 60 degrees, anisotropy is the considerably less serious issue.

Comforting as is the conclusion that errors are not so large when the medium is *both* inhomogeneous and anisotropic, we should still note that the errors for the poorly migrated isotropic medium are correctable (with, for example, a phase-shift algorithm), whereas those for the anisotropic medium would require that we have adequate information about the four pertinent elastic moduli of the medium and that we use an imaging algorithm that takes the anisotropy into account.

The time-error curves in the lower part of Figure 8 tell a comparable story, but they also show what appears to be a disturbing instability near 90-degree dip. Actually, the behavior is not so troubling as it may appear. For a plane reflector near vertical, a huge error in reflection time would not be noticeable to the interpreter since the temporal period of migrated reflections becomes large without bounds as dip approaches 90 degrees. Similarly, a seemingly large error Δy in lateral position is inconsequential for small dip since the apparent wavelength in the lateral direction becomes large as dip approaches zero. Whether it be time error or position error,

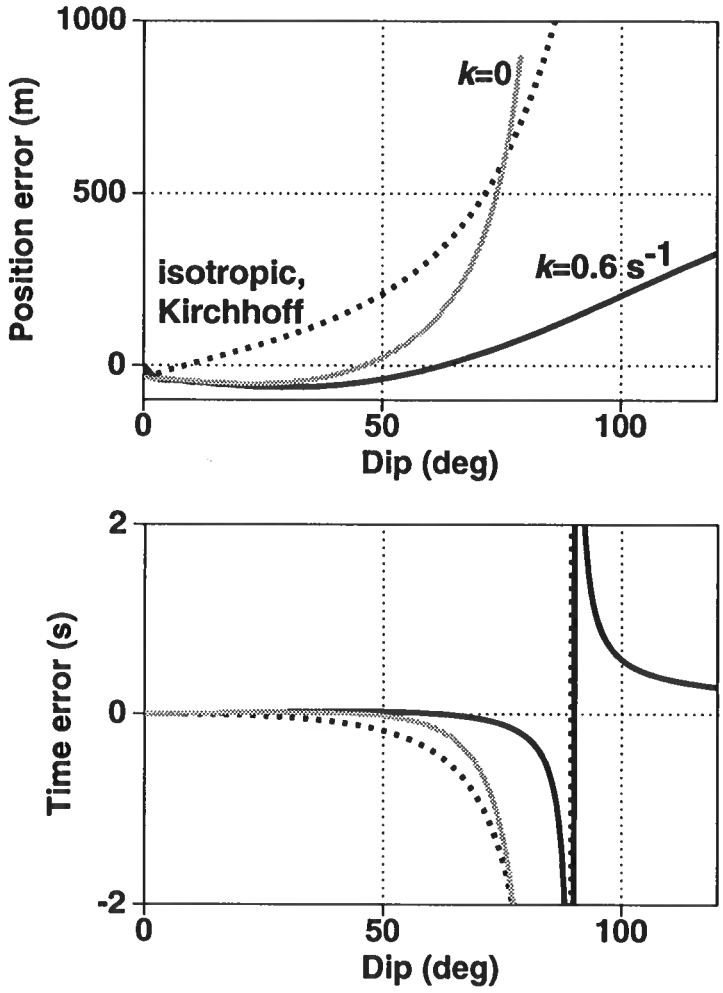

FIG. 8. Position error Δy (top) and time error ΔT (bottom) versus reflector dip for three different cases related to the transversely isotropic shale-limestone. Solid black: The actual medium is inhomogeneous with $v(z) = v_0 + 0.6z$ and anisotropic; the inhomogeneity is honored in the migration, and the plotted errors are due to neglect of the anisotropy. Gray: The medium is the anisotropic shale-limestone, but now velocity is constant; the plotted errors are again due to the neglect of anisotropy in the migration. Dotted: Now the actual medium is *isotropic* but inhomogeneous, with linear $v(z)$, as above; the plotted errors are due to neglect of the inhomogeneity (e.g., migration is done with a Kirchhoff-type algorithm that uses hyperbolic diffraction curves based upon stacking velocity).

the interpreter will be concerned only with errors that are large *relative to a period, or wavelength*, as the case may be. For that reason, henceforth, we shall study errors normalized, as follows, so that they are expressed in terms of multiples of the dominant period and wavelength in the migrated data.

Earlier, we saw that migration increases the slope of a reflection from p before migration to $p_m = 2\tan\phi/v(z)$, afterward. Migration also lowers frequencies such that horizontal wavelength λ is preserved. Consequently,

$$\frac{1}{\lambda} = f_m\, p_m = f\, p, \tag{14}$$

where f is frequency in the unmigrated reflection wavelet, and f_m is the frequency after migration.

Subsequent position error curves are plotted in terms of *normalized* values given by

$$\Delta\tilde{y} = \frac{\Delta y}{\lambda_d}, \tag{15}$$

where, from equation (14),

$$\lambda_d = \frac{1}{f_d\, p} \tag{16}$$

is the horizontal wavelength, after migration, corresponding to some assumed dominant frequency f_d in the unmigrated reflections.

If we, similarly, normalize time errors such that

$$\begin{aligned} \Delta\tilde{T} &= \frac{\Delta T}{\tau_d} \\ \tau_d &= p_m\, \lambda_d, \end{aligned} \tag{17}$$

from equation (12) it follows that, simply,

$$\Delta\tilde{T} = -\Delta\tilde{y}.$$

Note, that since $p_m < 0$ for dips exceeding 90 degrees, τ_d as defined in equation (17) is also negative for those large dips. This unusual choice, rather than defining τ_d to be always positive, is a convenience that ensures that the normalized time error is continuous at 90-degree dip—indeed that it is just the negative of the normalized position error.

Figure 9 shows the normalized position error $\Delta\tilde{y}$ corresponding to the error Δy in Figure 8. For the normalization here and in subsequent figures, the dominant frequency is taken as 30 Hz.

While the errors for the homogeneous shale-limestone can be very large for steep reflectors (more than ten wavelengths for dips exceeding about 60 degrees), errors for the inhomogeneous counterpart are about two wavelengths for vertical reflectors,

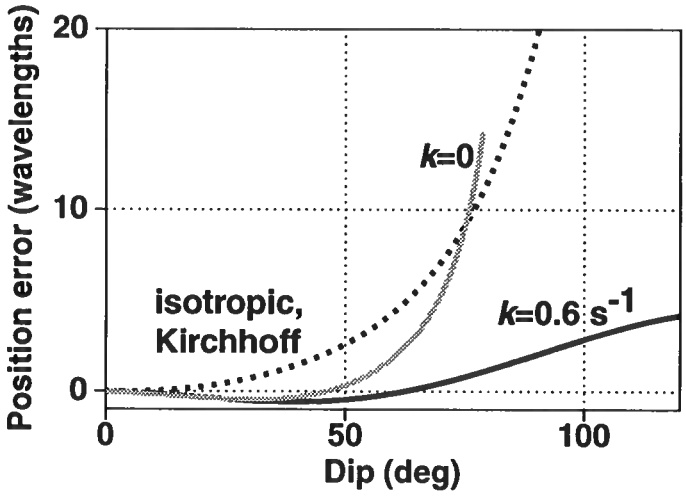

FIG. 9. Same as the top part of Figure 8 except that the position errors are now the *normalized* quantities $\Delta\tilde{y}$, expressed in multiples of post-migration wavelengths corresponding to unmigrated reflections with dominant frequency 30 Hz.

and just four wavelengths at 120-degree dip. Again, these errors are much smaller than the errors for isotropic media that are corrected when a phase-shift algorithm, as opposed to one that involves hyperbolic diffractions, is used for migration.

Dependence on Velocity Gradient

With reflector depth fixed at 1500 m and the vertical rms velocity at 3306 m/s, Figure 10 shows the dependence of normalized position errors on the velocity gradient, k, for the shale-limestone, and Figure 11 shows the normalized position errors for the four media listed in Table 1. For all four media, the failure to take anisotropy into account in migration is a less serious issue when the medium is inhomogeneous than if it were homogeneous, but for only the shale-limestone is the difference truly significant. For the others, failure to take anisotropy into account in the migration appears to be a less severe problem than is that for the shale-limestone.

Not surprising, errors in most cases tend to be larger for larger reflector dip. Of the four media, the Berea sandstone is most weakly anisotropic, and gives errors that are least influenced by the inhomogeneity. The shale-limestone is anomalous in that the position errors for larger dips are positive, whereas errors for the other media are negative. Thus, steep reflectors in the shale-limestone are *under-migrated* when anisotropy is not taken into account in the migration algorithm, while those in the other media are over-migrated. Intuition might lead one to predict that the presence of anisotropy would cause data to be under-migrated since isotropy-based migration algorithms fail to adapt to the higher propagation speeds that arise for waves that

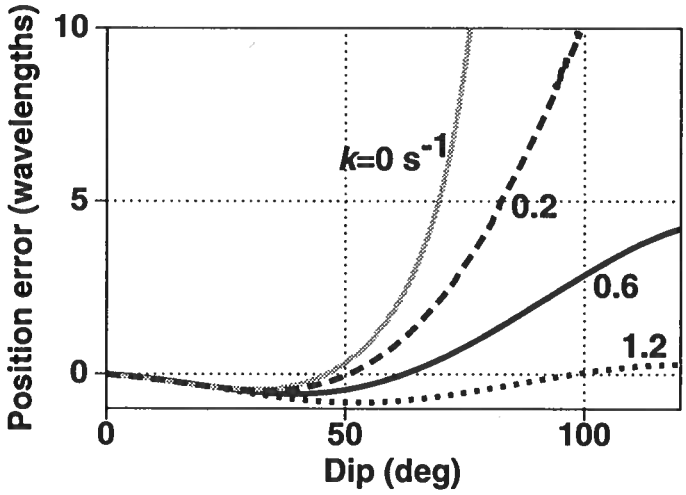

FIG. 10. Normalized position errors (at 30 Hz) as a function of reflector dip for the shale-limestone, with velocity gradients k=0.0, 0.2, 0.6, and 1.2 s^{-1}. All models have the same vertical rms velocity, 3306 m/s, and the reflector depth is 1500 m in all cases. In all cases the medium is inhomogeneous and anisotropic, and the inhomogeneity is honored in the migration. The plotted errors are due to neglect of the anisotropy in the migration. Each curve shows the errors for the indicated velocity gradient.

turn close to horizontal. As often happens, intuition fails when it comes to anisotropy. The diametrically opposing behavior of errors for the shale-limestone and the Cotton Valley shale is particularly striking, again because the ratio of horizontal to vertical velocity, V_A/V_C, is almost identical in the two media.

Based on the migration errors in Figure 11, we would infer that the shale-limestone has the greatest degree of anisotropy, followed by the Pierre shale and Cotton Valley shale, and finally the Berea sandstone—not quite the order that would be predicted on the basis of V_A/V_C. Note that errors for the Cotton Valley shale are somewhat less dependent on the velocity gradient than are those for the Pierre shale (note: the curve for gradient $k = 1.2$ s^{-1} is not shown).

While linear $v(z)$ is certainly not the norm for the earth's subsurface, to the extent that it is, $k = 0.6$ s^{-1} is a somewhat representative value: $k = 1.2$ s^{-1} is on the high side, and $k = 0.2$ s^{-1} is clearly too small to yield the velocity increases with depth that are normally encountered. Thus, for all four media the "representative" case, $k = 0.6$ s^{-1}, exhibits errors no larger than three or four wavelengths and periods even for dips as large as 120 degrees.

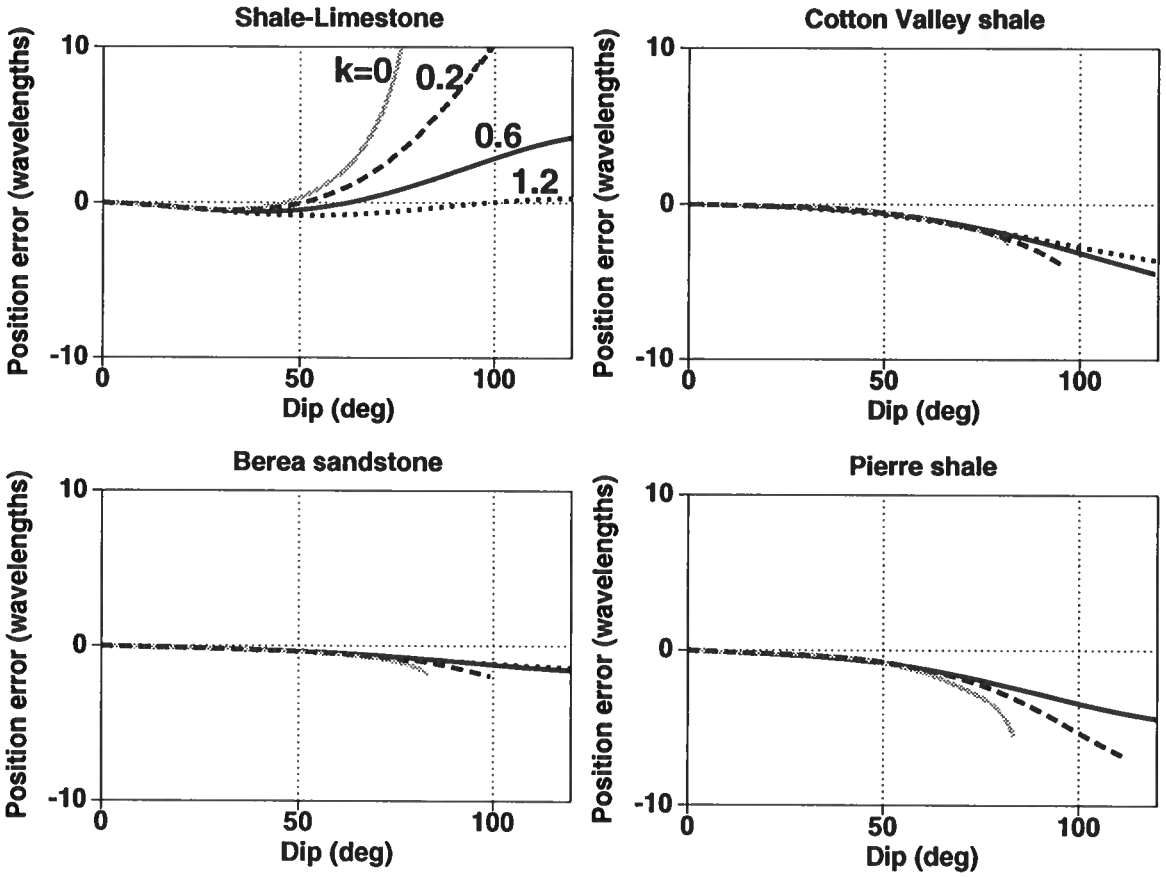

FIG. 11. Normalized position error (at 30 Hz) as a function of reflector dip for the four media listed in Table 1, with velocity gradients k=0.0, 0.2, 0.6, and 1.2 s^{-1}. The reflector depth is 1500 m in all cases.

Dependence on Reflector Depth and on Stacking Velocity

Focusing our attention on the shale-limestone medium, Figure 12 shows the dependence of migration error on medium velocity and reflector depth. As throughout this paper, the ratios of the four velocity quantities characterizing the transverse isotropy are independent of depth and match those for the velocities listed in Table 1. In generating the three curves shown in the top portion of the figure, the vertical velocity at the surface v_0 was set so as to yield vertical rms velocities of 3000 m/s, 2200 m/s, and 1500 m/s at the reflector depth. For linear $v(z)$ media characterized by equation (1), the relationship between surface velocity v_0 and vertical rms velocity $V_{rms}(z)$ is given by

$$V_{rms}^2(z) = \frac{v^2(z) - v_0^2}{2 \log \dfrac{v(z)}{v_0}}. \tag{18}$$

Given kz and V_{rms}, a Newton-Raphson search solves this equation for v_0.

In this figure, the solid black curve pertains to parameters that are close to those that generated the solid black curve in Figure 10. The dependence of errors on rms velocity and on depth exhibit much similarity. The errors tend to become less positive with either increasing reflector depth or decreasing velocity. Inspection of Figure 12 reveals a pattern that is better exhibited in Figure 13. There, it is seen that the shape of an error curve is almost independent of either the depth or rms velocity so long as the ratio of the two is held constant. Since this ratio approximates migrated reflection time, we infer that the shape and, indeed, the *sign* of the error curve for the shale-limestone is governed by the migrated reflection time. Thus *depending on the migrated reflection time* the data may be either over-migrated or under-migrated when anisotropy is not taken into account in the migration process.

Results of similar tests on the other three media listed in Table 1 confirm this dependence of error on migrated reflection time. Thus, inferences, made in the preceding section, about the relative importance of anisotropy for the four different media must be reviewed in the light that error behavior for any given medium can vary considerably with migrated reflection time. The complexity of the migration-error behavior for the different media emerges in Figure 14.

For all the models treated in Figure 14, the velocity gradient is 0.6 s^{-1}. The three error curves shown for each of the four media pertain to rms velocity and reflector depth chosen such that the migrated reflection time is approximately 0.67, 1.0, and 2.0 s (here, we ignore the inconsequential—for our purposes—distinction between rms velocity and average velocity).

While it is satisfying to find that the migration errors depend only on migrated reflection time, that dependence, nevertheless, can be significant. For the shale-limestone medium, for example, ignoring anisotropy leads to under-migration for shallow reflectors, but to over-migration of deeper reflectors. Moreover, at migrated times later than about 1 s, reflections in the Cotton Valley shale become significantly

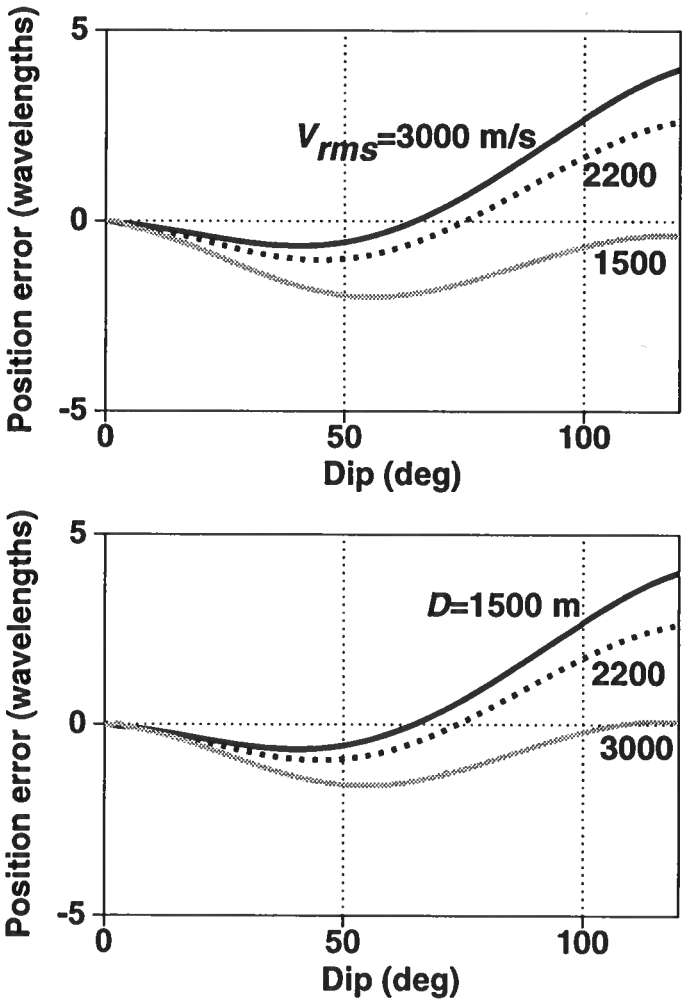

FIG. 12. Velocity dependence (top) and depth dependence (bottom) of normalized position errors as a function of reflector dip for FAI shale-limestone. All models have the "representative" velocity gradient, $k = 0.6\ s^{-1}$. Depth is held constant (1500 m) for the velocity tests on the top, and vertical rms velocity is held constant (3000 m/s) for the depth tests on the bottom.

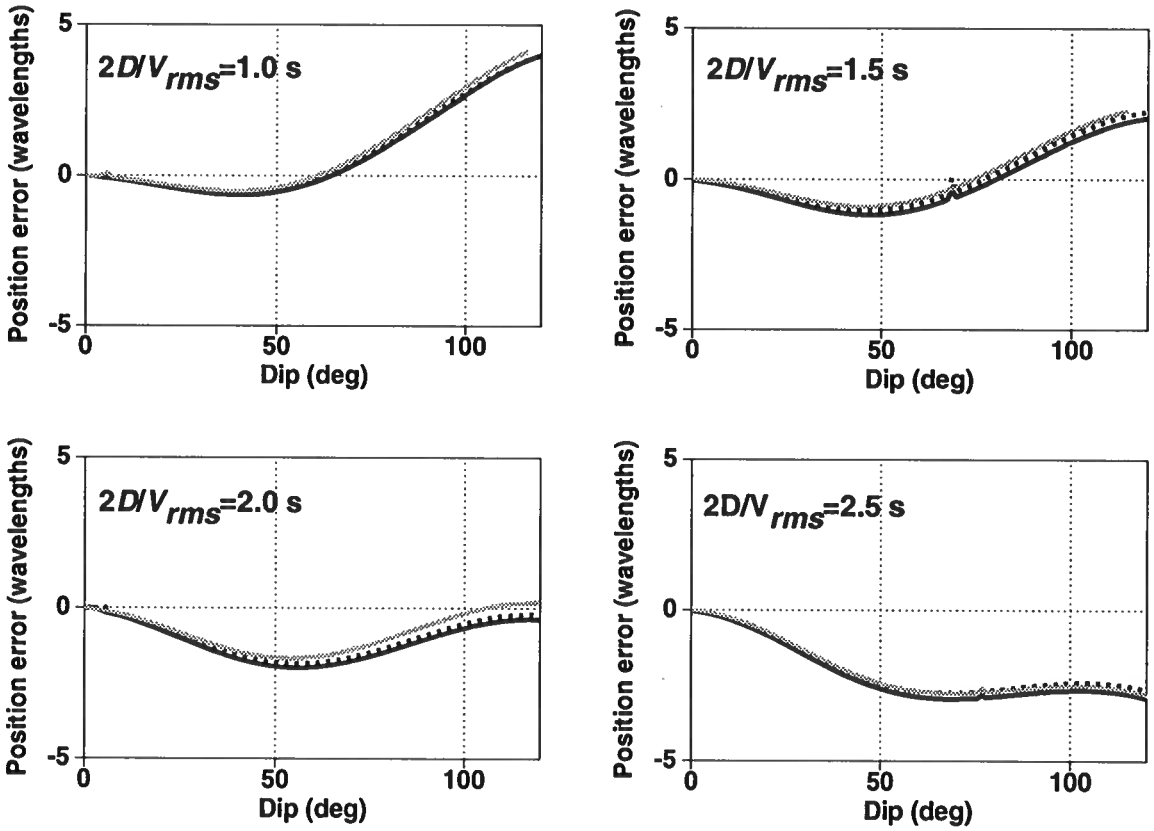

FIG. 13. Normalized position errors as a function of reflector dip for FAI shale-limestone, for four values of approximate migrated reflection time $2D/V_{rms}$. All models have the same velocity gradient, $k = 0.6\ \mathrm{s}^{-1}$. Within each box, are plotted three nearly overlapping curves. Each curve is for a different choice of D and V_{rms}, with values ranging over a factor of two.

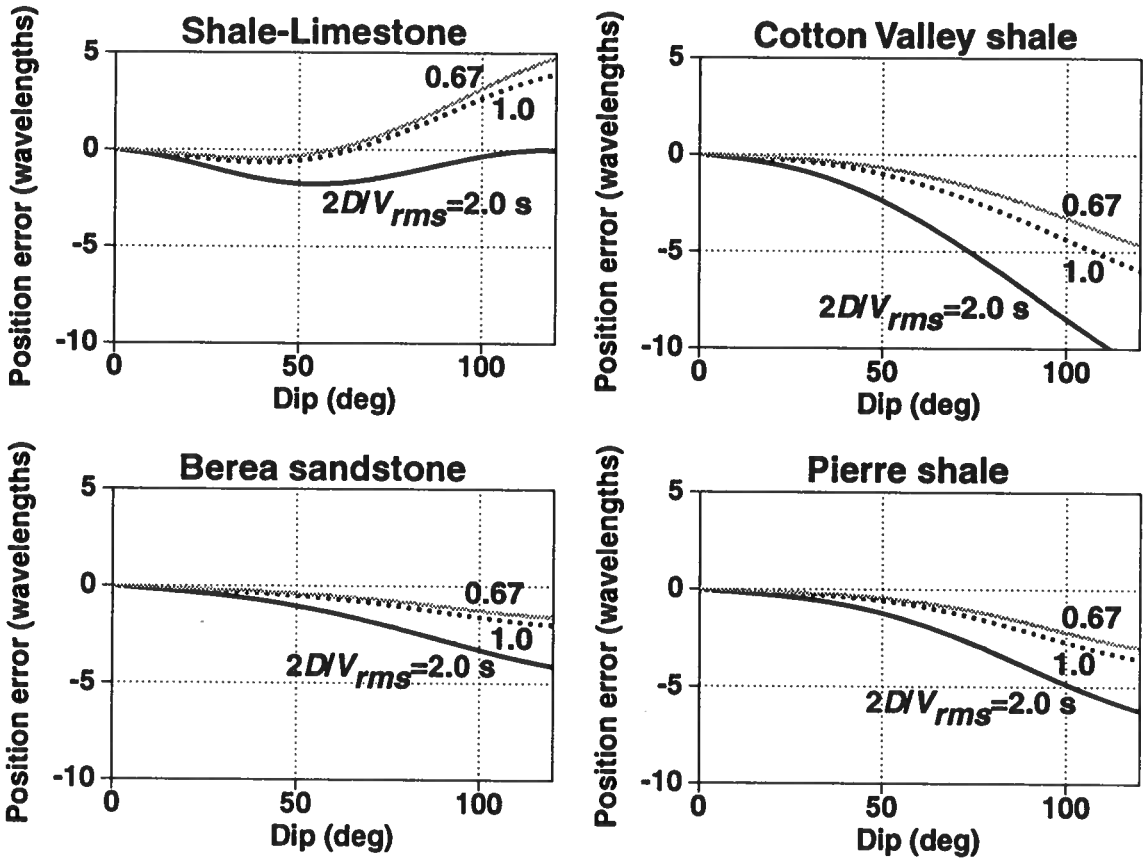

FIG. 14. Normalized position errors as a function of reflector dip for the four media listed in Table 1, for three values of approximate migrated reflection time $2D/V_{rms}$. All models have the same velocity gradient, $k = 0.6\ \mathrm{s}^{-1}$.

over-migrated. Even the "relatively isotropic" Berea sandstone exhibits a growing over-migration of the later reflections. If we were to rank degree of anisotropy on the basis of migration error for reflections at or later than 2 s, migrated time, we would say that the Cotton Valley shale is the most anisotropic, followed by the Pierre shale, Berea sandstone, and then the shale-limestone— a different ordering than what we inferred above, when all the reflectors were at the same depth and the vertical rms velocities were given in Table 1.

DISCUSSION AND CONCLUSION

Failure to take anisotropy into account in migration leads to position errors whose magnitude and sign both depend not only on the various elastic moduli of the subsurface medium, but also on migrated reflection time. These migration errors cannot at all be predicted on the basis of the ratio V_A/V_C of the horizontal to vertical velocity. (Recall that this ratio is nearly identical for the shale-limestone and Cotton Valley shale, which exhibit greatly differing error behavior in Figure 14.) In fact, any attempt to determine which of several media is "most" anisotropic and which is "least" is doomed to frustration. The answer is "it depends on the situation."

If, for example, our problem is one of converting from time to depth based on velocity analysis, then for an elliptically anisotropic medium, the measure of importance would be the ratio V_A/V_C. However, elliptical anistropy is a poor assumption for p-wave behavior, and, as Thomsen (1986) has pointed out, that ratio has no influence whatsoever on the relationship between vertical velocity and the velocity estimated from conventional velocity analysis. Alternatively, if our problem is one of assessing migration error, then our ranking of degree of anisotropy might be based on size of error—and even then, the answer would depend on migrated reflection time.

Of course the correct thing to do is migrate with an algorithm that takes anisotropy into account. Verwest (1989) discussed migration in elliptically anisotropic media, and Uren, Gardner, and McDonald (1990) have shown results on model-tank data migrated with a frequency-wavenumber-domain approach that takes rather general anisotropy into account. However, it is not algorithmic limitations that prevent the use, in practice, of migration approaches that understand how to treat anisotropy. Our information about the anisotropic characteristics of the subsurface is woefully inadequate. We have seen that the most readily accessible measure of anisotropy—the ratio of stacking velocity to vertical velocity—does not provide sufficient information about the pertinent elastic moduli. In fact, the elastic modulus F is not at all obtainable from surface seismic data alone. While we do not have a good means of quantifying anisotropic behavior either routinely or otherwise in practice, those studies that have been done suggest that anisotropy is the rule, and the degree of anisotropy is often considerable.

The limitations go deeper than this, however. Consider, for example, the many assumptions about the medium made in order to do the analysis in this paper. The

models studied are all (1) transversely isotropic, with (2) vertical axis of symmetry, with (3) velocity variation in depth only, with (4) constant gradient, and (5) all ratios among the four pertinent elastic moduli are independent of depth. While this combination of assumptions enabled efficient ray-trace calculation of the diffraction times required in the analysis, We can give little justification of the appropriateness of the models other than: (1) they provide more generality, and perhaps more realism, than do isotropic models and (2) there is even less justification for models of anisotropy that differ substantially from those used here.

Clearly, the studies here show that models of anisotropy are inadequate in describing migration error when inhomogeneity is not also taken into account. Also, while the subsurface is, of course, not a constant-gradient medium, the range of gradients studied here do provide examples of highly inhomogeneous media.

Ratcliff, et al. (1992) and Hale, et al. (1992) have presented examples from the Gulf of Mexico of stunning, apparently quite accurate, migrations of overhanging salt-dome flanks and of thin salt intrusions (100-m wide with more than 1-km vertical relief) into faults surrounding salt domes. How could such features be imaged so well given that the migration algorithms did not take anisotropy into account? While the errors for some of the test cases here become sizeable for dips approaching and exceeding 90 degrees, results here also suggest that if the subsurface in the Gulf of Mexico is not "strongly anisotropic" in some appropriate sense, migration errors due to the combination of anisotropy and inhomogeneity may be no more than two or three wavelengths even for dips beyond 90 degrees. While two or three wavelengths is not insignificant to explorationists, the common practice of trial-and-error selection of migration velocity can readily accommodate errors of that size.

The error analysis in this study was limited to that for post-stack migration. The straightforward extension of the methodology to pre-stack time migration and dip-moveout is the subject of a future paper. One final comment: While numerical estimation of migration error of the sort done here can be no substitute for actual application of migration algorithms on synthetic and field data, such actual migration demonstrations would have been totally impractical and inadequate for attempts to understand the dependence of migration error on the range of model parameters considered here.

ACKNOWLEDGMENTS

We thank Dave Hale for his useful insights at critical stages of this study and Michel Dietrich for his critical review of the paper. Financial support for this work was provided in part by the United States Department of Energy, Grant Number DE-FG02-89ER14079 (this support does not constitute an endorsement by DOE of the views expressed in this paper) and by the members of the Consortium Project on Seismic Inverse Methods for Complex Structures at the Center for Wave Phenomena, Colorado School of Mines.

REFERENCES

Byun, B., 1984, Seismic parameters for transversly isotropic media: Geophysics, **49**, 1908–1914.

Červený V., 1989, Ray tracing in factorized anisotropic inhomogeneous media: Geophys. J. Int., **99**, 91–100.

Dietrich, M. and Cohen, J. K., 1992, 3-D migration to zero offset for a constant velocity gradient: an analytical formulation: CWP report, CWP-113P, 26 p.

Gazdag, J., 1978, Wave equation migration with the phase shift method: Geophysics, **43**, 1342–1351.

Hale, D., Hill, N. R., and Stefani, J. P., 1991, Imaging salt with turning waves: Soc. Explor. Geophys., 61st Ann. Intl. Mtg., Houston, 1171–1174.

Larner, K., 1992, Ray tracing in factorized, transversely isotropic media with linear spatial variation of velocity: Center for Wave Phenomena Report, **CWP-120**, Colorado SWchool of Mines, Golden, CO.

Levin, F. K., 1979, Seismic velocities in transversely isotropic media: Geophysics, **44**, 918–936.

Levin, F. K., 1990, Reflection from a dipping plane—Transversely isotropic solid: Geophysics, **55**, 851–855.

Ratcliff, D. W., Gray, S. H., and Whitmore Jr., N. D., 1992, Seismic imaging of salt structures in the Gulf of Mexico: The Leading Edge, **11**, 15–31.

Schneider, W. A., 1978, Integral formulation for migration in two and three dimensions: Geophysics, **43**, 49–76.

Seriff, A. J., 1986, Velocity anisotropy of seismic waves—illustrations: Geophys. Soc. of Houston Continuing Education Seminar, 1–25.

Shearer, P. M. and Chapman, C. H., 1988, Ray tracing in anisotropic media with linear velocity gradient: Geophys. J. Int., **94**, 575–580.

Thomsen, L., 1986, Weak elastic anisotropy: Geophysics, **51**, 1954–1966.

Uren, N. F., Gardner, G. H. F., and McDonald, J. A., 1990, The migrator's equation for anisotropic media: Geophysics, **55**, 1429–1434.

Verwest, B. J., 1989, Seismic migration in elliptically anisotropic media: Geophys. Prosp., **37**, 149–166.

White, J. E., 1983, Underground sound: Application of sound waves: Elsevier, 253 p.

CWP-119

Dip-Moveout Error in Transversely Isotropic Media with Linear Velocity

Ken Larner and Dave Hale

Center for Wave Phenomena
Colorado School of Mines
Golden, Colorado 80401
(303) 273-3557

Dip-moveout error in transversely isotropic media with linear velocity variation in depth

Ken Larner and Dave Hale

ABSTRACT

Levin (1990) modeled the moveout, within CMP gathers, of reflections from plane-dipping reflectors beneath homogeneous, transversely isotropic media. For some media, when the axis of symmetry for the anisotropy was vertical, he found departures in stacking velocity from predictions based upon the familiar cosine-of-dip correction for isotropic media. Here, we do similar tests, again with transversely isotropic models with vertical axis of symmetry, but now allowing the medium velocity to vary linearly with depth.

Results for the same four anisotropic media studied by Levin show behavior of dip-corrected stacking velocity with reflector dip that, for all velocity gradients considered, differs little from that for the counterpart homogeneous media. As with isotropic media, traveltimes in an inhomogeneous, transversely isotropic medium can be modeled adequately with a homogeneous model with vertical velocity equal to the vertical rms velocity of the inhomogeneous medium.

In practice, dip-moveout (DMO) is based on the assumption that either the medium is homogeneous or its velocity varies with depth, but in both cases isotropy is assumed. For only one of the transversely isotropic media considered here—shale-limestone—would $v(z)$ DMO fail to give an adequate correction within CMP gathers. For the shale-limestone, fortuitously the constant-velocity DMO gives a better moveout correction than does the $v(z)$ DMO.

INTRODUCTION

Given the complexity possible for subsurface structure, moveout of reflections within common-midpoint (CMP) gathers can have all manner of complication. Nevertheless, the approximation that moveout is hyperbolic over typical spreadlengths is

adequate in much routine practice. Moreover, Levin (1979) and (1990) has shown that the hyperbolic approximation remains valid for homogeneous, transversely isotropic media. To whatever degree moveout approximates a hyperbola, however, stacking velocity for anisotropic media can depart significantly from the vertical velocity. Given the recognition today that anisotropy is the rule rather than the exception, it is of interest to study stacking velocity for anisotropic media.

Levin (1979) considered reflections from horizontal interfaces in homogeneous, transversely isotropic media with vertical axis of symmetry. (A transversely isotropic medium is one in which the velocity of plane waves—the so-called *phase velocity*—varies with direction of propagation from an axis of symmetry, but is independent of direction within the plane perpendicular to the axis of symmetry.) Levin showed that the stacking velocity, both for finite-length offset and in the limit of small source-to-receiver offset, could depart substantially from the propagation velocity in the vertical direction.

For each wave type—sh, (quasi)sv, or (quasi)p—the departure is a complicated function of the five elastic moduli that characterize a transversely isotropic medium. For sh-waves, for example, the stacking velocity exactly equals the velocity of propagation in the *horizontal* direction. For p-waves, depending on the ratios among the four pertinent elastic moduli, the stacking velocity may approximate either the vertical or horizontal velocity; it may be somewhere between the two; or it can actually be larger or smaller than both.

In his theoretical analysis of properties of weakly anisotropic media, Thomsen (1986) obtained an expression for small-offset stacking velocity for p-wave reflections from a horizontal interface. There, he showed that both the size and magnitude of the departure of stacking velocity from vertical velocity are governed by a measure of anisotropy that is totally unrelated to the ratio of horizontal to vertical velocity—the most commonly quoted measure of p-wave anisotropy.

In numerical studies of traveltimes of reflections from plane-dipping interfaces beneath homogeneous, transversely isotropic media, Levin (1990) found that moveout remains approximately hyperbolic and that stacking velocity depends on the orientation of the symmetry axis for the anisotropy, as well as on reflector dip. When the symmetry axis is normal to the reflecting plane, he found that the stacking velocity $V_{stack}(\phi)$ for reflector dip ϕ satisfies

$$V_{stack}(\phi) \approx V_{stack}(0)/\cos\phi. \tag{1}$$

Thus, for such symmetry, stacking velocity can be "dip-corrected" with the same $\cos\phi$ correction that is used for reflections from a dipping interface beneath a homogeneous, *isotropic* medium.

For all of the media he studied (see Table 1), Levin found more complicated behavior of stacking velocity with reflector dip when the axis of symmetry is vertical. His shale-limestone medium exhibited the most extreme behavior. For that medium,

$\cos\phi$-corrected stacking velocity exceeded the stacking velocity for horizontal reflectors by almost 40 percent at a dip of 60 degrees.

Medium	$\sqrt{C/\rho}$ m/s	$\sqrt{A/\rho}$ m/s	$\sqrt{F/\rho}$ m/s	$\sqrt{L/\rho}$ m/s	V_A/V_C	$V_{stack(0)}/V_C$
Berea sandstone	4206	4210	1961	2664	1.001	1.02
Shale-limestone	3306	3721	2076	1819	1.126	1.00
Cotton Valley shale	4721	5320	3095	2890	1.127	1.19
Pierre shale	2202	2235	1803	969	1.015	1.06

Table 1. Velocity-type quantities and velocity ratios related to the four elastic moduli—A, C, L, and F, of White (1983)—that are pertinent to p-waves in transversely isotropic media. The four media listed are the same as those studied by Levin (1990). Here, ρ is bulk density, $V_A = \sqrt{A/\rho}$ is p-wave velocity in the horizontal direction, $V_C = \sqrt{C/\rho}$ is that in the vertical direction, $V_L = \sqrt{L/\rho}$ is s-wave velocity in the vertical direction, anf $V_F = \sqrt{F/\rho}$ is a velocity-like quantity that has no ready intepretation.

Levin's numerical results support analytically-based calculations of Byun (1984). Byun's insightful analysis addressed moveout of reflections from plane-dipping reflectors in transversely isotropic media under the assumption of small source-to-receiver offset. While Byun's development allowed for multi-layered media, with homogeneous layers bounded by plane interfaces of arbitrary dip, his numerical examples pertained to just the case of a single homogeneous layer above a dipping reflector—the same model used by Levin.

While one may debate the nature of anisotropy present in the Earth's subsurface, without question the Earth is not homogeneous. In this study, we mimick Levin's 1990 studies of $V_{stack}(\phi)$ in media with vertical axis of symmetry, extending his approach to treat media that are *vertically inhomogeneous* as well as transversely isotropic. To limit the endless possibilities for ways in which an anisotropic medium can be vertically inhomogeneous, we follow Červený (1989) in considering just media for which the ratios among the various elastic moduli are independent of position. Červený calls such media *factorized anisotropic inhomogeneous* (FAI). Yet another restriction placed on the media considered here is that velocity varies only linearly with depth.

Despite having lifted the restriction that media be homogeneous, the limitations on the media that will be studied here are considerable. Justifications for these restrictions are varied. Primarily, as Shearer and Chapman (1988) show, the restriction to FAI media with linear velocity variation with depth affords simplicity and efficiency in the required traveltime computations. Beyond that, given the meager information available about elastic moduli for the subsurface, consideration of only FAI media with vertical variation seems a reasonable way to restrict the endless possibilities for

inhomogeneous behavior. The choice of vertical axis of symmetry is based on Levin's result that anisotropy exerts little influence on stacking velocity when the symmetry axis is perpendicular to the reflector, but considerable influence when the symmetry axis is vertical. Vertical axis of symmetry seems to be an end-case of likely geologic importance. In contrast, the restriction to media with constant velocity gradient has less geologic justification. Constant-gradient media, at least, can model sizeable velocity variation with depth.

As in Levin's studies, iteration is required to do the ray tracing between specified source and receiver positions and to model Snell's law reflection in anisotropic media. Whereas raypaths are straight for homogeneous media, they are curved here. However, for the transversely isotropic FAI media considered here, the two-point ray-tracing, based on a method of Shearer and Chapman, requires no costly numerical integration.

Our interest in stacking-velocity behavior stems from implications for quality of CMP-stacked data and of data that are corrected for dip-moveout (DMO). Routinely, DMO is based on the assumption that the subsurface medium is homogeneous, and, increasingly, DMO is based on velocity v increasing with depth z—so-called $v(z)$ DMO. In neither case, however, is anisotropy taken into account. The primary purpose of this study is to assess, at least for the models considered here, implications of ignoring anisotropy in DMO when the subsurface is transversely isotropic.

SHEARER AND CHAPMAN RESULT

Consider just two-dimensional (2-D) propagation along the reflection raypath connecting specified source and receiver locations on the horizontal surface. As illustrated in Figure 1, the planar reflector is at the base of a single layer in which velocity increases linearly with depth (as suggested by the shading in the figure). In progressing from (1) homogeneous, isotropic models, to (2) homogeneous, transversely isotropic ones, and then to (3) our FAI models, ray tracing and thus traveltime computation becomes progressively more difficult. Traveltimes of reflections from a dipping interface in homogeneous, isotropic media are obtained simply from the law of cosines. Levin (1971) showed that the resulting moveout within CMP gathers is exactly hyperbolic, with stacking velocity given by

$$V_{stack}(\phi) = V_{stack}(0)/\cos\phi. \tag{2}$$

As Levin (1990) shows, for anisotropic (but still homogeneous) media, an iterative search is required to find the raypath from a source at the surface to the reflector and back to a receiver at the surface. First, a straight ray is sent in a trial direction from the source to the reflector. At the reflector, Snell's law is used to give the direction of the reflected ray. For anisotropic media, however, Snell's law does not directly relate the angles of incidence and reflection associated with the raypaths (i.e., the paths along which energy travels). Instead, it relates the angles of incidence and reflection

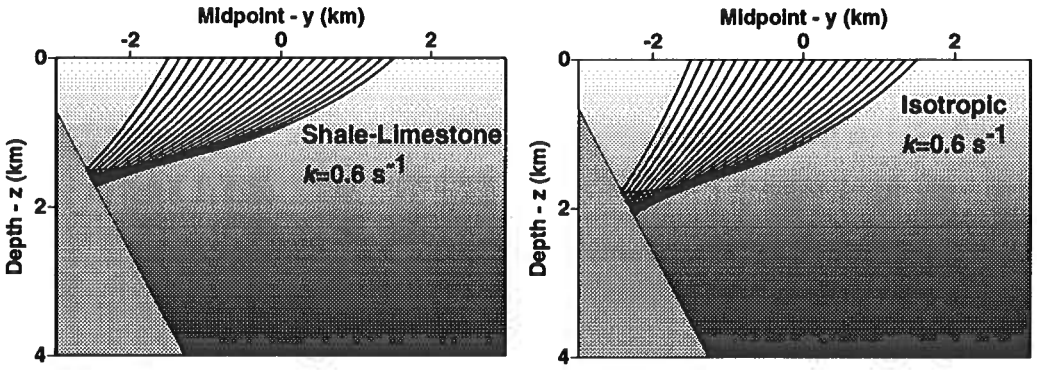

FIG. 1. Raypaths for reflections, in a CMP gather, from a dipping interface beneath a medium with linear $v(z)$. The velocity function in the isotropic medium is identical to the vertical velocity function in the transversely isotropic shale-limestone medium listed in Table 1. Raypaths are circular for the isotropic medium, but not so for the shale-limestone. Note the differences in locations of reflection points.

of *plane* waves—so-called *phase angles*. In general, the direction along which energy travels differs from the travel direction for corresponding plane waves, but the two directions are related to one another (Levin, 1990) and (Byun, 1984). These two authors describe the procedure for calculating the direction of the ray at an interface:

- given the incident ray direction relative to the direction of the symmetry axis, compute the related incident plane-wave direction;
- given that plane-wave direction and the orientation of the reflector, use Snell's law to compute the reflected plane-wave direction; and
- from that computed plane-wave direction, compute the related direction of the reflected ray.

Levin points out that for anisotropic media, Snell's law gives a transcendental equation which is solved iteratively. The transcendental character comes from the fact that Snell's law involves both the direction and the velocity of the reflected plane wave, but that velocity is not known at the outset because it *itself* is a function of the (as yet to be determined) direction of the reflected wave.

For homogeneous media, once the direction has been determined for the reflected ray, the location where the ray intersects the horizontal surface is just the point of intersection of two straight lines. Recalling that this raypath initially left the source point in some trial direction, it is unlikely that the reflected ray that was just computed will intersect the surface at the desired receiver location. Following conventional two-point ray tracing, different take-off directions are then tried until

the correct intersection point is found. The secant-search procedure (Press et al., 1986, p. 248) generally converges within two to four iterations. Since the medium is homogeneous, traveltime along each straight leg of the raypath is just the quotient of the distance along the leg and the ray velocity in the direction of the ray.

When the medium is inhomogeneous as well as anisotropic, the procedure is much the same except that raypaths are now curved, so the ray tracing requires more computation than does just the intersection of two straight lines. When a medium is generally inhomogeneous, this ray tracing requires numerical integration. Therefore, the integration step size and, thus, cost of the ray tracing increase with increase in desired accuracy. We avert the bulk of the costly ray tracing with the assumption that velocity varies linearly in space.

For an *isotropic* medium with linear velocity variation, raypaths are just circles (Slotnick, 1959). Take-off ray directions, raypaths, and traveltimes are related analytically, so two-point ray tracing involves little more effort than that for straight raypaths. While raypaths and ray tracing are not so simple for anisotropic media, in an elegant proof, Shearer and Chapman (1988) have shown that raypaths in FAI media with linear velocity variation can be simply described and, hence, efficiently computed. For our model of transverse isotropy with symmetry axis and velocity gradient in the vertical direction, their result is as follows: raypaths in such media are merely scaled, 90-degree rotated versions of *phase slowness* (i.e., reciprocal of phase velocity) curves. Clearly, this property holds for isotropic media, for which both phase slowness curves and raypaths are circles.

For homogeneous, transversely isotropic media, phase velocity as a function of angle θ from the axis of symmetry is given by (White, 1983)

$$\begin{aligned} 2\rho v^2(\theta) &= (A+L)\sin^2\theta + (C+L)\cos^2\theta \pm \\ &\quad \{[(A-L)\sin^2\theta + (C-L)\cos^2\theta]^2 + \\ &\quad 4(L+F)^2\sin^2\theta\cos^2\theta]^2\}^{\frac{1}{2}}, \end{aligned} \tag{3}$$

where A, C, F, and L are the four pertinent elastic moduli governing p- and sv-wave behavior. In equation (3), the plus sign in front of the radical pertains to p-waves, and the minus sign to sv-waves. We shall be interested in only p-waves here. Dividing both sides of equation (3) by $2\rho v^2(\theta)$ yields the slowness curve governing 2-D wave propagation.

$$\begin{aligned} 1 &= 0.5\{(a+l)p_1^2 + (c+l)p_3^2 + \\ &\quad \{[(a-l)p_1^2 + (c-l)p_3^2]^2 + \\ &\quad 4(l+f)^2p_1^2p_3^2]^2\}^{\frac{1}{2}}\}, \end{aligned} \tag{4}$$

where $a \equiv A/\rho$, etc., are the *density-normalized* elastic moduli, and

$$p_1 = \frac{\sin\theta}{v(\theta)}$$

$$p_3 = \frac{\cos\theta}{v(\theta)} \tag{5}$$

are the components of the phase slowness vector in the x_1 (horizontal) and x_3 (vertical) directions, respectively. p_1 is commonly called the ray parameter.

Now, consider an FAI medium in which all velocity quantities (e.g., $V_C = \sqrt{c}$) are linear functions of depth z. That is,

$$\begin{aligned} V_A(z) &= V_A(0)\,(1+gz) \\ V_C(z) &= V_C(0)\,(1+gz) \\ V_F(z) &= V_F(0)\,(1+gz) \\ V_L(z) &= V_L(0)\,(1+gz), \end{aligned} \tag{6}$$

and, in general,

$$v(z,\theta) = v_0(\theta)\,(1+gz), \tag{7}$$

where $V_C(0)$ is the vertical velocity at the surface, etc.; g is the gradient factor, which is common to all velocity quantities in an FAI medium; $v(z,\theta)$ denotes the phase velocity in the θ direction at depth z; and $v_0(\theta)$ denotes that at the surface.

Following Shearer and Chapman (1988), let $x_{30} \equiv 1/g$, and define a new, shifted vertical coordinate

$$x_3 = z + x_{30}. \tag{8}$$

Then, equation (7) becomes

$$v(x_3,\theta) = v_0(\theta)\,gx_3, \tag{9}$$

and so on for the other velocity quantities.

Shearer and Chapman's remarkable result is that, for an FAI medium in which velocity varies as described here, a scaling and 90-degree rotation of the slowness curve, equation (4), gives the following equation for a raypath characterized by the ray parameter p_1 in x_1, x_3 coordinates

$$\begin{aligned} \frac{2g^2}{p_1^2} &= (a+l)x_3^2 + (c+l)x_1^2 + \\ &\quad \{[(a-l)x_3^2 + (c-l)x_1^2]^2 + \\ &\quad 4(l+f)^2 x_3^2 x_1^2]^2\}^{\frac{1}{2}}\}. \end{aligned} \tag{10}$$

In equation (10), the four elastic moduli are the values at the *surface* $z = 0$.

Given a ray parameter p_1, to trace a ray trajectory we compute x_1 at different depths z (or, equivalently, different vertical coordinates x_3). Squaring equation (10) gives a quadratic equation for x_1^2

$$\alpha x_1^4 + \beta(p_1, x_3^2)x_1^2 + \gamma(p_1, x_3^2) = 0, \tag{11}$$

where the coefficients α, β, and γ all depend on the elastic moduli at the surface. Figure 2 depicts a raypath in the x_1, x_3 coordinates. One of the four roots x_1 for a given x_3 is pointed out in the figure. Another is just at the arrow along the raypath to the right of the x_1 axis. The other two roots give positions along a raypath for sv-waves.

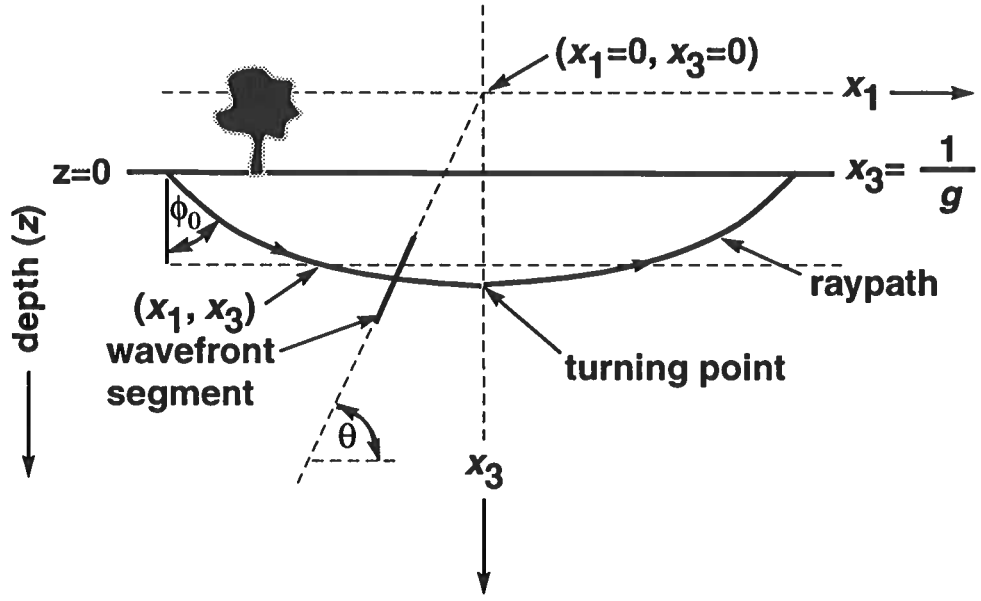

FIG. 2. Raypath in a linear $v(z)$, transversely isotropic FAI half-space, shown in (x_1, x_3) coordinates. The medium's surface, $z = 0$, is equivalent to $x_3 = 1/g$. Also, $x_1 = 0$ at the turning point, i.e., $x_1 = 0$ is a line of symmetry.

For an isotropic medium with the same linear $v(z)$ behavior, the moduli satisfy $a = c = f + 2l$, and equation (11) reduces to the familiar equation of a circle (Slotnick, 1986)

$$x_1^2 + x_3^2 = \left(\frac{1}{g \sin\theta_0}\right)^2 = \left(\frac{1}{gV_0 p_1}\right)^2, \tag{12}$$

where V_0 is now independent of θ.

From equation (10), full description of the transversely isotropic FAI medium requires just $V_C(z)$ and the three ratios a/c, f/c, and l/c. For the studies below, we write the linear $V_C(z)$ behavior slightly differently than in equation (6), as follows:

$$V_C(z) = V_0 + kz, \tag{13}$$

where, clearly $k = gV_0$, and, for shorthand, V_0 is the vertical velocity at the surface $z = 0$.

TRAVELTIME COMPUTATION

While it is of interest to see the curved raypaths that result from the ray-tracing (e.g., those in Figure 1), our true interest is in computation of traveltimes between

specified point on the raypaths. Here, we follow Červený (1989), who gives a comprehensive discussion of general FAI media along with a particularly lucid summary of the Shearer and Chapman result. Červený shows that the vertical component of slowness p_3 behaves as follows

$$p_3(u) = p_3(u_0) - g(u - u_0), \tag{14}$$

where u is a variable along the ray related to traveltime, and u_0 is the value of that variable at the starting point of the raypath. He also shows that the traveltime along the raypath requires the numerical integration

$$\tau_3(u) = \tau_3(u_0) + \int_{u_0}^{u} g x_3(u) du. \tag{15}$$

The 90-degree rotation of the slowness curve to obtain the raypath was based on the observation that in the x_1, x_3 coordinate system, the components of slowness along a raypath must satisfy

$$p_1 x_1 + p_3 x_3 = 0. \tag{16}$$

That is, the position vector $\mathbf{x}$ and the slowness vector $\mathbf{p}$ are orthogonal everywhere along a raypath. This is obviously the case for the circular raypaths in an isotropic medium. For an anisotropic medium, however, recall that the ray and phase directions differ, so that raypaths are not generally normal to wavefronts (see Figure 2), whereas phase directions are.

Eliminating p_3 from equations (14) and (16) and setting the arbitrary value u_0 to zero gives

$$x_1 = \frac{x_3}{p_1}\left(\frac{u}{g} - p_{30}\right). \tag{17}$$

Substituting this expression for x_1 in equation (11) gives another quadratic equation, this one giving $x_3^2(u)$, which provides the integrand for equation (15).

Thus, although numerical integration is required to compute traveltime, that integration is straightforward. We use the efficient scheme of Press et al. (1986, p. 110) for integration by the extended trapezoidal rule.

TWO-POINT RAY TRACING FOR REFLECTION RAYPATHS

In ray-trace modeling, we generally wish to compute the path and traveltime between specified source and receiver positions in some x, z coordinate system. Therefore, to use the method described above, it is necessary to relate the x_1, x_3 and x, z coordinates to one another. Equation (8) gives the simple translation required for the vertical coordinates. We can express the required translation for the lateral coordinate transformation as $x_1 = x - x_c$, where x_c is the x coordinate of the origin in x_1. To get at x_c, consider a ray from some point x_s, z_s to its intersection with depth z_r. The raypath is characterized by a fixed ray parameter p_1, and that fixed value also

fixes the location of x_c. With p_1 given, we solve equation (11) twice, once with depth $x_3 = x_{3s}$ and again with $x_3 = x_{3r}$. The x coordinate x_r of the raypath at depth z_r is then given by

$$x_s + (x_{1r} - x_{1s}) = x_s + (x_r - x_c) - (x_s - x_c) = x_r. \tag{18}$$

We can now address two-point ray tracing along a reflection path, such as in Figure 1, between a specified source and receiver location. For all but the simplest models, in two-point ray tracing one does not know at the outset the value of ray parameter that describes the path connecting the two points. Therefore, starting with an educated guess for the value of the ray parameter, some systematic search procedure is required to arrive at the correct value. Such is also the case here.

In principle, we would first solve the appropriate equations that give the intersection of a downward ray from the source (specified by a trial ray parameter, or equivalently, trial starting direction) with the dipping reflector. For the linear $v(z)$, transversely isotropic FAI medium considered here, computation of that intersection point would require determination of the correct root of a quartic equation for x_3. Rather than working with quartic equations, we follow the two-phase search procedure illustrated in Figure 3.

Instead of solving directly for the location of a trial reflection point R_t along the dipping reflector (Figure 3a), we first specify a trial depth z_t for the reflection-point position and a trial ray parameter. The point x_t at which the trial raypath arrives at depth z_t is the solution of quadratic equation (11). We next do a secant search to find the ray parameter that yields $x_t \approx R_t$, the point along the reflector at the trial depth z_t.

At the trial reflection point (Figure 3b), we exercise Snell's law to get the starting direction for the upward portion of the raypath. For anisotropic media, Snell's law involves a relationship between the phase angles and phase velocities, which themselves are functions of the phase angles. The incident phase angle at the interface is readily obtained from equation (16) (see, also, Figure 2).

$$\frac{p_1}{p_3} = -\frac{x_3}{x_1} = \tan\theta, \tag{19}$$

where, again, θ is phase angle with respect to vertical. Given this angle and the reflector dip ϕ, we follow the iterative solution of the transcendental Snell's law equation described by Levin (1990) to find the reflection ray angle. Once that angle is determined, we then use equation (19) to get the ray parameter for the upward path.

Again, we solve quadratic equation (11), this time to get the location e of the intersection of the upward path with the surface $z = 0$. Since this point, in general will miss the desired receiver location, we do a second stage of secant search by varying the trial depth z_t of the reflection point (Figure 3c), and thus we continue to vary z_t and p_1 until $e \approx g$.

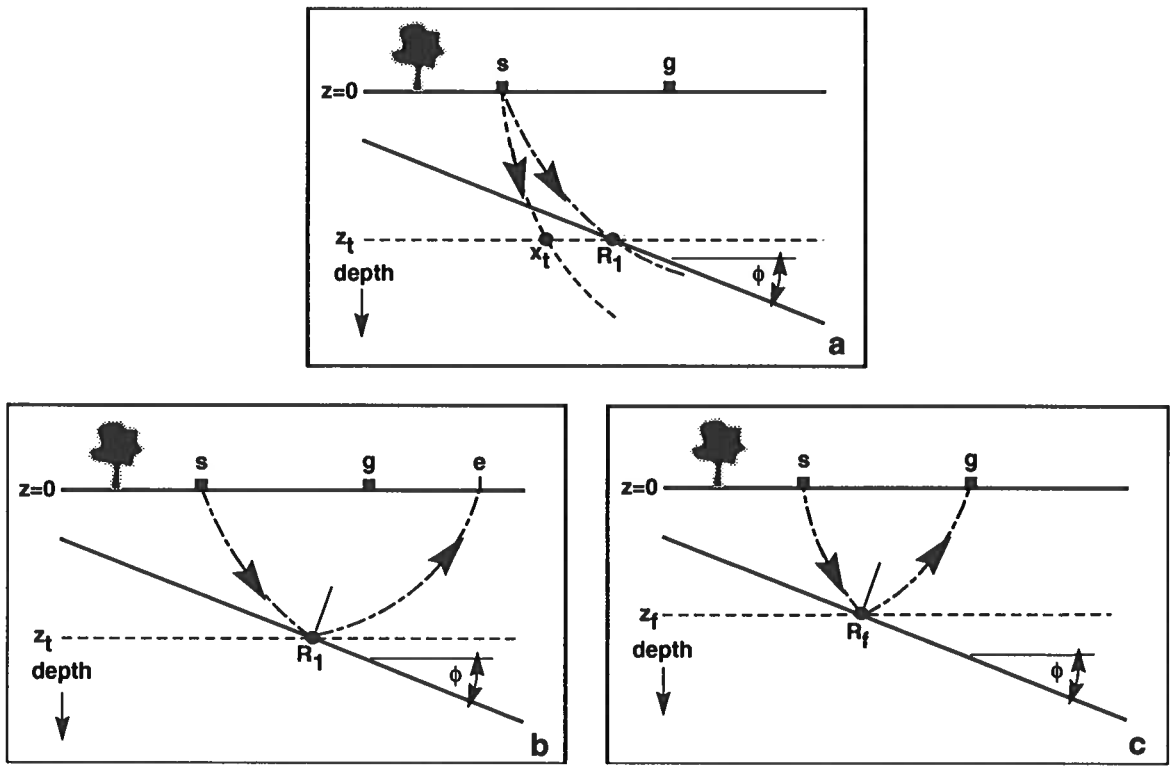

FIG. 3. Steps in the two-point ray tracing to obtain the raypath from a source to a dipping reflector and back up to a receiver. (a) Solve a quadratic equation for the lateral coordinate x_t at which the downward ray with trial ray parameter p_t intersects trial depth z_t. Then do a secant search to find the ray parameter for the raypath to the trial reflection point R_t at depth z_t along the reflector. (b) Apply Snell's law (for transverse isotropy) to find the ray parameter for the reflected portion of the raypath. This path intersects the surface at e, which differs from the desired receiver location g. (c) Do another secant search to find the depth of the reflection point and the ray parameter for the downward portion of the reflection raypath to the receiver.

MOVEOUT BEHAVIOR

In his studies with the four homogeneous media listed in Table 1, Levin (1990) found that for spreadlength X_{max} comparable to the distance from the CMP to the dipping interface, moveout was approximately hyperbolic for even the most anisotropic of the four media—the shale-limestone. While we expect the hyperbolic approximation to hold for small angles even when the medium is both anisotropic and inhomogeneous, it is of interest to know if that approximation can also hold for routinely used spreadlengths (i.e., spreadlength comparable to distance from CMP to reflection point).

Figure 4 is a plot of T^2 versus X^2, where $T(X)$ is reflection time at offset X, for the shale-limestone with different choices of velocity gradient k [equation (13)]. For all cases, the root-mean-square (rms) vertical velocity down to $z = 3000$ m is 3306 m/s, the value for V_C used by Levin, and the spreadlength equals 3000 m, the

distance from the CMP to the reflector. While velocities in the Earth's subsurface are not linear, this range of values for k spans the spectrum from homogeneous to highly variable with depth. We consider $k = 1.2\ \mathrm{s}^{-1}$ to be quite large, and $k = 0.6\ \mathrm{s}^{-1}$ to be fairly representative.

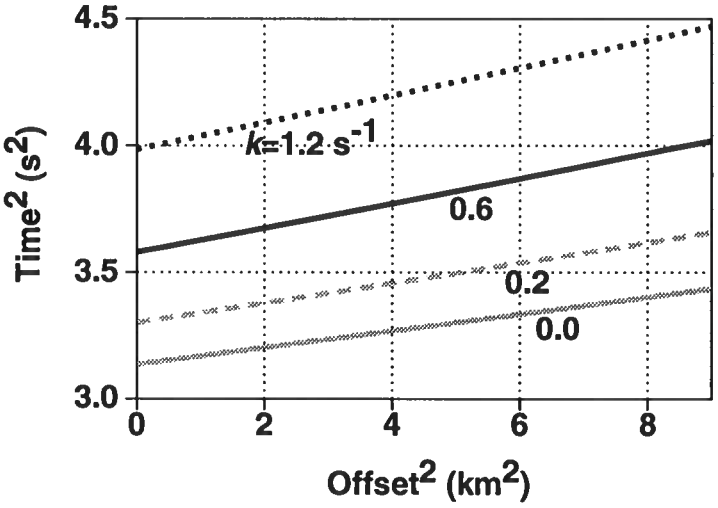

FIG. 4. $T^2 - X^2$ curves for reflections from a dipping reflector (dip = 40 degrees) beneath various media with the transversely isotropic properties of the shale-limestone. The four media, all of which have the same rms velocity between the surface and depth = 3000 m, differ only in the velocity gradient k.

All curves in Figure 4 are approximately linear, indicating that the hyperbolic assumption continues to be valid for our linear $v(z)$, transversely isotropic models. We shall consider this assumption more closely below.

The initial purpose of this study was to extend Levin's numerical studies of stacking velocity to media that are inhomogeneous, as well as transversely isotropic. Figure 5 is an independent reproduction of the dip-corrected stacking velocities in Figure 3 of Levin (1990). Stacking velocity was computed from a least-squares linear fit to the $T^2 - X^2$ moveout data over a spreadlength of 3000 m; then the velocities were "dip-corrected" by multiplication with $\cos\phi$ in accordance with equation (2). For a homogeneous, isotropic medium, this dip correction should bring stacking velocity for all dips to the value for zero dip. This is just what DMO would accomplish when applied to data from such a model. Byun (1984) did this same correction, calling the corrected stacking velocity *diffractor velocity.*

From the variation of the dip-corrected curves with dip in Figure 5, we would infer that the shale-limestone is the "most anisotropic" of the four media tested, with the Cotton Valley shale a distant second, followed by the Pierre shale and Berea sandstone. Also, as observed by Levin, the variations exhibit no simple or predictable

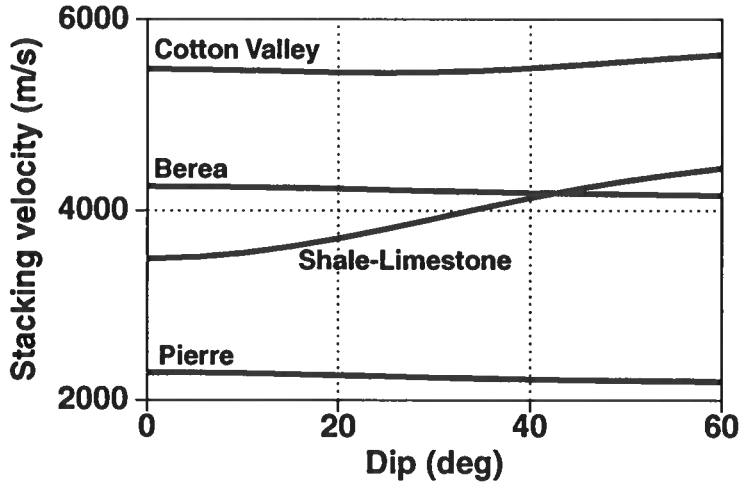

FIG. 5. Cosine-of-dip corrected stacking velocity as a function of reflector dip for the four homogeneous, transversely isotropic media in Table 1. These results duplicate those of Levin (1990). The distance from the CMP to the reflector is 3000 m in all cases.

behavior with dip. The difference in behavior of the curves for the shale-limestone and the Cotton Valley shale is particularly noteworthy since the ratios of horizontal to vertical velocity of these two media are almost identical (see Table 1). This failure of the ratio V_A/V_C as a predictor of much anisotropic behavior was explained by Thomsen (1986), who showed that the ratio of normal-moveout velocity to rms velocity had no relationship whatsoever to V_A/V_C. The values computed for V_{stack}/V_C tabulated in Table 1 quantitatively match Thomsen's predictions.

Now, consider inhomogeneous media of the type treated in this paper. Figure 6 shows dip-corrected stacking velocity as a function of reflector dip for several variants of the same four media treated by Levin. Superimposed in this figure are curves for media with velocity gradients $k = 0$ (Levin's homogeneous media), and $k = 0.2, 0.6$, and $1.2\ s^{-1}$. The results show a remarkable insensitivity to the degree of inhomogeneity. The only noticeable tendency is for an increase in velocity gradient to *reduce* the dip-dependence of the dip-corrected velocities for the shale-limestone. Thus, the inhomogeneity has a benign influence on the curves, mitigating somewhat the stacking-velocity variations introduced by the anisotropy. This general tendency of $v(z)$ to reduce the influence of anisotropy was observed in a concurrent study of migration-velocity error as a function of reflector dip (Larner and Cohen, 1992).

Two points of clarification about the curves in Figure 6 are necessary. First, let us be more specific about our meaning in stating that curves with different values of velocity gradient k pertain to "variants" of one of Levin's media. We mean two things:

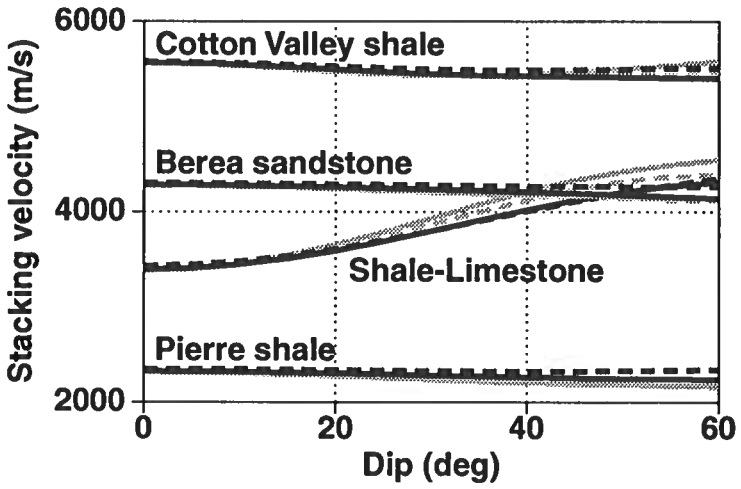

FIG. 6. Dip-corrected stacking velocity as a function of reflector dip for inhomogeneous variants of the same four transversely isotropic media shown in Figure 5. The velocity gradients for the solid gray, dashed gray, solid black, and dashed black curves are, respectively, $k = 0.0, 0.2, 0.6$, and $1.2\ \mathrm{s}^{-1}$.

for a given medium, say shale-limestone, independent of k the ratios among all the elastic moduli at a given depth are the same as those obtained from the moduli for shale-limestone listed in Table 1. Second, the vertical velocity at the surface differs for media with different gradients in such a way that the rms velocity down to the reflector depth is the same for all variants and is equal to the value of V_C listed in Table 1. Any other choice would have resulted in a large separation of the curves for the different gradients in Figure 6.

The similarity of the curves in that figure thus supports a working hypothesis that has been of much value in analysis and processing of isotropic data: the traveltime behavior for $v(z)$ media can be largely predicted through modeling with a homogeneous model having velocities comparable to the rms velocities in the inhomogeneous medium. Examples of this are the so-called *straight-ray assumption* and the adequacy of applying Kirchhoff migration with use of rms velocities to image data where reflectors are not too steep. Thus, we can use simple homogeneous models, such as those in Levin's studies, for study of some anisotropic phenomena where the true medium velocity actually varies with depth.

The second point of clarification relates to the nature of the dip correction. For homogeneous media, the dip correction to apply to stacking velocity is just the cosine of the reflector dip. For $v(z)$ media, however, the dip correction is more complicated and differs substantially from $\cos\phi$, but still ignores anisotropy, just as does the $\cos\phi$ correction for homogeneous media. Therefore, we seek an analytic expression for the

small-offset or normal-moveout (NMO) velocity V_{nmo} associated with reflections from a dipping interface beneath a linear $v(z)$ medium.

Shah (1973) and Hubral and Krey (1980) have shown the direct relationship that in general exists between NMO velocity abd wavefront curvature near where the normal-incident ray intersects the surface. For small offset, NMO velocity is given approximately by

$$V_{nmo}^2 = \frac{1}{T_0}\frac{dX}{dp}, \tag{20}$$

where T_0 is the normal-incidence reflection time, X is source-to-receiver offset, and p is the ray parameter, which we have previously called p_1. For $v(z)$ media, $X(p)$ is given by

$$X(p) = \int_0^{z_r} \frac{pv(\sigma)}{\sqrt{1-p^2v^2(\sigma)}}d\sigma, \tag{21}$$

where z_r is the depth at the normal-incidence reflection point. Differentiating gives

$$\frac{dX}{dp} = \int_0^{z_r} \frac{v(\sigma)}{[1-p^2v^2(\sigma)]^{3/2}}d\sigma. \tag{22}$$

Also, T_0 satisfies

$$T_0(p) = \int_0^{z_r} \frac{d\sigma}{v(\sigma)\sqrt{1-p^2v^2(\sigma)}}. \tag{23}$$

Evaluation of these integrals for $v(z) = v_0 + kz$ gives

$$V_{nmo}^2(\phi) = \frac{v_0^2(\cos\theta_0 - \cos\phi)}{\sin^2\theta_0 \cos\theta_0 \cos\phi \log\left[\dfrac{v(z_r)}{v_0}\dfrac{1+\cos\theta_0}{1+\cos\phi}\right]}. \tag{24}$$

Here, we have used the fact that for the zero-offset path, $\theta(z) = \phi$. For reflections from a horizontal reflector (i.e., the normal-incidence path is vertical), similar evaluation of the appropriate integrals gives

$$V_{nmo}^2(0) = \frac{v^2(z_r) - v_0^2}{2\log\left[\dfrac{v(z_r)}{v_0}\right]}. \tag{25}$$

The dip-correction factor $h(\phi)$ applied to the stacking velocities in Figure 6 and in subsequent figures is then

$$h(\phi) = \frac{V_{nmo}(0)}{V_{nmo}(\phi)}. \tag{26}$$

IMPLICATIONS FOR DIP-MOVEOUT

Figure 7 suggests the importance of applying the dip correction $h(\phi)$ and the large difference between it and $\cos\phi$. In Figure 7a are shown three curves of stacking

velocity versus dip for the shale-limestone with the "representative" velocity gradient, $k = 0.6$ s^{-1}. The gray curve has had no correction for dip; it is directly the velocity that gives the best fit to moveout over a spreadlength. The black curve has the $h(\phi)$ correction, and the dotted curve has a correction that is close to, but not quite, $\cos\phi$. The correction used in the dotted curve (same as the black curve for shale-limestone in Figure 6) is $\cos\hat{\phi}$, where $\hat{\phi}$ is the *apparent dip* as perceived by a constant-velocity DMO process. It is given by

$$\sin\hat{\phi} = pV_{stack}(0). \tag{27}$$

That is, the apparent dip is the value that one would compute under the simplistic assumption that the subsuface is homogeneous with velocity equal to the observed stacking velocity for horizontal reflectors. Constant-velocity DMO makes this same simplistic assumption.

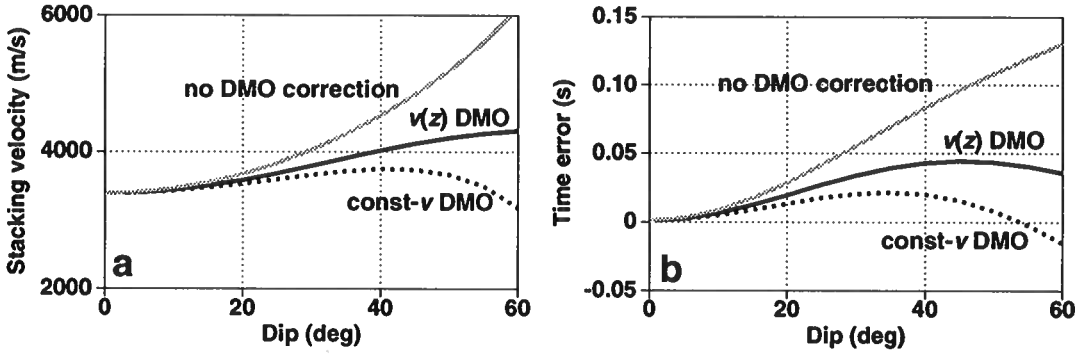

FIG. 7. (a) Stacking velocity as a function of reflector dip for the shale-limestone medium with velocity gradient $k = 0.6$ s^{-1}—uncorrected for dip (gray), after DMO correction with a $v(z)$ DMO process (black), and after DMO correction with a constant-velocity DMO process (dotted). (b) Residual moveout Δt at offset $X = 3000$ m as a function of reflector dip for the same shale-limestone data uncorrected (gray), DMO corrected with $v(z)$ DMO (black), and DMO corrected with constant-velocity DMO (dotted).

Clearly, from Figure 7a, either of the dip corrections brings the corrected stacking velocity closer to the desired zero-dip velocity than does no correction. It appears, in fact, that for the shale-limestone, the most anisotropic of the four media studied, the constant-velocity DMO actually would perform better than a $v(z)$ DMO (recall that both ignore anisotropy; as a result neither properly corrects the stacking velocities).

Beyond the qualitative observations on relative behavior of the velocity curves, we should be concerned with just how important are these differences in stacking velocity. Errors in stacking velocity leave primary reflections misaligned across individual CMP gathers and hence cause those primaries—particularly the higher-frequency components— to be attenuated when the data are stacked. Therefore, ultimately it is this misalignment that should be of most concern.

Let us postulate that, as is routinely done in practice, data receive an NMO correction, with or without DMO, that is based on the observed stacking velocity for horizontal reflections. Then, since the moveout of reflections from dipping reflectors differs from this NMO, reflections will be misaligned prior to CMP stacking. With the stacking velocities measured in our study, we can quantify the resulting timing misalignment. Our measure of misalignment, which we shall *time error* or *residual moveout*, is the difference in time that would arise on the far-offset trace. In these tests, the largest offset is 3000 m, comparable to the distance to the reflector from the CMP.

Plotted in Figure 7b are the time errors that arise when the data are simply NMO corrected (no dip correction) and when they are DMO corrected with either a constant-velocity DMO or a $v(z)$ DMO. Timing errors are reduced substantially when either of the (isotropic) DMO algorithms is used, but neither of the DMO approaches reduces the error as much as would be desired. Also, note that although the medium is inhomogeneous, the constant-velocity DMO correction yields the better result of the two. As we shall see, this is a fortuitous result peculiar to the shale-limestone medium.

The dependence of these moveout errors on velocity gradient for the shale-limestone is exhibited in Figure 8. The curves for $k = 0.6$ s^{-1} are identical to those in Figure 7b. In addition, Figure 8 shows curves for a larger gradient, $k = 1.2$ s^{-1}, and for a homogeneous medium. For the homogeneous medium, $k = 0$, constant-velocity DMO and $v(z)$ are identical; both involve just the $\cos\phi$ correction. Note that the larger the velocity gradient, the less serious is the residual moveout when the data are just NMO-corrected. Also, while the errors that arise when constant-velocity DMO is applied vary considerably with velocity gradient, those that arise when $v(z)$ DMO correction is done are less sensitive to the gradient.

The curves in the bottom right portion of the figure pertain to an *isotropic* medium with velocity gradient of $k = 0.6$ s^{-1}. Since ignoring isotropy in DMO is no issue for these data, the residual moveout goes to nearly zero when the correct $v(z)$ DMO is applied. If, instead, constant-velocity DMO is applied, the data become over-corrected for the errors that arise when NMO alone is performed. All of the linear $v(z)$ models studied exhibit this known tendency for the constant-velocity DMO to over-correct data from isotropic models. Also, in all cases the error after over-correction is smaller than the error when no DMO is applied.

Similar curves of residual moveout error for the four media—shale-limestone, Cotton Valley shale, Berea sandstone, and Pierre shale—are compared in Figure 9. Here, we see that, in terms of expected DMO performance, the shale-limestone on which we have focused most of our attention is the most anomalous, indeed the most anisotropic, of the four media. $v(z)$ DMO corrects the timing misalignment for the other three media almost as well as if they were isotropic.

Based on residual moveout after $v(z)$ DMO in Figure 9, the anisotropy of the Pierre shale appears to be a distant second to that of the shale-limestone, with the Cotton

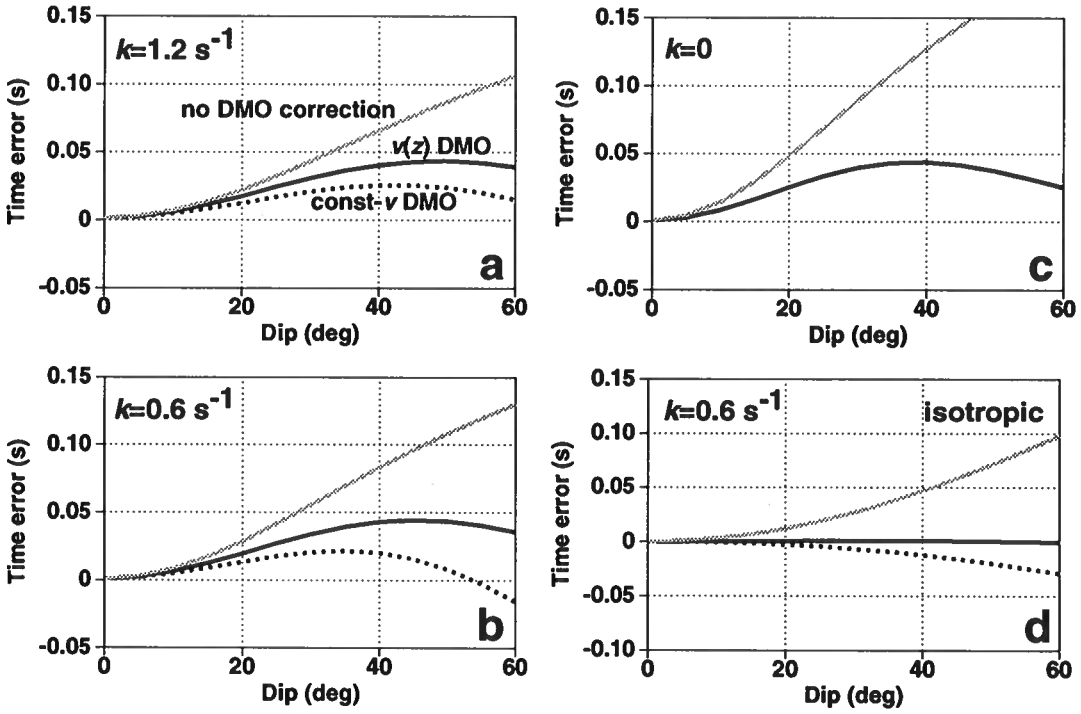

FIG. 8. Residual moveout Δt at offset $X = 3000$ m as a function of reflector dip for variants of the shale-limestone—data uncorrected for dip (gray), DMO corrected with $v(z)$ DMO (black), and DMO corrected with constant-velocity DMO (dotted). In (a), (b), and (c), the medium is transversely isotropic with velocity gradient $k = 1.2, 0.6,$ and 0.0 s^{-1}, respectively. In (d) the gradient is again $k = 0.6$ s^{-1}, but here the medium is isotropic. Note that data from the isotropic medium are well corrected with a $v(z)$ DMO correction. Also, in (c), since the medium is homogeneous, the $v(z)$ DMO is identical to constant-velcoity DMO.

Valley shale and Berea appearing to be only weakly anisotropic. This ranking of the relative "degree of anisotropy" among the four media differs somewhat from that estimated on the basis of the curves in Figures 5 and 6, where the Cotton Valley shale showed larger variation in stacking velocity with dip than did the Pierre shale. The variability of the stacking velocities, however, is misleading. Since the Cotton Valley shale is a much higher-velocity medium than is the Pierre shale, a given moveout error would give rise to a larger variation in velocity for the Cotton Valley than for the Pierre. For this reason, the behavior of residual timing errors likely is the more appropriate measure of the relative importance of anisotropy in DMO correction.

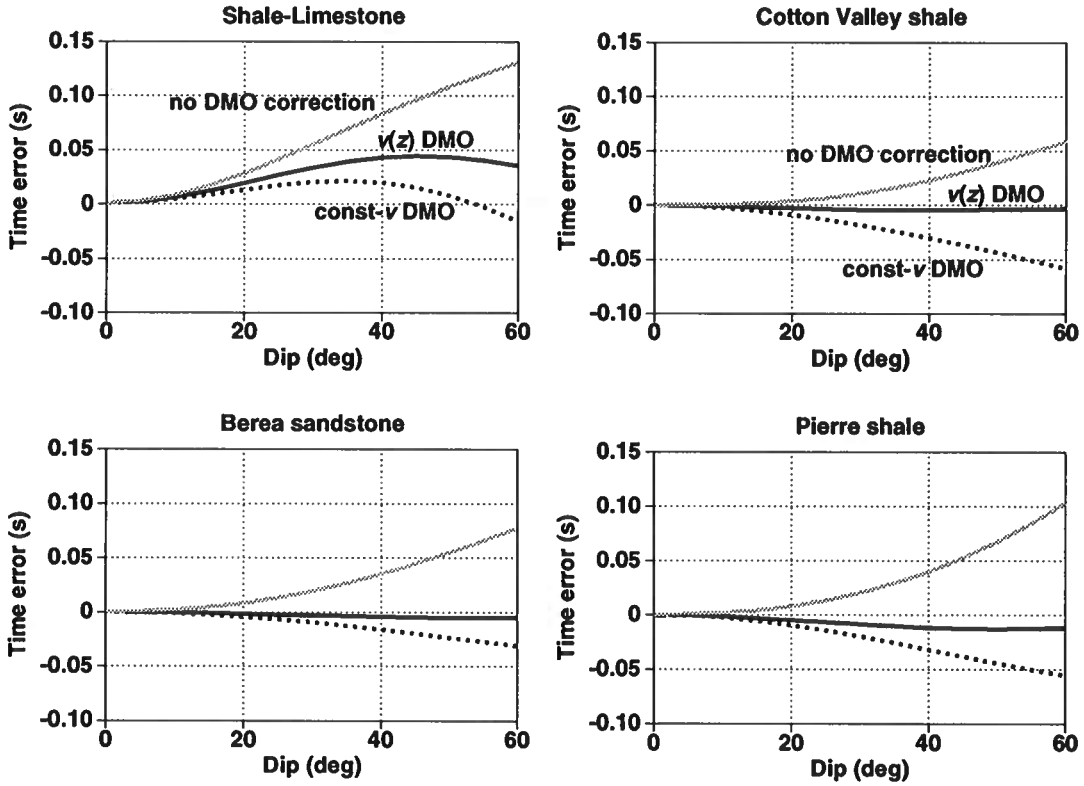

FIG. 9. Residual moveout Δt at offset $X = 3000$ m as a function of reflector dip for four media—data uncorrected for dip (gray), DMO corrected with $v(z)$ DMO (black), and DMO corrected with constant-velocity DMO (dotted). The vertical velocity gradiant is $k = 0.6$ s $^{-1}$ in all cases. Note that $v(z)$ DMO with anisotropy ignored is adequate for both the weakly anisotropic Berea sandstone and the considerably anisotropic Cotton Valley shale.

NORMAL-MOVEOUT VELOCITY VERSUS STACKING VELOCITY

As seen in Figure 4, data from our transversely isotropic, FAI linear $v(z)$ models all have moveout that is well approximated by hyperbolas for spreadlengths typically used in practice. This suggests that an efficient alternative to hyperbolic fitting of traveltimes to obtain the stacking velocity V_{stack} would be evaluation of an analytic expression for the small-offset moveout velocity, which we earlier called V_{nmo} [see equation (24)]. The relative simplicity of the ray-tracing equations for linear $v(z)$, isotropic media allowed us to derive the analytic expression in that equation.

For our transversely isotropic FAI media, also with linear $v(z)$, it happens that we can obtain such an analytic expression for V_{nmo} once we have done the ray tracing for the zero-offset raypath. Whether or not a medium is isotropic, V_{nmo} can always be written as in equation (20). The ray tracing for the zero-offset raypath provides the measured normal-incidence traveltime T_0, so we require an expression for the

derivative dX/dp. Equation (11) gives an expression in x_1 as a function of p, which we called p_1 there. Differentiating that equation with respect to p gives

$$\frac{dx_1}{dp} = -\frac{x_1^2 \frac{d\beta}{dp} + \frac{d\gamma}{dp}}{2x_1(2\alpha x_1^2 + \beta)}. \tag{28}$$

All the quantities on the right-hand side in equation (28) are known from the ray tracing along the normal-incidence ray. The desired derivative dX/dp is given by

$$\frac{dX}{dp} = \frac{dx_{10}}{dp} - \frac{dx_{1r}}{dp}, \tag{29}$$

where x_{10} is the value of x_1 at the surface of the medium, and x_{1r} is the value of x_1 at the reflector. Equation (29) gives the change in the lateral coordinate x_{10} at the surface relative to the fixed reflector point at normal-incidence reflection. Of course, when sources and receivers change within a CMP gather, the reflection point moves as well. Holding the reflection point fixed in this computation is justified on the basis of Fermat's principle, which implies that the traveltime will differ little with small difference in reflection point.

Figure 10 compares V_{stack}, based on the hyperbolic fit over a spreadlength, with V_{nmo}, computed from equations (29), (28), and (20). The curves show stacking velocity, uncorrected for dip, for the four media with gradient $k = 1.2\ \mathrm{s}^{-1}$. The match is excellent for the three media other than the shale-limestone. While the match is good for the shale-limestone, perceptible differences between the two types of velocity suggest that the hyperbolic assumption is violated to some extent for some dips. These differences are an indication that the $T^2 - X^2$ curves are not as quite as straight for the shale-limestone medium as are those for the other media.

CONCLUSION

The behavior of dip-corrected stacking velocity with reflector dip computed by Levin holds with remarkably little change when vertical inhomogeneity is incorporated into the model of transverse isotropy, as long as the dip-correction is appropriate to $v(z)$ media. Without the dip correction, the larger the velocity gradient the smaller is the residual moveout that exists in NMO-corrected data. For the media considered here, stacking-velocity dependence on reflector dip can be adequately investigated with homogeneous models having velocities that equal counterpart rms velocities of the inhomogeneous media.

Only one of the four media studied—the shale-limestone— exhibits dramatic influence of anisotropy on stacking-velocity behavior. This, despite the fact that, in other respects, two of the other media—Cotton Valley shale and Pierre shale—are considered to be equally or more anisotropic than the shale-limestone. For example, the ratio of horizontal to vertical velocity in the Cotton Valley shale is almost identical to that of the shale-limestone. Moreover, the NMO velocity of the Cotton Valley

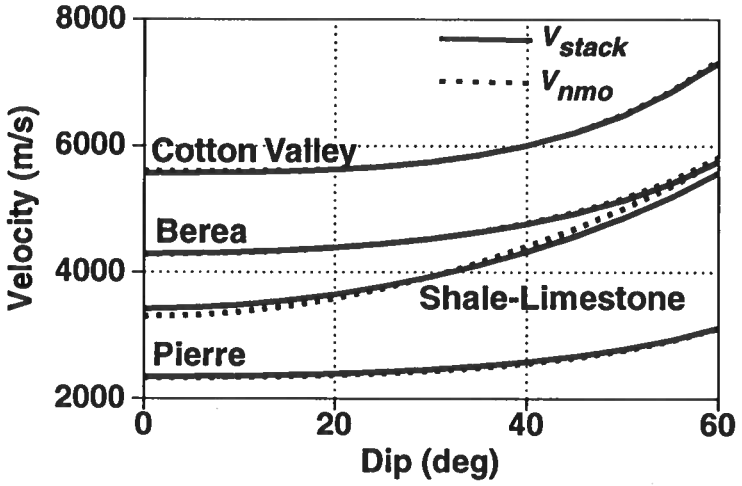

FIG. 10. Comparison of stacking velocity (solid) and normal-moveout velocity (dashed)—both uncorrected for dip—as a function of reflector dip, for the four media under study. Stacking velocity was computed by least-squares fitting of a straight line to $T^2 - X^2$ over an offset distance of $X = 3000$ m, while the normal-moveout velocity is based on small-offset wavefront curvature. The largest departures are for the shale-limestone, indicating that the hyperbolic approximation for moveout for that medium is not valid for such as large offset X. Here, $k = 1.2$ s $^{-1}$.

shale exceeds the vertical rms velocity by 20 percent, whereas the two quantities are almost identical in the shale-limestone. Pending similar study of other models, we conclude from the computations here that transverse isotropy will seldom be an issue of practical importance in DMO processing.

As with other seismic phenomena, stacking velocity behavior in transversely isotropic media differs from that expected for isotropic media in ways that are not readily predictable from one medium to another. Those variations depend on the ratios of the four pertinent elastic moduli—quantities that are neither often nor well determined in rock units, on either a small or large scale. With the derived expression for NMO velocity as a function of reflector dip in a linear $v(z)$, transversely isotropic FAI medium, one could do a proper dip correction of stacking velocity, if the elastic moduli and its depth dependence were known. Perhaps, this expression for the dip correction will also give clues as to how DMO could be modified to accommodate both $v(z)$ and anisotropy. In practice, however, our information on the elastic moduli and their variation within the subsurface is meager. Moreover, it is unlikely that the subsurface would rather consistently have the properties of, say, the shale-limestone from surface to dipping reflector. These considerations provide little motivation to develop a DMO process for transversely isotropic media.

ACKNOWLEDGMENTS

Financial support for this work was provided in part by the United States Department of Energy, Grant Number DE-FG02-89ER14079 (this support does not constitute an endorsement by DOE of the views expressed in this paper), and by the members of the Consortium Project on Seismic Inverse Methods for Complex Structures at the Center for Wave Phenomena, Colorado School of Mines.

REFERENCES

Byun, B., 1984, Seismic parameters for transversely isotropic media: Geophysics, **49**, 1908–1914.

Červený V., 1989, Ray tracing in factorized anisotropic inhomogeneous media: Geophys. J. Int., **99**, 91–100.

Hubral, P. and Krey, T., 1980, Interval velocities from seismic reflection time measurements: Soc. of Explor. Geophys., Tulsa, OK, 203 p.

Larner, K. and Cohen, 1992, Migration error in transversely isotropic media with linear velocity variation in depth: 62nd Ann. Intl. Mtg. of the Soc. of Explor. Geophys., New Orleans.

Levin, F. K., 1971, Apparent velocity from dipping interface reflections: Geophysics, **36**, 510–516.

Levin, F. K., 1979, Seismic velocities in transversely isotropic media: Geophysics, **44**, 918–936.

Levin, F. K., 1990, Reflection from a dipping plane—Transversely isotropic solid: Geophysics, **55**, 851–855.

Press, W. H., Flannery, B. P., Teukolsky, S. A., and Vetterling, W. T., 1986, Numerical recipes: Cambridge Univ. Press.

Shah, P. M., 1973, Use of wavefront curvature to relate seismic data with subsurface parameters: Geophysics, **38**, 812–825.

Shearer, P. M. and Chapman, C. H., 1988, Ray tracing in anisotropic media with linear velocity gradient: Geophys. J. Int., **94**, 575–580.

Slotnick, M. M., 1986, Lessons in seismic computing: Soc. of Explor. Geophys., 268 p.

Thomsen, L., 1986, Weak elastic anisotropy: Geophysics, **51**, 1954–1966.

White, J. E., 1983, Underground sound: Application of sound waves: Elsevier, 253 p.

Differential Equation-Based Seismic Data Filtering

Jianchao Li and Ken Larner

Center for Wave Phenomena
Colorado School of Mines
Golden, Colorado 80401
(303) 273-3557

Differential Equation-Based Seismic Data Filtering

Jianchao Li and Ken Larner

ABSTRACT

Suppressing noise and enhancing useful seismic signal by filtering is one of the important tasks of seismic data processing. Conventional filtering methods are implemented through either the convolution operation or various mathematical transforms. In this paper, we describe a methodology for studying and implementing filters, which, unlike those conventional filtering methods, is based on solving differential equations in the time and space domain. We call this kind of filtering *differential equation-based filtering* (DEBF). DEBF does not require that seismic data be stationary, so filtering parameters can vary with every time and space point. Also, in 2-D and 3-D, DEBF has higher computational efficiency than do conventional multiple-trace filtering methods.

Examples with synthetic and field seismic data show the DEBF methods presented here to be efficient and effective.

INTRODUCTION

Filtering in one form or another is universal in seismic data processing. Geophysicists use it to suppress harmful noise and enhance useful seismic signal, thereby improving the signal-to-noise ratio of seismic data.

Many different 1-D and 2-D filtering methods have been used in seismic data processing, in both the time and the frequency domains. Conventional 2-D moveout filtering methods for suppressing coherent, dipping events, for example, include time-space domain convolution filtering (Treitel et al., 1967) and frequency-wavenumber (f-k) domain filtering (Wiggins, 1966). Although these methods have been applied successfully in seismic data processing, some issues remain outstanding.

- Most commonly used filtering methods have directly or indirectly, explicitly or implicitly, a common basic theoretical assumption: the statistical characteristics

of seismic data do not vary with time and space. Seismic data, however, can be quite non-stationary. The amplitudes of seismic traces gradually attenuate, and the dominant frequency of seismic traces gradually reduces with time; spatial variations of underground media and underground structures must cause spatial variations of the characteristics of seismic data; and within common-midpoint (CMP) gathers, the characteristics of seismic traces also vary in both spatial and temporal directions, among other things because of moveout and of differences in incident angle at reflectors. As a result, the stationarity assumption of typical filtering methods is incorrect.

- To deal with spatial and temporal variations in data, one typically divides the data into several time- and space-windows, within which the characteristics of the filters are kept constant. The final filtered result is a combination of the results obtained from all the time- and space-windows. Thus, the parameters of these filters do not vary arbitrarily with time and space.

The implementation of conventional 2-D time-space domain convolution filtering methods is a process of multitrace convolution. To get well-controlled filtered results, we generally have to use long time and space convolution operators. In such cases, this filtering method generally has lower computational efficiency than does the f-k method. Despite its relative speed, in addition to its problems with handling non-stationary data, the f-k domain filtering has further shortcomings:

- It often produces some harmful artifacts, related to Gibb's phenomena, spatial aliasing, and side effects.
- It often requires a great deal of core computer memory.
- It has some requirements for the length of traces and the number of input traces to avoid wraparound problems and to meet demands of its algorithm.
- It cannot deal well with seismic data whose spatial sampling intervals are variable.

To overcome these shortcomings of conventional filtering methods, new filtering methods, especially in 2-D, have been developed in recent years. These include *tau-p* domain filtering (Noponen and Keeney, 1983), median filtering (Hardage, 1983), depth filtering (McMechan and Sun, 1991), recursive dip filtering (Claerbout, 1985) and adaptive filtering. *Tau-p* domain filtering can be time-variable, but it is difficult for this method to deal with space variation. While the two parameters of median filtering—length of running window and number of iterations—can be made to vary with space and time, neither offers fine control for the desired suppression of noise. Depth filtering is based on the idea of wavefield downward and upward continuation to remove near-surface effects, such as the direct wave and ground roll. This method,

however, is computational inefficient. Recursive dip filtering method is a form of filtering that can deal with variations of filter parameters with time and space. However, because this method uses a recursive algorithm in the time direction, data must be transposed from trace sequence to time sequence.

The adaptive filtering methods can be divided into two main classes. The first (Anderson and McMechan, 1988) still requires that seismic signal or noise be stationary; the second class (Katz and Katz, 1990), which is suitable for variations of seismic data with both time and space, is based on the joint use of several sets of linear basis filters.

With the increasing emphasis on 3-D seismic exploration, a variety of 3-D seismic data processing techniques, such as 3-D velocity analysis, 3-D dip-moveout (DMO) and 3-D migration, have been developed. As far as we know, however, no truly 3-D filtering methods have been put into practice. Typically, in order to filter 3-D seismic data, one uses existing 2-D filtering methods to filter 2-D sections, first in the inline direction, and then in the crossline direction. When doing so, the 3-D seismic data must be transposed from the inline direction to the crossline direction—a costly step, especially for unstacked data. Other than with these two-pass approaches, many practical difficulties arise in generalizing directly the various above-mentioned methods to 3-D.

In this paper, we shall describe a methodology for studying and developing filtering methods based on differential equations. The key steps of this methodology are: (1) design the filters and set up the filtering equations in the frequency domain or in the f-k domain, (2) transform these equations back into the time or time-space domains, as variable-coefficient differential equations, and (3) use a finite-difference algorithm to solve these equations. The approach we use here is similar to those used in some migration methods. These differential-equation-based filtering (DEBF) methods do not require that seismic data be stationary, so their filtering parameters can arbitrarily vary at every temporal and spatial point. That is, the theoretical foundation of these methods is based on non-stationary processes, and thus better fits typical physical processes.

Although our main purpose in this paper is to develop 2-D and 3-D DEBF methods, for simplicity we shall start our discussion with the 1-D case.

1. ONE-DIMENSIONAL PROBLEM

1.1 Principle of 1-D DEBF

Similar to the forms of 1-D Butterworth filters, we define the transfer functions of 1-D filters as follows.

Low-frequency-pass filters:

$$H_1(x,y,\omega) = \frac{\alpha}{\alpha + \omega^{2n}}, \tag{1}$$

High-frequency-pass filters:

$$H_2(x,y,\omega) = \frac{\omega^{2n}}{\alpha + \omega^{2n}}, \tag{2}$$

and the relation,

$$H_1(x,y,\omega) + H_2(x,y,\omega) = 1, \tag{3}$$

where x and y are the spatial coordinates; ω denotes the angular frequency, $\omega = 2\pi f$; f is the frequency; α is a filtering parameter determined by the cut-off frequency; and n is a positive integer that determines the steepness of the boundary between the filter's pass and reject zones. The amplitude curves of $H_1(x,y,\omega)$ are shown in Figure 1, for $n = 1, 2, \cdots, 10$. From this figure we can see that the larger is n, the steeper the boundary between pass and reject zones. Given relation (3), we need discuss only the low-pass filter $H_1(x,y,\omega)$. Furthermore, any band-pass filter can be formed by cascading a high- and a low-pass filter. Note, in equation (1), that $H_1(x,y,\omega_N) = 1/2$ gives

$$\alpha = {\omega_N}^{2n} = (2\pi f_N)^{2n},$$

where f_N is the cut-off frequency. Suppose we use the 1-D low-pass filter defined by equation (1) to filter seismic data. In the frequency-space domain, we have

$$Q(x,y,\omega) = H_1(x,y,\omega) \cdot P(x,y,\omega),$$

or

$$(\alpha + \omega^{2n}) \cdot Q(x,y,\omega) = \alpha \cdot P(x,y,\omega), \tag{4}$$

where $P(x,y,\omega)$ is the Fourier transform of the input seismic data $p(x,y,t)$ with respect to t, and $Q(x,y,\omega)$ is the filtered output in the frequency-space domain. Although we are discussing 1-D filtering here, the seismic data with which we usually deal are generally 2-D or 3-D. That is why we use as arguments (x,y,ω). Inverse Fourier transformation of equation (4) into the time-space domain yields

$$[\alpha(x,y,t) + (-1)^n \frac{\partial^{2n}}{\partial t^{2n}}] \cdot q(x,y,t) = \alpha(x,y,t) \cdot p(x,y,t). \tag{5}$$

Here, the filtering parameter α in equation (4) has become the time- and space-dependent coefficient of differential equation (5). Equation (5), with parameter $\alpha(x,y,t)$ varying as desired in space and time, is just the 1-D filtering differential equation we want.

Actually, we can choose a large value of n when solving equation (5). But as we will see, we can benefit conceptually and computationally from choosing $n = 1$. Then we obtain

$$[\alpha(x,y,t) - \frac{\partial^2}{\partial t^2}] \cdot q(x,y,t) = \alpha(x,y,t) \cdot p(x,y,t), \tag{6}$$

with

$$\alpha(x,y,t) = 4\pi^2 f_N^2(x,y,t). \tag{7}$$

We see that, through $\alpha(x,y,t)$, the user-specified cut-off frequency f_N in general can vary in both time and space. However, for our simplified 1-D argument in this section, we shall use (t) as short-hand for (x,y,t).

1.2 Algorithm for 1-D DEBF

Having derived filtering differential equation (5) or (6) to filter seismic data, the key problem lies in finding a stable and efficient method of solving these equations. Mathematically, many algorithms are available to solve this kind of differential equation. Here we use the finite-difference method. Instead of using the ordinary middle-difference pattern, we choose (Claerbout, 1985)

$$\frac{\partial^2 q(t)}{\partial t^2} \approx -\frac{\mathbf{T}}{\Delta t^2(\mathbf{I} - \beta\mathbf{T})}\mathbf{q}_n, \tag{8}$$

where Δt is the time sampling interval, and

$$\begin{aligned} \beta &= 0.25 - 1/\pi^2, \\ \mathbf{I} &= [0,1,0], \\ \mathbf{T} &= [-1,2,-1], \\ \mathbf{q}_n &= [q_{n-1}, q_n, q_{n+1}]^T, \\ q_n &= q(n\Delta t), \quad n = 1,2,3,\cdots,L, \end{aligned} \tag{9}$$

and where L denotes the maximum length, in sample points, of seismic traces to be processed. Substituting equation (8) and (9) into equation (6), we find

$$[\alpha_n \mathbf{I} + \frac{\mathbf{T}}{\Delta t^2(\mathbf{I} - \beta \mathbf{T})}] \cdot \mathbf{q}_n = \alpha_n \mathbf{I} \cdot \mathbf{p}_n, \tag{10}$$

$$n = 1, 2, 3, \cdots, L,$$

where

$$\begin{aligned} \alpha_n &= \alpha(n\Delta t), \\ \mathbf{p}_n &= [p_{n-1}, p_n, p_{n+1}]^T, \\ p_n &= p(n\Delta t), \\ p_0 &= 0, \quad p_{L+1} = 0. \end{aligned}$$

If let

$$\begin{aligned} \theta_n &= \Delta t^2 \alpha_n = 4\pi^2 \Delta t^2 f_{Nn}^2, \\ f_{Nn} &= f_N(n\Delta t), \end{aligned} \tag{11}$$

equation (10) can be written as

$$\begin{aligned} [\theta_n \mathbf{I} + (1 - \theta_n \beta)\mathbf{T}] \cdot \mathbf{q}_n &= \theta_n (\mathbf{I} - \beta \mathbf{T}) \cdot \mathbf{p}_n, \\ n &= 1, 2, 3, \cdots, L. \end{aligned}$$

We may express this equation in matrix terms as

$$\mathbf{A} \cdot \mathbf{q} = \mathbf{B}, \tag{12}$$

where

$$\mathbf{B} = \mathbf{C} \cdot \mathbf{p},$$

$$\mathbf{A} = \begin{bmatrix} b_1 & c_1 & 0 & 0 & \cdots & 0 & 0 \\ a_2 & b_2 & c_2 & 0 & \cdots & 0 & 0 \\ 0 & a_3 & b_3 & c_3 & \cdots & 0 & 0 \\ \vdots & \vdots & \vdots & \vdots & \ddots & \vdots & \vdots \\ 0 & 0 & 0 & 0 & \cdots & a_L & b_L \end{bmatrix},$$

$$\mathbf{C} = \begin{bmatrix} e_1 & f_1 & 0 & 0 & \cdots & 0 & 0 \\ d_2 & e_2 & f_2 & 0 & \cdots & 0 & 0 \\ 0 & d_3 & e_3 & f_3 & \cdots & 0 & 0 \\ \vdots & \vdots & \vdots & \vdots & \ddots & \vdots & \vdots \\ 0 & 0 & 0 & 0 & \cdots & d_L & e_L \end{bmatrix},$$

$$\begin{aligned} \mathbf{q} &= [q_1, q_2, q_3, \cdots, q_L]^T, \\ \mathbf{p} &= [p_1, p_2, p_3, \cdots, p_L]^T, \\ a_n &= c_n = \theta_n \beta - 1, \\ b_n &= \theta_n - 2(\theta_n \beta - 1), \\ d_n &= f_n = \theta_n \beta, \\ e_n &= \theta_n (1 - 2\beta). \end{aligned}$$

Equation (12) is a differential equation-based, implicit finite-difference implementation of 1-D filtering. It can be seen that equation (12) is a diagonally dominant tridiagonal system of equations, so, we can use a well-known fast algorithm to solve this special system (Clearbout, 1985). This algorithm ensures a solution of equation (12) that is stable and efficient. The tridiagonal nature of the equation is a result of the choice $n = 1$. To get sharper cut-off action, we see in Figure 1 that we would have to choose the larger value of n in equation (5). If we did so, however, the resulting system of equations would no longer be tridiagonal, but rather a system of equations with progressively increasing number of nonzero diagonals as n increases. As a result, we would lose the computational advantage of the tridiagonal system. Fortunately, however, we would have some other efficient solutions, such as the Cholesky decomposition method. The computational cost of this solution grows only linearly with the size L. By solving equation (12) with the user-specified cut-off frequency $f_N(x, y, t)$, differential equation-based 1-D filtering of seismic data can be implemented trace-by-trace.

1.3 Examples with synthetic data

To test the effectiveness of the 1-D filtering method presented in this section, we shall study a synthetic data example. The wavelet we used to create synthetic seismic sections is defined by

$$s(t) = \frac{20}{t} e^{-2000t^2} \sin(30\pi t) \cos(62.5\pi t).$$

Frequencies of this wavelet are in the range of typical seismic signals.

Figure 2a is a synthetic seismic section consisting of two horizontal reflections with low-frequency (1-10 Hz) "noise" superimposed. Figure 2b shows the amplitude spectra of four traces from Figure 2a. The results of applying time- and space-variable filtering of the data in Figure 2a are shown in Figure 3. The low cut-off frequency in this test is governed by the following parameters,

at the second trace: $t200f1, t400f10$ and $t450f40$,

and at the 19th trace: $t200f40, t400f10$ and $t450f1$.

Here, for example, $t200f1, t400f10$ and $t450f40$ means that before 200 ms, the low cut-off frequency is 1 Hz; at 400 ms, 10 Hz; and after 450 ms, 40 Hz. The low cut-off frequencies at all other points are obtained by linear interpolation. Laterally, these cut-off frequencies are also interpolated linearly between traces along which values are specified. Figure 3a is the filtered section, and Figure 3b is the so-called noise section, the difference between Figure 2a and Figure 3a. Figure 3c shows the amplitude spectra for the 1st, 5th, 10th and 15th traces of Figure 3a. The results in these three figures are just what we expect.

2. TWO-DIMENSIONAL PROBLEM

2.1 Principle of 2-D DEBF

Having introduced the conception of DEBF with the 1-D case, we now discuss 2-D DEBF. In the f-k domain, we define the transfer functions of 2-D moveout filters we use as follows.

High-dip-pass filter:

$$H_1(k_x, y, \omega) = \frac{\alpha}{\alpha + \omega^2/ik_x}, \tag{13}$$

Low-dip-pass filter:

$$H_2(k_x, y, \omega) = \frac{\omega^2/ik_x}{\alpha + \omega^2/ik_x}, \tag{14}$$

and the relation,

$$H_1(k_x, y, \omega) + H_2(k_x, y, \omega) = 1, \tag{15}$$

where k_x is the wavenumber in the x-direction, and α is a 2-D filtering parameter determined by the user-specified cut-off "dip" or by a combination of the user-specified dominant frequency and cut-off apparent velocity.

Actually, we might have defined other forms for the transfer function, such as $H_1(k_x, y, \omega) = \alpha/(\alpha + \omega^2/k_x^2)$. While such a choice would give a response that is strictly a function of slope k_x/ω, we choose the above forms for simplicity of development, computational efficiency, and stability. Given relation (15), we need only discuss the high-dip-pass filter $H_1(k_x, y, \omega)$. Its amplitude and phase spectra are, respectively,

$$|H_1(k_x, y, \omega)| = \frac{1}{\sqrt{1 + \omega^4/\alpha^2 k_x^2}}, \tag{16}$$

and

$$\theta_1(k_x, y, \omega) = \tan^{-1}(\frac{\omega^2}{\alpha k_x}). \tag{17}$$

Letting $|H_1(k_x, y, \omega)| = \varepsilon$, some chosen amplitude level, then from equation (16)

$$k_x = \pm \frac{\varepsilon}{\sqrt{1 - \varepsilon^2}} \cdot \frac{\omega^2}{\alpha}, \tag{18}$$

where ε is a positive constant, less than 1. For different values of ε, equation (18) describes different parabolas that are symmetric with respect to both the ω- and k_x-axis and pass through the origin. That is, the contours of amplitude spectrum of the 2-D filter $H_1(k_x, y, \omega)$ defined by equation (13) are symmetric parabolas. If, further, we let $\varepsilon = 1/\sqrt{2}$, we get a special contour,

$$k_x = \pm \frac{\omega^2}{\alpha}. \tag{19}$$

This is the expression of the half-power contour of $H_1(k_x, y, \omega)$. Now let us see the relationship between $H_1(k_x, y, \omega)$ and the response of an ideal dip filter. In Figure 4a, covering only the range $\omega \geq 0$ and $k_x \geq 0$, the straight line denotes the boundary $k_x = \omega/V_N$ between the pass and reject zone of an ideal dip filter, while the parabola is the boundary of the filter $H_1(k_x, y, \omega)$ defined by equation (19). Here, V_N is the cut-off apparent velocity. Therefore, when using the filter $H_1(k_x, y, \omega)$ as a dip filter, we

are, in effect, replacing the straight-line boundary of the ideal filter with the parabolic boundary. To get desired filtered results, we should make the parabolic boundary of $H_1(k_x, y, \omega)$ as close to the straight line boundary of the ideal dip filter as possible within the range of ω and k_x of interest. This can be done by minimizing the area between the straight line and the parabolic boundary. Over the frequency range of interest, for example, if the range is from 0 to f_{max}, we get an expression for the filtering parameter α,

$$\alpha = 2^{4/3}\pi f_N V_N. \tag{20}$$

Here, we take $f_N = f_{max}/2$ as the user-specified dominant frequency. If we use the concept of apparent velocity to characterize 2-D filters, $H_1(k_x, y, \omega)$ is a low-apparent-velocity-pass filter. Figure 4b shows three contours, $\varepsilon = 0.707, 0.6$ and 0.5, of the amplitude spectrum $|H_1(k_x, y, \omega)|$, when α takes the form of equation (20), for $f_N = 35$ Hz and $V_N = 3000$ m/s. We see that $H_1(k_x, y, \omega)$ is an approximation of the ideal dip filter, and the transition of its boundary from the pass to the reject zone is smooth.

Using $H_1(k_x, y, \omega)$ defined by equation (13) and (20) to filter seismic data, the filtering equation in the f-k domain can be expressed as

$$Q(k_x, y, \omega) = H_1(k_x, y, \omega) \cdot P(k_x, y, \omega),$$

or

$$(i\alpha k_x + \omega^2)Q(k_x, y, \omega) = i\alpha k_x P(k_x, y, \omega), \tag{21}$$

where $P(k_x, y, \omega)$ is the Fourier transformation of the input seismic data $p(x, y, t)$ with respect to x and t; $Q(k_x, y, \omega)$ is the filtered result in the f-k domain. Inverse Fourier transformation of equation (21) into the time-space domain yields

$$[\alpha(x, y, t)\frac{\partial}{\partial x} - \frac{\partial^2}{\partial t^2}]q(x, y, t) = \alpha(x, y, t)\frac{\partial p(x, y, t)}{\partial x}.$$

If the seismic data with which we deal are only 2-D, we can use the short-hand (x, t) instead of (x, y, t) for the arguments. Thus, the above equation becomes

$$[\alpha(x, t)\frac{\partial}{\partial x} - \frac{\partial^2}{\partial t^2}]q(x, t) = \alpha(x, t)\frac{\partial p(x, t)}{\partial x}, \tag{22}$$

with

$$\alpha(x, t) = 2^{4/3}\pi f_N V_N(x, t). \tag{23}$$

Here, $q(x, t)$ is the filtered output in the time-space domain, and the filtering parameter $\alpha(x, t)$, determined by f_N and $V_N(x, t)$, is a function of both time and space, i.e. it can vary arbitrarily in both temporal and spatial directions. Equation (22) is just the variable-coefficient differential equation we want for 2-D high-dip-pass, or

low-apparent-velocity-pass, filtering. To solve this partial differential equation, we use the following conditions:

$$\begin{aligned} p(x,t)|_{x=-\Delta x} &= \eta \cdot p(x,t)|_{x=0}, \\ q(x,t)|_{x=-\Delta x} &= \eta \cdot q(x,t)|_{x=0}, \\ q(x,t)|_{t=0} = 0, &\quad q(x,t)|_{t=t_{max}} = 0, \end{aligned} \tag{24}$$

where η is a constant, $0 \leq \eta \leq 1$, Δx is the trace spacing, and $x = 0$ is the location of the first trace in the seismic data.

2.2 Algorithm for 2-D DEBF

Using the modified Crank-Nicholson difference pattern (Claerbout, 1985) to solve the determined problem (22) and (24), we obtain the following difference equation

$$\begin{aligned} &\frac{\alpha_m(n)}{\Delta x}\mathbf{I}[\mathbf{q}_m(n) - \mathbf{q}_{m-1}(n)] + \frac{\mathbf{T}}{2\Delta t^2(\mathbf{I} - \beta\mathbf{T})}[\mathbf{q}_m(n) + \mathbf{q}_{m-1}(n)] \\ &\qquad = \frac{\alpha_m(n)}{\Delta x}\mathbf{I}[\mathbf{p}_m(n) - \mathbf{p}_{m-1}(n)], \\ &n = 1, 2, 3, \cdots, L, \qquad m = 0, 1, 2, \cdots, M, \end{aligned} \tag{25}$$

and the discrete expressions of the conditions for determining solution

$$\begin{aligned} \mathbf{p}_{-1} &= \eta \cdot \mathbf{p}_0, \\ \mathbf{q}_{-1} &= \eta \cdot \mathbf{q}_0, \\ q_m(0) &= 0, \quad q_m(L+1) = 0, \end{aligned} \tag{26}$$

where Δt is the time sampling interval, L is the maximum length of seismic traces in sample points, M is the maximum number of traces processed, and

$$\begin{aligned} \mathbf{I} &= [0, 1, 0], \\ \mathbf{T} &= [-1, 2, -1], \\ \alpha_m(n) &= \alpha(m\Delta x, n\Delta t), \\ \beta &= 0.25 - 1/\pi^2, \\ q_m(n) &= q(m\Delta x, n\Delta t), \\ p_m(n) &= p(m\Delta x, n\Delta t), \\ \mathbf{q}_m(n) &= [q_m(n-1), q_m(n), q_m(n+1)]^T, \end{aligned}$$

$$\begin{aligned}
\mathbf{p}_m(n) &= [p_m(n-1), p_m(n), p_m(n+1)]^T, \\
\mathbf{q}_m &= [q_m(1), q_m(2), q_m(3), \ldots, q_m(L)]^T, \\
\mathbf{p}_m &= [p_m(1), p_m(2), p_m(3), \ldots, p_m(L)]^T.
\end{aligned}$$

Let

$$\theta_m(n) = 2\Delta t^2 \alpha_m(n)/\Delta x = 2^{7/3}\pi \Delta t^2 f_N V_{Nm}(n). \tag{27}$$

Then the difference equation (25) becomes

$$\begin{aligned}
[\theta_m(n)\mathbf{I} + (1 - \theta_m(n)\beta)\mathbf{T}] \cdot q_m(n) &= [\theta_m(n)\mathbf{I} - (1 + \theta_m(n)\beta)\mathbf{T}] \cdot q_{m-1}(n) \\
&+ \theta_m(n)(\mathbf{I} - \beta\mathbf{T})[p_m(n) - p_{m-1}(n)], \qquad (28) \\
n = 1, 2, 3, \cdots, L, &\qquad m = 0, 1, 2, \cdots, M.
\end{aligned}$$

If we let

$$\mathbf{A} = \begin{bmatrix}
b_1 & a_1 & 0 & 0 & \cdots & 0 & 0 \\
a_2 & b_2 & a_2 & 0 & \cdots & 0 & 0 \\
0 & a_3 & b_3 & a_3 & \cdots & 0 & 0 \\
\vdots & \vdots & \vdots & \vdots & \ddots & \vdots & \vdots \\
0 & 0 & 0 & 0 & \cdots & a_L & b_L
\end{bmatrix},$$

$$\mathbf{B} = \begin{bmatrix}
d_1 & c_1 & 0 & 0 & \cdots & 0 & 0 \\
c_2 & d_2 & c_2 & 0 & \cdots & 0 & 0 \\
0 & c_3 & d_3 & c_3 & \cdots & 0 & 0 \\
\vdots & \vdots & \vdots & \vdots & \ddots & \vdots & \vdots \\
0 & 0 & 0 & 0 & \cdots & c_L & d_L
\end{bmatrix},$$

$$\mathbf{C} = \begin{bmatrix}
f_1 & e_1 & 0 & 0 & \cdots & 0 & 0 \\
e_2 & f_2 & e_2 & 0 & \cdots & 0 & 0 \\
0 & e_3 & f_3 & e_3 & \cdots & 0 & 0 \\
\vdots & \vdots & \vdots & \vdots & \ddots & \vdots & \vdots \\
0 & 0 & 0 & 0 & \cdots & e_L & f_L
\end{bmatrix},$$

$$\begin{aligned}
a_n &= \theta_m(n)\beta - 1, \\
b_n &= \theta_m(n) + 2(1 - \theta_m(n)\beta),
\end{aligned}$$

$$
\begin{aligned}
c_n &= 1 + \theta_m(n)\beta, \\
d_n &= \theta_m(n) - 2(1 + \theta_m(n)\beta), \\
e_n &= \theta_m(n)\beta, \\
f_n &= \theta_m(n)(1 - 2\beta),
\end{aligned}
$$

equation (28) can be expressed in matrix terms as

$$
\begin{aligned}
\mathbf{A}\mathbf{q}_m &= \mathbf{B}\mathbf{q}_{m-1} + \mathbf{C}(\mathbf{p}_m - \mathbf{p}_{m-1}), \\
m &= 0, 1, 2, \cdots, M.
\end{aligned}
\tag{29}
$$

This equation is an example of differential equation-based implementation of 2-D filtering. As for the 1-D example, equation (29) is a diagonally dominant tridiagonal system of equations, so it too can be solved by using a fast algorithm. Also, from equation (28) and (29), to get the filtered result at a given point, only six adjacent points on two adjacent traces are involved; thus to obtain one output trace, only two input traces are used. So, on the one hand, computational operators of this kind of filter are quite short in both temporal and spatial directions and computational efficiency is high; on the other hand, through use of the implicit approach in the time direction and the explicitly recursive approach in the space direction, we, in effect, achieve an extended 2-D impulse response.

So far, we have been discussing 2-D high-dip-pass filtering. By relation (15), instead of applying directly $H_2(k_x, y, \omega)$ defined by equation (14), we subtract the filtered result of 2-D high-dip-pass filtering from the original input seismic data to get the result of 2-D low-dip-pass filtering.

2.3 Examples with synthetic and field data

We demonstrate the action of the 2-D filtering method first on synthetic and then on field seismic data. Figure 5a contains horizontal events and events with moveout we shall call small, moderate, and large. Figure 5b shows a time- and space-variable high-apparent-velocity-pass (or low-dip-pass) filtered result of Figure 5a. In this section any given dipping event has been passed at some time and space points and rejected at the others. In this example, the dominant frequency is 20 Hz, and the cut-off apparent-velocity $V_N(x,t)$ was governed by the following parameters,

at the first trace: $t1500V5500$ and $t3510V50$,

at the 250th trace: $t1500V5500$ and $t2510V50$,

and at 500th trace: $t1500V5500$ and $t1510V50$.

Here, for example, $t1500V5500$ and $t3510V50$ means that before 1510 ms, the cut-off apparent-velocity is 5500 m/s and after 3510 ms, 50 m/s. The values of V_N at all other points are obtained by linearly interpolation.

Figure 5c is a detail, corresponding to the box position in Figure 5a, of the high-apparent-velocity-pass filtered results of Figure 5a obtained by using 2-D DEBF, and Figure 5d is that obtained by f-k filtering. Our purpose is to reject the steep events and to pass the horizontal events and those three events with small dips. The cut-off boundary just coincides with the events with moderate dip. Comparing Figure 5c with 5d, we see that f-k filter has a sharper cut-off boundary than does DEBF, but has some artifacts on the side, while DEBF does not.

The second example is a demonstration of noise suppression on a field shot record. Figure 6a shows the raw data, which are contaminated by large-moveout coherent noise in the upper part, and Figure 6b shows the 2-D time- and space-variable DEBF filtered result of Figure 6a showing suppression of the coherent noise. Here, $f_N =$ 30 Hz and $V_N(x,t)$ was governed by the following parameters,

at the first trace: $t700V2700$ and $t1000V3500$,

at the 32nd trace: $t1500V3500$,

at the 52nd trace: $t800V2200$ and $t1500V3500$,

and at the 72nd trace: $t1100V1700$ and $t2000V3500$.

The final 2-D filter example is a common-offset field seismic section. The raw section (Figure 7a), especially the right part of this section, has much steeply dipping background noise. In Figure 7b, this noise has been reduced, and the signal-to-noise ratio thereby has been improved.

Clearly, although we do not show it here, this kind of filtering method could also be used to separate down-going and up-going waves in VSP data.

For a test data set consisted of 1024 traces, each containing 1024 samples, we have compared the computational efficiency of the 2-D DEBF program written in FORTRAN with that of an f-k filtering program in C on an IBM RS/6000 work-station. Under the same conditions, the 2-D DEBF method took 1 minute and 20 seconds, while the f-k-domain filtering method in the SU system took 1 minute and 37 seconds. This test suggests that speeds of the 2-D DEBF and f-k methods are comparable.

3. THREE-DIMENSIONAL PROBLEM

3.1 Principle and algorithm of 3-D DEBF

In the previous section, we defined the high-dip-pass filter and discussed its implementation in detail. One way for us to define the transfer function of a 3-D high-dip-pass filter is as follows,

$$H(k_x,k_y,\omega)=\frac{\alpha_x}{\alpha_x+\omega^2/ik_x}\cdot\frac{\alpha_y}{\alpha_y+\omega^2/ik_y}=H_1(k_x,\omega)\cdot H_1(k_y,\omega), \qquad (30)$$

where both $H_1(k_x,\omega)$ and $H_1(k_y,\omega)$ are 2-D high-dip-pass filters, where $H_1(k_x,\omega)$ is used in the x-direction (say, the inline direction), while $H_1(k_y,\omega)$ is used in the y-direction (say, the crossline direction). Using $H(k_x,k_y,\omega)$ to filter 3-D seismic data, we obtain the filtering equation in the f-k domain

$$\begin{aligned} Q(k_x,k_y,\omega) &= H(k_x,k_y,\omega)\cdot P(k_x,k_y,\omega) \\ &= H_1(k_y,\omega)\cdot H_1(k_x,\omega)\cdot P(k_x,k_y,\omega). \end{aligned} \tag{31}$$

If we let

$$G(k_x,k_y,\omega) = H_1(k_x,\omega)\cdot P(k_x,k_y,\omega) = \frac{\alpha_x}{\alpha_x+\omega^2/ik_x}\cdot P(k_x,k_y,\omega), \tag{32}$$

then equation (31) becomes

$$Q(k_x,k_y,\omega) = H_1(k_y,\omega)\cdot G(k_x,k_y,\omega) = \frac{\alpha_y}{\alpha_y+\omega^2/ik_y}\cdot G(k_x,k_y,\omega). \tag{33}$$

Inverse Fourier transformation of equation (32) and (33) into the time-space domain yields a system of 3-D high-dip-pass filtering differential equations,

$$[\alpha_x(x,y,t)\frac{\partial}{\partial x}-\frac{\partial^2}{\partial t^2}]g(x,y,t) = \alpha_x(x,y,t)\frac{\partial p(x,y,t)}{\partial x}, \tag{34}$$

and

$$[\alpha_y(x,y,t)\frac{\partial}{\partial y}-\frac{\partial^2}{\partial t^2}]q(x,y,t) = \alpha_y(x,y,t)\frac{\partial g(x,y,t)}{\partial y}, \tag{35}$$

where $p(x,y,t)$ is the original input; $g(x,y,t)$ is the intermediate filtered result obtained after equation (34) is used in the x-direction; and $q(x,y,t)$ is the 3-D final filtered result.

Because both equations (34) and (35) are 2-D variable-coefficient differential equations, we can solve them using the algorithm described in the 2-D case. However, in practice, we wish to avoid the costly transposition of 3-D seismic data when implementing the 3-D DEBF method so that the total computational efficiency can be further raised. Fortunately, we can alternately and recursively solve equation (34) and (35) between two adjacent traces in the x-direction and between two adjacent lines in the y-direction. The scheme is shown in Figure 8. That is, we first get the intermediate result, $g(x+1,y+1,t)$, using $g(x,y+1,t)$, $p(x,y+1,t)$ and $p(x+1,y+1,t)$, then get the final result, $q(x+1,y+1,t)$, using $q(x+1,y,t)$, $g(x+1,y,t)$ and $g(x+1,y+1,t)$. As a result, we need not transpose 3-D seismic data from the inline direction to the crossline direction and then from the crossline direction to the inline direction for subsequent processings. To our knowledge, no other existing filtering methods can do 3-D filtering in this way.

As before, implementation of 3-D low-dip-pass DEBF requires only subtraction of the high-dip-pass filtered result from the input data.

3.2 Application to synthetic data

Figure 9 is a sketch map of a 3-D common-shot experiment with 20 lines and 121 receivers on each line. Figure 10a simulates the direct arrival, along with four horizontal reflection events. Moveout of the direct arrival varies with both time and azimuth. Figure 10b, the filtered result of the 3-D DEBF method with f_N=35 Hz and V_N=6000 m/s, shows that the dipping event has been strongly suppressed in both the inline and the crossline directions, while the horizontal events have been preserved.

CONCLUSIONS

We have developed the method and shown examples of DEBF filtering in 1-D, 2-D, and 3-D. Unlike conventional filtering techniques, which use convolution operations or mathematical transforms, the method presented here directly solves variable-coefficient differential equations, and, as a result, the filtering parameters can vary at every time and space point. When we use a finite-difference algorithm to solve these filtering differential equations, the filtering processes are transformed into the solution of tridiagonal systems of equations, which have known, efficient solutions. From the principles and algorithms of these filtering methods and the examples with synthetic and field seismic data we have done, we conclude that the DEBF methods have the following characteristics.

1. DEBF filter parameters can arbitrarily vary with both time and space.

2. Because their operators are short, the computational efficiency of DEBF is quite high. (Its speed for 2-D processing is comparable to that of f-k filtering, which lacks flexibility for addressing non-stationarity.) Furthermore, because we use an implicit solution in the time direction and a recursive approach in the space direction, their impulse responses, in effect, are long.

3. Because these DEBF methods process seismic data trace-by-trace, they need not do any transposition of seismic data. This further raises the total computational efficiency, especially for 3-D filtering. Moreover, these methods therefore require less inner computer memory.

4. DEBF methods do not have any specific requirements for the length and the number of input traces.

5. Because these methods need relatively little core memory and are relatively efficient, they are well suited for use not only on large computers, but also on microcomputers and workstations.

6. Although not shown here, they can be adapted to treat seismic data with non-uniform space sampling intervals. While non-uniform sampling makes the computation more complicated, it poses no fundamental limitation.

7. 2-D and 3-D dip filters cannot distinguish between events with positive dips and those with negative dips.

8. For the simple filter examples considered here, the cut-off boundary of DEBF is not as steep as that readily obtainable with f-k filtering.

ACKNOWLEDGEMENTS

The authors gratefully acknowledge the support of the sponsors of the Consortium Project on Seismic Inversion Methods for Complex Structures at the Center for Wave Phenomena, Colorado School of Mines.

REFERENCES

Anderson, R. G. and McMechan, G. A., 1988, Noise-adaptive filtering of seismic shot records: geophysics, **53**, 638-649.

Claerbout, J. F., 1985, Imaging the earth's interior: Blackwell Scientific Publications.

Hardage, B. A., 1983, Vertical seismic profiling: Geophysical Press, London-Amsterdam.

Katz, A. and Katz, S., 1990, Multichannel adaptive filters: 60th Annual International Meeting, Society of Exploration Geophysicists, Expanded Abstracts, 1697-1700.

McMechan G. A. and Sun R., 1991, Depth filtering of first breaks and ground roll: Geophysics, **56**, 390-396.

Noponen, I. and Keeney, J., 1983, Attenuation of waterborne coherent noise by application of hyperbolic velocity filtering during the tau-p transform: presented at 53rd Annual International Meeting, Society of Exploration Geophysicists.

Treitel, S., Shanks, J., and Frasier, C., 1967, Some aspects of fan filtering: Geophysics, **32**, 789-800.

Wiggins, R., 1966, $\omega - k$ filter design: Geophysical Prospecting, **14**, 427-440.

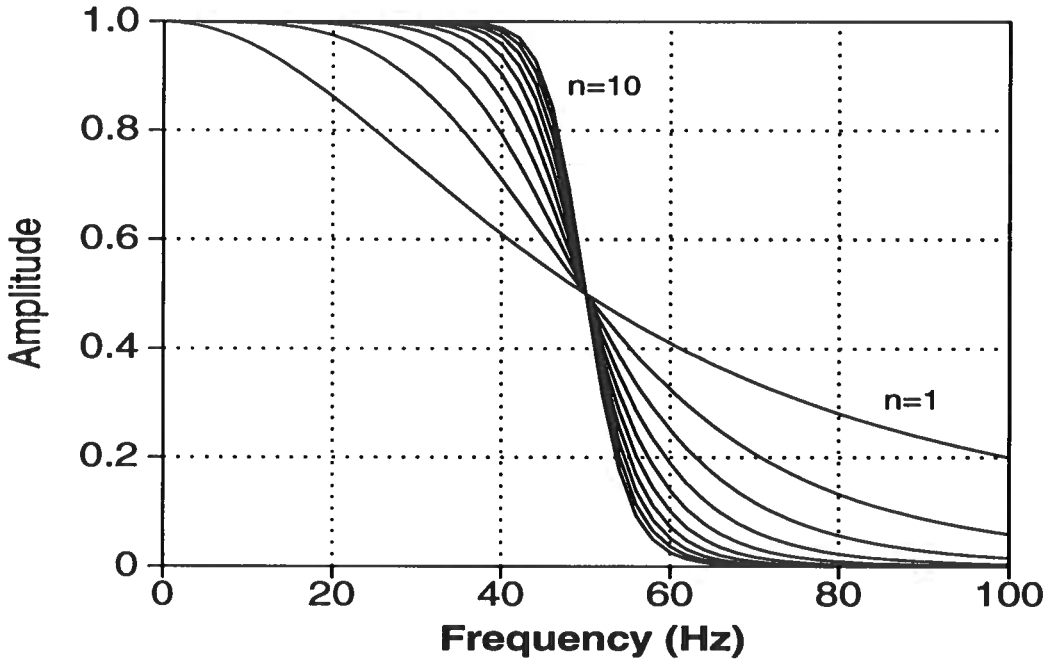

FIG. 1. Amplitude curves of the low-frequency-pass filter $H_1(\omega)$ for $n = 1, 2, 3, \cdots, 10$.

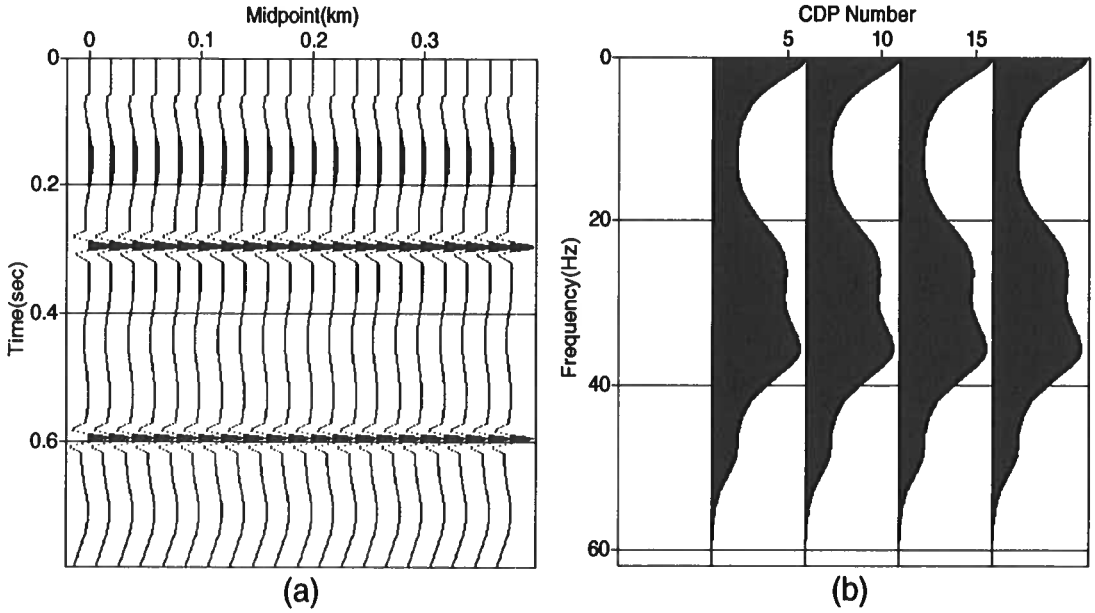

FIG. 2. (a) Synthetic data contaminated by 1-10 Hz low-frequency "noise". (b) Amplitude spectra of four of the traces in (a).

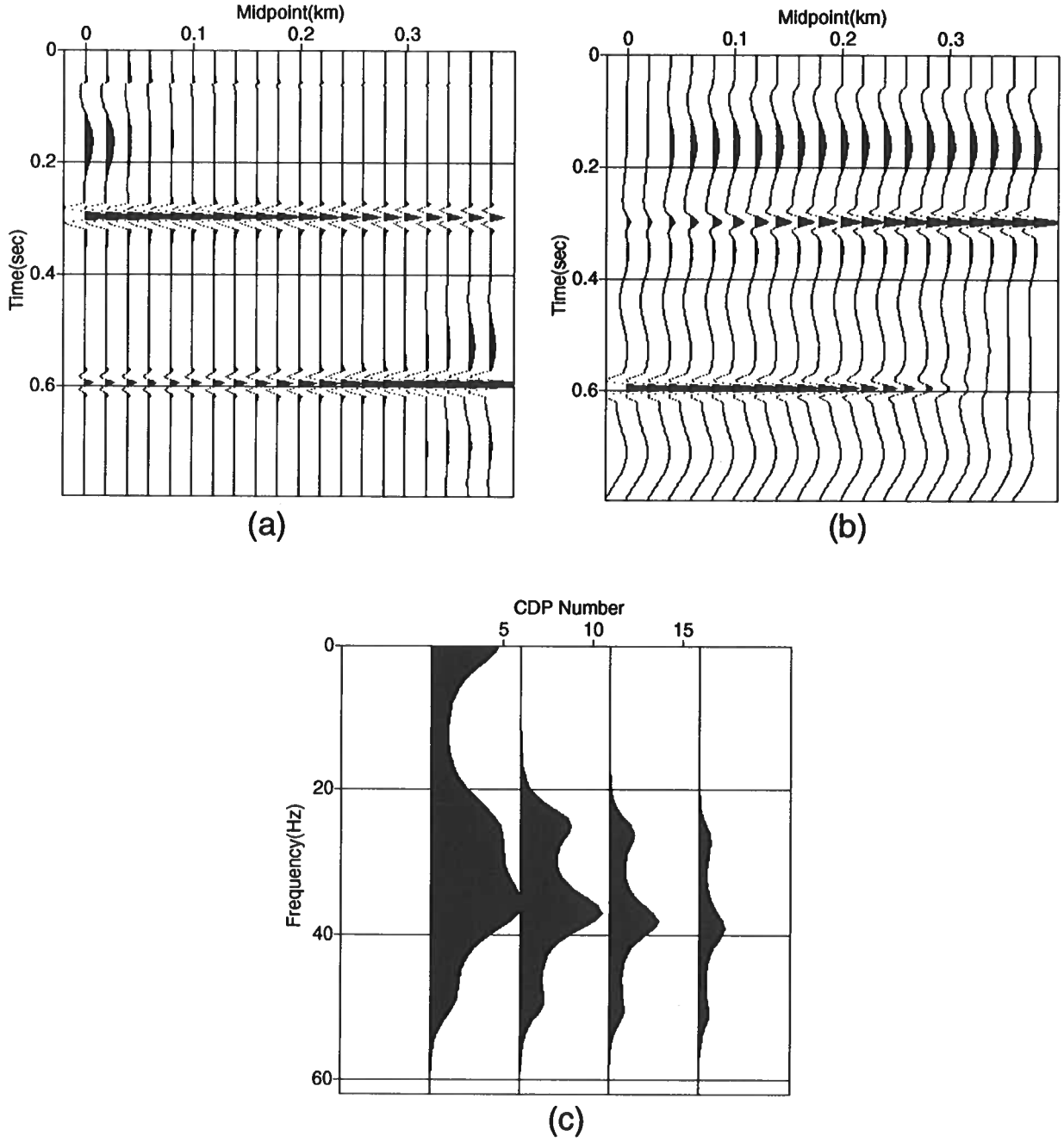

FIG. 3. (a) Time- and space-variable filtered result of Figure 2a. The low cut-off frequencies are both time- and space-variable. (b) Time- and space-variable filtered "noise" section. (c) Amplitude spectra of the time- and space-variable filtered section (a) within a 400 ms time window centered on 200 ms.

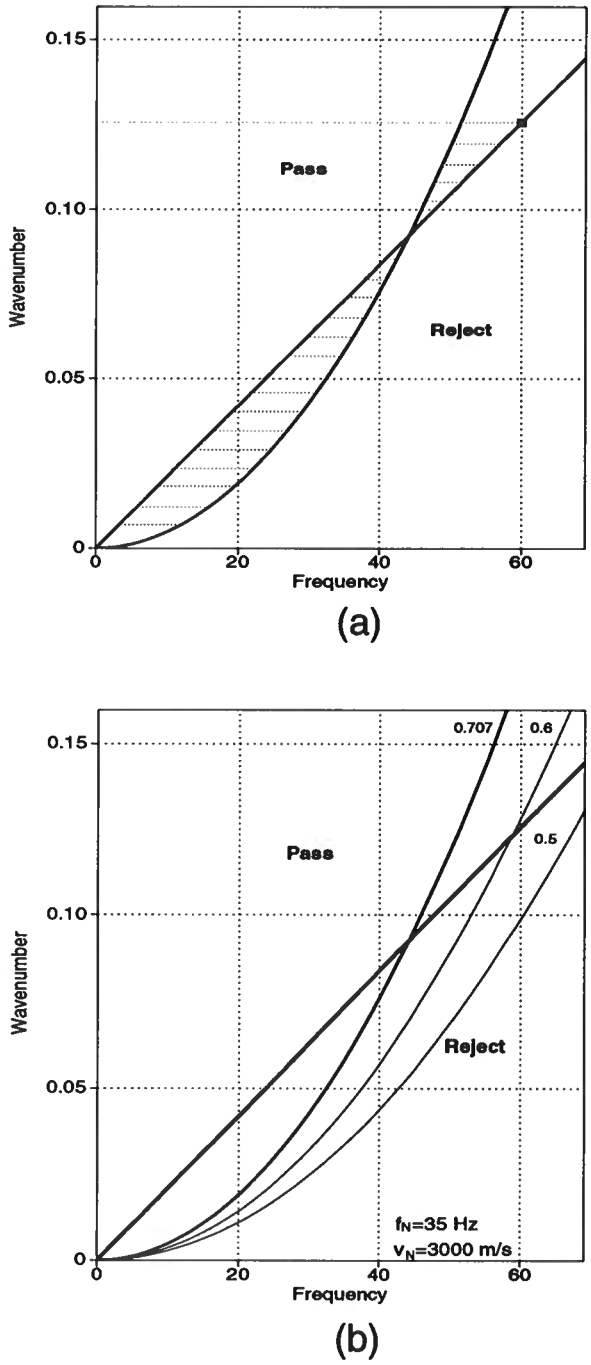

FIG. 4. (a) Area between the straight-line boundary of an ideal dip filter and the parabolic boundary of the 2-D high-dip-pass DEBF filter. (b) Straight-line boundary of an ideal dip filter and three contours of the amplitude spectrum $|H_1(k_x, y, \omega)|$.

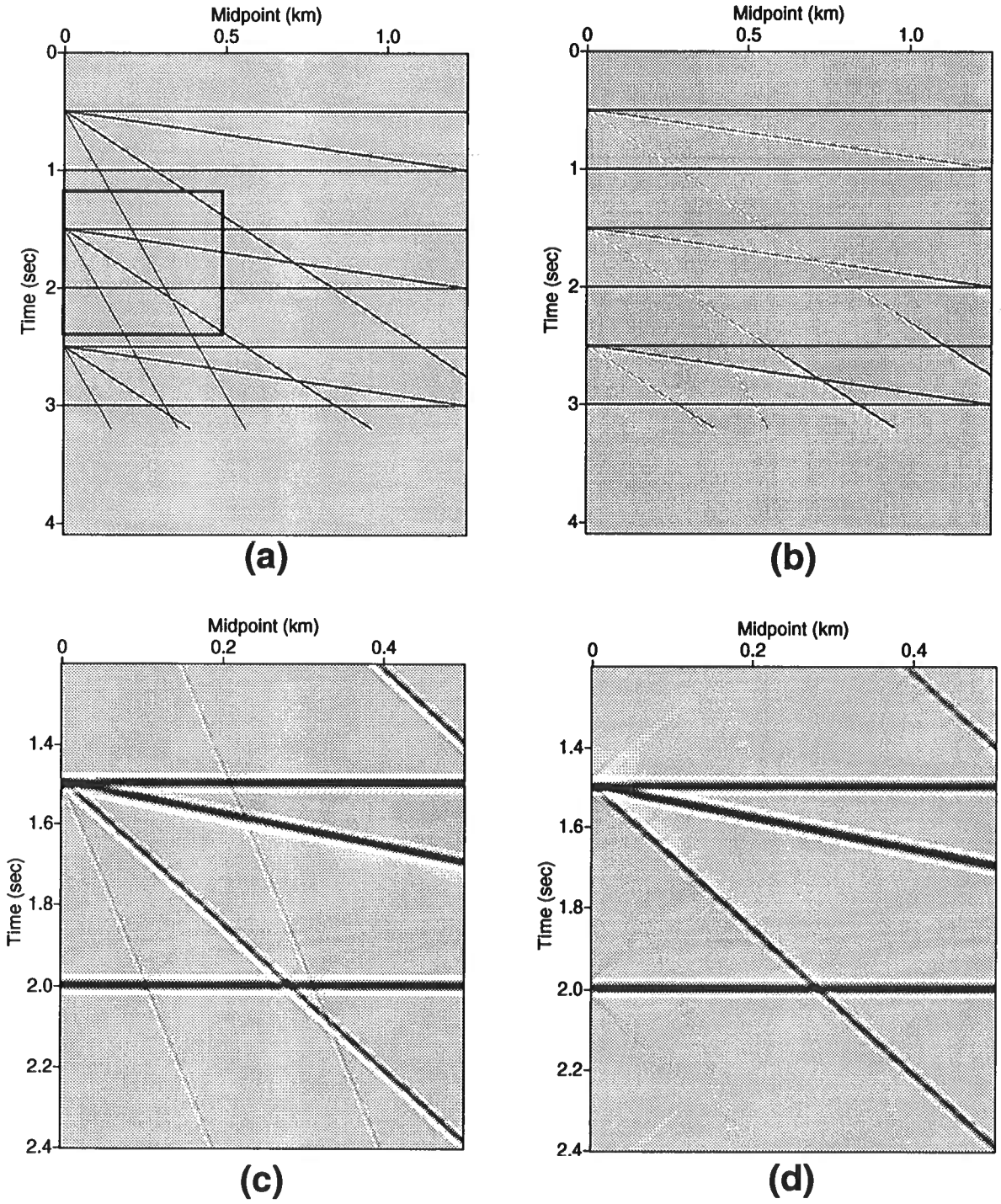

FIG. 5. (a) Synthetic seismic section with six horizontal and nine dipping events. (b) Time- and space-variable DEB low-dip-pass filtered section of (a). (c) Detail of DEB low-dip-pass filtered section of (a) to compare with (d). (d) Detail of low-dip-pass filtered section of (a) obtained by using f-k filtering.

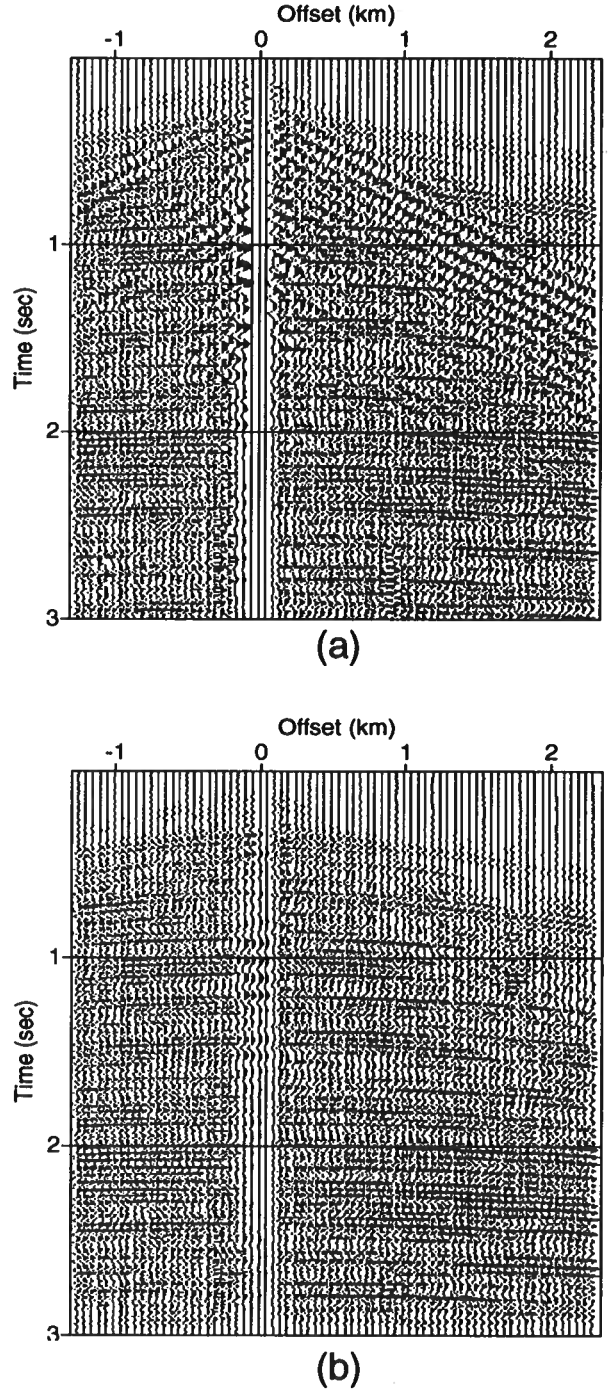

FIG. 6. (a) Field shot record with strong, dipping coherent noises in the upper part. (b) Time- and space-variable filtered result of (a). All dipping noises have been removed, improving the signal-to-noise ratio.

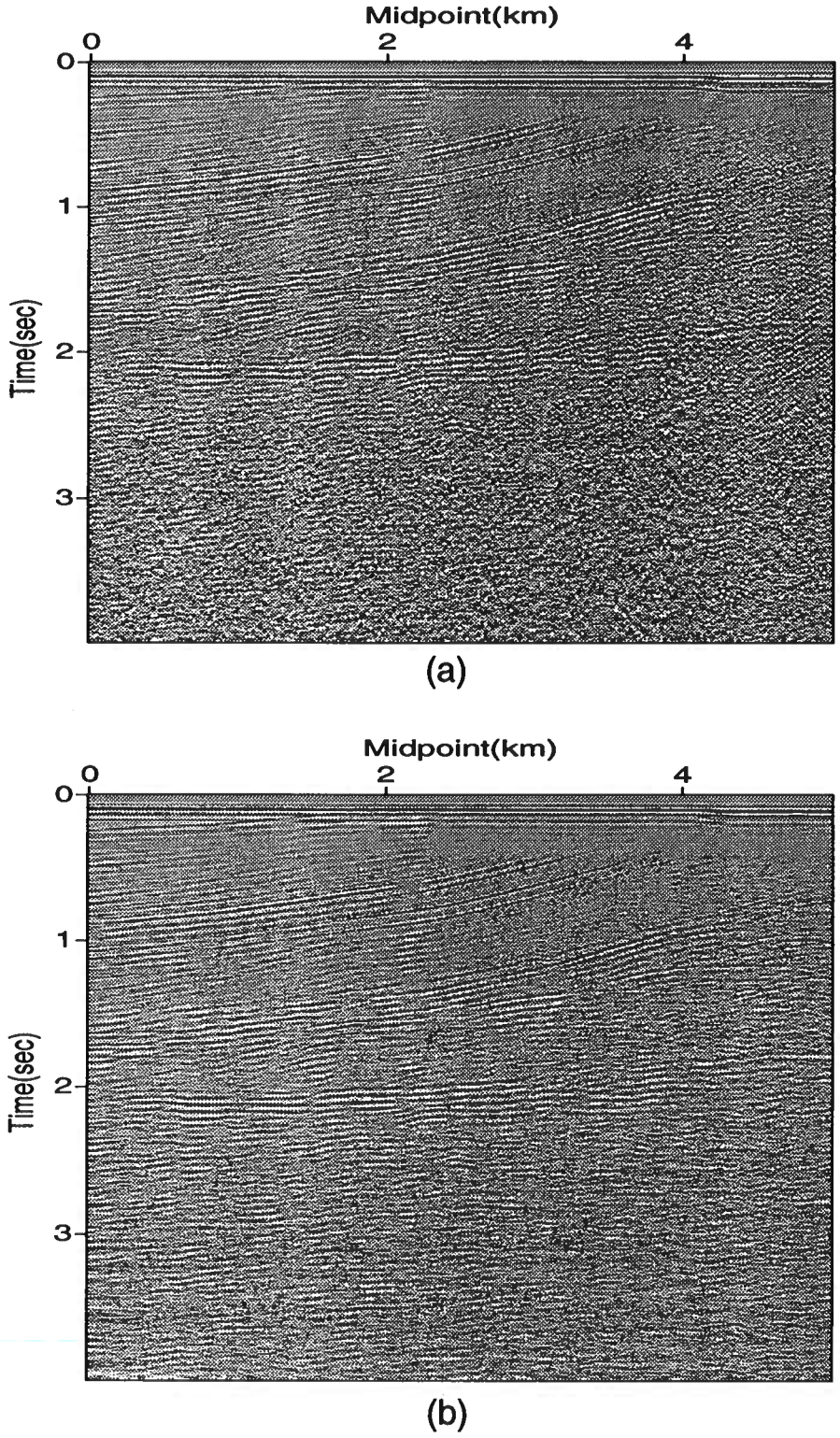

FIG. 7. (a) Common-offset field seismic section with some dipping background noise. (b) DEB filtered section of (a).

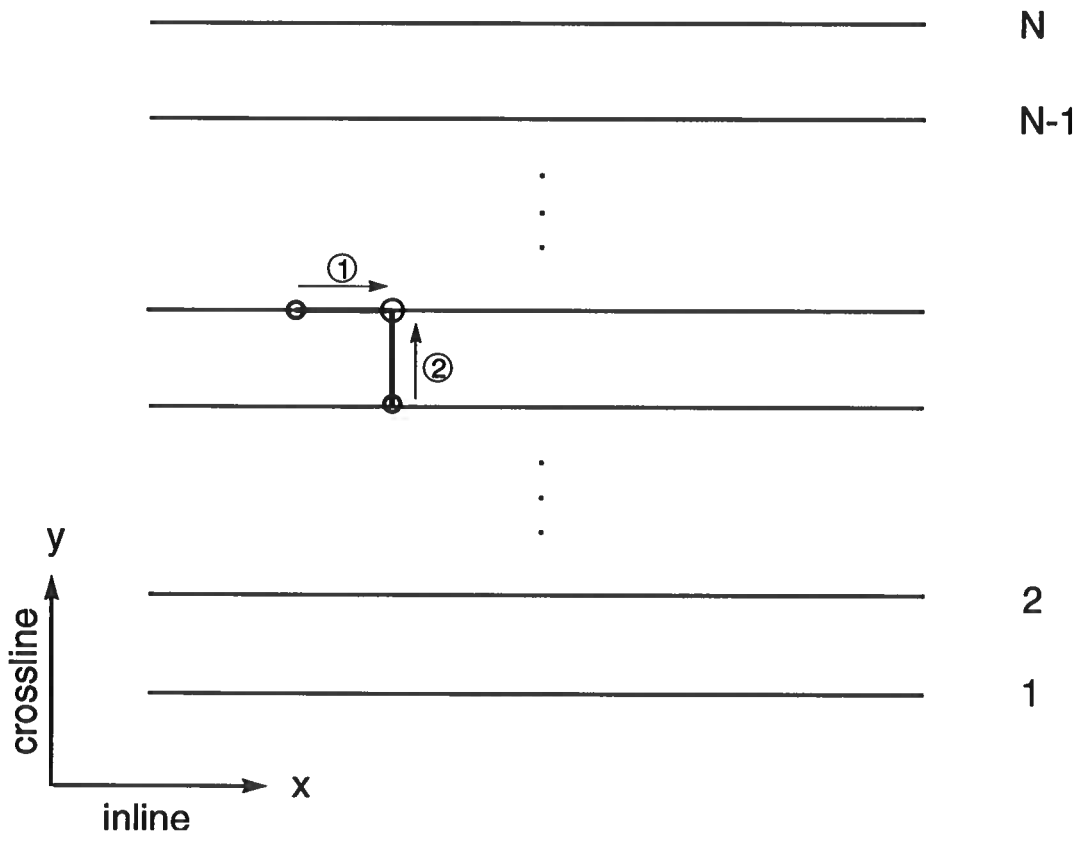

FIG. 8. Sketch plan view showing lines of data used in an implementation of the 3-D DEBF method.

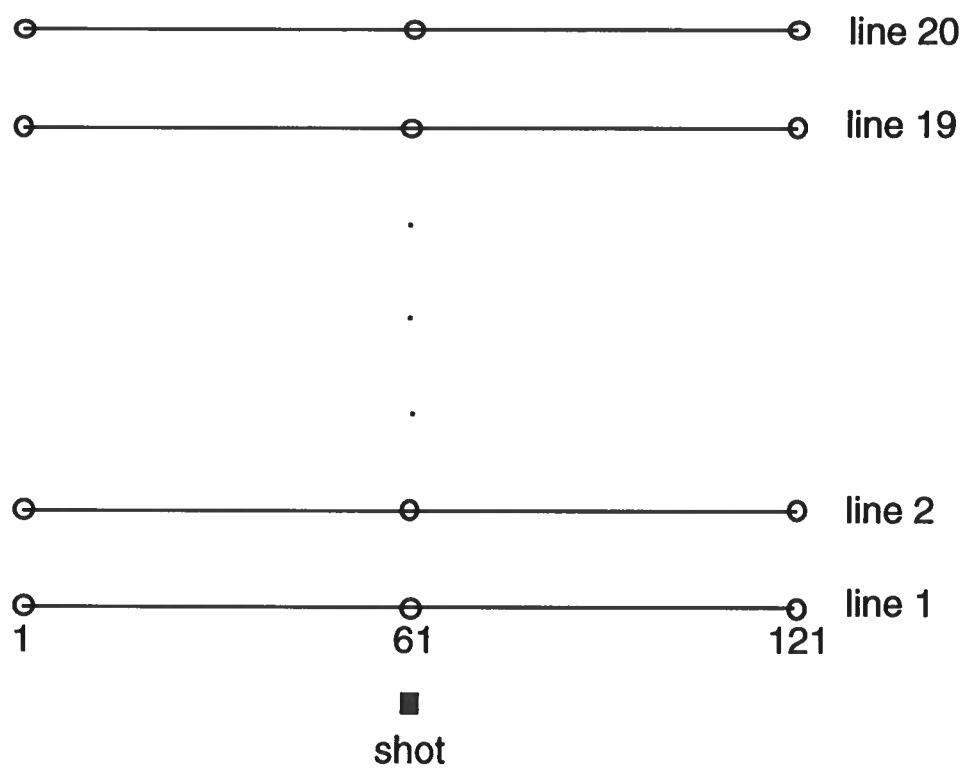

FIG. 9. Plan-view sketch map of a 3-D common-shot experiment.

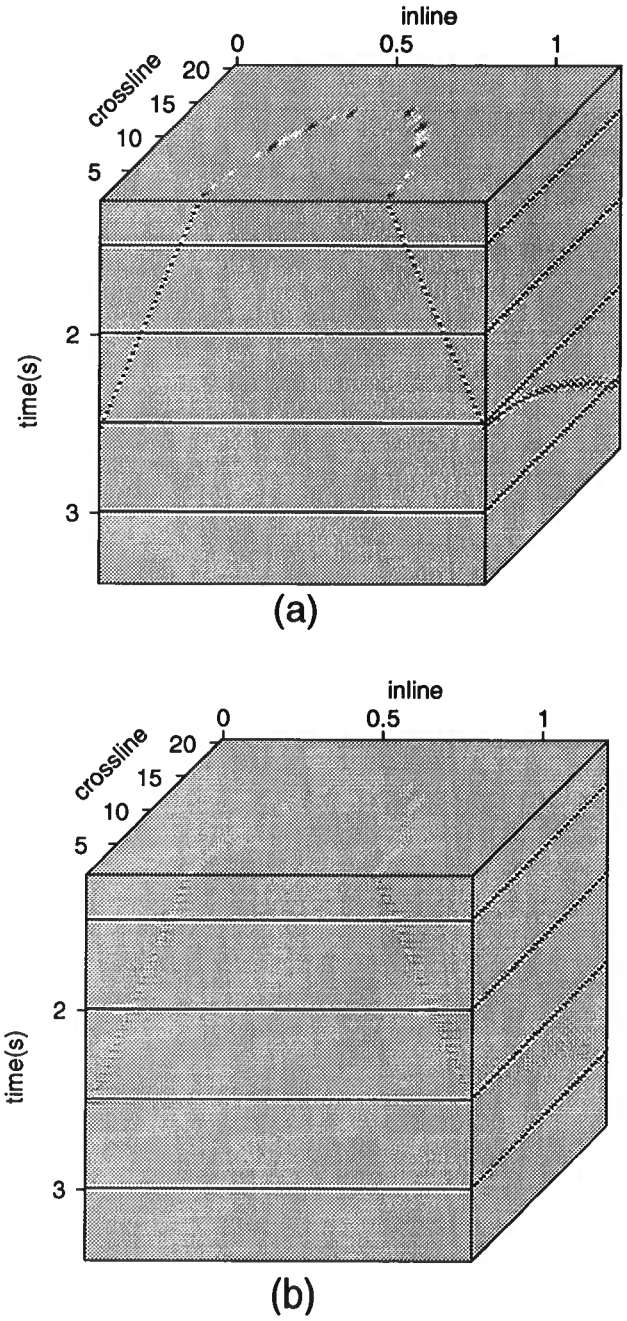

FIG. 10. (a) Part of a synthetic seismic data set. The dipping event simulates the direct wave in a 3-D case. (b) 3-D low-dip-pass filtered result of (a). The dipping event has been strongly suppressed.

Velocity Analysis by Residual Moveout

Zhenyue Liu and Norman Bleistein

Center for Wave Phenomena
Colorado School of Mines
Golden, Colorado 80401
(303) 273-3557

Velocity Analysis by Residual Moveout

Zhenyue Liu and Norman Bleistein

ABSTRACT

Velocity analysis by normal moveout encounters problems in handling dipping reflectors or lateral variation of velocity. Prestack migration provides a powerful tool to do velocity analysis, which is based on the following principle: the imaged depths at a common location are independent of source-receiver offset when the correct velocity is used. Conventional approaches, such as depth focusing analysis, generally involve iteration, which requires repeated prestack migration. In this paper, a residual moveout method for velocity analysis on multi-offset data is presented that needs only a single prestack migration. A number of theoretical problems in this method are studied. When the velocity has a lateral anomaly, we derive a formula to calculate the interval velocity from the stacking velocity by perturbation theory. A suggested data processing technique based on our method is composed of prestack migration with a constant velocity, velocity analysis, residual moveout, stacking, velocity conversion, and poststack residual migration.

INTRODUCTION

Normal moveout, typically used to do velocity analysis in seismic data processing, is robust when reflectors are flat and velocity is laterally invariant. However, this method encounters difficulty when reflectors are dipping or velocity varies laterally. Some geophysicists, therefore, have concentrated on doing velocity analysis by migration, such as the focusing analysis and common location imaging methods (Jeannot, 1986; Al-Yahya, 1989). When the background velocity is correct, the imaged depths at a common location are independent of source-receiver offset. Otherwise, if an incorrect background velocity is used, the imaged depths at a common location change with offset. In this situation, a residual moveout is observed in common-location images of migrated data. The principle of velocity analysis is to choose a background velocity so that the common-location images are close to a horizontal alignment.

Conventional methods use iteration to correct velocities. In each step of iteration, prestack migration is required. Consequently, the total computation is so huge that application of this method is limited.

It would be desirable to estimate velocity directly from the residual moveout. If this is successful, only one prestack migration is required. To make this estimate, we need a quantitative relationship between the residual moveout and the error in background velocity. Some geophysicists applied this idea to velocity analysis (Doherty, 1976; Deregowski, 1990). However, no general formula was derived.

In this paper, the residual moveout is used to do velocity analysis on multi-offset migrated data. By means of the reflector equation, we derived a general formula for the residual moveout. Theoretically, an arbitrary background velocity can be used to do velocity analysis. However, we prefer using a constant background velocity so that the residual moveout is an explicit function of the velocity error. Furthermore, we may use Stolt migration for constant velocity; this is much faster than other algorithms. Under the assumption of a small offset, we obtain an analytic expression for the residual moveout that is an explicit function of background velocity, curvature of unmigrated data, and slope of unmigrated data. Furthermore, this residual moveout is independent of the dip of the reflectors when the true velocity is a constant. Parallel to NMO velocity analysis, we can use a semblance and velocity scans to do RMO velocity analysis. Therefore, the program for RMO velocity analysis is similar to the existing program for NMO velocity analysis, except in the residual term.

After velocity analysis, we obtain the stacking velocity that is assumed to equal RMS velocity for a laterally invariant medium. However, when velocity has an anomaly, this assumption is invalid. Lynn and Claebout(1982) proposed a formula that gives a relationship between the anomaly of the stacking velocity and the anomaly of the interval velocity. But this formula requires a stratified medium. In this paper, we derive a formula that is valid for arbitrary velocity. This formula computes the anomaly of the interval velocity from the anomaly of the stacking velocity by an integral equation.

We have two ways to do migration: residual prestack migration or residual post stack migration. We prefer the latter because poststack migration runs much faster than prestack migration. The residual moveout, stacking, and residual poststack migration are recommended to obtain the final structural image.

REFLECTION EQUATION

Seismic signals consist of amplitude information and phase information. Under the high frequency assumption, phase information is simplified to traveltime information. Therefore, seismic signals can be described approximately by traveltime-offset curves. A traveltime-offset curve in seismic record corresponds to a specific reflector in the earth. Given a reflector, we can compute the traveltime-offset curve by modeling. On the other hand, given a traveltime-offset curve, we also can compute the reflector

position (subsurface) by migration. Now, we will show how the geometry of reflector is determined by the geometry of the traveltime-offset curve.

We shall denote by X a 2-D vector, $X = (x, z)$. Let x_s be source position and x_r be receiver position located on the horizontal datum surface L with y the midpoint and h the half-offset:

$$x_s = y - h, \qquad x_r = y + h.$$

For any point X below the surface, $\tau_s(x_s, X)$ and $\tau_r(X, x_r)$, respectively, denote traveltimes from x_s to X, and from X to x_r.

Suppose we know the total reflection travetime $T(y, h)$ and a background velocity $c(x, z)$. Then, for each half-offset h, the reflector is determined such that

$$\tau_s(x_s, X) + \tau_r(X, x_r) = T(y, h), \tag{1}$$

$$\frac{\partial \tau_s}{\partial y} + \frac{\partial \tau_r}{\partial y} = \frac{\partial T}{\partial y}, \tag{2}$$

where $X = (x, z)$ is the point on the reflector. Equations (1) and (2) show: if we know the traveltime-offset curve $T(y, h)$ (therefore, $\partial T/\partial y$) for some h, we can compute a imaged depth z for a fixed location x. If $c(x, z)$ equals the true velocity, then the imaged depth z is independent of offset h; otherwise, for wrong background velocity, z varies with offset h. Consequently, the imaged depth provides us information on velocity.

Equations (1) and (2) are for the common offset case. Similarly, we have the reflector equation

$$\tau_s(x_s, X) + \tau_r(X, x_r) = T(y, h), \tag{3}$$

$$\frac{\partial \tau_r}{\partial x_r} = \frac{\partial T}{\partial x_r}, \tag{4}$$

for the common shot case; the equation

$$\tau_s(x_s, X) + \tau_r(X, x_r) = T(y, h), \tag{5}$$

$$\frac{\partial \tau_s}{\partial x_s} = \frac{\partial T}{\partial x_s}, \tag{6}$$

for the common receiver case; the reflector equation

$$\tau_s(x_s, X) + \tau_r(X, x_r) = T(y, h), \tag{7}$$

$$\frac{\partial \tau_r}{\partial h} - \frac{\partial \tau_s}{\partial h} = \frac{\partial T}{\partial h}, \tag{8}$$

for the common midpoint case. Among these cases, only common offset has a symmetric imaged-depth function, which allows for the possibility of approximating the imaged-depth function by a hyperbola.

Specifically, when the background velocity is the constant, c, then

$$\tau_s(X, x_s) = \rho_s/c, \qquad \tau_r(X, x_r) = \rho_r/c,$$

where

$$\rho_s = \sqrt{(x_s - x)^2 + z^2}, \qquad \rho_r = \sqrt{(x_r - x)^2 + z^2}.$$

For this case, equations (1) and (2) are simplied to

$$\rho_s + \rho_r = cT(y, h), \tag{9}$$

$$\frac{\partial \rho_s}{\partial y} + \frac{\partial \rho_r}{\partial y} = c\frac{\partial T}{\partial y}. \tag{10}$$

Next, we will study the quantitative properies of $z(h)$ when $c(x, z)$ differs from the true velocity.

RESIDUAL MOVEOUT

When the background velocity $c(x, z)$ differs from the true velocity, there is a deviation between the imaged depths of different offsets; i.e., a residual moveout from a horizontal alignment is observed. We expect that this residual moveout can be used to measure the error of the velocity and be independent of the dip of a reflector.

Constant Velocity and Horizontal Reflector

Suppose that the true velocity and background velocity are constants and the reflector is horizontal. In this special situation,

$$T^2(y, h) = T^2(y, 0) + 4h^2/v^2,$$

$$\rho_s = \rho_r = \sqrt{(z^2 + h^2)} = \frac{c}{2}T(y, h),$$

so that

$$z^2(h) = \frac{c^2}{4}T^2(y, h) - h^2 = \frac{c^2}{4}T^2(y, 0) + (c^2/v^2 - 1)h^2 = z^2(0) + (c^2/v^2 - 1)h^2.$$

That is, the moveout is the hyperbola

$$z^2(h) = z^2(0) + (c^2/v^2 - 1)h^2. \tag{11}$$

Equation (11) shows that the residual moveout is the exact hyperbola for constant velocity v and horizontal reflector. This result is parallel to that of moveout in unmigrated data.

General Case

For general velocity or arbitrary reflector, one should not expect a simple expression such as (11). Instead of that, we consider the asymptotic expression under the assumption of small offset.

First, because z is a symmetric function of h, we get

$$\frac{dz}{dh}\mid_{h=0}= 0, \qquad \frac{d^3z}{dh^3}\mid_{h=0}= 0, \ etc.$$

This implies the Taylor series expansion

$$z^2(h) = z^2(0) + \frac{1}{2}\frac{d^2z^2}{dh^2}\mid_{h=0} h^2 + O(h^4). \tag{12}$$

Now let us try to estimate the second derivative,

$$\frac{d^2z^2}{dh^2}\mid_{h=0} .$$

For fixed x, the midpoint y and the imaged depth z are functions of offset h. differentiating equation (1) with respect to h, we have

$$\left[\frac{\partial\tau_s}{\partial y} + \frac{\partial\tau_r}{\partial y}\right]\frac{dy}{dh} + \left[\frac{\partial\tau_s}{\partial h} + \frac{\partial\tau_r}{\partial h}\right] + \left[\frac{\partial\tau_s}{\partial z} + \frac{\partial\tau_r}{\partial z}\right]\frac{dz}{dh} = \frac{\partial T}{\partial y}\frac{dy}{dh} + \frac{\partial T}{\partial h}. \tag{13}$$

Using (2), we get

$$\left[\frac{\partial\tau_s}{\partial z} + \frac{\partial\tau_r}{\partial z}\right]\frac{dz}{dh} = \frac{\partial T}{\partial h} - \left[\frac{\partial\tau_s}{\partial h} + \frac{\partial\tau_r}{\partial h}\right]. \tag{14}$$

Notice that y is symmetric in h, so

$$\frac{dy}{dh}\mid_{h=0}= 0.$$

Lemma. Suppose that $f(x, y, z)$ is a smooth enough function. For any function $y = y(x)$ and $z = z(x)$, if

$$\frac{dy}{dx}\mid_{x=0}= 0, \qquad \frac{dz}{dx}\mid_{x=0}= 0,$$

then

$$\frac{d}{dx}f(x, y(x), z(x))\mid_{x=0}= \frac{\partial f}{\partial x}\mid_{x=0} .$$

Proof. By the definition of the total differential,

$$\frac{df}{dx}\mid_{x=0}= \frac{\partial f}{\partial x}\mid_{x=0} + \left[\frac{\partial f}{\partial y}\frac{dy}{dx}\right]\mid_{x=0} + \left[\frac{\partial f}{\partial z}\frac{dz}{dx}\right]\mid_{x=0}= \frac{\partial f}{\partial x}\mid_{x=0} .$$

This completes the proof.

Using this lemma, and

$$\frac{dy}{dh}\mid_{h=0}= 0, \qquad \frac{dz}{dh}\mid_{h=0}= 0,$$

we get

$$\frac{d}{dh}\left(\frac{\partial T}{\partial h}-\left[\frac{\partial \tau_s}{\partial h}+\frac{\partial \tau_r}{\partial h}\right]\right)\mid_{h=0}=\frac{\partial^2 T}{\partial h^2}\mid_{h=0}-\left[\frac{\partial^2 \tau_s}{\partial h^2}+\frac{\partial^2 \tau_r}{\partial h^2}\right]\mid_{h=0}. \tag{15}$$

Also, from $\frac{dz}{dh}\mid_{h=0}=0$, we have

$$\frac{d}{dh}\left[(\frac{\partial \tau_s}{\partial z}+\frac{\partial \tau_r}{\partial z})\frac{dz}{dh}\right]\mid_{h=0}=\left[(\frac{\partial \tau_s}{\partial z}+\frac{\partial \tau_r}{\partial z})\frac{d^2z}{dh^2}\right]\mid_{h=0}. \tag{16}$$

Differentiating equation (14) with respect to h, and using (15) and (16), we set up the following equation for $d^2z/dh^2\mid_{h=0}$

$$\left[(\frac{\partial \tau_s}{\partial z}+\frac{\partial \tau_r}{\partial z})\frac{d^2z}{dh^2}\right]\mid_{h=0}=\frac{\partial^2 T}{\partial h^2}\mid_{h=0}-\left[\frac{\partial^2 \tau_s}{\partial h^2}+\frac{\partial^2 \tau_r}{\partial h^2}\right]\mid_{h=0}. \tag{17}$$

Equation (17) holds for any velocity function $v(x,z)$, any background velocity $c(x,z)$, and an arbitrary reflector. Now we will simplify equation (17) for the laterally invariant background velocity.

Suppose the background velocity is the constant, c. Then

$$\tau_s=\sqrt{z^2+(x-y+h)^2}/c, \qquad \tau_r=\sqrt{z^2+(x-y-h)^2}/c.$$

After calculation,

$$\frac{\partial \tau_s}{\partial z}\mid_{h=0}=\frac{\partial \tau_r}{\partial z}\mid_{h=0}=\frac{z}{c\rho},$$

$$\frac{\partial^2 \tau_s}{\partial h^2}\mid_{h=0}=\frac{\partial^2 \tau_r}{\partial h^2}\mid_{h=0}=\frac{z^2}{c\rho^{3/2}},$$

where

$$\rho=\sqrt{z^2+(x-y)^2}.$$

We have

$$\left[\frac{\partial \tau_s}{\partial z}+\frac{\partial \tau_r}{\partial z}\right]\mid_{h=0}=\frac{2z}{c\rho},$$

$$\left[\frac{\partial^2 \tau_s}{\partial h^2}+\frac{\partial^2 \tau_r}{\partial h^2}\right]\mid_{h=0}=\frac{2z^2}{c\rho^3}=\frac{2}{c\rho}-\frac{2(x-y)^2}{c\rho^3}.$$

Using these results, equation (17) is simplified by

$$[\frac{2z}{c\rho}\frac{d^2z}{dh^2}]\mid_{h=0}=\frac{\partial^2 T}{\partial h^2}\mid_{h=0}+\frac{2(x-y)^2}{c\rho^3}-\frac{2}{c\rho}. \tag{18}$$

Furthermore,

$$\left[2z\frac{d^2z}{dh^2}\right]\mid_{h=0}=\frac{d^2z^2}{dh^2}\mid_{h=0},$$

$$\rho = \frac{c}{2} T \mid_{h=0},$$

$$\frac{(y-x)}{\rho} = \frac{c}{2}\frac{\partial T}{\partial y} \mid_{h=0}.$$

Thus, we obtain the result

$$\frac{d^2 z^2}{dh^2} \mid_{h=0} = \frac{c^2}{2}\left[T\frac{\partial^2 T}{\partial h^2} + \left(\frac{\partial T}{\partial y}\right)^2\right] \mid_{h=0} -2, \tag{19}$$

or

$$\frac{d^2 \tau^2}{dh^2} \mid_{h=0} = 2\left[T\frac{\partial^2 T}{\partial h^2} + \left(\frac{\partial T}{\partial y}\right)^2\right] \mid_{h=0} -\frac{8}{c^2}, \tag{20}$$

where τ is the migration time.

From equation (19), we conclude that after migration, the the main part of the residual moveout is determined by the background velocity c, traveltime T, curvature of unmigrated data $\partial^2 T/\partial h^2$, and slope of unmigrated data $\partial T/\partial y$. This is true for a constant background velocity c, any velocity function $v(x,z)$, and arbitrary reflector. In addition, the stacking velocity is defined by

$$\frac{1}{[c_{stk}]^2} = \frac{1}{4}\left[T\frac{\partial^2 T}{\partial h^2} + \left(\frac{\partial T}{\partial y}\right)^2\right] \mid_{h=0}, \tag{21}$$

which can be directly estimated from the residual moveout. Compared to NMO, we have the new term, $\partial T/\partial y$. In the follow examples, one will see this term removes the dip effect in RMO velocity analysis.

For a small gradient velocity $c(z)$ or a small dip of the reflector, equation (20) can be modified to

$$\frac{d^2 \tau^2}{dh^2} \mid_{h=0} = 2\left[T\frac{\partial^2 T}{\partial h^2} + \left(\frac{\partial T}{\partial y}\right)^2\right] \mid_{h=0} -\frac{8}{[c_{rms}]^2}, \tag{22}$$

where c_{rms} is the root-means-squared velocity of $c(z)$.

Examples For Constant Background Velocity

We use constant background velocity for these examples. For arbitrary $c(x,z)$, the residual moveout formula will become too complex to do velocity analysis. Furthermore, prestack migration is fastest for constant velocity. In addition to the normal moveout formula (11), we now compute residual moveout by the formula (19) and (20) for several special cases. These results are similar to normal moveout, except that the former is insensitive to the dip of the reflector.

1. Constant velocity and dipping reflector

Suppose that the true velocity is a constant, v, and the reflector dip is θ. In this case,

$$T^2(y,h) = 4y^2\sin^2\theta/v^2 + 4h^2\cos^2\theta/v^2.$$

We have,

$$\left[T\frac{\partial^2 T}{\partial h^2}\right]|_{h=0} = 4\cos^2\theta/v^2,$$

$$\frac{\partial T}{\partial y}|_{h=0} = 2\sin\theta/v.$$

Therefore,

$$\frac{d^2z^2}{dh^2}|_{h=0} = 2(c^2/v^2 - 1). \tag{23}$$

$$z^2(h) = z^2(0) + (c^2/v^2 - 1)h^2 + O(h^4). \tag{24}$$

or

$$\tau^2(h) = \tau^2(0) + (1/v^2 - 1/c^2)4h^2 + O(h^4). \tag{25}$$

Equation (25) shows that the residual moveout is independent of the reflector dip and the stacking velocity is v, when the true velocity v is a constant.

2. Constant velocity and diffraction from a scattering point

Suppose that the true velocity is a constant, v, and a scatterer is located at the point (x^*, z^*). In this case,

$$T(y,h) = \left[\sqrt{(y-h-x^*)^2 + (z^*)^2} + \sqrt{(y+h-x^*)^2 + (z^*)^2}\right]/v$$

We have,

$$\left[T\frac{\partial^2 T}{\partial h^2}\right]|_{h=0} = \frac{4}{v^2}\frac{(z^*)^2}{(y-x^*)^2 + (z^*)^2},$$

$$\left(\frac{\partial T}{\partial y}\right)^2|_{h=0} = \frac{4}{v^2}\frac{(y-x^*)^2}{(y-x^*)^2 + (z^*)^2}.$$

Therefore,

$$\frac{d^2z^2}{dh^2}|_{h=0} = 2(c^2/v^2 - 1). \tag{26}$$

$$z^2(h) = z^2(0) + (c^2/v^2 - 1)h^2 + O(h^4). \tag{27}$$

or

$$\tau^2(h) = \tau^2(0) + (1/v^2 - 1/c^2)4h^2 + O(h^4). \tag{28}$$

Again, equation (28) shows that the residual moveout is independent of the lateral offset from the point scatterer and the stacking velocity is v, when the true velocity v is a constant.

3. Laterally invariant velocity and horizontal reflector

Suppose that the true velocity is a laterally invariant function, $v(z)$, and the reflector is horizontal, with depth z^*. In this case,

$$T^2(y,h) = T^2(y,0) + 4h^2/[v_{rms}(z^*)]^2 + O(h^4).$$

We have,

$$\left[T\frac{\partial^2 T}{\partial h^2}\right]|_{h=0} = 4/[v_{rms}(z^*)]^2,$$

$$\frac{\partial T}{\partial y}|_{h=0} = 0.$$

Therefore,

$$\frac{d^2 z^2}{dh^2}|_{h=0} = 2\left(\frac{c^2}{[v_{rms}(z^*)]^2} - 1\right). \tag{29}$$

$$z^2(h) = z^2(0) + \left(\frac{c^2}{[v_{rms}(z^*)]^2} - 1\right)h^2 + O(h^4). \tag{30}$$

Notice that $z(0) \neq z^*$. That is, in depth migration, the imaged depth is inconsistent with the desired point at which the root-mean-square (RMS) velocity is determined from the residual moveout. However, if we let

$$\tau^* = 2\int_0^{z^*} \frac{ds}{v(s)},$$

then

$$\tau^2(h) = \tau^2(0) + \left(\frac{1}{[v_{rms}(\tau^*)]^2} - \frac{1}{c^2}\right)4h^2 + O(h^4), \tag{31}$$

and $\tau(0) = \tau^*$. Therefore, time migration can give us the correct location at which the RMS velocity is determined by the residual moveout.

Equation (31) shows that when the true velocity is laterally invariant, the stacking velocity determined from RMO is consistent with RMS velocity at the imaged time.

4. Laterally invariant velocity and dipping reflector

Suppose that the true velocity is a laterally invariant function, $v(\tau)$, and the reflector is a dip, with angle θ. In this case,

$$T(y,0) = \int_0^{\tau^*} \left(1 - p^2 v^2(\sigma)\right)^{-1/2} d\sigma,$$

$$\frac{\partial^2 T}{\partial h^2}|_{h=0} = \frac{4}{\int_0^{\tau^*} v^2(1-p^2v^2)^{-3/2}d\sigma},$$

$$\frac{\partial T}{\partial y}|_{h=0} = 2p,$$

where τ^* is the vertical time at the reflection point and

$$p = \frac{\sin\theta}{v(\tau^*)}.$$

Therefore,

$$\left[T\frac{\partial^2 T}{\partial h^2} + \left(\frac{\partial T}{\partial y}\right)^2\right] |_{h=0} = 4\,\frac{\int_0^{\tau^*}(1-p^2v^2)^{-3/2}d\sigma}{\int_0^{\tau^*} v^2(1-p^2v^2)^{-3/2}d\sigma}. \tag{32}$$

The stacking velocity is estimated by

$$[c_{stk}]^2 = \frac{\int_0^{\tau^*} v^2(\sigma)(1-p^2v^2(\sigma))^{-3/2}d\sigma}{\int_0^{\tau^*}(1-p^2v^2(\sigma))^{-3/2}d\sigma}. \tag{33}$$

Notice that c_{stk} does not equal the RMS velocity v_2 that is defined by

$$v_2^2 = \frac{1}{\tau^*}\int_0^{\tau^*} v^2(\sigma)d\sigma. \tag{34}$$

In fact,

$$[c_{stk}]^2 = v_2^2 + \frac{3}{2}(v_4^4 - v_2^4)p^2 + O(p^4), \tag{35}$$

where

$$v_4^4 = \frac{1}{\tau^*}\int_0^{\tau^*} v^4(s)ds.$$

v_4 is always greater than v_2 and they are equal only if $v(z)$ is a constant. Therefore, c_{stk} is always greater than v_2 and they are close for small p or a small gradient of $v(z)$. Furthermore, the imaged time, $\tau(0)$, is different from τ^*, and

$$[v_2(\tau(0))]^2 = v_2^2(\tau^*) + \frac{1}{2}(v_2^2(\tau^*) - c^2)(v^2(\tau^*) - v_2^2(\tau^*))p^2 + O(p^4). \tag{36}$$

Usually, v is bigger than v_2, so $v_2(\tau(0))$ is bigger than $v_2(\tau^*)$ when c is smaller than $v_2(\tau^*)$. If c is chosen suitably small, c_{stk} may be a good approximation to $v_2(\tau(0))$.

we conclude that for a suitable background velocity, the stacking velocity from RMO velocity analysis may approximate the RMS velocity at the imaged time.

Higher Residual Terms

The residual moveout is hyperbola-like only for small offset. In fact, offsets should not be too small so that we can have a high resolution in velocity analysis. (See Liu and Bleistein.) Therefore, we require an error estimate for formulas in nonzero offset. This work is partially implemented in Mathematica.

Using the rule of differential for a compound function in equation (14) and setting c constant, the fourth order derivative of z with respect to h satisfies

$$\frac{d^4 z}{dh^4}|_{h=0}\left[\frac{\partial(\rho_s+\rho_r)}{\partial z}\right]|_{h=0} = c\left[\frac{\partial^4 T}{\partial h^4} + 3\,\frac{d^2y}{dh^2}\frac{\partial^3 T}{\partial h^2\partial y}\right]|_{h=0} - \frac{\partial^4(\rho_s+\rho_r)}{\partial h^4}|_{h=0}$$
$$-6\left[\frac{d^2z}{dh^2}\frac{\partial^3(\rho_s+\rho_r)}{\partial h^2\partial z}\right]|_{h=0} - 3\left[\frac{d^2y}{dh^2}\frac{\partial^3(\rho_s+\rho_r)}{\partial h^2\partial y}\right]|_{h=0}. \tag{37}$$

For a constant velocity v and a dipping reflector with angle θ, we can obtain

$$\frac{d^4\tau^2}{dh^4}\,|_{h=0}= -\frac{24(1/v^2-1/c^2)\sin^2 2\theta}{(z^*)^2}, \tag{38}$$

where τ is the migration time and z^* is the reflection depth. Therefore, from (38) and (23), a more accurate expression for the residual moveout is

$$\begin{aligned}\tau^2(h) &= \tau^2(0)+4\left(\frac{1}{v^2}-\frac{1}{c^2}\right)h^2-\frac{(1/v^2-1/c^2)\sin^2 2\theta}{(z^*)^2}h^4+O(h^6)\\ &= \tau^2(0)+4\left(\frac{1}{v^2}-\frac{1}{c^2}\right)h^2\left(1-\frac{1}{4}(\frac{h}{z^*})^2\sin^2 2\theta\right)+O(h^6).\end{aligned} \tag{39}$$

For a constant velocity v and a scattering point at (x^*, z^*),

$$\frac{d^4\tau^2}{dh^4}\,|_{h=0}= -\frac{24(1/v^2-1/c^2)\sin^2 2\theta}{(z^*)^2}, \tag{40}$$

where

$$\theta = \arctan\frac{y-x^*}{z^*}.$$

By the way, for the unmigrated data, the higher residual term is

$$\frac{\partial^4 T^2}{\partial h^4}\,|_{h=0}= \frac{24\sin^2 2\theta\cos^2\theta}{v^2(z^*)^2}. \tag{41}$$

Equations (38) and (40) show that when the true velocity is a constant, small higher-residual terms of moveout are obtained for a closed background velocity, small ratio of offset to the imaged depth, and the dipping angle that is near 0 or 90 degree.

For laterally invariant velocity and a horizontal reflector with depth z^*,

$$\frac{d^4\tau^2}{dh^4}\,|_{h=0}= \frac{24(v_2^4-v_4^4)}{t_0^2 v_2^8}, \tag{42}$$

where t_0 is the zero-offset time, and

$$v_2^2 = \frac{1}{t_0}\int_0^{t_0} v^2(s)ds,$$

$$v_4^4 = \frac{1}{t_0}\int_0^{t_0} v^4(s)ds.$$

The result in (42) is the same as in the unmigrated data.

Equation (42) shows that when the true velocity is laterally invariant, a small higher-residual term is obtained for small gradient of the velocity.

VELOCITY CONVERSION

In the previous chapter, we show how stacking velocity is obtained by moveout methods. However, an interval velocity function is required for migration and inversion. Usually, we assume that the stacking velocity equals the RMS velocity. Then the interval velocity is computed by Dix equation or other algorithms. Unfortunately, this assumption fails when the velocity has a lateral anomaly. Now we will give an equation to solve for the laterally varying interval velocity. This equation requires the small lateral variation and horizontal reflector.

Suppose the true slowness $w(x,z)$ can be written as

$$w(x,z) = \bar{w}(z)(1+\alpha(x,z)), \tag{43}$$

where $\bar{w}(z)$ is a reference slowness and $\alpha(x,z)$ is a small perturbation. We obtain the equation

$$\delta w_s(y,z) = \frac{1}{\bar{T}_0 \bar{v}_s(z)} \int_0^z \left[\frac{\partial^2 \alpha}{\partial x^2} \left(\frac{\int_\sigma^z \bar{v} ds}{\bar{v}_s(z)} \right)^2 + \alpha \left(1 + \frac{\bar{v}^2(\sigma)}{\bar{v}_s^2(z)}\right) \right] \frac{d\sigma}{\bar{v}} \tag{44}$$

where δw_s is the anomaly of the stacking slowness, $\bar{T}_0$ is the zero offset time, and $\bar{v}_s$ is the RMS velocity from the referenced velocity. When α and $\bar{w}$ are depth independent, the result in equation (44) is the same as that of Lynn and Claerbout. Equation (44) shows that the second derivative of α determines the anomaly of the stacking velocity; the anomaly of the stacking velocity at a depth results from the anomaly of the interval velocity above this depth. Furthermore, $\int_\sigma^z \bar{v} ds$ increases as σ decreases, so the anomaly of the interval velocity near the surface has the largest effect.

Applying Fourier transform, with respect to y, to equation (44), we obtain

$$\delta w_s(k_x,z) = \frac{1}{\bar{T}\bar{v}_s(z)} \int_0^z \alpha(k_x,\sigma) \left[-k_x^2 \left(\frac{\int_\sigma^z \bar{v} ds}{\bar{v}_s(z)} \right)^2 + \left(1 + \frac{\bar{v}^2(\sigma)}{\bar{v}_s^2(z)}\right) \right] \frac{d\sigma}{\bar{v}}. \tag{45}$$

Equation (45) is a First-kind Volterra integral equation that is ill-posed. Therefore, the recursive alogrithm for equation (45) is unstable. To obtain a stable solution, we may apply the damping least-squared method to equation (45).

SYNTHETIC DATA EXAMPLE

To test the residual moveout method, we applied this method to synthetic seismograms computed for a subsurface model in which velocity increases linearly with depth z, according to $v(z) = 1.5 + 0.8z$ km/s. The model, shown in Figure 1, consists of five reflectors, each with a dipping and horizontal segment. Dips for the dipping segments range from 30 to 90 degrees in 15-degree increments. The seismograms contain 10 offsets, ranging from 100 m to 1900 m in 200 m increments. Because of dipping reflectors and depth dependent velocity, the stacking velocity in equation (33)

and the RMS velocity are not same but close each other. The error between the both, shown in Figure 2, increses with depth and dip.

After prestack migration with the constant velocity, $c = 1.5$ km/s, one of the CDP gathers is plotted in Figure 3. Because the background velocity is lower than the true velocity, all event locations increase with offset. The velocity scan for this CDP is plotted in Figure 4. Unlike the velocity scans in NMO, velocity peaks here are single-valued. After residual moveout, all events are corrected to horizontal ones (in Figure 5). The stacking result is shown in Figure 6, which is equivalent to the poststack migration with the constant velocity, c. By using the interval velocity converted from the stacking velocity, poststack residual migration gives the correct reflector positions (in Figure 7).

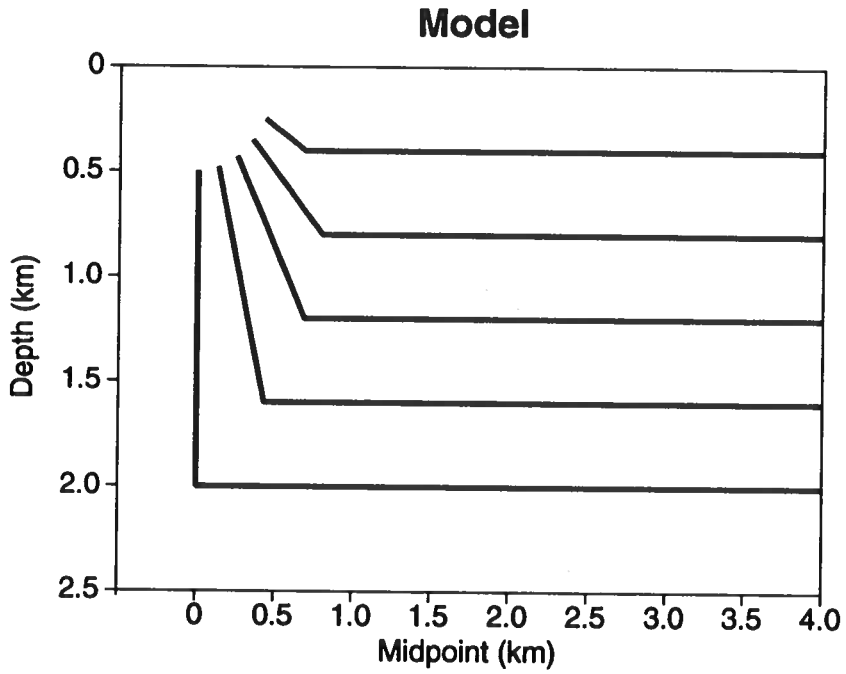

FIG. 1. Subsurface model used to generate synthetic seismic traces.

CONCLUSION

Velocity analysis by prestack migration can handle dipping reflectors. Conventional approaches use iteration, which results in larger computation than the method proposed in this paper. Using the relationship between the residual moveout and the error in the background velocity, we can estimate directly the true velocity without iteration. Furthermore, stacking after the residual moveout provides a partial migration output. With this output, a residual post migration should yield a more accurate structural image. Using a more general background velocity, we may handle

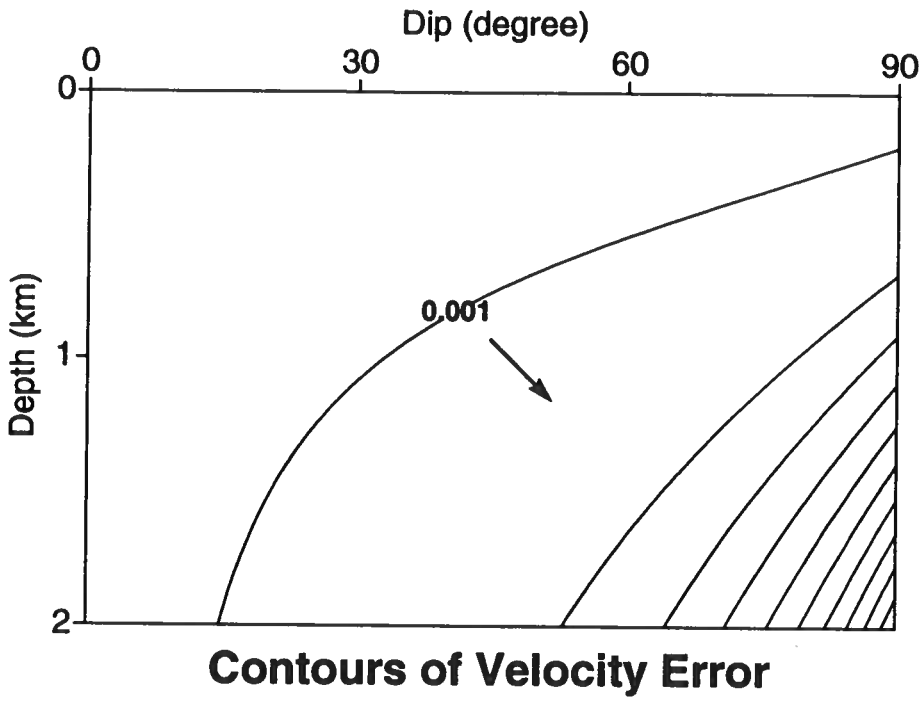

FIG. 2. The relative error between the stacking velocity and RMS velocity. The difference of contours is 0.002. The arrow direction indicates increase of the error.

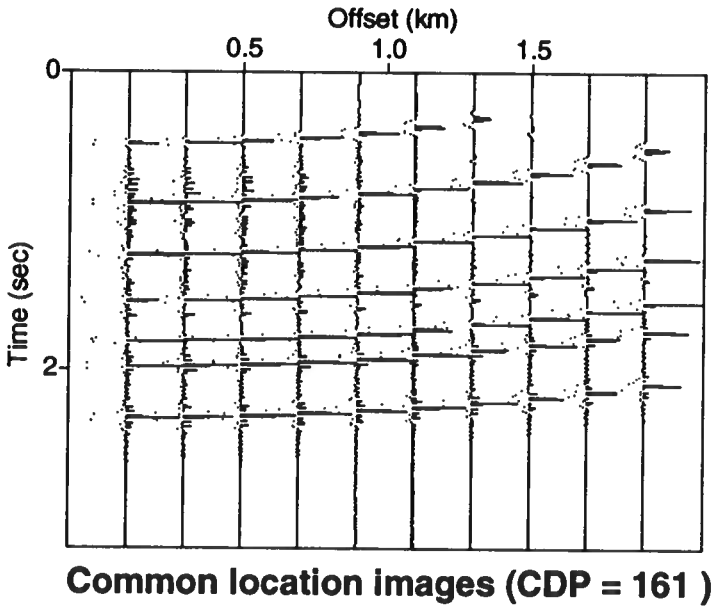

FIG. 3. One of the CDP gathers after the migration with the constant velocity.

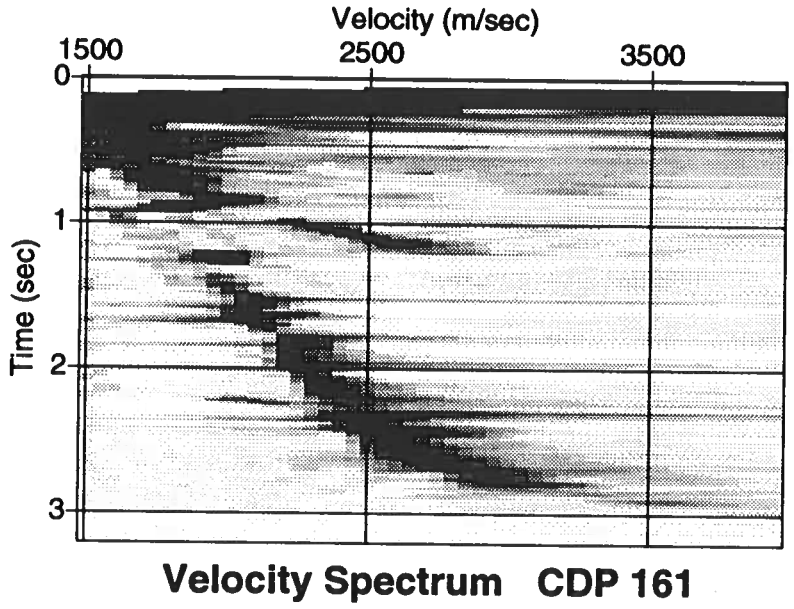

FIG. 4. Velocity analysis for the CDP gather in Fig. 2.

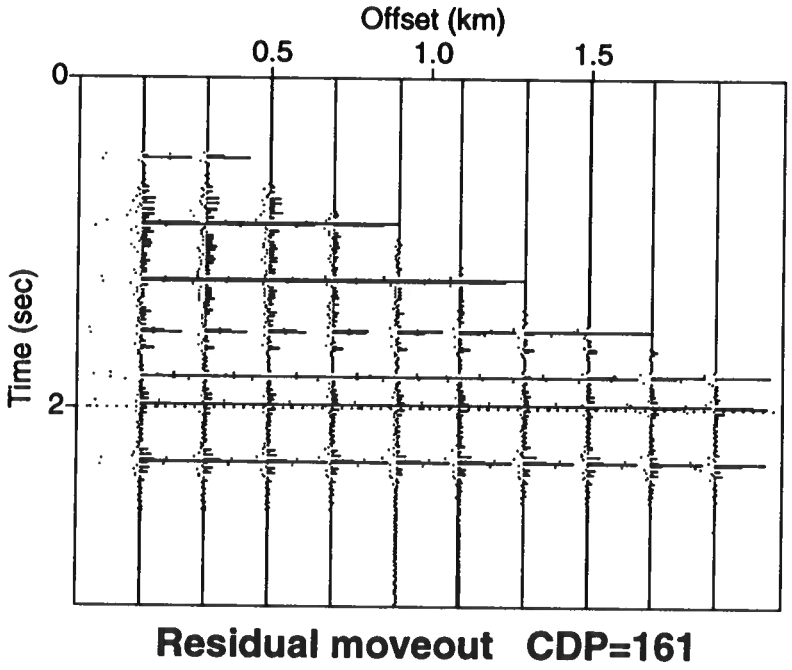

FIG. 5. Residual moveout for the CDP gather in Fig. 2.

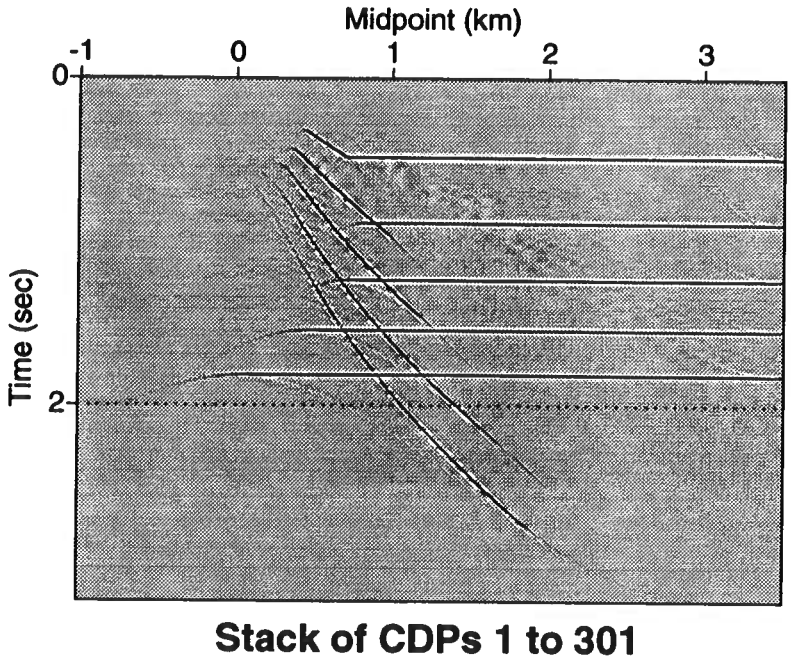

FIG. 6. Stacking for the ten offsets.

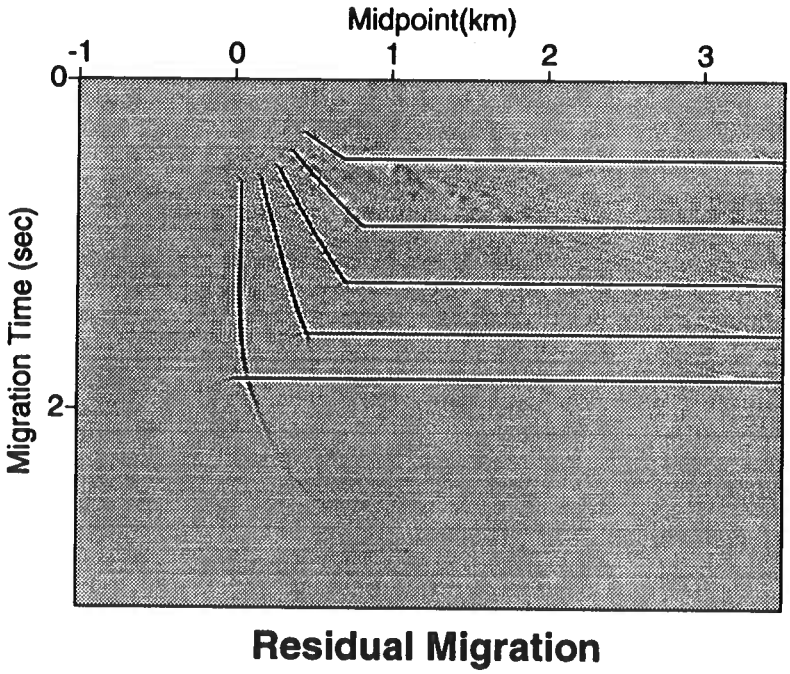

FIG. 7. Poststack residual time migration.

the lateral variation of velocity, but it will require a complicated algorithm. The perturbation method here is suggested to handle the lateral variation of velocity.

ACKNOWLEDGEMENTS

The authors gratefully acknowledge the support of the Office of Naval Research, Mathematics Division, and members of the Consortium Projection on Seismic Inverse Methods for Complex Structures at the Center for Wave Phenomena, Colorado School of Mines.

REFERENCES

Al-Yahya, K., 1989, Velocity analysis by iterative profile migration: Geophysics, **54**, 718-729.

Deregowski, S. M., 1990, Common-offset migrations and velocity analysis: First break, **8**, 6, 225-234.

Dothrty, S., and Claertbout, J., 1976, Structure independent velocity estimation: Geophysics, **41**, 850-881.

Jeannot, J. P., Faye, J. P., and Dennelle, E., 1986, Prestack migration velocities from depth-focusing analysis: 56th Ann. Internat. Mtg., Soc. Expl. Geophys., Expanded Abtracts, 438-440.

Liu, Z. and Bleistein, N., 1991, Velocity analysis by inversion: Project Review In CWP Consortium Meeting.

Lynn, W. S. and Claerbout, J. F., 1982, Velocity estimation in laterally varying media: Geophysics, **47**, 884-897.

APPENDIX A: DERIVATION OF EQUATIONS (35) AND (36)

From Taylor's expansion,

$$(1-p^2v^2(\sigma))^{-3/2} = 1+\frac{3}{2}v^2(\sigma)p^2+O(p^4),$$

so that

$$\int_0^{\tau^*} v^2(\sigma)(1-p^2v^2(\sigma))^{-3/2}d\sigma = \int_0^{\tau^*} v^2(\sigma)d\sigma+\frac{3}{2}p^2\int_0^{\tau^*} v^4(\sigma)d\sigma = \tau^*(v_2^2+\frac{3}{2}v_4^4p^2),$$

$$\int_0^{\tau^*}(1-p^2v^2(\sigma))^{-3/2}d\sigma = \tau^*(1+\frac{3}{2}v_2^2p^2).$$

Using these results and the definition in (33), we obtain

$$[c_{stk}]^2 = \frac{\tau^*(v_2^2+3/2\ v_4^4p^2)}{\tau^*(1+3/2\ v_2^2p^2)} = v_2^2+\frac{3}{2}(v_4^4-v_2^4)p^2+O(p^4). \qquad \text{(A-1)}$$

This completes the proof of equation (35).

From the Taylor's expansion,

$$\begin{aligned} v_2^2(\tau) &= v_2^2(\tau^*)+(\tau-\tau^*)\frac{dv_2^2}{d\tau}\mid_{\tau=\tau^*}+O((\tau-\tau^*)^2) \\ &= v_2^2(\tau^*)+(\tau/\tau^*-1)(v^2(\tau^*)-v_2(\tau^*))+O((\tau-\tau^*)^2), \end{aligned} \qquad \text{(A-2)}$$

where we use the fact that

$$\frac{dv_2^2}{d\tau}\mid_{\tau=\tau^*} = (v^2(\tau^*)-v_2^2(\tau^*))/\tau^*.$$

From

$$\tau(0) = T(y,0)\sqrt{1-c^2p^2} = T(y,0)(1-\frac{1}{2}c^2p^2)+O(p^4),$$

and

$$T(y,0) = \int_0^{\tau^*}(1-p^2v^2(\sigma))^{-1/2}d\sigma = \tau^*(1+\frac{1}{2}v_2^2p^2)+O(p^4),$$

we have

$$\tau(0) = \tau^*(1+\frac{1}{2}(v_2^2(\tau^*)-c^2)p^2)+O(p^4).$$

Subsitituting the above formula into equation (A-2) and setting $\tau = \tau(0)$, we obtain

$$v_2^2(\tau(0)) = v_2^2(\tau^*)+\frac{1}{2}(v_2^2(\tau^*)-c^2)(v^2(\tau^*)-v_2^2(\tau^*))p^2+O(p^4). \qquad \text{(A-3)}$$

This completes the proof of equation (36).

APPENDIX B: DERIVATION OF EQUATION (44)

Suppose reflectors are horizontal and the true velocity $v(x,z)$ can be written by

$$\frac{1}{v(x,z)} = \frac{1}{\bar{v}(z)}(1+\alpha(x,z)), \tag{A-4}$$

where $\bar{v}(z)$ is a reference velocity and $\alpha(x,z)$ is a small perturbation. Under the assumption of the small perturbation, we can calculate the two-way traveltime by

$$T(h,y) = \bar{T}(h,y) + 2\int_0^z \frac{\alpha(\xi(\sigma),\sigma)}{\bar{v}(\sigma)\cos\theta} d\sigma \tag{A-5}$$

where θ is the angle of the ray path from the vertical, (ξ,σ) is a point on the ray path, and

$$\xi(\sigma) = y + \int_\sigma^z \tan\theta ds. \tag{A-6}$$

Therefore,

$$\frac{\partial^2 T(h,y)}{\partial h^2}\,|_{h=0} = \frac{\partial^2 \bar{T}(h,y)}{\partial h^2}\,|_{h=0} + 2\int_0^z \frac{\partial^2}{\partial h^2}\left(\frac{\alpha(\xi,\sigma)}{\cos\theta}\right)|_{h=0}\,\frac{d\sigma}{\bar{v}}. \tag{A-7}$$

From

$$\frac{\partial^2}{\partial h^2}\left(\frac{\alpha(\xi,\sigma)}{\cos\theta}\right) = \frac{\partial^2\alpha}{\partial h^2}\frac{1}{\cos\theta} + 2\frac{\partial\alpha}{\partial h}\frac{\partial}{\partial h}\left(\frac{1}{\cos\theta}\right) + \alpha(\xi,\sigma)\frac{\partial^2}{\partial h^2}\left(\frac{1}{\cos\theta}\right), \tag{A-8}$$

and

$$\frac{\partial}{\partial h}\left(\frac{1}{\cos\theta}\right)|_{h=0} = 0,$$
$$\cos\theta\,|_{h=0} = 1,$$

we have

$$\frac{\partial^2}{\partial h^2}\left(\frac{\alpha(\xi,\sigma)}{\cos\theta}\right)|_{h=0} = \frac{\partial^2\alpha}{\partial h^2}\,|_{h=0} + \alpha(y,\sigma)\frac{\partial^2}{\partial h^2}\left(\frac{1}{\cos\theta}\right)|_{h=0}. \tag{A-9}$$

Notice that ξ is a function of h, so that

$$\frac{\partial^2\alpha}{\partial h^2} = \frac{\partial^2\alpha}{\partial\xi^2}\left(\frac{\partial\xi}{\partial h}\right)^2 + \frac{\partial\alpha}{\partial\xi}\frac{\partial^2\xi}{\partial h^2}. \tag{A-10}$$

From (A-6), $\xi - y$ is an odd function of h; hence

$$\frac{\partial^2\xi}{\partial h^2}\,|_{h=0} = \frac{\partial^2(\xi-y)}{\partial h^2}\,|_{h=0} = 0.$$

This result and formula (A-10) give

$$\frac{\partial^2\alpha}{\partial h^2}\,|_{h=0} = \frac{\partial^2\alpha}{\partial y^2}\left(\frac{\partial\xi}{\partial h}\right)^2|_{h=0}. \tag{A-11}$$

Here we use the fact that $\xi = y$ at $h = 0$. To do the further calculation, we introduce the slope parameter

$$p = \frac{\sin\theta}{\bar{v}(\sigma)},$$

which is independent of σ. Then

$$\xi(\sigma) = y + \int_\sigma^z \frac{\bar{v}p}{\sqrt{1-(\bar{v}p)^2}} ds,$$

$$h = \int_0^z \frac{\bar{v}p}{\sqrt{1-(\bar{v}p)^2}} ds.$$

These formulas imply that

$$\frac{\partial \xi}{\partial p} = \int_\sigma^z \frac{\bar{v}}{(1-(\bar{v}p)^2)^{3/2}} ds,$$

$$\frac{dh}{dp} = \int_0^z \frac{\bar{v}}{(1-(\bar{v}p)^2)^{3/2}} ds. \tag{A-12}$$

$$\frac{\partial \xi}{\partial h}\,|_{h=0} = \frac{\partial \xi}{\partial p}\,|_{h=0} \,/\, \frac{dh}{dp}\,|_{h=0} = \frac{\int_\sigma^z \bar{v} ds}{\int_0^z \bar{v} ds}. \tag{A-13}$$

From

$$\frac{1}{\cos\theta} = \frac{1}{\sqrt{1-(\bar{v}p)^2}},$$

we have

$$\frac{\partial^2}{\partial h^2}\left(\frac{1}{\cos\theta}\right) = \frac{\partial^2}{\partial h^2}\left(\frac{1}{\sqrt{1-(\bar{v}p)^2}}\right)$$

$$= \frac{\partial^2}{\partial p^2}\left(\frac{1}{\sqrt{1-(\bar{v}p)^2}}\right)\left(\frac{\partial p}{\partial h}\right)^2 + \frac{\partial}{\partial p}\left(\frac{1}{\sqrt{1-(\bar{v}p)^2}}\right)\frac{\partial^2 p}{\partial h^2}. \tag{A-14}$$

Again, p is an odd function of h, so that

$$\frac{\partial^2 p}{\partial h^2}\,|_{h=0} = 0.$$

This result, formulas (A-12), and (A-14) give

$$\frac{\partial^2}{\partial h^2}\left(\frac{1}{\cos\theta}\right)|_{h=0} = \frac{\partial^2}{\partial p^2}\left(\frac{1}{\sqrt{1-(\bar{v}p)^2}}\right)|_{h=0}\frac{1}{(\int_0^z \bar{v} ds)^2} = \frac{\bar{v}^2(\sigma)}{(\int_0^z \bar{v} ds)^2}. \tag{A-15}$$

By formulas (A-9), (A-11), (A-13) and (A-15), we obtain

$$\frac{\partial^2}{\partial h^2}\left(\frac{\alpha(\xi,\sigma)}{\cos\theta}\right)|_{h=0} = \frac{\partial^2 \alpha}{\partial y^2}\left(\frac{\int_\sigma^z \bar{v} ds}{\int_0^z \bar{v} ds}\right)^2 + \alpha(y,\sigma)\frac{\bar{v}^2(\sigma)}{(\int_0^z \bar{v} ds)^2}. \tag{A-16}$$

Substituting this formula into equation (A-7), we have

$$\frac{\partial^2 T(h,y)}{\partial h^2}\mid_{h=0}=\frac{\partial^2 \bar{T}(h,y)}{\partial h^2}\mid_{h=0}+2\int_0^z\left[\frac{\partial^2\alpha}{\partial y^2}\left(\frac{\int_\sigma^z \bar{v}ds}{\int_0^z \bar{v}ds}\right)^2+\frac{\alpha\bar{v}^2(\sigma)}{(\int_0^z \bar{v}ds)^2}\right]\frac{d\sigma}{\bar{v}}. \quad \text{(A-17)}$$

The stacking velocity v_s is defined by

$$\frac{1}{v_s^2(y,z)}=\frac{1}{4}\left[T(y,h)\frac{\partial^2 T(h,y)}{\partial h^2}\right]\mid_{h=0}. \quad \text{(A-18)}$$

By using formula (A-5) and (A-17), we have

$$\left[T\frac{\partial^2 T}{\partial h^2}\right]\mid_{h=0}=\left[\bar{T}\frac{\partial^2 \bar{T}}{\partial h^2}\right]\mid_{h=0}+2\frac{\partial^2 \bar{T}}{\partial h^2}\mid_{h=0}\int_0^z\alpha(y,\sigma)\frac{d\sigma}{\bar{v}}+$$
$$2\bar{T}(0,y)\int_0^z\left[\frac{\partial^2\alpha}{\partial y^2}\left(\frac{\int_\sigma^z \bar{v}ds}{\int_0^z \bar{v}ds}\right)^2+\frac{\alpha\bar{v}^2(\sigma)}{(\int_0^z \bar{v}ds)^2}\right]\frac{d\sigma}{\bar{v}}. \quad \text{(A-19)}$$

From

$$\left[\bar{T}\frac{\partial^2 \bar{T}}{\partial h^2}\right]\mid_{h=0}=\frac{4}{\bar{v}_s^2(z)},$$

(A-19) becomes

$$\frac{4}{v_s^2(y,z)}-\frac{4}{\bar{v}_s^2(z)}=\frac{8}{\bar{T}\bar{v}_s^2}\int_0^z\frac{\alpha d\sigma}{\bar{v}}+2\bar{T}\int_0^z\left[\frac{\partial^2\alpha}{\partial y^2}\left(\frac{\int_\sigma^z \bar{v}ds}{\int_0^z \bar{v}ds}\right)^2+\frac{\alpha\bar{v}^2(\sigma)}{(\int_0^z \bar{v}ds)^2}\right]\frac{d\sigma}{\bar{v}},$$

or

$$\delta w_s(y,z)=\frac{1}{\bar{T}\bar{v}_s}\int_0^z\frac{\alpha d\sigma}{\bar{v}}+\frac{\bar{T}\bar{v}_s}{4}\int_0^z\left[\frac{\partial^2\alpha}{\partial y^2}\left(\frac{\int_\sigma^z \bar{v}ds}{\int_0^z \bar{v}ds}\right)^2+\frac{\alpha\bar{v}^2(\sigma)}{(\int_0^z \bar{v}ds)^2}\right]\frac{d\sigma}{\bar{v}} \quad \text{(A-20)}$$

where we use the relation

$$\delta w_s(y,z)=\frac{1}{v_s(y,z)}-\frac{1}{\bar{v}_s(z)}=\frac{\bar{v}_s(z)}{2}\left(\frac{1}{v_s^2(y,z)}-\frac{1}{\bar{v}_s^2(z)}\right).$$

From

$$\int_0^z \bar{v}ds=\frac{\bar{T}}{2}\bar{v}_s^2(\tau),$$

equation (A-20) becomes

$$\delta w_s(y,z)=\frac{1}{\bar{T}\bar{v}_s(z)}\int_0^z\left[\frac{\partial^2\alpha}{\partial y^2}\left(\frac{\int_\sigma^z \bar{v}ds}{\bar{v}_s(z)}\right)^2+\alpha\left(1+\frac{\bar{v}^2(\sigma)}{\bar{v}_s^2(z)}\right)\right]\frac{d\sigma}{\bar{v}}. \quad \text{(A-21)}$$

Explicit Depth Extrapolation Filters for Transverse Isotropic Media

Omar Uzcategui

Center for Wave Phenomena
Colorado School of Mines
Golden, Colorado 80401
(303) 273-3557

Explicit Depth Extrapolation Filters for Transverse Isotropic Media

Omar Uzcategui

ABSTRACT

Stable explicit depth extrapolation filters have been used recently in the downward continuation of seismic wavefields for isotropic 2D and 3D migration. Similar filters can also be developed for transversely isotropic (TI) media. The downward continuation operator for TI media has basically the same form as that for isotropic media, but now the phase velocity is a function of the propagation angle. Therefore, for a given frequency, the wavenumber k_x will no longer be a function of a single velocity, a fact that has to be considered in the design of the filter.

A constrained least-squares method is used to calculate N-coefficients of a finite-length filter such that the amplitude and phase errors with respect to the ideal response of the downward continuation operator are minimized for a given range of propagation angles. In the evanescent region, the amplitude response of the filter is forced to be less than unity in order to get stability.

I have obtained explicit depth-extrapolation filters that do the propagation of plane waves corresponding to the qP (quasi-p propagation) mode for a transversely isotropic medium. The resulting operators are stable and give accurate results for the range of angles used in the design of the filter.

INTRODUCTION

Depth extrapolation of seismic wavefields is a fundamental process used in various algorithms for depth migration. Traditionally, implicit methods based on finite-difference algorithms (Claerbout, 1985) are used to get the extrapolated wavefield. However, the use of explicit depth extrapolation filters (Holberg, 1988; Hale, 1991) has become now as an important and efficient alternative to accomplish this goal.

For transversely isotropic media, explicit depth extrapolation filters can be obtained following the same steps used in the isotropic case but now considering the anisotropic nature of the phase-velocity. The Taylor series method, which tries to match the first N terms corresponding to the Taylor series of the Fourier transform of the filter to the desired response, could not be applied for TI media, because the matching of the derivatives is done for vertical propagation ($k_x = 0$) and only the vertical velocity is considered in the design of the filter. Another approach (Holberg, 1988) is try to minimize the amplitude and phase error of the filter in a given range of propagation angles. By doing this, we are considering the different values that the phase velocity takes for different propagation angles, so the anisotropic characteristics of the phase velocity are taken into acount in the design of the filters.

In addition to the minimization of the amplitude and phase errors, it is also desired that the amplitude response of the filter be equal to unity in the propagation region (to avoid growing or decaying of this energy) and less than unity outside the range of propagation angles (i.e., in the evanescent region to get stability). This leads to the solution of a non-linear constrained least squares problem.

FILTER DESIGN

The theoretical downward-continuation operator for transversely isotropic media can be obtained from the equations of motion for elastic plane waves propagating in the vertical plane (x, z) (Kitchenside, 1991). The solution for the qP propagation mode can be expressed as,

$$k_z = \frac{\omega}{V_p(\theta)} cos(\theta) \qquad k_x = \frac{\omega}{V_p(\theta)} sin(\theta), \tag{1}$$

with

$$V_p^2(\theta) = \alpha_0^2(1 + \epsilon sin^2(\theta) + D(\theta)^*), \tag{2}$$

where k_z is the vertical wavenumber, ω is the frequency in radians, θ is the phase propagation angle with respect to the vertical axis, $V_p(\theta)$ is the phase velocity for the qP propagation mode and α_0 is the vertical velocity $[V_p(0)]$, ϵ and $D^*(\theta)$ are functions of the elastic constants of the medium (Thomsen, 1986).

After obtaining the downward-continuation operator for transversely isotropic media, the basic problem in the construction of explicit depth extrapolation filters is; for a given frequency ω, try to find N coefficients W_l of a finite-length filter with a Fourier transform $W(k)$ that "matches" the theoretical Fourier transform of the downward extrapolation operator given by

$$D(k_x(\theta), \omega) = exp\left\{ i\Delta z \frac{\omega}{V_p(\theta)} \left(1 - \frac{k_x^2(\theta) V_p^2(\theta)}{\omega^2} \right)^{\frac{1}{2}} \right\}, \tag{3}$$

where Δz is the vertical sampling interval. We want to do the matching over just a range of propagation angles ($\theta = 0 \ldots \theta_{max}$), or equivalently, over a range of wavenumbers $|k_x| < \frac{\omega sin(\theta_{max})}{V_p(\theta_{max})}$. Also, for stability in the evanescent region we impose the condition $|W(k_x)| < 1.0$.

The match with the theoretical response of the extrapolation operator has to be done following some error criteria. Following Holberg's (1988) criteria, we do the matching by minimizing the sum of the square errors in the amplitude and phase responses of the filter,

$$J(k_x, w) = \int_{\theta=0}^{\theta=\theta_{max}} (\delta^2 + \alpha^2) dk_x, \tag{4}$$

subject to the constraints $|W(k_x, \omega)| = 1.0$ for $|k_x| < \frac{\omega sin(\theta_{max})}{V_p(\theta_{max})}$ and $|W(k_x, \omega)| < 1.0$ for $|k_x| > \frac{\omega sin(\theta_{max})}{V_p(\theta_{max})}$. Here, α is the amplitude error of the filter given by $\alpha = 1.0 - |W(k_x, \omega)|$, and δ is the phase error of the filter given by $\delta = k_z \Delta z - tan^{-1} \frac{Im(W(k_x,\omega))}{Re(W(k_x,\omega))}$.

Due to the symmetry with respect to k_x of the downward-continuation operator, the filter coefficients must also have this symmetry so that we need work with only a half-length of the operator. Then, the complex response of the filter will be given by

$$W(k_x, \omega) = \sum_{j=0}^{j=N} 2w_r(j) \cos(k_x j \Delta x) + \sum_{j=0}^{j=N} 2w_i(j) \cos(k_x j \Delta x), \tag{5}$$

with Δx equal to the sampling interval in the x direction, and $w_r(l)$ and $w_i(l)$ the real and imaginary parts of the l^{th} coefficient of the filter.

For the minimization of (4) I used the IMSL subroutine *NCONF*, which solves a non-linear minimization problem subject to non-linear constraints, such as those impossed following equation (4). The number of constraints used in a given calculation depends on the number of filter-coefficients desired. In general, stable results are obtained when the total number of constraints used is equal to one-half of the total number of filter coefficients.

NUMERICAL APPLICATION

Depth-extrapolation filters were calculated for a homogenous medium whose elastic constants correspond to the so called Taylor sandstone (Thomsen, 1986). The vertical P-wave velocity for this sandstone is $\alpha_0 = 3368\ m/s$ and the vertical shear wave velocity is $\beta_0 = 1829\ m/s$. The ratio of the horizontal to the vertical P-wave velocity for this sandstone is almost 1.1.

In Figures 1 and 2 we see the amplitude response and the amplitude error of the filter calculated for a single frequency of $\omega = 2\pi(20)$. A filter of 23 coefficients (half-length=12) was used, and a maximum angle of propagation of $\theta = 75°$ was

considered. For this example we use $\Delta x = \Delta z = 10$ m. We can see that for almost all the propagation region ($k_x < 0.07$) the amplitude error in the filter is very small (less than 1/1000). This means that we can apply this filter for at least 1000 steps of depth extrapolation, getting an amplification or reduction factor less than 2.7169 for this given frequency.

In Figure 3, we see the phase error response in cycles for the same frequency ($f = 20\ Hz$). In general, the phase error is small for propagating angles less than 60° ($\Delta\delta < 0.05$ cycles). Near to $\theta_{max} = 75°$ and beyond, the phase error reaches a maximum of 0.01 cycles.

Figure 4 shows a contour display for the amplitude error for the range of frequencies $0 \leq f \leq 50$. The white areas correspond to amplitude errors less than 0.001. The darkest areas correspond to amplitude errors of more than 0.01. We can see that for the propagation region, the filter error is very small (< 0.001). In the evanescent region, the darkest areas correspond to amplitudes less than 0.99, so in general, we get stability in this region because the amplitude values are less than unity.

Figure 5 shows a contour display for the phase error in the propagation region ($\theta = 0, \ldots, 90°$). The thin contours correspond to phase errors equal to 0.01 cycles and the thick ones correspond to phase errors of 0.1 cycles. In general, the phase error is large for the high frequencies ($f > 30\ Hz$) and for angles greater than 60°. The results obtained for the phase error are not so good as those for the amplitude error. Holberg (1988) pointed out that a better result could be obtained by considering in the minimization process the derivatives of the amplitude and phase error with respect to ω and k_x. We should also note that we did not impose any constraints about the phase error, so this error was allowed to change with more freedom than that for the amplitude error.

CONCLUSION

The methodology used to obtain depth-extrapolation filters for an isotropic medium can be easily extended to the case of transversely isotropic media. It is necessary to consider only the changes in the phase velocity with respect to the propagation angle when we do the calculation of the theoretical depth-propagation operator. A method that tries to match the filter response with the theoretical operator for different wavenumbers or propagation angles was considered. This approach differs from that used in the Taylor series method for isotropic media, where the match of the filter and theoretical response is done for only vertical propagation ($k_x = 0$). For TI media, phase-velocity values for different propagation angles need to be considered. In this way, the anisotropic character of the phase velocity is taken into account in the design of the filters.

Filter coefficients were calculated by solving a minimization problem subject to non-linear constraints in the amplitude response of the filter. The accuracy in the amplitude response obtained with the filters for TI media is comparable with that

obtained by Holberg (1988) and Hale (1991) for isotropic media. However, the phase response needs to be improved. The use of constraints for the phase error and the minimization of not only the phase and amplitude errors, but also their gradients with respect to ω and k_x, could improve the phase response.

ACKNOWLEDGMENTS

Thanks to Ken Larner for his review of this paper. This project is supported by the members of the Consortium Project on Seismic Inverse Methods for Complex Structures at the Center for Wave Phenomena, Colorado School of Mines.

REFERENCES

Claerbout, J. F., 1985, Imaging the earth's interior: Blackwell Scientific Publications, Inc.

Kitchenside, P. W., 1991, Phase shift-based migration for transverse isotropy: 61 th Ann. Internat. Mtg., Soc. Expl. Geophys., Expanded Abstracts, 993–946

Hale, I. D., 1991, Stable explicit depth extrapolation of seismic wavefields: Geophysics, **56**, 1770–1777.

Holberg, O., 1988, Toward optimum one-way wave propagation: Geophys. Prosp., **36**, 99–114.

Thomsen, L., 1986, Weak elastic anisotropy: Geophysics, **51**, 1954–1966

Uren, N. F., Gardner G. H. F., and McDonald, J. A., 1990, The migrator's equation for anisotropic media: Geophysics, **55**, 1429–1434.

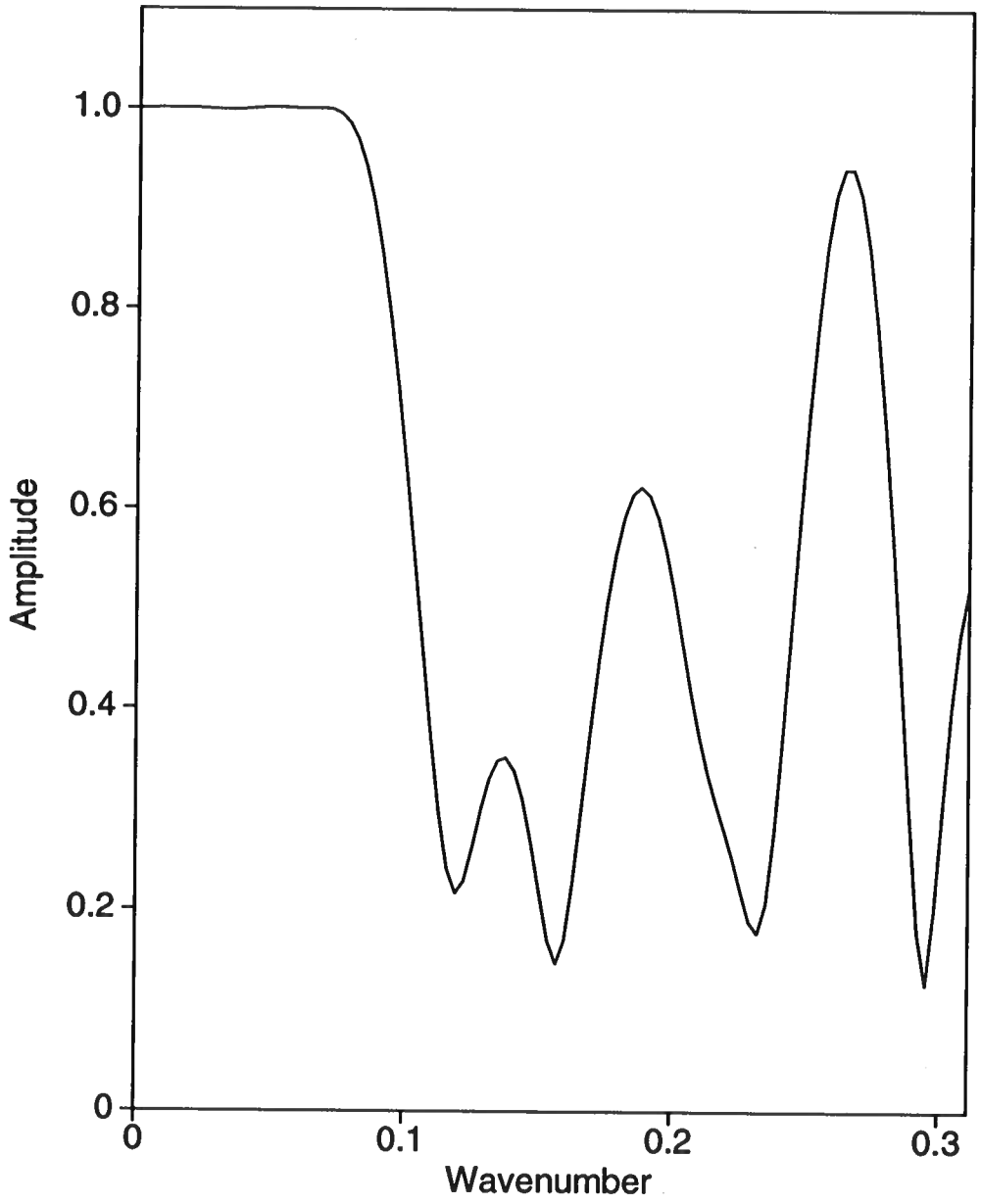

FIG. 1. Amplitude response of the filter (N=23) for a frequency of 20 Hz.

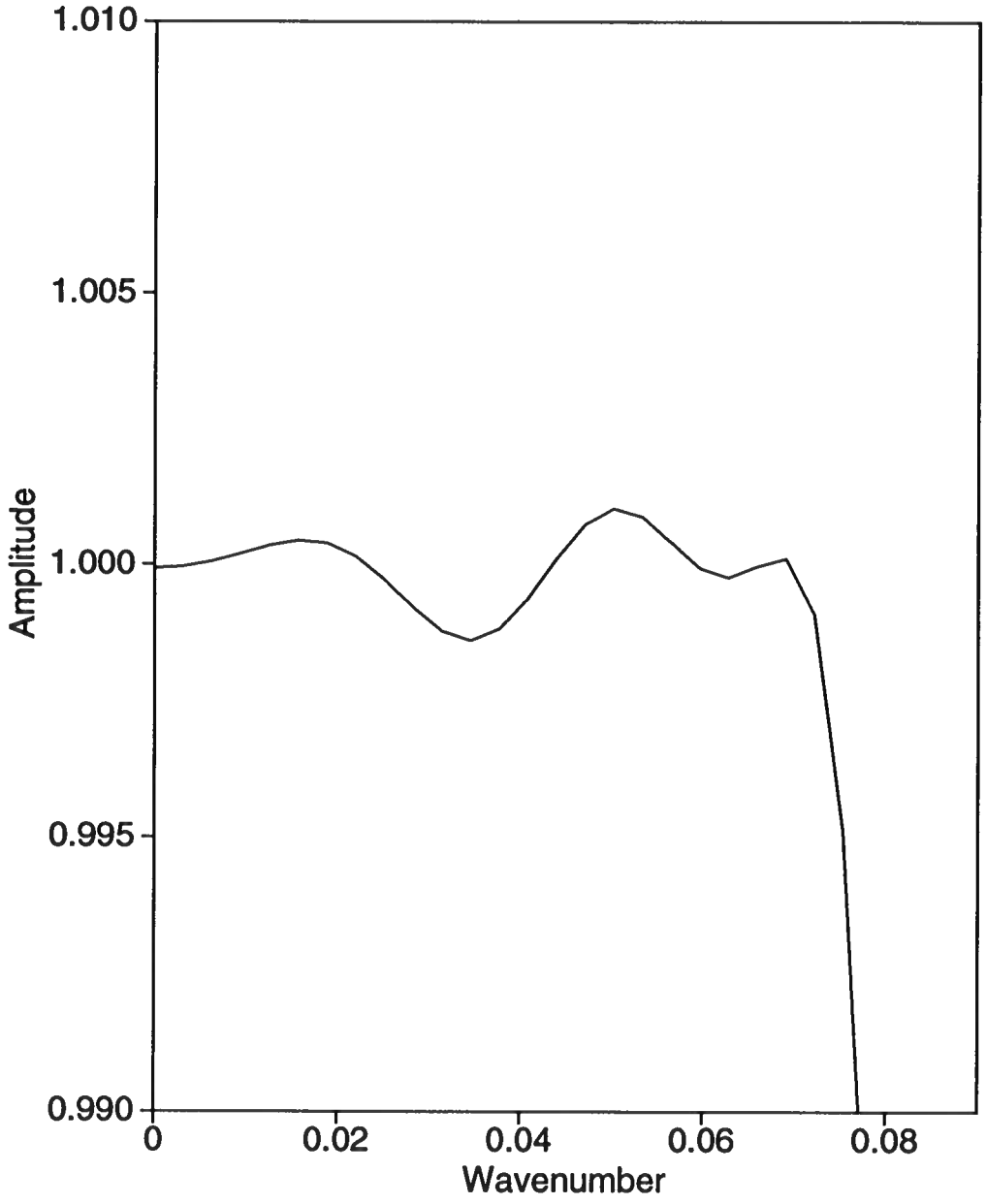

FIG. 2. Magnification of the amplitude response in Figure 1 showing an amplitude error less than 0.001 for the propagation region.

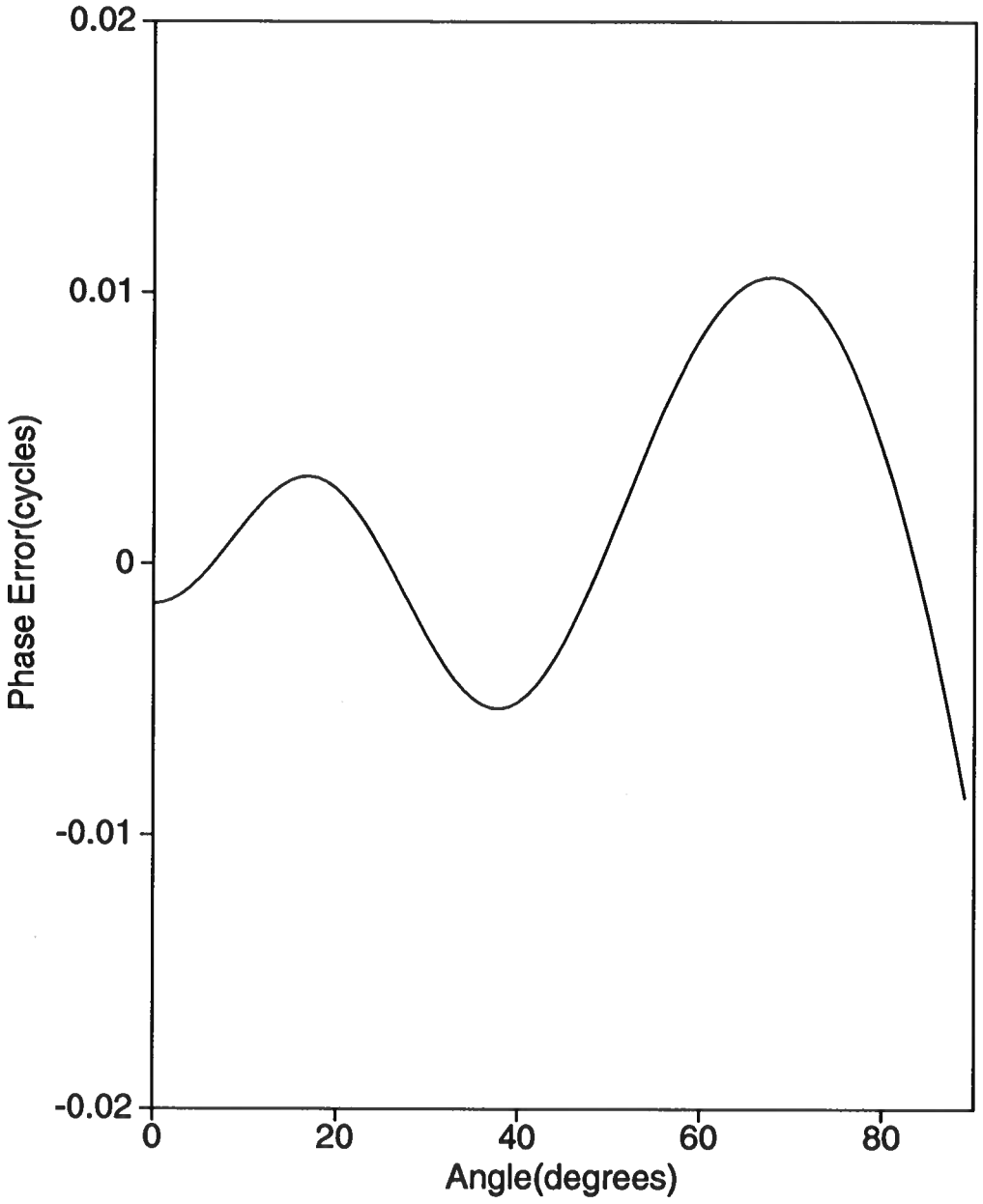

FIG. 3. Phase error for the same filter (N=23) considered in Figures 1 and 2, and for f=20 Hz.

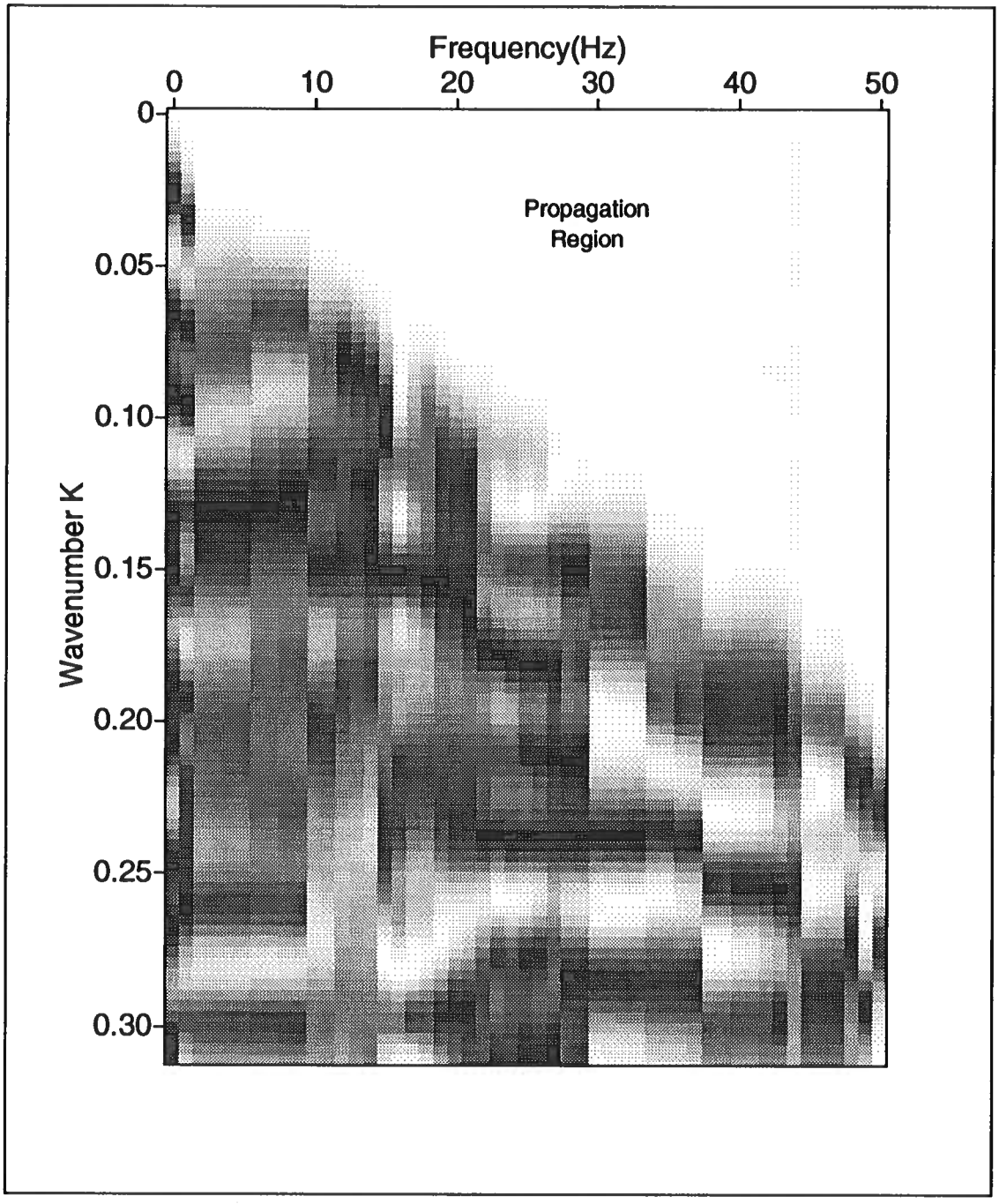

FIG. 4. Amplitude-response error for frequencies between 0 and 50 Hz. White zones correspond to errors less than 0.001. Black zones correspond to errors greater than 0.01.

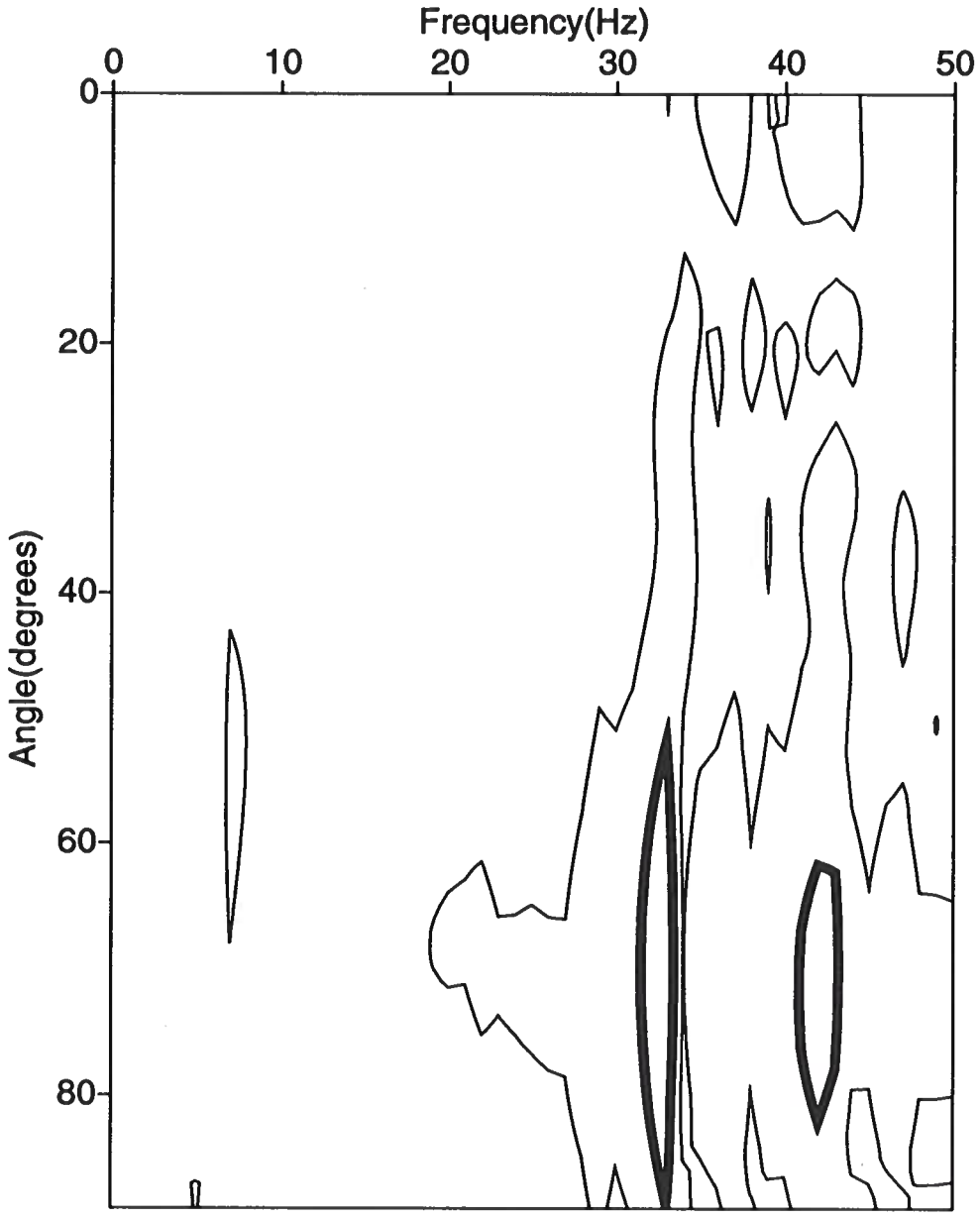

FIG. 5. Phase error for frequencies between 0 and 50 Hz. Thin contours correspond to errors of 0.01 cycles. Thick contours correspond to errors equal to 0.1 cycles.

Sponsors Mailing List: Technical Contacts

The Center for Wave Phenomena gratefully acknowledges the support of the companies listed here. We provide this list as a convenience to the sponsors.

Advance Geophysical Corp.
Mr. S. Rutt Bridges
7409 S. Alton Ct., Suite 100
Englewood, CO 80112

Amerada Hess Corp.
Dr. J. Bee Bednar
Geophysical Computer Applications
P.O. Box 2040
Tulsa, Oklahoma 74102

Amoco Production Co.
Dr. Samuel L. Gray
Research Center
P.O. Box 3385
Tulsa, OK 74102

ARAMCO
Mr. James L. White
PE & E Department
P.O. Box 4534
Houston, TX 77250-4534

ARCO Exploration and Production Technology
Dr. Dennis Corrigan
2300 West Plano Parkway
Plano, TX 75075-8499

BP Exploration Inc.
Dr. Bruce G. Secrest
BP/Statoil Alliance
Ranheimsveien 10
Postutt
N-7004
Norwa

CWP-121

Bure
Mr. X
P.O. I
Zhou
Peopl

Con
Mrs.
6, ru
9134
Frar

Chevron Oil Field Research Co.
Dr. Leroy C. Pusey
Exploration Research Department
P.O. Box 446
La Habra, CA 90633

Conoco, Inc.
Dr. Doug Hanson
Exploration Research Division
1000 South Pine
Ponca City, OK 74603

Errata for

Migration Error in Transversely Isotropic Media with Linear Velocity Variation in Depth

Ken Larner and Jack K. Cohen

To be inserted in Project Review,
May 26-29, 1992,
CWP-121

Center for Wave Phenomena
Colorado School of Mines
Golden, Colorado 80401
(303) 273-3557

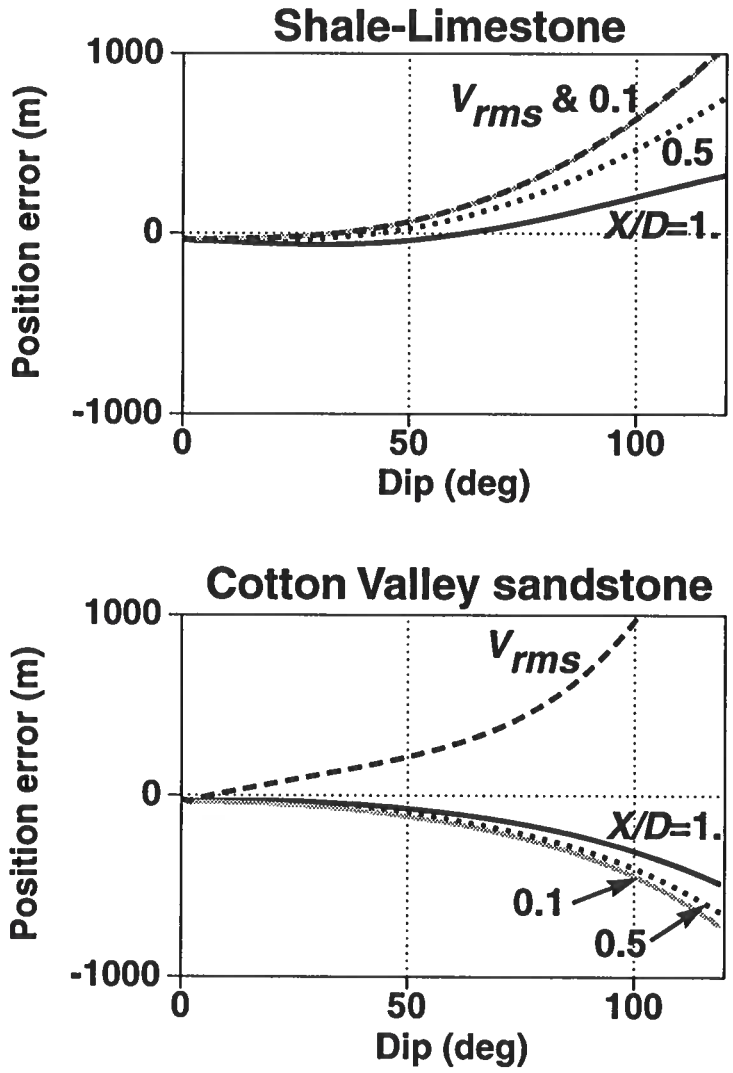

FIG. 7. Position error Δy versus reflector dip for shale-limestone (top) and Cotton Valley shale (bottom). For each, the reflector depth is $D = 1500$ m and the vertical velocity gradient is $k = 0.6$ s^{-1}. For the dashed curve, the $v(z)$ velocity function used for migration is derived from the vertical rms velocity to the reflector. For the other three curves, the $v(z)$ velocity function used for migration is derived from the stacking velocity to a horizontal reflector at depth D, with different choices of ratio of spread-length to depth X/D used in the stacking-velocity computation.

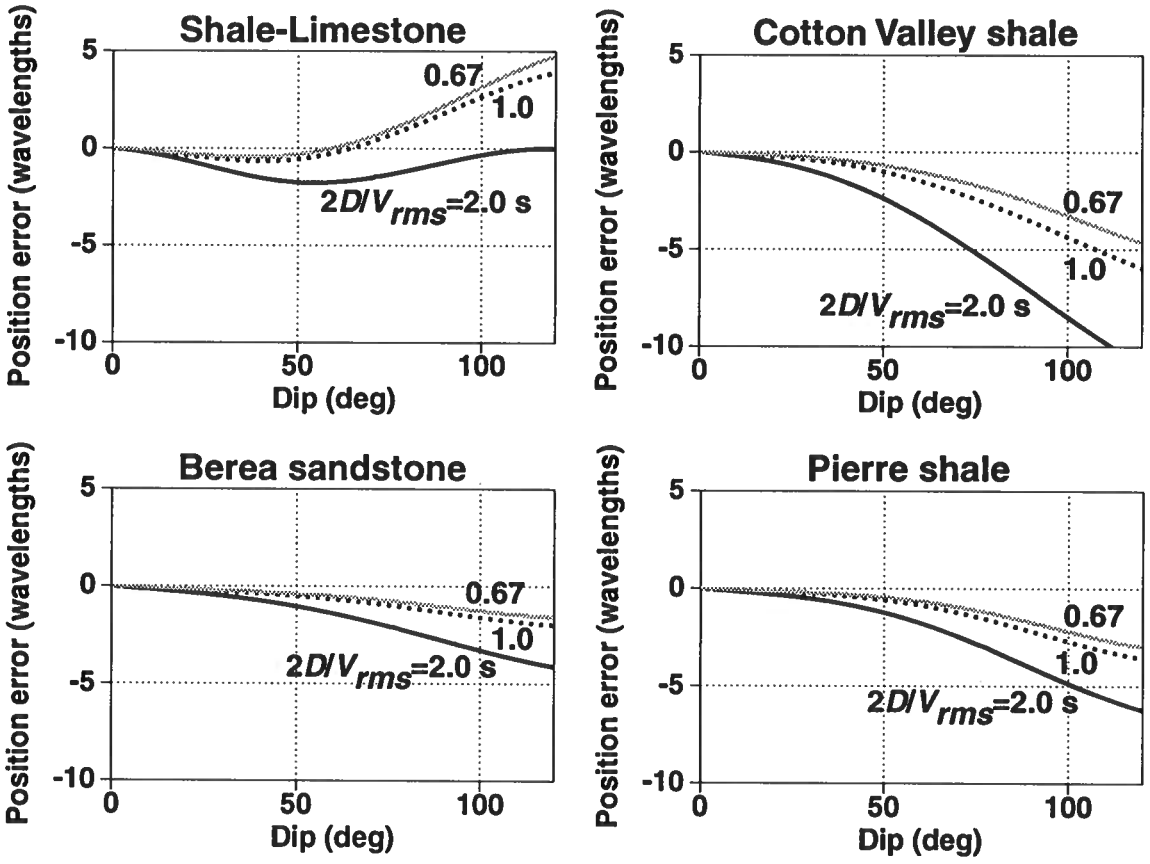

FIG. 14. Normalized position errors as a function of reflector dip for the four media listed in Table 1, for three values of approximate migrated reflection time $2D/V_{rms}$. All models have the same velocity gradient, $k = 0.6\ \mathrm{s}^{-1}$.